

University of Warwick institutional repository: <http://go.warwick.ac.uk/wrap>

A Thesis Submitted for the Degree of PhD at the University of Warwick

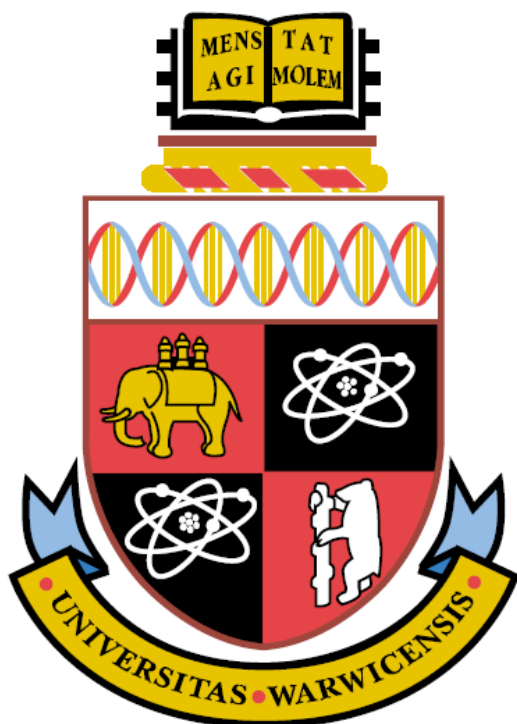
<http://go.warwick.ac.uk/wrap/67018>

This thesis is made available online and is protected by original copyright.

Please scroll down to view the document itself.

Please refer to the repository record for this item for information to help you to cite it. Our policy information is available from the repository home page.

The use of zinc oxide in hybrid inorganic-organic photovoltaic devices



By Chloe Louise Argent Dearden

A thesis submitted for the degree of **Doctor of Philosophy**
at the University of Warwick

Supervised by Prof. Tim S. Jones
Department of Chemistry
University of Warwick, Coventry

January 2015

Abstract

Organic photovoltaics (OPV) and hybrid organic-inorganic photovoltaics (HOPV) have the potential to provide alternative and economical energy sources; with the long-term goal of delivering renewable resources with longevity. Recent improvements in cell design and material combinations have revealed the true potential of this field. For this to be reached, continuous advancements in materials, concept development, encapsulation and scientific understanding are necessary.

This thesis focuses on the use of zinc oxide (ZnO) in the field of both HOPVs and OPVs. ZnO had been successfully implemented for decades in a range of applications, including light emitting diodes and biological sensors due to its diverse chemical and physical properties along with the ease of fabrication. Initially ZnO is investigated as a direct replacement for a fullerene acceptor offering the potential of improved energetic matching to the donor material used. The latter stages of this thesis looks at the use of ZnO as an electron extracting layer for a polymeric active layer.

Chapter 1 provides a brief introduction to the field of photovoltaics and the materials used in this thesis. In **Chapter 2** an overview of the experimental techniques used is given. In **Chapter 3**, inverted HOPV devices are fabricated. The potential of ZnO as a promising electron acceptor is shown, utilizing the donor material boron subphthalocyanine chloride (SubPc), a typical small molecule (SM) organic semiconductor. X-ray photoelectron spectroscopy (XPS) shows subtle differences in the electronic structure of ZnO films in terms of Zn:O ratio when the processing temperature is varied, and Kelvin Probe (KP) revealed a significant difference in the surface work function. Variation in annealing temperature is shown to improve the open circuit voltage (from 0.82 V to 1.23 V) of the device and therefore enhance the performance.

Chapter 4 compares two methods used to probe energy levels. The chapter compares the differences between the data obtained for identical ZnO samples using ultra-violet photoelectron spectroscopy (UPS) and KP. The surface composition is also monitored throughout by XPS. The chapter reveals that ZnO is susceptible to UV irradiation and the impact on the measurements is discussed.

One of the main limitations of the planar HOPV is photocurrent. **Chapter 5** looks to improve this through the implementation of a molybdenum oxide (MoO_x) optical spacer layer. Optical modelling is initially used to predict the impact of varying the layer thickness of SubPc and MoO_x . The model is developed further by including the diffusion length (L_D) of the SubPc donor material. The improved estimates are compared to an experimental data set of 40 different thickness combinations. Optical optimisation resulted in a 62 % improvement in device performance, compared to the layer thicknesses used in **Chapter 3**.

The use of ZnO as an electron extracting layer with a polymeric active layer is investigated in **Chapter 6**. Two methods for ZnO layer formation, electrodeposition (ED) and sol-gel (SG) are compared using two different transparent electrodes, indium tin oxide (ITO) and transparent gold (tAu). ED ZnO layers have issues with transparency and reproducibility lowering the overall averaged performance.

This thesis highlights the important role ZnO can play in the development of OPV and HOPV devices. The research provides an important step for understanding the fundamental principles governing the operation of hybrid solar cells and helps to close the gap between TMO/polymer and TMO/SM devices. The performances of these TMO/SM devices reach efficiencies exceeding 0.70 %, compared to previous published devices only reaching 0.017 %.

Contents

Abstract	i
Contents	iii
Declaration	vii
Acknowledgments.....	viii
List of Publications	x
List of presentations	xi
Abbreviations	xiii
General Abbreviations.....	xiii
Symbols/Notations	xvi
Chemical Compounds	xix
1 Introduction	1
1.1 World Energy Review	1
1.2 History of Photovoltaics	4
1.2.1 Advances in Small Molecule Organic Photovoltaics.....	7
1.3 Hybrid Devices.....	10
1.3.1 Material Groups	10
1.3.2 Other ‘Hybrid’ Cells	16
1.4 Basic Semiconductor Theory	18
1.5 Working Principles of OPVs	22
1.5.1 Absorption of Incident Photon η_A	23
1.5.2 Exciton Diffusion η_{ED}	25
1.5.3 Exciton Dissociation η_{CT}	27
1.5.4 Charge Collection η_{CC}	29
1.6 Material Properties	30
1.6.1 Electrodes and Interlayers	30
1.6.2 Zinc Oxide.....	33
1.6.3 Photoactive Materials.....	36
1.7 Thesis Outline.....	43
2 Experimental	45
2.1 Layer Preparation	45
2.1.1 Substrate Cleaning	45

2.1.2	Solution Processing.....	45
2.1.3	Vacuum Deposition.....	51
2.2	Thin Film Analysis.....	54
2.2.1	Absorption spectroscopy.....	54
2.2.2	Photoluminescence Spectroscopy.....	55
2.2.3	Ellipsometry.....	57
2.2.4	Optical Modelling.....	59
2.2.5	Atomic force microscopy.....	60
2.2.6	Electron Microscopy.....	64
2.2.7	X-Ray Diffraction.....	66
2.3	Energetic Characterisation.....	68
2.3.1	Kelvin Probe.....	68
2.3.2	Photoelectron Spectroscopy.....	71
2.4	Device Characterisation.....	77
2.4.1	Sun and Solar Spectrum.....	77
2.4.2	Current density-voltage Curves.....	79
2.4.3	External Quantum Efficiency.....	83
3	Hybrid Device Fabrication.....	86
3.1	Introduction.....	86
3.1.1	Hybrid Devices.....	86
3.1.2	Aims.....	88
3.2	Film Optimisation.....	89
3.2.1	Sol-gel process.....	89
3.2.2	Morphology Control.....	90
3.3	Characterisation of the Optimised Layer.....	96
3.3.1	Conductivity of ZnO layer.....	96
3.3.2	Absorption spectroscopy.....	98
3.3.3	Quenching Ability.....	99
3.3.4	Energetic Analysis.....	100
3.4	Impact of processing temperature.....	104
3.5	Device Fabrication.....	108
3.6	Donor Layer Comparison.....	112
3.7	Conclusions.....	115

4	Evaluation of energetic measurement techniques	116
4.1	Introduction	116
4.1.1	Aims	118
4.2	UPS Studies on ZnO.....	119
4.2.1	Probing energy levels of sol-gel ZnO _{120 °C}	119
4.2.2	Probing energy levels of sol-gel ZnO _{160 °C}	121
4.3	Comparison of Techniques.....	122
4.3.1	Charge neutrality level	123
4.4	Film Stability with Various Techniques.....	125
4.4.1	UPS	125
4.4.2	XPS	133
4.4.3	KP with light	135
4.5	Conclusion.....	138
5	Optical Spacing	140
5.1	Introduction	140
5.1.1	Background	140
5.1.2	Aims	143
5.2	Film Optimisation and Characterisation.....	144
5.2.1	Sol-gel process	144
5.2.2	Morphology and Structure	144
5.2.3	Absorption spectroscopy.....	146
5.2.4	Refractive index	148
5.3	Optical Modelling.....	150
5.3.1	Electric Field	150
5.3.2	Predicted Current Generation.....	153
5.4	Device Fabrication	156
5.5	Conclusion.....	161
6	Electron Extracting Layers.....	162
6.1	Aims	162
6.2	SubPc/C ₆₀ system.....	163
6.2.1	Absorption Spectroscopy	163
6.2.2	Regular vs Inverted Devices	163
6.2.3	ZnO as an ETL.....	167

6.3	ZnO with polymer blend	169
6.3.1	Transparent Conductive Electrodes	169
6.3.2	Deposition Techniques.....	170
6.3.3	Transmittance.....	171
6.3.4	Surface Morphology and Conductivity.....	172
6.3.5	Structural Characterisation.....	182
6.3.6	Compositional Differences.....	184
6.3.7	Work function measurements	186
6.3.8	Device Performance	188
6.4	Conclusions	193
7	Conclusions and Future Work.....	195
7.1	Overview	195
7.1.1	ZnO as an acceptor material.....	195
7.1.2	Probing material energetics.....	197
7.1.3	Improvement in J_{SC}	198
7.1.4	ZnO as an Efficient Electron Extracting Layer.....	199
7.2	Future work	201
	References.....	203

Declaration

This thesis is submitted to the University of Warwick in support of my application for the degree of Doctor of Philosophy. It has been composed by myself and has not been submitted in any previous application for any degree.

I declare I carried out the work presented, except where specifically stated otherwise, (including data generated and data analysis) in the Department of Chemistry at the University of Warwick between October 2010 and September 2014 under the supervision of Prof. Tim Jones.

The XPS and UPS measurements (**Chapter 3, 4, 5**) were carried out by Dr. Marc Walker, Department of Physics, University of Warwick. I prepared all films prior to the experiments and carried out the subsequent data analysis.

In **Chapter 5**, the refractive index data for ZnO and MoO_x films was obtained by Dr. James Bowen, School of Chemical Engineering, University of Birmingham. The transfer matrix simulations were carried out on a program adapted by Dr. Thomas Howells.

The CAFM data was obtained by Dr. Ian Hancox on films I had prepared and I completed the subsequent data analysis.

In **Chapter 6** the transparent gold films were produced by Dr. Helena Stec, Department of Chemistry, University of Warwick. The electrodeposition ZnO films, and XRD analysis was carried out by Dr. Amy Cruickshank, Materials, Imperial College London.

Acknowledgments

Firstly I would like to thank Prof. Tim Jones for his help and support throughout the PhD and for giving me the opportunity to work in the field of organic photovoltaics at the University of Warwick. I am eternally grateful for all the opportunities that have arisen from working in this field, being part of cutting edge research has given me opportunities to travel across the globe to present my research and to collaborate with other universities. I have thoroughly enjoyed this challenging and rewarding part of my studies.

I would like to thank the Department of Chemistry for funding via the Engineering and Physical Sciences Research Council (EPSRC) grant. My thanks also go to everyone in the department that has helped make the past four years run smoothly. I would also like to thank everyone that I have been luckily enough to work with during my time at Warwick: Prof Chris McConville and Marc Walker; Prof Ross Hatton and Dr Helena Stec; Prof Mary Ryan, Amy Cruickshank and Fatemeh Pisbin; Dr. James Bowen; and Prof Tim Bender and the entire Prof. Bender group.

I would of course like to thank all of the Tim Jones Group (Paul, Ian, Stefan, Raff, Tomasz, V, Mark, Tom, Nicola, Jay, Luke, Edd, Nat, Gavin, Ricky, Dawn and all our MChems) and the Hatton Group (Helena, Oli and Martin) for their help, support and amusement along the way. I would particularly like to thank Paul and Ian for their guidance and patience both in experimental work and the fun job of reading my thesis! I would like to thank Nicola for all laughs, plentiful cups of tea and keeping me sane throughout both my PhD and MChem. Nat and Gavin, I am so glad we went through this challenge together and I can't wait to celebrate properly once we all

have finished! Nat, thanks for keeping me together, organised and all the swimming lessons (just to name a few reasons), Gavin thanks for the natters, and pints whilst watching football. Ed(d), fellow C110 member, thanks for all the pub trips and amusing moments. Ricky, I am at a loss of what to write, you were sadly taken from us too soon. Thank you for my crash course in organic chemistry before my trip to Toronto, you are deeply missed and will never be forgotten.

My thanks of course also go to all my friends that I have made during my eight years at the University of Warwick (Tachbrook Street, Hit and Miss, Girl Guiding, Nic and Tassie bunch, just to name a few). If it wasn't for all of you, I would not have made it this far or even considered doing a PhD. You have all been a part of some of the most enjoyable years of my life, with many great memories and stories and I am looking forward to many more to come.

Last but not least I would like to thank all of my family; I would like to thank my grandparents for their love and support since I was a little girl. Mum, Hannah and Beth, thank you for everything, I love you three so much and would not have got here without you.

List of Publications

Publications:

High Voltage Hybrid Organic Photovoltaics using a Zinc Oxide Acceptor. **C. Argent Dearden**, M. Walker, N. Beaumont, I. Hancox, N. K. Unsworth, P. Sullivan, C. F. McConville, T. S. Jones. *Phys. Chem. Chem. Phys.*, 2014, 16, 18926-18932

Highly conductive spray deposited poly(3,4-ethylenedioxythiophene):poly(styrenesulfonate) electrodes for indium tin oxide-free small molecule organic photovoltaic devices. N. K Unsworth, I. Hancox, **C. Argent Dearden**, T. Howells, P. Sullivan, R.S. Lilley, J. Sharp and T.S. Jones, *Appl. Phys. Lett.*, 2013, 103, 173304

Comparison of dimethyl sulfoxide treated highly conductive poly(3,4-ethylenedioxythiophene):poly(styrenesulfonate) electrodes for use in indium tin oxide-free organic electronic photovoltaic devices N.K. Unsworth, I. Hancox, **C. Argent Dearden**, P. Sullivan, M. Walker, R. S. Lilley, J. Sharp, T.S. Jones. *Organic Electronics*, 15, 2014, 2624 - 2631

Organic Photovoltaic Cells Utilizing ZnO Electron Extraction Layers Produced Through Thermal Conversion of ZnSe E. New, I. Hancox, L. Rochford, M. Walker, **C. Argent Dearden**, C. F. McConville, T. S. Jones. *J. Mater. Chem. A*, 2, 2014, 19201 - 19207

Submitted:

Morphological Control of ZnO Nanostructures Electrodeposited on to Molecular Thin Films A. C. Cruickshank, S. E. R. Tay, B. Illy, **C. Argent Dearden**, Tim S. Jones, M. A. McLachlan, D. W. McComb, D. J. Riley, S. E. Heutz and M. P. Ryan.
Submitted.

List of presentations

- Poster - 18th Interdisciplinary Surface Science Conference, April 2011, University of Warwick, UK
- Poster - Frontiers in Organic, Dye-sensitized and Hybrid Solar Cells, June 2011, Krutyn, Poland
- Poster - Organext “Photovoltaics at the nanoscale,” October 2011, Hasselt University, Belgium
- Poster - Society for Information Display Organic Electronics, September 2011, Imperial College London, UK
- Poster – Postgraduate Research Symposium, May 2012, University of Warwick, UK
- Contributing speaker, The 2013 Materials Research Society Fall Meeting & Exhibit, December 2012, Boston, USA
- Contributing speaker, Monash-Warwick Symposium, February 2013, University of Warwick, UK
- Contributing speaker, The 5th International Conference on Hybrid and Organic Photovoltaics, May 2013, Seville, Spain

- Contributing speaker, Postgraduate Symposium, May 2013, University of Warwick, UK
- Visiting speaker, June 2013, University of Toronto, Canada
- Contributing speaker, 11th International Conference on Materials Chemistry, July 2013, University of Warwick UK

Abbreviations

General Abbreviations

AFM	Atomic force microscopy
AM	Air mass
AO	Atomic orbital
BHJ	Bulk heterojunction
BP	British Petroleum
BSEs	Back scattered electrons
CAFM	Conductive atomic force microscopy
CB	Conduction band
CBM	Conduction band minimum
CNL	Charge neutrality level
CPD	Contact potential difference
CS	Charge separated states
CT	Charge transfer
CV	Cyclic voltammetry
D/A	Donor/acceptor
DSSC	Dye Sensitised Solar Cell
EA	Electron affinity
ED	Electrodeposition
EIA	Energy Information Administration
EM	Electron microscopy
EQE	External quantum efficiency
ETL	Electron transporting layer

FEG-SEM	Field emission gun scanning electron microscope
FWHM	Full width at half maximum
HOMO	Highest occupied molecular orbital
HOPG	Highly oriented pyrolytic graphite
HOPV	Hybrid organic photovoltaics
HTL	Hole transporting layer
IL	Interfacial layer
IP	Ionisation potential
IPA	Isopropyl alcohol
IPES	Inverse Photoemission Spectroscopy
IQE	Internal quantum efficiency
ISC	Intersystem crossing
ITO	Indium-tin oxide
KP	Kelvin Probe
LIXPS	Low intensity x-ray photoemission spectroscopy
LUMO	Lowest unoccupied molecular orbital
NASA	National Aeronautics and Space Administration
NREL	National Renewable Energy Laboratory
OLED	Organic light emitting diodes
OMBD	Organic molecular beam deposition
OPV	Organic photovoltaics
PCE	Power conversion efficiency
PES	Photoelectron spectroscopy
PESA	Photoelectron spectroscopy in air
PL	Photoluminescence
PLD	Pulsed laser deposition
PV	Photovoltaic

QCM	Quartz crystal microbalance
RSF	Schofield relative sensitivity factors
SAM	Self Assembled Monolayer
SE	Secondary electrons
SEM	Scanning electron microscopy
SERI	Solar Energy Research Institute
SG	Sol-gel
SIMS	Secondary Ion Mass Spectrometry
TCE	Transparent conductive electrode
TCO	Transparent conductive oxide
TEM	Transmission Electron Microscope
TMO	Transition metal oxide
TW	Terawatts
TWh	Terawatt-hour
UHV	Ultra-high vacuum
UPS	Ultra-violet photoelectron spectroscopy
UV	Ultra-violet
VB	Valence band
XPS	X-ray photoelectron spectroscopy
XRD	X-ray diffraction

Symbols/Notations

Φ	Work function
A	Absorbance
\AA	Angstrom
α	Absorption coefficient
b	Path length
c	Concentration
D	Diffusion coefficient
d_{hkl}	Lattice plane spacing (hkl)
ϵ	Dielectric constant
ϵ_{λ}	Molar extinction coefficient
E_b	Incident electron beam
E_{BE}	Binding energy of electron
E_{cutoff}	Secondary electron cutoff
E_{Fs}	Surface Fermi energy
E_g	Energy gap (optical band gap)
E_{KB}	Kinetic energy of electron
E_{VL}	Vacuum level
ΔE	Energy gap
F	Spectral irradiance
FF	Fill factor
h	Planck's constant
I	Attenuated light
I_b	Electron beam current
I_0	Incident light intensity

I_g	Interface gap
$J-V$	Current density-voltage
k	Extinction coefficient
k	Boltzmann's constant
k_{nr}	Non-radiative decay
k_r	Radiative decay
L	Film thickness
L_D	Exciton diffusion length
n	Refractive index
J_{SC}	Short circuit current density
P_{inc}	Incident optical power density
P_m	Maximum power point
q	Electron charge
R_L	Load resistance
R_q	Surface roughness parameter
R_S	Series resistance
R_{SH}	Shunt resistance
T	Temperature
$TC(hkl)$	Texture coefficient of each specific plane
ν	Frequency of radiation (Hz)
V_{OC}	Open circuit voltage
Δ	Phase difference
Ω	Amplitude ratio
λ	Wavelength
$\Omega \text{ s}^{-1}$	Ohms per square

θ	Angle of incidence
η	Efficiency
η_A	Quantum efficiency of Absorption of Incident Photon
η_{ED}	Quantum efficiency of Exciton Diffusion
η_{CT}	Quantum efficiency of Exciton Dissociation
η_{CC}	Quantum efficiency of Charge Collection

Chemical Compounds

Ag	Silver
AgCl	Silver chloride
Al	Aluminium
APTMS	3-aminopropyltrimethoxysilane
AZO	Aluminium doped zinc oxide
Au	Gold
BCP	Bathocuproine
C ₆₀	Buckminster-Fullerene
ClAlPc	Chloroaluminium phthalocyanine
Cl ₆ -SubPc	Hexachloro boron subphthalocyanine chloride
CdS	Cadmium sulfide
CdSe	Cadmium selenide
Cr	Chromium
CuPc	Copper phthalocyanine
H ₂ Pc	Metal free phthalocyanine
InO	Indium oxide
ITO	Indium tin oxide
KCl	Potassium chloride
MDMO-PPV	Poly(2-methoxy-5-(3',7'-dimethyloctyloxy)-1,4-phenylene-vinylene)
MEH-PPV	Poly(2-methoxy-5-(2'-ethylhexyloxy)-1,4-phenylene vinylene)
MPTMS	3-mercaptopropyltrimethoxysilane
MoO _x	Molybdenum oxide
NiO	Nickel oxide
Pc	Phthalocyanine

PCBM	Phenyl-C ₆₁ -butyric acid methyl ester
PCPDTBT	Poly(2,6-(4,4-bis-(2ethylhexyl)-4H-cyclopenta[2,1-b;3,4-b']dithiophene)-alt-4,7(2,1,3-benzothiadiazole))
PEDOT	Poly(3,4-ethylenedioxythiophene)
PET	Polyethylene terephthalate
PPS	Polystyrene sulfonic acid
P3HT	Poly(3-hexylthiophene)
SnO ₂	Tin oxide
SubPc	Boron Subphthalocyanine
tAu	Transparent gold electrode
TiO _x	Titanium oxide
WO _x	Tungsten oxide
V ₂ O ₅	Vanadium oxide
Zn(NO ₃) ₂	Zinc nitrate
ZnO	Zinc oxide
ZnPc	Zinc phthalocyanine

1 Introduction

1.1 World Energy Review

Global energy demand has been increasing since the Industrial Revolution with vast energy requirements being a necessity for economic development. The U.S Energy Information Administration (EIA) has calculated the energy demand in terawatts (TW) since 1990 and estimated the future demand up to 2035. To date the average consumption is 18 TW worldwide and this is due to reach 25 TW in 2035.¹ Early predictions expect this value to increase to 30 TW by 2050 in line with the growth of developing nations.

Figure 1.1 shows a statistical review of world energy consumption published by British Petroleum (BP). The supply is mainly provided by fossil fuels (approximately 86 %).² The reason for this is simple; fossil fuels are dominant in the energy market due to their abundance, government subsidies and the existing infrastructure from decades of expense. This contribution is significant compared to a field such as renewable energy, which at the moment provides a mere 8.5 % of the annual energy required.

Realistically, fossil fuels can provide sufficient energy for the near future, but supply is not the only concern. Fossil fuels are not a clean source of energy, causing acid rain along with air, water and thermal pollution.³ Climate destruction is also an issue due to the release of harmful gases such as carbon dioxide, methane and nitrous oxides. One alternative energy source that has been suggested is nuclear power, but in light of the recent event in Fukushima in 2011 (with current clean-up cost

estimated to be \$250 billion),⁴ it has to be questioned about its potential as a long-term energy solution.

In an interesting study by Darling *et al.*, the viability of different renewable sources to solve the 30 TW demand is calculated, with the ideal scenario offering a diverse collection of energy sources.⁵ It is estimated that hydropower, wind, ocean and geothermal could only feasibly supply 8 TW,⁶ unlike solar energy that has the potential of supplying 67 TW. This estimate is calculated using reasonable assumptions; solar cells covering 2 % of the Earth's land surface (receiving ~560 TW from the sun), and utilising devices with a power conversion efficiency (*PCE*) of only 12 %.

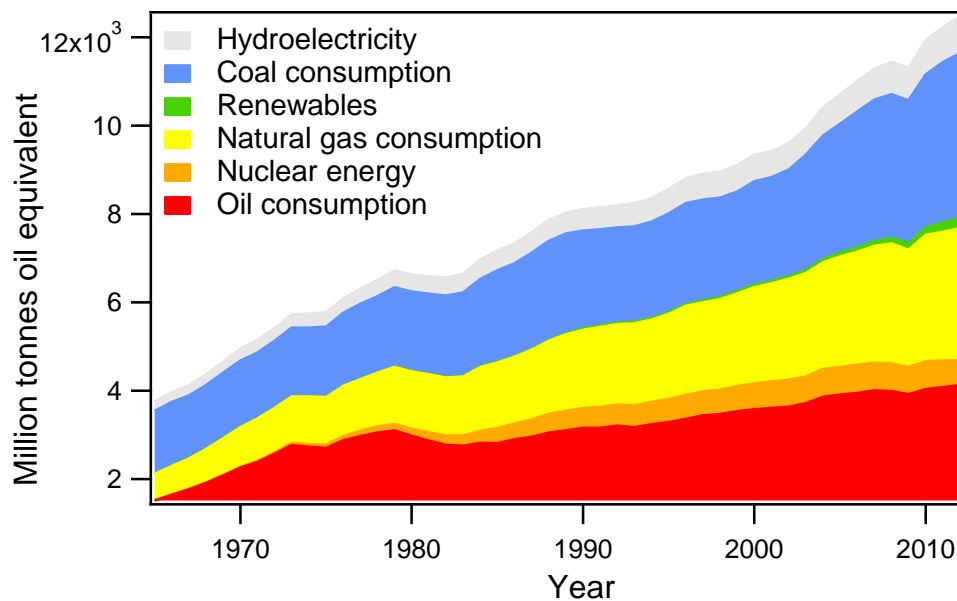


Figure 1.1 Primary energy of world energy consumption of million tonnes of oil equivalent per year. The data was sourced from the BP statistical review of world energy 2013.²

Figure 1.2 shows the cumulative installed photovoltaic (PV) power worldwide, which is currently dominated by Europe, which has a total of 77 % of the PV market.

Germany alone has the largest share of any country worldwide by a substantial margin, with a remarkable 22 % of the cumulative power. In 2013, Germany generated 30 terawatts-hours (TWh) of PV power, which translated as 5.7 % of their net electricity consumption,⁷ with the country regarding PV as an essential source for sustainable energy in the future. Currently Germany produces 29 % of their total net consumption from renewable energy sources, compared to the UK where the latest figures predict this could be 14 % (up from 4.1 % in 2012).⁸

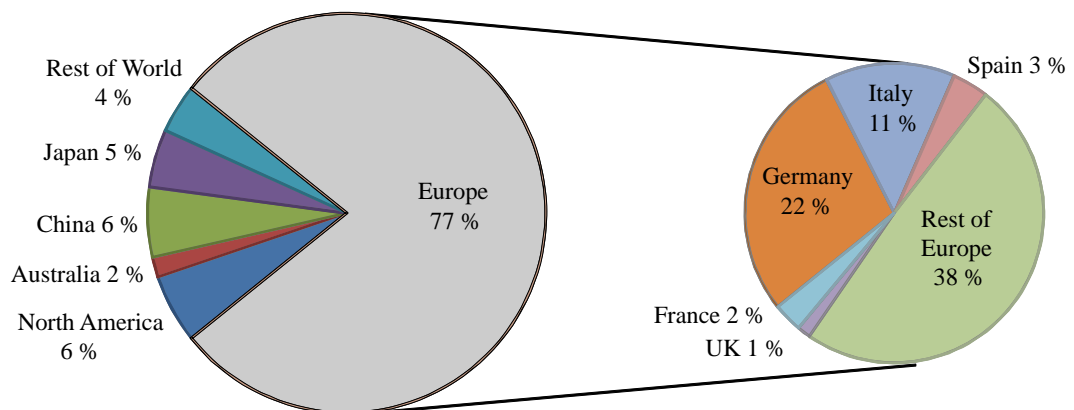


Figure 1.2 Cumulative installed PV power. The data was sourced from the BP statistical review of world energy 2013.²

1.2 History of Photovoltaics

The most significant discovery in the history of solar energy was the PV effect in 1839 by Edmund Becquerel, a 19 year old French physicist.⁹ The next milestone was the discovery of photoconductivity in solid selenium by Smith,¹⁰ which led to Professor William Grylls Adams and Richard Evans Day recording the production of electricity when selenium plates were exposed to light. In 1883 Charles Fritts devised a solar cell based on selenium wafers by compressing molten selenium between plates from two different metals. The selenium only adhered to one metal plate and gold leaf was pressed onto the exposed surface to create the first thin-film solar cell.¹¹

Despite all these developments it was not until 1941 that the first silicon solar cell was developed by Ohl using melt grown junctions, with a performance $< 1\%$.¹² In 1953 Bell Labs (Chapin, Fuller and Pearson) developed diffuse junctions and from here a remarkable improvement in performance was achieved in two years from 4.5% (1953),¹³ 6% (1954)¹⁴ to over 10% (1955).¹⁵ The cells used a single-crystal silicon wafer for light absorption and a $p-n$ junction for charge separation, marking the potential for silicon based cells.

Since 1970 there has been a large-scale effort in the development of PV cells. Multicrystalline silicon solar cells have dominated the market with the share estimated at being $\sim 90\%$.¹⁶ This field has gained considerable interest due to crystalline silicon being a stable, non-toxic semiconductor. Further developments have focused on implementing surface passivation layers to reduce detrimental electronic activity, with the highest cell achieving a PCE of $\sim 25\%$ efficiency with a crystalline silicon cell employing thermally grown silicon dioxide.¹⁷ Other silicon

technologies include thin film technology, where thinner layers are deposited on glass/stainless steel by sputtering, offering low cost, flexible devices. Amorphous silicon which has a larger band gap (E_g) of ~ 1.7 eV has also been optimised allowing the material to absorb more in the visible spectrum. Despite significant progress, the theoretical maximum for a single-junction, stands at $\sim 30\%$.¹⁸ The efficiency is limited because the excess photon energy is larger than the optical band gap, leading to the production of heat via the scattering of photo-generated carriers.

In the 1980's, SERI (Solar Energy Research Institute) (which is now known as the National Renewable Energy Laboratory (NREL)) began testing some of the key silicon cells.¹³ Prior to this, the majority of devices were measured at 28°C using a National Aeronautics and Space Administration (NASA) calibrated reference. SERI introduced other reference cells in 1984 which accounted for spectral mismatch and therefore all previous cell performances had to be corrected. **Figure 1.3** shows a recent publication by NREL monitoring the improvement in certified solar cells of each generation.

1.2.1 Advances in Small Molecule Organic Photovoltaics

Organic semiconductor materials are extending the capabilities of modern electronic and photonic devices from light-emitting displays, to integrated organic circuits and organic photovoltaics (OPVs). This has become possible due to increasingly sophisticated designs, the ability to control architectures on the nanometre length scale, and the employment of new materials.²⁰

The field of OPVs has attracted considerable attention due to its potential for low cost solar energy conversion and its compatibility with non-rigid substrates. Organic materials allow many fabrication techniques to be employed that are simply not available for inorganic PVs,²⁰ including the use of printable semiconductors and electrodes,²¹ spray coating,²² and spin coating,²³ as well as the viability of large-scale, low cost production methods such as roll-to-roll processing.^{24, 25} Improvements have been achieved through the development of new absorbing materials, the use of interfacial layers (IL), novel multi-stack architectures and through the effective use of dopants.²⁶

It was not until the beginning of the twentieth century that photoconductivity was first measured for an organic compound, anthracene, by Pochettino (1906)²⁷ and Volmer (1913).²⁸ From here, the first OPV consisted of a single organic layer sandwiched between two metals of different work functions. This architecture relied on a Schottky barrier between the organic layer and the metal with a lower work function to separate charges.²⁹ As this is an inefficient process, the early OPVs generally had $PCE < 0.1\%$.³⁰ Many organic materials have since been shown to possess photovoltaic properties, from common dyes such as methylene blue to biological materials like chlorophyll and porphyrins.

In a breakthrough in 1986, Tang produced an OPV with an efficiency of 0.95 %, 1-2 orders of magnitude larger than any other organic device that had previously been produced.³¹ The device fabricated by Tang employed a single donor-acceptor (D/A) heterojunction; a phthalocyanine derivative (a *p*-type semiconductor) and a perylene derivative (an *n*-type semiconductor). Tang proposed that the performances observed were due to the introduction of a field at the interface between the two materials; which aids the dissociation into free electrons and holes. Tang's discovery prompted the rapid expansion in the field of OPVs.

One further improvement to Tang's structure has been the use of a bulk heterojunction (BHJ) structure which was first demonstrated by Hiramoto *et al.*³² In this work thermally evaporated organic materials formed a co-deposited three dimensional D/A structure. The BHJ structure has been widely adopted by the polymeric community as a higher probability of excitons reach the interface for dissociation, assisting the issue of short exciton diffusion length (L_D) of many organic materials.^{33,34} One issue with a vacuum deposited BHJ however is the fine mixing means that there are not clear transport paths to the respective electrodes, leading to charge accumulation. One approach to improve this has been through the use of neat organic layers at either side of the BHJ mixed layer, aiding charge extraction, with interlayers in a DBP:C₇₀ device showing an improvement in cell performance from 5.7 % to 6.4 %.³⁵

Another key progress has been through the development of new materials or the optimisation of IL. The use of finely tuned organic active layers allows absorption to be maximised and excitons to be dissociated with minimal energy loss. The development of new ILs has paved the way for the progress of inverted devices and tandem cells both of which heavily depend on the use of appropriately designed ILs.

ILs in inverted organic devices reverse the polarity of the device which can result in potential benefits such as improved current generation and increased stability.^{36, 37}

Tandem cells consist of two or more sub cells with complementary absorption stacked together to maximise absorption.³⁸ These cells rely on current matching of each subcell and a highly transparent recombination zone for effective recombination from each sub cell.^{39, 40} This field of research has shown its potential for commercialisation, with cells achieving efficiencies of up to 12 %.²⁶

1.3 Hybrid Devices

Hybrid devices consist of two classes of materials with different properties, typically one organic and one inorganic, with the ultimate aim to form a new material combination with the most appealing properties of each.⁴¹ In an ideal sense, the aim of hybrid organic photovoltaics (HOPVs) is to add further advantages to the system, whilst maintaining low cost processability.⁴² The role of the inorganic layer varies depending on application, it can improve environmental stability,⁴³⁻⁴⁵ contribute to light absorption,⁴⁶ increase induced charge transfer to the organic material,⁴⁷ tailor physical dimensions of the architecture to improve cell performance,⁴⁸ reduce cost or potentially increase the cell performance through modifying material properties to tune the band gap.⁴⁹ A desirable inorganic material would be able to harness all such properties, with the potential of several materials HOPV devices have been discussed in a range of reviews.^{42, 50, 51}

1.3.1 Material Groups

1.3.1.1 *Cadmium Compounds*

Cadmium compounds have gained considerable interest with Greenham, Peng and Alivisatos first showing the potential of colloidal cadmium sulphide (CdS) and cadmium selenide (CdSe) nanocrystals as light harvesting materials in 1996.⁵² The nanocrystals were combined with the polymer poly(2-methoxy-5-(2'ethylhexyloxy)-*p*-phenylenevinylene) (MEH-PPV) and despite giving a *PCE* of ~ 0.1 % it showed the potential of this type of hybrid solar cell.

Cadmium based nanocrystals have proven to be a good candidate for hybrid devices for a number of reasons. Firstly they have absorption characteristics which can be tuned for efficient harvesting with increasing band gap seen with decreasing particle size for crystallite below 10 nm.⁵³ For instance with CdSe nanoparticles the absorption maximum can be changed from 400 nm to 680 nm simply by varying particle size from ~ 1.5 nm to ~ 9 nm.^{54, 55} Particle size can also have an effect on the energy levels of the material, with a study by Brandenburg *et al.* showing an improvement in open circuit voltage (V_{OC}) from 0.52 V to 0.74 V for a CdSe / poly(3-hexylthiophene) (P3HT) cell by reducing the CdSe particle size from 10 nm to 2.3 nm.⁴⁹

Another desirable feature about cadmium hybrid devices are that the materials have a well-established synthesis.⁴² This has resulted in some promising *PCEs* when utilising various geometries from nanorods, tetrapods to hyperbranched nanocrystals, with tetrapods to date showing the most efficient performances when combined with polymeric materials. Dayal *et al.* reported a certified *PCE* of 3.13 % under AM 1.5 G illumination and a peak external quantum efficiency (*EQE*) of 55 % using a CdSe tetrapod and the low bandgap polymer poly(2,6-(4,4-bis-(2ethylhexyl)-4H-cyclopenta[2,1-b;3,4-b']dithiophene)-alt-4,7(2,1,3-benzothiadiazole)) (PCPDTBT).⁴⁶ 34 % of the absorption in the PCPDTBT : CdSe was attributed to CdSe resulting in a contribution to the *EQE* at ~480 nm. This shows the success of this material in contributing to the current and therefore improving the performance potential of the cell.

The material has also been shown to have an excellent stability with a cadmium only device showing a remarkable 13.6 % improvement in *PCE* after 13,000 hours exposure to light (under 100 mW cm⁻²). These features show the potential of

cadmium as the inorganic component in HOPVs, the major drawback of these cells however is the toxicity and it is this that may limit the potential of cadmium cells in the energy market.

1.3.1.2 *Metal Oxides*

There has been a drive to replace toxic precursors with more environmentally friendly, low cost inorganic materials such as TiO_x ⁵⁶ and ZnO .⁵⁷ Both materials are wide band gap semiconductors, so do not contribute to the photocurrent of the device, but acts as an interface for charge separation and charge extraction to the electrode. They have desirable properties such as a higher mobility than their organic counterparts. To date, TiO_x is the most widely studied transition metal oxide (TMO) due to the application for dye-sensitised solar cells (DSSC). However both materials have gained considerable scientific interest due to the ease of forming a family of architectures including vertically aligned nanorods, nanobelts and nanoribbons.^{58, 59}

TMO in hybrid devices can be optimised either in a regular structure or in inverted architecture where the polarity of the device is reversed and indium tin oxide (ITO) (the typical transparent conducting oxide (TCO) of choice) functions as an electron extracting electrode. Inverted architectures can often be more applicable for the formation of TMOs as they commonly involve high temperature treatments that would damage the organic layers. Heat treatment is a key requirement for high device performance as the electron transport layer needs to be smooth, continuous and sufficiently conductive.⁶⁰

To date this field has been dominated by the use of TMOs with polymeric donors such as poly(2-methoxy-5-(3',7'-dimethyloctyloxy)1,4-phenylenevinylene)

(MDMO-PPV) and P3HT.⁶¹⁻⁶³ In literature hybrid TMO : polymer devices have focused on three different architectures, shown schematically in **Figure 1.4**. These structures include: **[a]** a bilayer TMO/polymer structure; **[b]** a TMO/polymer BHJ cell and **[c]** TMO nanorod/polymer hybrid cell.

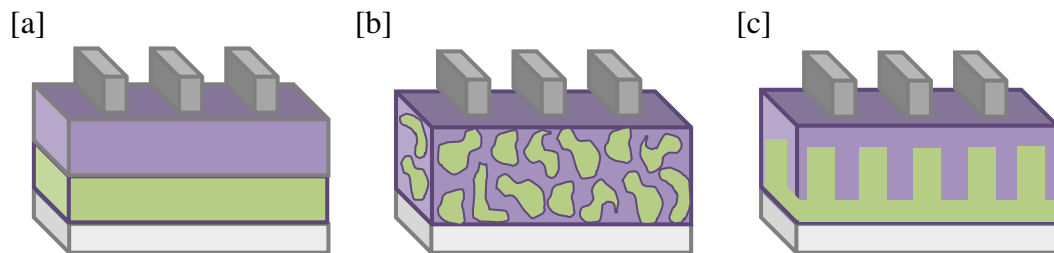


Figure 1.4 Schematic of the three TMO (green) / polymer (purple) device architectures: **[a]** bilayer TMO/polymer, **[b]** BHJ TMO/polymer and **[c]** TMO nanorod/polymer.

Arguably, the simplest structure is the bilayer architecture shown in **Figure 1.4 [a]**, with the TMO deposited initially on the TCO followed by deposition of the polymeric material.⁵⁷ Typically a bilayer TMO devices has a performance < 0.4 % owing to low current generation. This current generation is limited by the low interfacial area between the two materials. The *PCE* can be improved through doping of the TMO layer and using surface modification. Olson *et al.* improved the performance by doping a ZnO layer with Mg, altering the effective electronic band gap of the D/A interface and resulting in a maximum performance of 0.49 %.⁶⁴ Goh *et al.* improved the performance of TiO₂/P3HT devices from 0.34 % to 0.60 % through a series of molecule interface modifiers (*para*-substitued) benzoic acids and ruthenium (II) sensitizing dyes.⁶⁵ However in both these devices despite the improvements, the current generation remained the limiting factor.

TMO/polymer BHJ architectures (**Figure 1.4 [b]**) can be used to improve the D/A interfacial area, leading to increased charge separation and therefore current generation. TMO nanoparticles can be processed in a range of organic solvents which gives the potential of blending the polymer materials.⁶⁶ Another approach is *in-situ* synthesis, Davenas *et al.* have shown that titanium alkoxide can be hydrolysed in the bulk of the semiconducting polymer, leading to the formation of the BHJ structure.⁶⁷ The most successful TMO/polymer cell to date has been the exceptionally high performance achieved by employing P3HT and ZnO nanocrystals,⁶⁸ ($PCE \sim 2\%$) with the high short circuit current density (J_{SC}) benefiting considerably from the increased D/A interfacial area. The authors investigated a range of film thicknesses and found that thicker BHJ layers led to phase separation on a smaller scale which is favourable due to increased charge separation at the D/A interface.

Vertically aligned nanorods (NR) (**Figure 1.4 [c]**) are regarded as potentially the most ideal structure for hybrid TMO/polymer devices due to possibility of systematic growth of the nanorods, with a high interfacial area between the active materials and highly efficient charge transport pathways to the electrode. Experimentally however, this structure is not easy to achieve, with problems associated with reproducibility, polymer infiltration, wettability and slow kinetics. The degree of infiltration is influenced by numerous factors that need to be controlled including molecular weight of the polymer, the tendency to crystallise, solvent and surface interaction energy between the two materials.⁵¹ Despite this, early studies by Olson *et al.* showed a high performing ZnO/P3HT device of $\sim 0.5\%$, the issues associated with this device however was the distance between the ZnO nanorods being in the order of 100 nm.⁶⁹ This is problematic as the L_D of the

polymer material is ~ 8 nm, so many of the excitons generated are unable to reach the interface and dissociate, limiting the potential current.⁷⁰ This cell design has been successfully improved via a number of modifications by various groups. Baeten *et al.* showed that annealing the substrates to the melting temperature of the polymer improved the crystallinity of the polymer and in turn improved the performance, achieving 0.76 % for a ZnO/P3HT NR structure⁷¹ There has also been considerable improvement through the use of surface modifiers, with derivatized squaraine molecules on the ZnO NR giving a *PCE* of 1.02 %.⁷² Another recent approach has been using an *in-situ* generated ZnO/P3HT on a scaffolded TiO₂ NR array, enabling a much thicker active layer to be used and resulting in an optimum *PCE* of 2.46 %.⁷³

The substitution of the polymeric donor by different materials such as small molecule (SM) organic semiconductors offers an alternative means of improving the performance of HOPV devices.⁷⁴ The use of vacuum deposition offers reproducible film growth on the nanometre scale and a well-defined TMO/organic heterojunction. Surprisingly, there have only been a few reports of these types of SM organic materials being used in a true D/A hybrid device. Two publications use copper phthalocyanine (CuPc); Sharma *et al.* used CuPc as a donor material with randomly dispersed zinc nanocrystals, however these devices had a poor J_{SC} of 3.6×10^{-5} mA cm⁻²,⁷⁵ whilst Shen *et al.* used CuPc only as a sensitizer in a ZnO/CuPc/P3HT device.⁷⁶ Izaki *et al.* has also investigated TMO/SM with a 200 nm thick phthalocyanine/ZnO buffer/n-ZnO photovoltaic device which achieved a J_{SC} of 1.5×10^{-2} mA cm⁻² and a *PCE* of 1.6×10^{-3} %.⁷⁷ The most efficient TMO/SM cell to-date has been published by the same author who inserted a CuPc:Gallium doped ZnO BHJ layer between layers of CuPc and ZnO and achieved a *PCE* of 0.017 %.⁷⁸ This

difference in *PCE* between TMO/polymer and TMO/SM is remarkable and suggests that future studies are needed reduce this difference in performance.

1.3.2 Other ‘Hybrid’ Cells

Other classes of solar cells have been termed as hybrid solar cells due to their use of inorganic and organic materials. DSSC were first demonstrated in the seminal paper by O’Regan and Grätzel in 1991.⁷⁹ These cells replaced the classical solid-state junction device, forming a photo-electrochemical cell by contacting the semiconductor through the use of an electrolyte, liquid, gel or solid.⁸⁰ The principle relies on five components: a mechanical support coated with a TCO; a sintered mesoporous semiconductor oxide layer (commonly anatase); a sensitizer attached to the surface of the semiconductor; an electrolyte containing a redox mediator and a counter electrode capable of regenerating the mediator.

In a DSSC, the dye material is responsible for light harvesting and upon photo excitation, an electron is injected into the conduction band (CB) of the oxide. This electron travels through the semiconductor network to the contact and then through the external load to the counter electrode to reduce the redox mediator. The sensitizer is then regenerated.^{48, 81, 82} This diverse system has resulted in a wealth of studies with thousands of dyes being investigated and developments in electrolyte systems and mesoporous films.

Since 2012, inorganic/organic halides with the perovskite structure have attracted a strong research interest due to their performance in solid state solar cells, delivering efficiencies of over 10 %.⁸³⁻⁸⁵ Perovskites are hybrid layered materials typically with a AMX_3 structure where A is an organic cation (typically methylammonium,

ethylammonium or formadinium), M a smaller metal cation (Pb^{2+} , Sn^{2+} or Ge^{2+}) and X an anion from the halide series (I^- , Cl^- or Br^-).⁸⁶ Recent advancements in this field of hybrid devices have used $\text{CH}_3\text{NH}_3\text{PbI}_3$ with a “meso-superstructured” metal oxide-framework infiltrated with the material to maximise the interfacial area.⁸³ A 10.9 % efficient cell was produced through the use of an insulating mesoporous alumina layer (replacing TiO_2) which functions as an inert scaffold for the perovskite and results in electrons transporting through the material. Remarkably 15 % solar cells have also been shown in a planar junction without the need for a nanostructured acceptor.⁸⁷

These astonishing improvements in performance over two years has resulted in a considerable scientific effort due to the impact perovskite materials have on the future of renewable energy, with the energy pay back for these systems estimated to be less than one year.⁸⁸ Numerous studies have looked at different architectures and contact layers incorporating this effective material class.⁸⁹⁻⁹² However Pb^{2+} needs to be replaced with a less toxic alternative along with a deeper understanding of the PV principles and degradation mechanisms for the true potential to be realised.

1.4 Basic Semiconductor Theory

The wavefunction for an atom such as hydrogen consists of a discrete energy level known as the atomic orbital (AO). When two atoms approach (i.e. forming a molecule of hydrogen), the addition of two AOs produces two molecular orbitals (MOs); a bonding orbital and an anti-bonding orbital. The bonding MO has an increased stability compared to a single AO with greater electron density between the two nuclei, therefore it is lower in energy. However the anti-bonding MO formed has a reduced stability compared to the individual AOs. This is shown schematically in **Figure 1.5**.

In a more complex system, the overlap of all the AOs from each atom contribute to the overall MO, with N AOs = N MOs. For instance, in a ten AO system there are five bonding and five anti-bonding MOs. When there are a large number of AOs in the system, such as in the case of metals, the discrete energy levels are so closely spaced that the energy levels are considered to be nearly continuous.

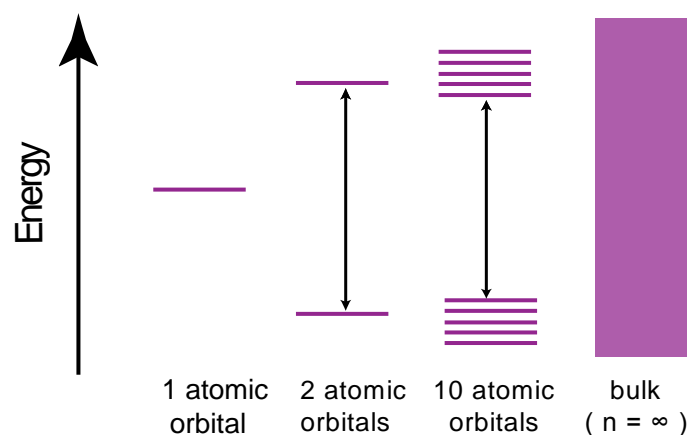


Figure 1.5 A schematic showing the position of the discrete energy levels, from a simple one atom system to a bulk metallic material.

Solid state materials can be classified into three groups; conductors, insulators and semiconductors. The classification of materials depends on the relative positions of the anti-bonding orbitals (the CB) and the bonding orbitals (the valence band, (VB)), shown in **Figure 1.6**. For a conductor, the CB is either partly filled (the Fermi level, E_{Fs} is located in the middle of the CB) or it overlaps with the VB so there is no E_g . If the material of interest has a band completely filled with electrons and an empty band above, the material has an E_g . The E_g is defined by the energy difference between the last filled energy band at $T = 0$ K (the VB) and the first unfilled band at $T = 0$ K (the CB). The conductivity of a material is extremely sensitive to how the discrete bands are filled and the magnitude of the E_g . An insulating material typically has an $E_g \sim 4$ eV, valence electrons form strong bonds with neighbouring atoms and no free electrons are available to participate in conduction. Semiconducting materials however are a class of materials that are in-between the two, with a typical $E_g \sim 1$ eV, as the gap is sufficiently small, electrons can populate the CB with an input of energy.

The Fermi-Dirac distribution, *Equation 1.1*, describes the occupation probability of an electron $f(E)$ existing at a given energy, E , at temperature T .

$$f(E) = \frac{1}{e^{\frac{E-E_{Fs}}{k_B T}} + 1} \quad \text{Equation 1.1}$$

where k_B is Boltzmann's constant and E_{Fs} is the surface Fermi level. The E_{Fs} is defined as the energy at which the probability of occupation by an electron is exactly a half. From the Fermi-Dirac distribution, at absolute zero, all energy states below the E_{Fs} will be filled, and no electrons will have enough energy to rise. *Equation 1.1* describes the temperature dependence of a system on the occupation of the various bands.

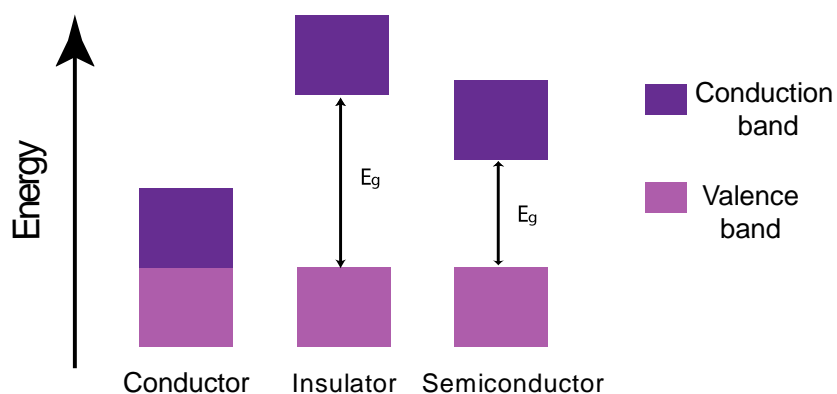


Figure 1.6 A schematic showing the position of the energy levels for a conductor, insulator and semiconductor.

There are two types of semiconductor material, intrinsic and extrinsic, shown in **Figure 1.7**. Pure semiconductors are intrinsic semiconductors meaning they have an equal number of electrons and holes and therefore the E_{FS} is located half way between the VB and CB. For intrinsic semiconductors at room temperature, the occupation of thermally excited carriers tends to be very small, $\sim 10^7$ electrons cm^{-3} (compared to metal which is in the region of 10^{28} electrons cm^{-3}). For an organic material however, the level of the last filled energy level at $T = 0$ K is referred to as the highest occupied molecular orbital (HOMO) and the first unfilled level at $T = 0$ K is the lowest unoccupied molecular orbital (LUMO).

Extrinsic semiconductors differ as they have had substitutional atoms added to the lattice through doping (either *n*-type or *p*-type). For *n*-type extrinsic semiconductors, typically group IV semiconductors are doped with group V atoms such as phosphorous or arsenic. These atoms donate additional electrons to the lattice of the group IV material which increases the conductivity of the semiconductor. This shifts

the position of the E_{Fs} closer to the CB. For p -type extrinsic semiconductors however, group IV materials are doped with group III atoms such as boron resulting in an additional hole in the system, which improves the conductivity. This doping shifts the position of the E_{Fs} closer to the VB.

Four key parameters can be obtained for each system and are indicated in **Figure 1.7**. The work function (Φ) of a given material is defined as the energy required to remove an electron from the E_{Fs} to the vacuum level (V_L). Also indicated on the diagram is the position of the electron affinity (EA) which is the difference from the CB edge to the V_L , along with the ionization potential (IP) which is defined as the energy required to remove an electron from the VB to the V_L . Finally the E_g is the minimum amount of energy required for an electron to be promoted to the CB.

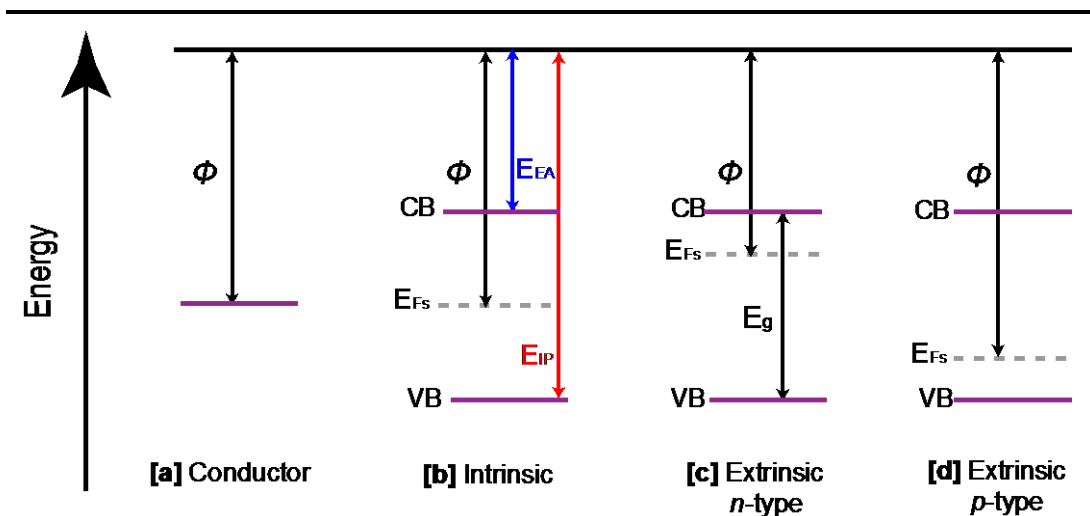


Figure 1.7 Energy level diagrams of a conducting material and the semiconducting materials: intrinsic inorganic, extrinsic n -type and extrinsic p -type.

1.5 Working Principles of OPVs

The conversion of light to electrical energy relies on four consecutive steps, each with its own quantum efficiency (η). The first step involves the absorption of a photon (η_A) resulting in the formation of a neutral coulombically bound electron-hole pair (exciton). This exciton then diffuses randomly throughout the layer (η_{ED}) to an interface or region where charge separation occurs (η_{CT}). In the final step, charge collection (η_{CC}), the separated charges are transported to the appropriate electrodes. These four steps are summarised schematically for a typical planar heterojunction OPV device (**Figure 1.8**).

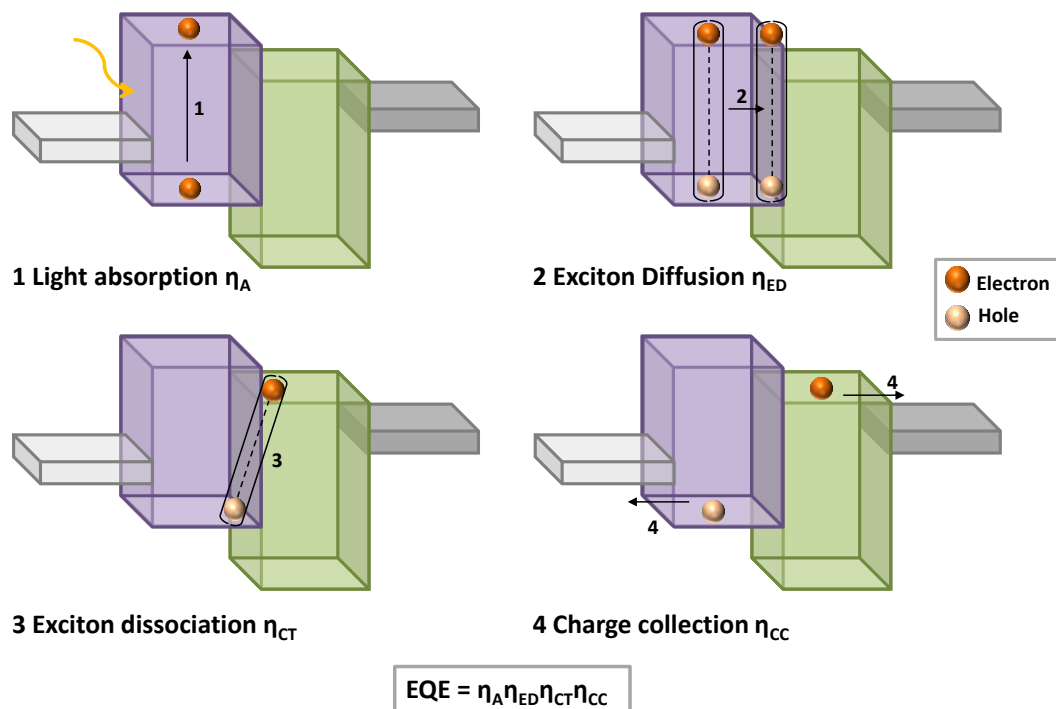


Figure 1.8 A schematic showing the four steps of an OPV device (1) light absorption, η_A , (2) exciton diffusion, η_{ED} , (3) exciton dissociation, η_{CT} and (4) charge collection, η_{CC} .

The EQE of the overall process is also shown in **Figure 1.8**, which is a product of each of the single steps:

$$EQE = \eta_A \eta_{ED} \eta_{CT} \eta_{CC} \quad \text{Equation 1.2}$$

1.5.1 Absorption of Incident Photon η_A

The absorption of an incident photon by either the donor or acceptor material results in the promotion of an electron from the HOMO/VB to the LUMO/CB providing the energy is greater than or equal to the E_g of the absorbing material. This process results in the formation of a neutral, coulombically bound mobile excited state called an exciton. The potential well over which the exciton is formed can be explored by looking at the relationship between the binding energy of two opposite charges:

$$E_B = \frac{q^2}{4\pi\epsilon_r\epsilon_0 r_c} \quad \text{Equation 1.3}$$

where r_c is the distance between two charges, ϵ_0 is the permittivity of free space, ϵ_r is the dielectric constant and q is the electronic charge. This shows the correlation between the dielectric constant and the binding energy of the excitons formed. This relationship results in a striking difference between inorganic and organic materials.

Inorganic materials have a much larger dielectric constant ($\epsilon \sim 15$) and due to the large distance ~ 10 nm between the electron and hole they are screened from one another, which results in the formation of Wannier-Mott excitons.⁹³ This results in a low coulombic attraction ~ 10 meV so the Wannier-Mott excitons can be separated into free charges by thermal dissociation at room temperature (~ 26 meV). For organic semiconductors however a Frenkel exciton is formed with a typical

interaction between the electron and hole in the range of several hundred meV.⁹⁴ A Frenkel exciton forms due to the low dielectric constant of organic materials (typically $\epsilon \sim 3-5$) resulting in the attractive coulomb potential well extending over a greater volume than for inorganic semiconductors.⁹⁵ This is a result of the weaker non-covalent electronic interactions between organic molecules compared to strong interactions for covalently bonded inorganic materials such as silicon, and as a result the wave function of the electron is localised to individual molecules.⁹⁶

Charge-transfer excitons can also occur in overlapping conjugated systems, whereby owing to the dielectric constants of the organic materials, the binding energy is estimated to be one order of magnitude greater than $k_B T$. The comparison between Frenkel, Wannier-Mott and charge transfer excitons is shown schematically in

Figure 1.9.

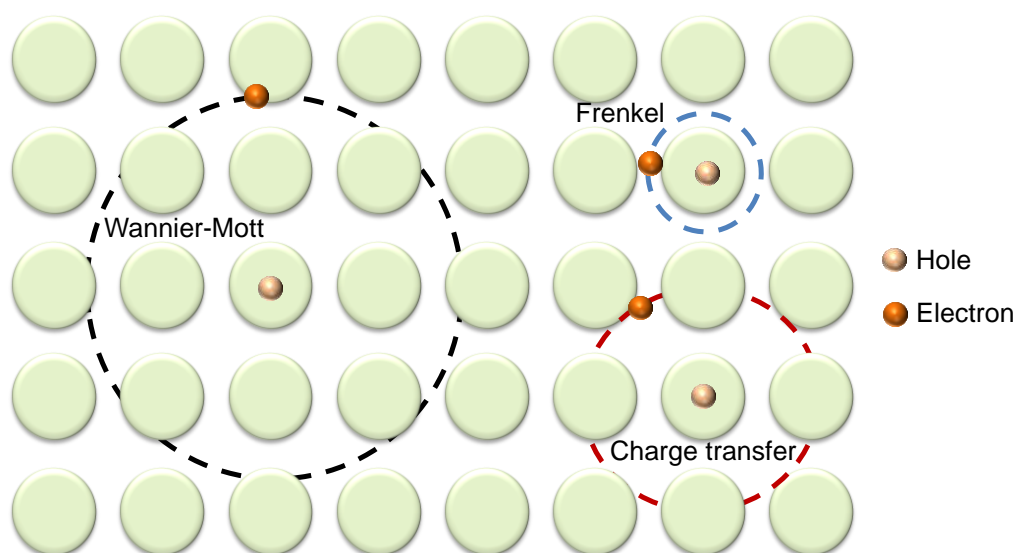


Figure 1.9 Schematic showing the three types of excitons formed depending on the dielectric constant of the material, a Wannier-Mott exciton, a Frenkel exciton and a charge-transfer exciton.

The absorption quantum efficiency η_A is dependent on the absorption coefficient, the layer thickness and the internal reflections within the device.²⁹ Organic materials have strong absorption coefficients, generally peaking at $> 10^5 \text{ cm}^{-1}$, but due to well defined absorption bands, the achievable spectral coverage is reduced, especially when compared to an inorganic material. In the ideal case, the absorbing materials would cover the whole wavelength range of the solar spectrum. This can be achieved by using donor and acceptor materials with complementary absorption and/or by using multiple absorbers in organic multijunction cells connected in series. Another approach to improve absorption can be utilising organic materials that have absorption bands at longer wavelengths, since around 50 % of photons have energies corresponding to the 600 – 1000 nm wavelength range.⁹⁷

1.5.2 Exciton Diffusion η_{ED}

The quantum efficiency of this process is related to the L_D of the given material and the absorber layer thickness, giving a measure of the fraction of excitons that reach the D/A interface. The L_D is defined by:

$$L_D = \sqrt{D\tau} \quad \text{Equation 1.4}$$

where D is the diffusion coefficient and τ is the exciton lifetime. Typically the L_D of an organic material is in the range of 5-20 nm, although literature values differ significantly. This means that if an exciton is generated at a length scale greater than the L_D of the material the excitons are less likely to result in separated charges. There

are competing processes to contend with which cause decay of the exciton such as luminescence and radiative recombination.

The movement of an exciton through a layer can be described in terms of random hops that are not influenced by the electric field. This movement relies on resonance energy transfer in the form of Förster energy transfer or Dexter energy transfer. Both processes are summarised in **Figure 1.10**. The movement of singlet excitons is usually described by a generalised Förster energy transfer mechanism, as it preserves the spin of the two molecules.⁹⁸ This long-range process uses resonant dipole-dipole coupling with the stipulation that donor-acceptor transitions must be allowed (i.e. an overlap of their absorption spectra). For singlet and triplet excitons, Dexter energy transfer is used which follows Wigner spin conservation rules (the overall spin angular momentum of the system should not change). This process occurs over a much shorter distance so hops are restricted to adjacent sites.

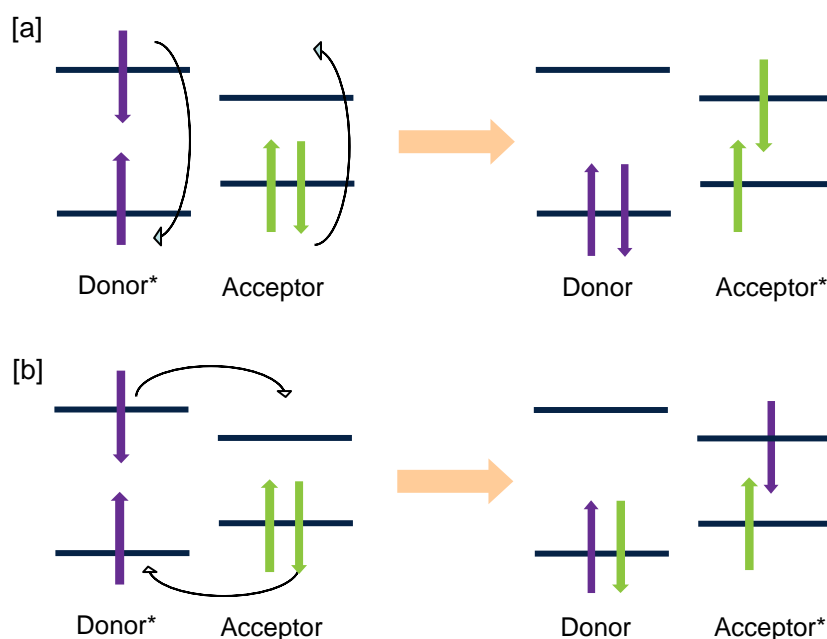


Figure 1.10 A model showing the different types of energy transfer; **[a]** Förster energy transfer and **[b]** Dexter energy transfer.

The low L_D of the majority of organic semiconductors is a major limitation in producing efficient OPV cells, as the device architecture becomes a trade-off between absorption losses (due to low active layer thicknesses) and exciton diffusion losses (with excitons decaying back to the ground state before they reach an interface). Material design to improve crystallinity and reduce recombination sites is one approach to improving the L_D of organic materials. Ideally the D/A heterojunction should be distributed so it is accessible by all excitons in the layer. This is achieved through the use of a BHJ architecture whereby the intermixing at length scales less than L_D increases the charge generation due to more excitons reaching an appropriate interface, allowing for thicker active layers.

1.5.3 Exciton Dissociation η_{CT}

When an exciton reaches the D/A interface it undergoes charge transfer to form a geminate pair, with the hole remaining in the donor and the electron in the acceptor. This process is very efficient and happens in a matter of a few hundred femtoseconds.⁹⁹ The electron-hole pair however still remains coulombically bound across the interface. From this state there are three possibilities: complete dissociation of the geminate pair (to make free charges carriers), relaxation of the geminate pair and recombination at the interface. To overcome the geminate pair binding energy an energy offset is required in the EA/IP of the acceptor/donor.¹⁰⁰ The mechanism of charge dissociation is still under debate in literature. The general consensus is that it occurs via a charge transfer (CT) state to charge separated states (CS), **Figure 1.11 [a]**.¹⁰⁰ One proposal suggests that this process is temperature and field dependent, whilst others have shown that the energy offset provides enough

energy for spontaneous dissociation, with the CT state more closely resembling that of free charges.^{101, 102}

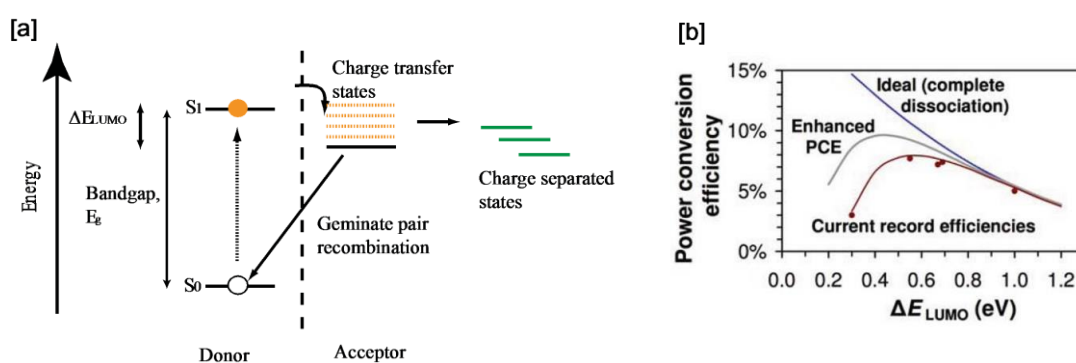


Figure 1.11 [a] Organic energy level diagram adapted from Servaites *et al.*¹⁰⁰ [b] is taken from reference 100. The red line shows the trend in *PCE* with different ΔE_{LUMO} offsets, the efficiency limits are also shown (blue line), along with the hypothetical enhanced *PCE* shown in grey.^{100, 103}

It is generally accepted in the literature that providing the LUMO offset (ΔE_{LUMO}) and HOMO offset (ΔE_{HOMO}) between the donor and acceptor material is greater than 0.3 eV (a typical exciton binding energy), efficient charge transfer occurs. Large ΔE values have a geminate pair dissociation yield approaching 100 %, and as a result these cells produce nearly ideal *J-V* curves, with high fill factors (*FF*). For moderate ΔE values however, experimental and modelling studies have shown that less photocurrent generated at low applied bias giving a reduction in *FF*. Owing to a large ΔE of 1.0 eV ideal *J-V* curves can be produced for P3HT:PCBM cells; however the problem with this is that over half of the exciton energy is expended during charge separation. Therefore for maximum performance there is a compromise between small ΔE to maximise the V_{OC} whilst maintaining photocurrent generation and larger ΔE for efficient charge separation, with the ideal cell having high charge dissociation yields at low energy offsets.

The importance of this ΔE gap has been explored by Servaites *et al.* and a summary of their findings is shown in **Figure 1.11 [b]**.¹⁰⁰ The authors compared *PCEs* reported in literature to ΔE_{LUMO} gap (red line) and found that as the ΔE_{LUMO} gap is decreased the efficiency limit substantially increases. At large ΔE_{LUMO} values the current record efficiencies are in line with the modelled efficiency limits (blue line), however the same cannot be said for low ΔE_{LUMO} values. This shows the importance of truly understanding the significance of this energy gap, with the opportunity to improve *PCEs* (grey line) by optimising the materials and interface.¹⁰⁴

1.5.4 Charge Collection η_{CC}

Once separated, the holes travel through the donor and the electrons through the acceptor material to their respective electrodes. In regular device architectures holes are transported to the transparent conductive electrode (TCE) and electrons to the metallic electrode. The electrical current an OPV device delivers depends on the yield of generated charges that are collected at the electrode to be extracted to the external circuit for current flow. The movement of charges through the layer depends on the mobility of the material, these are typically low for organic materials due to disorder and limited overlap of electronic wavefunctions (van der Waals interactions).¹⁰⁵ The low mobility can be detrimental to device performance as it leads to charge build up. The energetics of both electrodes are also vital, with losses produced if the contacts are none ohmic. Ohmic contacts are usually achieved through the use of transport layers.

1.6 Material Properties

1.6.1 Electrodes and Interlayers

1.6.1.1 Electrodes

Currently indium oxide In_2O_3 , doped with approximately 10 % of tin oxide (SnO_2) by weight, is the transparent conductor of choice as it offers the highest available transmissivity combined with a low electrical resistivity $\sim 2 \times 10^{-4} \Omega \text{ cm}^{-1}$.¹⁰⁶ ITO has a $E_g \sim 3.7 \text{ eV}$ with a high optical transmission across the visible spectrum and is reflective in the IR regions.¹⁰⁷ These properties deem ITO suitable for a broad range of applications including optoelectronic devices,^{108, 109} transparent heating elements for car and aircraft windows, infrared reflectors,¹¹⁰ displays and sensors.¹¹¹

ITO is an *n*-type degenerate semiconductor, with a free carrier density $\sim 10^{20} - 10^{21} \text{ cm}^{-3}$.¹¹² This high level of carrier charge density is a consequence of the degeneracy caused by oxygen vacancies and tin dopants. Tin essentially replaces the In^{3+} in the cubic bixbyite structure of indium oxide forming an interstitial bond with oxygen. It is the combination of the tin doping and oxygen vacancies that contribute to the high conductivity of the film.^{112, 113} The quality of the ITO films produced depends on the technique and processing conditions, with magnetron sputtering commonly deemed the best technique to form low resistivity films.

ITO is not without its limitations. The availability of indium is scarce,¹¹⁴ the production methods or surface treatment can lead to an inhomogeneous electrical conductivity,^{115, 116} the work function can vary in the presence of air or exposure to light¹¹⁷ and it is also incompatible with many common donor materials. Therefore

there has been a drive to find an appropriate replacement (discussed in more detail in **Section 6.3.1**).

At the other side of the device is the metallic reflective back electrode which is an important feature for enhancing absorption within the active layers. In the literature the electrode of choice ranges from gold ($\Phi \sim 5.1$ eV) to barium ($\Phi \sim 2.7$ eV), with aluminium a common electrode of choice due to the abundance, low work function ($\Phi \sim 4.3$ eV) and compatibility with vacuum deposition. However if a pristine metal electrode is used, the devices tend to have a reduced performance as metal atoms can diffuse into the organic layer and due to the energetic mismatch between the active material and the work function of the metal.¹¹⁸

1.6.1.2 Interlayers

The drawbacks of bare electrodes have paved the way for ILs to be adopted as they: can improve layer homogeneity; act as a protection layer to the organics; can provide an ohmic contact with the active layer maximising the V_{OC} of the device and have also been shown to improve device stability.^{119, 120} ILs can also act as an optical spacer layer or be used to invert the polarity of the device, allowing ITO to function as either a hole or electron extracting electrode, shown below in **Figure 1.12**. These layers can be semiconducting (inorganic or organic) or dipole layers such as self-assembled monolayers^{121, 122} and salts (such as LiF and Cs₂O₃).^{123, 124}

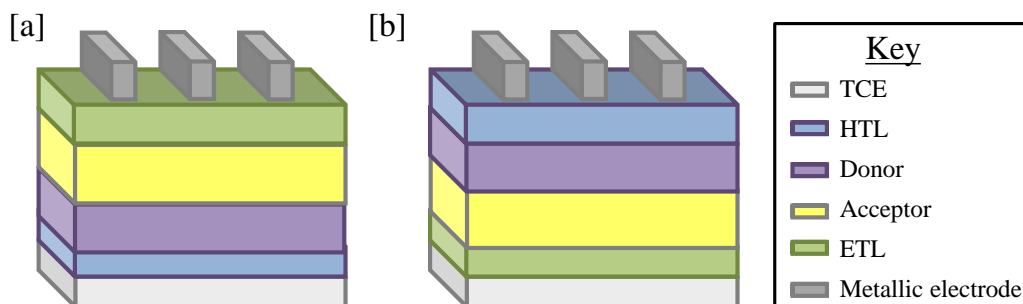


Figure 1.12 Schematic of [a] a regular OPV structure and [b] an inverted architecture. The TCE, hole transporting layer (HTL), donor, acceptor, electron transporting layer (ETL) and metallic electrode are indicated.

One of the most commonly used organic ILs for electron transport is bathocuproine, 2,9-dimethyl-4,7-diphenyl-1,10-phenanthroline, (BCP), **Figure 1.13**. BCP can be vacuum deposited and is commonly inserted between the acceptor and the electron extracting electrode. BCP acts as an exciton blocking layer, preventing diffusion of the excitons to the electrode where they can be quenched, and it also protects the organic layer from damage.¹²⁵ This has been shown in the case of a C_{60}/Al interface, where without the addition of BCP, charge transfer states are created in the acceptor material (caused by aluminium) which is detrimental to the performance due to exciton quenching.¹²⁶

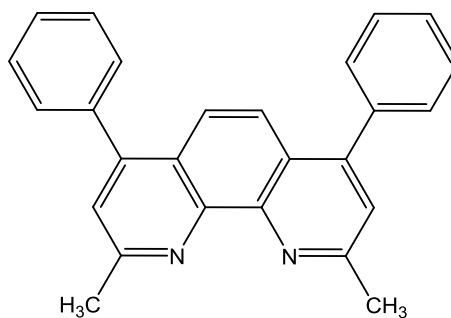


Figure 1.13 Molecular structure of BCP

Other organic ILs include the hole transporting material poly(3,4-ethylenedioxythiophene) (PEDOT) which is usually doped with polystyrene sulfonic acid (PSS) to improve conductivity and solubility. PEDOT:PSS has been shown to modify the work function of the transparent electrode and improve the homogeneity of the surface.^{22, 127} As the material is highly transparent across the visible spectrum, thick layers of the material can be used with only minimal absorption of solar radiation. One of the concern about PEDOT:PSS is the fact that it is acidic in nature and retains water which has been shown to damage organic solar cells and etch the ITO surface.¹²⁸⁻¹³⁰ As a result inorganic materials are typically used where possible.¹²⁹

Inorganic layers such as tungsten oxide (WO_x),^{131, 132} nickel oxide (NiO),¹³³ vanadium oxide (V_2O_5),¹³⁴ molybdenum oxide (MoO_x),^{135, 136} TiO_x ¹³⁷ and ZnO ³⁶ have been successfully implemented with a range of OPV materials and architectures. Shrotryia *et al.* first successfully showed the potential of the inorganic layers V_2O_5 and MoO_x for replacement of PEDOT:PSS in 2006.¹²⁴ Prior to this date inorganic materials had been used as efficient hole injection materials in electroluminescent devices.¹³⁸

1.6.2 Zinc Oxide

Zinc oxide is a versatile wide band gap inorganic semiconductor that has been beneficial across a broad range of industries. It is estimated that over 1.2 million tonnes are used each year, this covers a range of uses including pharmaceutical, rubber, concrete, additives in human/animal food and varistors.¹³⁹ The versatility of ZnO stems from the fact that it can be processed using a number of methods

including electrodeposition (ED),¹³¹ pulsed laser deposition (PLD),¹⁴⁰ spray pyrolysis,^{141, 142} and the sol-gel (SG) process,¹⁴³ and it is widely used due to its low toxicity and its rich family of material properties and structures. The tunability of the material enables ZnO to be utilised in a range of electronic device applications such as light emitting diodes (LEDs),¹⁴⁴ chemical and biological sensors,¹⁴⁵ and HOPVs.¹⁴⁶

The compatibility with a wide range of processing methods is what has governed such an interest within the scientific community and it has been widely used in the literature with a large surge in the total number of relevant publications. This is shown in **Figure 1.14** with a steady increase in ZnO related publications over the past ten years, including a rise in the studies focused purely on the application of ZnO in solar cells. The interest is fuelled due to the many desirable properties of ZnO, in particular for its use in optoelectronic applications such as its large exciton binding energy of 60 meV, high electron affinity and high electron mobility. ZnO is also a wide band-gap semiconductor ($E_g \sim 3.3$ eV at 300 K) making it a desirable IL in OPV devices.¹⁴⁷

As a material, ZnO preferentially crystallises in either a hexagonal wurtzite type structure or a cubic zinc blende structure whereby one zinc atom is surrounded by four oxygen atoms in a tetragonal structure and vice versa. This structure is typical of a sp^3 covalent structure but ZnO also has substantial ionic contribution. ZnO is a direct band-gap semiconductor, with an electronic band structure of the CB minimum formed from the empty 4s states of Zn^{2+} (or antibonding sp^3 states) and the VB maximum formed from the occupied 2p orbitals of O^{2-} (or bonding sp^3 states).

Intrinsic ZnO is insulating due to the lack of charge carriers, but with selective and careful doping, the electrical properties can be changed from an insulator to an n -type semiconductor to a metal, with the possibility of doping up to $2 \times 10^{21} \text{ cm}^{-3}$ charge carriers.¹⁴⁸ This has been successfully achieved through the use of Group XIII dopants, such as gallium, indium and aluminium which are shallow and efficient donors, adding additional electrons into the zinc lattice and pushing the E_{F_S} towards the CB.¹⁴⁹ The highest conductivity of $8.12 \times 10^{-5} \Omega \text{ cm}^{-1}$ has been achieved with Ga-doped ZnO (GaZnO), along with excellent transparency $> 80 \%$ making the material particularly appealing for TCO applications. It has been postulated that gallium is the most successful dopant for ZnO due to the atomic radii matching of Ga and Ga^{3+} to that of Zn and Zn^{2+} compared to other dopants.¹⁴⁹⁻¹⁵³ As ZnO is a wide band gap semiconductor, bipolar doping is unusual, but p -type doping has been achieved with dopants from Group V (such as the addition of NH_3 into hydrogen carrier gas with excess Zn). However, a high quality and reproducible method for creating layers with p -type conductivity is still under debate.^{154, 155}

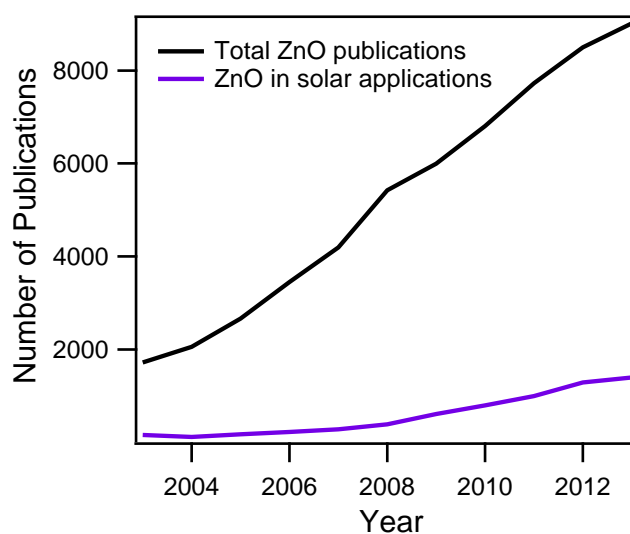


Figure 1.14 The total number of ZnO publications (black line) and the number corresponding to solar applications (blue line) from 2003 – 2013. The data was calculated from web of knowledge (accessed April 2014).

1.6.3 Photoactive Materials

1.6.3.1 Phthalocyanines

Phthalocyanines (Pcs) were first discovered accidentally in 1907 when they were produced as a bi-product in the chemical conversion of ortho-(1,2)-disubstituted benzene derivatives,¹⁵⁶ but it was not until 1934 during a collaboration between Linstead and Imperial Chemical Industries Ltd that the structure and synthesis of phthalocyanines was determined.¹⁵⁷ Pcs have been used in an extensive amount of industries and applications, covering anything from dyes and pigments, (with CuPc being the largest synthetic colourant used to date),¹⁵⁸ to liquid crystals, chemical sensors and catalysts. Pcs are applicable to such a range of fields due to many desirable properties including: high degree of aromaticity, unique electronic spectra, singular chemical structure and the flexibility during synthesis.¹⁵⁹ They have also received a great deal of attention as functional organic materials in organic field effect transistors (OFETs), organic light emitting diodes (OLEDs) and OPVs.

Pcs are highly aromatic 18 π -electron macrocycles which consist of four diiminoisoindole units, nitrogen-fused around the central core. The central cavity can accommodate up to 70 metallic or non-metallic ions as well as forming a stable metal free complex (H_2Pc). This degree of flexibility around the central cavity enables simple ways of altering the property of the molecule.¹⁶⁰ If the various central atoms are exchanged for other elements, they change the energetic and absorption properties of the molecule due to interactions of the metal with the π -system. Absorption spectra for Pcs show a Q-band and a Soret B-band. The most commonly used Pcs in OPVs, CuPc and zinc phthalocyanine (ZnPc) have a Q-band peaking at ~610 nm. If this central metal is replaced by others such as Sn, or Al (which exists as

a non-planar chloride) it causes the absorption to be shifted to longer wavelengths. Replacing the central atom can also alter the structure of the molecule, with both planar and non-planar molecules being formed. This is because larger metal atoms decrease the planarity of the molecule, changing the spatial structure and hence how it stacks. ZnPc and CuPc thin films tend to form herringbone structures depending on substrate and processing conditions. Chloroaluminium phthalocyanine (ClAlPc) however, which contains an Al metal centre with an out of plane Cl, is non-planar due to the dipole caused by the Cl atom, causing films to be largely amorphous.

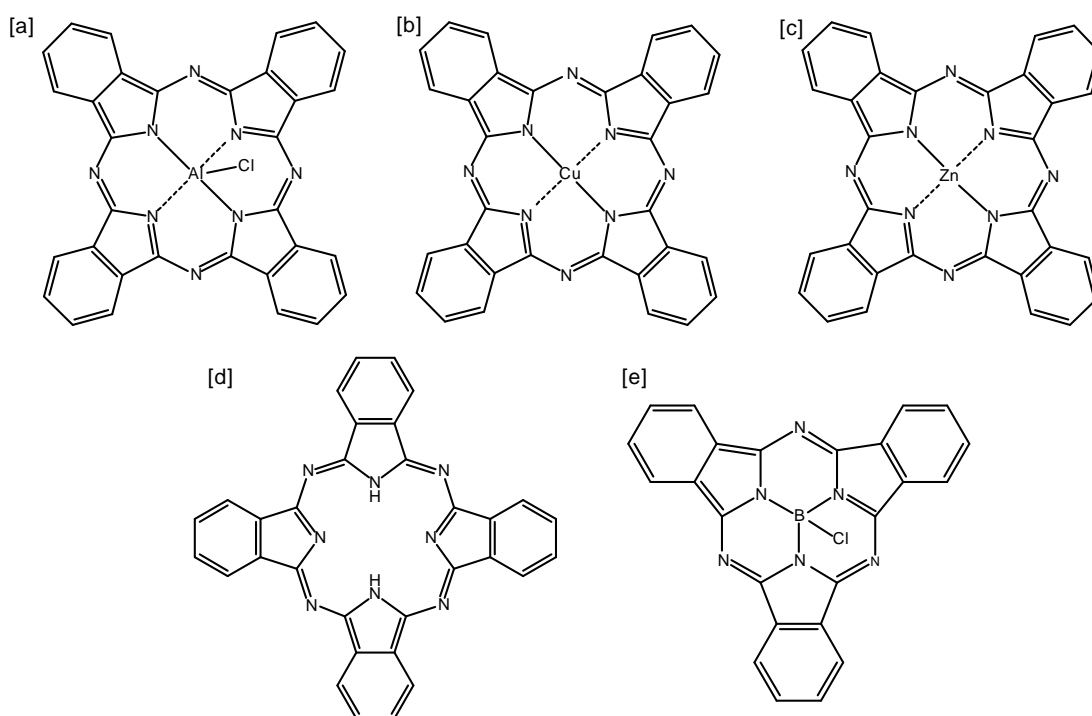


Figure 1.15 Molecular structures of the phthalocyanine family: **[a]** ClAlPc, **[b]** CuPc, **[c]** ZnPc, **[d]** H₂Pc and **[e]** SubPc

Subphthalocyanines (SubPc) are the lowest homologues of Pcs and consist only of a 14 π -electron aromatic macrocycle due to the structure only containing three

diiminoisoindole units arranged round a boron atom with a substituent, usually a halogen. The molecule was discovered by Meller and Ossko whilst trying to produce boron phthalocyanine in 1972.¹⁶¹ The typical method for producing SubPc in good yield is the reaction of phthalonitrile with a boron trihalide, typically BCl_3 , and most effectively purified using a soxhlet extraction. SubPcs have a cone-shaped geometry (C_{3v}) due to the loss of a ligand around the boron centre.¹⁶² This reduction in π -conjugation also causes the Soret and Q-band in the UV-Vis spectra to shift to shorter wavelengths.¹⁶³

Pcs are utilised in OPVs as donor materials due to their high absorption coefficients, complementary absorption with fullerene based acceptors and the ability to vacuum deposit allowing for controlling growth down to the nanometre scale. SubPc offers a substantial advantage over other Pcs due to its low lying HOMO level reported to be 5.6 eV in numerous studies.^{134, 164} This offers the potential of high V_{OC} when paired with electron acceptor materials such as C_{60} giving the potential of improved *PCEs*. This has been shown by varying the donor layer with a C_{60} acceptor, the V_{OC} increases from 0.45 V to 0.80 V to 1.05 V for CuPc, ClAlPc and SubPc respectively.¹³⁵ This increase in V_{OC} has resulted in an improvement in *PCE* from 1.0 % to 2.6 % to 3.0 % respectively. Further studies have looked to exploit the properties of SubPc. A successful approach is achieved by peripheral substitution, for instance halogenating the molecule lowers the HOMO and LUMO positions enabling it to function as an effective acceptor material.¹⁶⁵

1.6.3.2 Fullerenes

In 1996 the Nobel Prize for Chemistry was awarded to Kroto, Curl and Smalley for their discovery of Buckminsterfullerene (C_{60}) in 1985.¹⁶⁶ The name was chosen after the architect R. Buckminster Fuller whose geodesic domes provided a guide to the cage structure. This discovery showed the potential of a range of cage like structures with unique and appealing properties. Krätschmer *et al.* introduced the second generation of fullerene research by proposing methods of producing C_{60} and other fullerenes in macroscopic quantities.¹⁶⁷ This was achieved by using an arc to vaporize graphite in a helium environment. This enabled fullerene based materials to be used in a range of applications including OPV research, with a current high demand for this product resulting in a typical cost of ~ £30/g.

The C_{60} structure is a truncated isohedron that consists of sixty carbon atoms that are linked to form a hollow cage structure (**Figure 1.16 [a]**). The polyhedron has sixty vertices and ninety bonds that make up twelve pentagons and sixty hexagons, with no five-membered ring adjacent to another. Due to its spherical nature not all of the carbons can be sp^2 hybridised in nature (despite forming one double and two single bonds) as this would involve them all being in the same plane. Instead, due to the ring strain an intermediate is formed that is closer to sp^3 (tetragonal) and is susceptible to nucleophilic attack from species such as oxygen which has been shown to cause a decrease in conductivity and enhanced recombination.

C_{60} is a suitable acceptor material for OPV devices for a number of reasons. Firstly, due to the extended conjugated system it is able to accept between six and twelve electrons. Secondly has a relatively long L_D (although values differ significantly in literature) as it has a near-unity intersystem crossing (ISC) yield of singlet to

triplet excitons. The lifetime of the triplet state is orders of magnitude longer than the singlet state, increasing the overall L_D .¹⁶⁸ C_{60} also has one of the highest electron mobilities of an organic semiconductor, $5.1 \times 10^{-2} \text{ V cm}^{-2}$, stemming from extensive π overlap in the condensed phase.¹⁶⁹ It also has a high electron affinity which makes it an energetically viable acceptor material when combined with a range of donors. There is however a drive to replace C_{60} to offer the ability to tune ΔE_{LUMO} depending on donor material used; this has led to the successful use of SMs or TMOs as an alternative acceptor material.

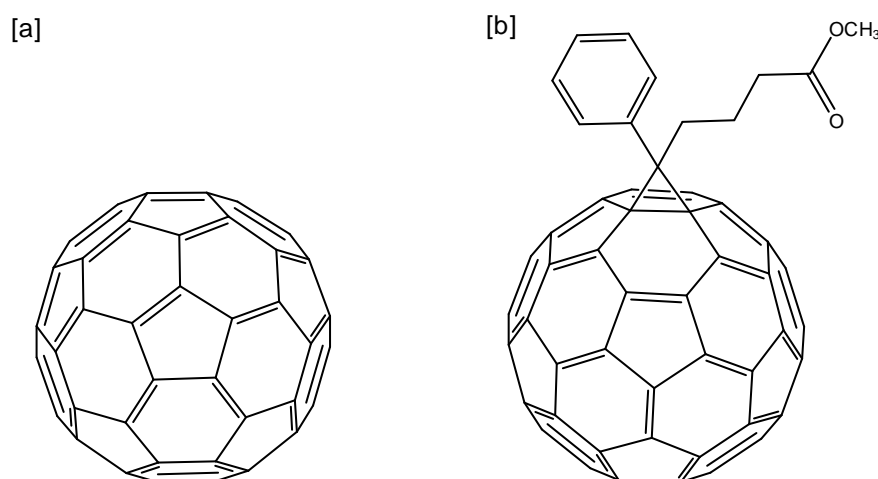


Figure 1.16 Molecular structure of [a] C_{60} and [b] PCBM

C_{60} has a low solubility in most organic solvents so therefore is typically vacuum deposited. Through the addition of organic groups the fullerene materials can be adapted for use with soluble donors, with the most heavily used acceptor for soluble devices being PCBM. This material was first shown in the BHJ device MEH-PPV:PCBM by Yu *et al.* in 1995 and since has been utilised in numerous device architectures owing to the advantageous properties of fullerene based acceptors.¹⁷⁰ Also by the addition of more soluble groups to the fullerene cage, there is an

increased saturation of the double bonds pushing the LUMO level closer to the V_L . This has been successful in the formation of bis-PCBM adduct, enhancing the V_{OC} of the device and subsequently the PCE .¹⁷¹ In the field of solution processed devices there has also been some drive to replace fullerene based materials but to date the efficiency has been limited at $< 5 \%$, compared to 10% using fullerene based acceptors.^{172, 173} There is also the necessity to understand what makes fullerene acceptors the ‘wonder materials’ when planar SMs, which promote enhanced charge transport and have increased absorption, are still significantly behind solution processed devices.

1.6.3.3 Poly(3-hexylthiophene)

P3HT has evolved to be one of the most suitable and widely used polymers for OPV cells, with over 5,500 publications to date.¹⁷⁴ Considerable scientific research has focused on how to improve the performance of this material for applications in OPV devices. The main outcome has been related to the regioregularity (RR). A higher RR is achieved with an increased percentage of monomers adopting a head-to-tail configuration rather than head-to-head.¹⁷⁵ An improvement in performance is obtained with a higher degree of RR due to the closer packing of the molecule improving the electroconductivity,¹⁷⁶ field effect mobility¹⁷⁷ and magnetic properties.¹⁷⁸ RR P3HT also packs in a semi-ordered lamellae structure perpendicular to the substrate, increasing the interchain contributions and improving the stabilization of the P3HT chains.¹⁷⁹ This results in a red shift in the absorption with a series of vibronic peaks at 510 nm, 550 nm and 600 nm.¹⁸⁰

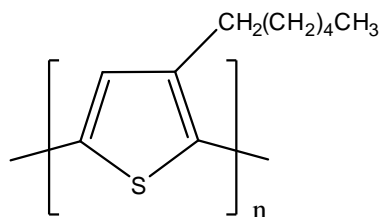


Figure 1.17 Molecular structure of P3HT

P3HT is commonly combined with the soluble fullerene PCBM. Owing to the low L_D of P3HT of 8.5 ± 0.7 nm,⁷⁰ a P3HT:PCBM BHJ is the architecture of choice. The performance of the BHJ varies significantly within literature, with a number of articles addressing the performance differences,^{174, 181, 182} which has on the whole been linked to differences in RR, molecular weight and purity, with the current average performance being estimated at 3 %.¹⁷⁴ Despite the variations, significant improvement has been found by a number of processing adaptations; mixed solvents without heat treatment,¹⁸⁰ varying solvent,¹⁸³ solvent vapour treatment¹⁸⁴ and through the use of additives.¹⁸⁵

1.7 Thesis Outline

The role of the TMO ZnO is the prominent theme throughout this thesis. The uses of ZnO have been explored to look at the viability of this cheap versatile material to function in different organic solar cells. This thesis explores the suitability of ZnO as an acceptor material in planar HOPV, focusing on improving the low performance either by altering the ZnO processing conditions to optimise the energetic profile or through the use of an optimised spacer layer. The use of zinc oxide in its more universally preferred role as an electron extracting layer is also explored, comparing both the processing methods of film formation and the influence of the underlying TCE.

Chapter 2 gives an overview of all experimental details required for thin film preparation along with thin-film analysis. Details are also included on the fabrication of devices and testing.

Chapter 3 introduces the use of ZnO layers produced by SG methods for the formation of hybrid ZnO/SubPc solar cells. In this chapter the ZnO solutions were prepared in an acetone solvent, and spin coated onto ITO substrates. Initially the chapter focuses on fabrication requirements to ensure smooth, reproducible ZnO thin films. Processing conditions were then explored for the improvement and understanding of cell performance, with energetic profiling obtained using Kelvin Probe (KP) and x-ray photoelectron spectroscopy (XPS). The optimum ZnO film was then implemented with two other donor materials to show the compatibility of ZnO in other hybrid devices.

Chapter 4 explores the electronic structures of the same cell architecture (ZnO/SubPc) using ultra-violet photoelectron spectroscopy (UPS). The differences in results between the UPS and the XPS measurements explored in **Chapter 3** are shown. The results obtained are discussed in terms of experimental difference and why each method may result in different conclusions.

In **Chapter 5** the use of an optical spacer layer in a ZnO/SubPc device is explored to monitor the changes in J_{SC} with spacer layer thickness. The performance is predicted using optical modelling prior to cell growth, accounting for L_D of the organic material. A series of cells are then fabricated and compared to the predicted values.

The use of ZnO as an electron extracting layer is covered in **Chapter 6**. This chapter focuses on the use of ZnO in an inverted structure for both bilayer organic cells and BHJ polymer cells. A comparison between electrodeposition (ED) and SG derived ZnO films on ITO and transparent gold electrodes (tAu) is presented and the influence both transparent electrode and interlayer have on the performance of polymer solar cells is discussed.

Chapter 7 concludes all the research presented along with the routes for future work.

2 Experimental

2.1 Layer Preparation

2.1.1 Substrate Cleaning

All the films were grown on ITO coated glass (sheet resistance $< 15 \Omega \text{ sq}^{-1}$) or quartz substrates. Two different ITO suppliers were used in this thesis. In **Chapter 3, 4** and **5** the supplier was Thin Film Devices. In **Chapter 6** ITO supplied by Psiotec was used for ED to be consistent with previous research explored in this area.^{131, 186} The Psiotec ITO was supplied with a layer of photoresist which was removed using an acetone rinse prior to the standard cleaning procedure. All substrates were cleaned by rinsing then sonicating in: 30:70 decon:water, water, propan-2-ol followed by drying with nitrogen and treating with UV-ozone for thirty minutes.

2.1.2 Solution Processing

2.1.2.1 *Sol-Gel Process*

The SG method is a versatile solution processing technique that allows for the simple production of high quality films at low cost. By utilizing the SG process, it is possible to fabricate advanced materials in a variety of forms: ultrafine or spherical powders, thin film coatings, fibres and porous or dense materials.^{187, 188} The process involves the transition of a solution system from a liquid colloid (sol) into a solid (gel) phase following the loss of solvent. This process forms a continuous network;

the sol loses its mobility and becomes able to maintain its shape due to the bond-bridging between the sol gel particles. The SG method has been used in literature for a variety of applications beyond photovoltaics. Transition metal oxide gels include one of the most successful products, IROXTM, which is used to coat architectural glass with TiO₂.¹⁸⁹

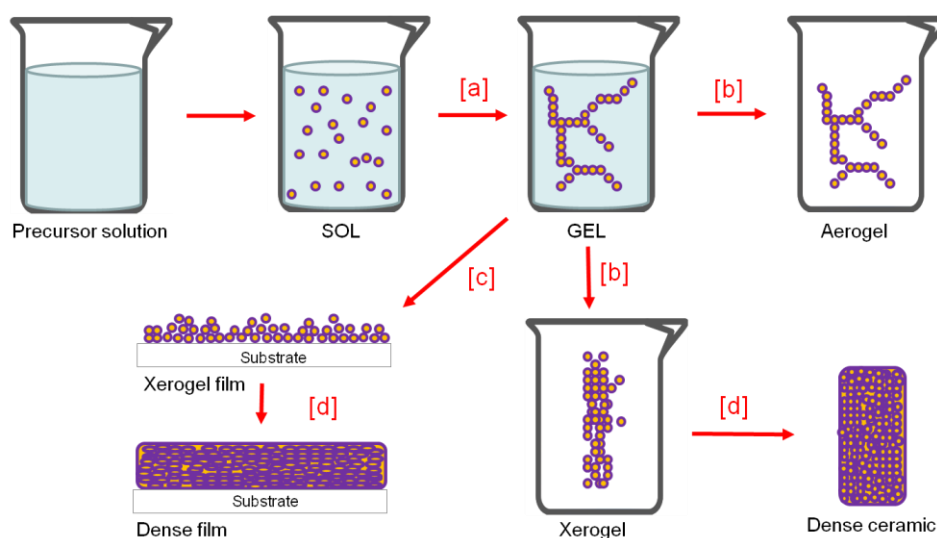


Figure 2.1 Schematic of the different processes of the SG process: [a] hydrolysis and condensation, [b] drying, [c] film formation and [d] sintering. The image has been adapted from Sol-Gel Science by C. Brinker and G. Scherer.¹⁹⁰

The sol, a liquid colloid, is a suspension in which the dispersed phase is small (1-1000 nm), the impact of the size of the particles means that the interactions are dominated by short-range forces such as van der Waals (vdW) whilst gravitational forces are negligible. In the SG process the precursors typically consist of a metal or metalloid surrounded by various ligands. There are two approaches; an aqueous sol-gel and non-aqueous (or non-hydrolytic) approach both of which have been explored extensively throughout the literature.^{191, 192} The aqueous route is typically used with metal oxide or metal alkoxide precursors as they react readily with water in a

hydrolysis reaction. One of the drawbacks of this approach is the high-reactivity of the precursors towards water which acts as both the ligand and solvent. This high-reactivity means that the reaction conditions (pH, temperature, hydrolysis, condensation rate and the nature of anions) need controlling in order to ensure reproducible products. The non-aqueous process, however, typically results in uniform, complex morphologies with good dispersity in organic solvents due to the much lower reactivity of the oxygen-carbon bond lowering the reaction rate. They also extend the use of precursors to metal acetates and metal acetylacetonates.

Commonly the definition of “sol-gel” is not completely satisfied as many procedures despite producing a sol do not result in the formation a gel. This was the case in this thesis, where TMO dispersions were formed using the non-aqueous method, due to its simplicity. The reaction process only requires an organic solvent (acetone or ethanol), zinc acetate as the precursor and the addition of ethanolamine (5 – vol %) (specific details are included in **Chapter 3** and **5**). This resulted in solutions that were stabilised due to electrostatic and steric forces preventing agglomeration. Films were directly spin coated from this solution rather than encouraging the formation of a gel as this resulted in the most consistent and reproducible device performances.

2.1.2.2 *Spin Coating*

Spin-coating is a widely used technique for the production of highly reproducible films, commonly with transition metal oxides or solution processed BHJs such as P3HT:PCBM. The process involves the application of an excess of solution on to a substrate. The substrate is then rotated at high speeds (typically > 1000 rpm) to spread the fluid by centrifugal forces. The solvent used then evaporates to form a

solid homogeneous film. During the spin coating process the interaction between the substrate and solution layer are stronger than the interaction between the solution surface layer and air. This process is effective for lab scale substrates up to ~ 30 cm in diameter.

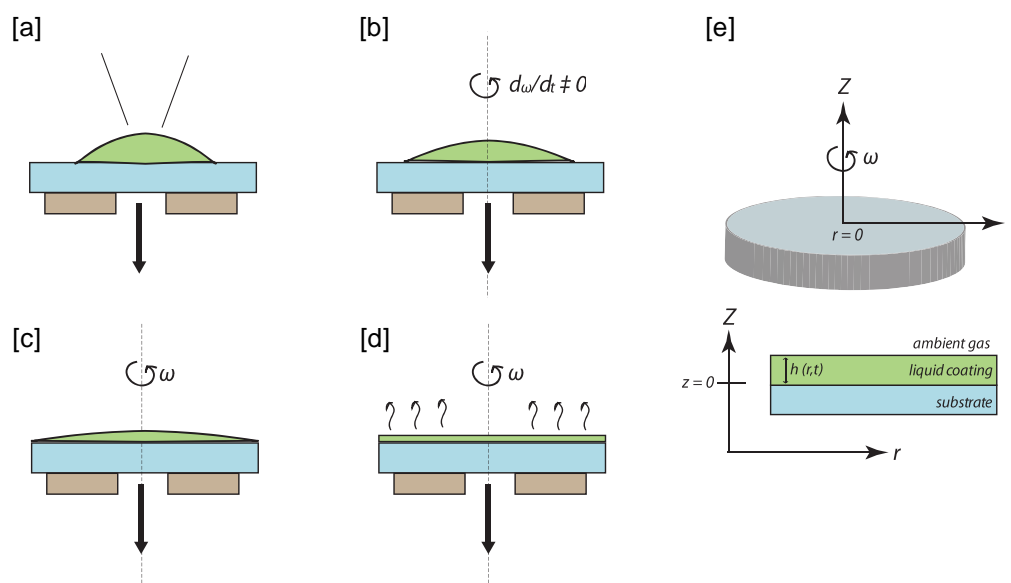


Figure 2.2 The different stages of spin coating [a] solvent dispersed onto the substrate, [b] acceleration of the substrate, [c] flow dominated, [d] evaporation dominated and [e] schematic illustrating the spin coating process with the appropriate variables.¹⁹³

The film properties; thickness, morphology and surface topography depend on the rotational speed, spinning time, viscosity, volatility and concentration.²⁵ When the disc is rapidly accelerated to high angular velocity, the solution is ejected from the disc, resulting in a thinner film. This is due to a combination of the adhesive forces at the interface of the liquid/substrate and the centrifugal forces acting on the rotating liquid.¹⁹⁴ As the solvent evaporates, the concentration increases, increasing viscosity which changes the rheology of the solution. Typical spin coaters have a closed lid and although not airtight, it minimises any unwanted external affects which improves the film thickness uniformity.

The required volume of ZnO solution was filtered (0.22 μm) immediately before spin coating. 50 μl of the solution was dropped onto the substrate and then the substrate was instantly rotated at 3000 rpm for one minute.

2.1.2.3 *Electrodeposition*

An alternative method for the production of thin films is ED, which has been modified more recently to be applicable for the formation of metal oxide thin films such as zinc oxide and was first used by Peulon *et al.*¹⁹⁵ and Izaki *et al.*¹⁹⁶ It involves dissolved precursors in aqueous solution (in this instance the metal hydroxide precursor) being reduced at the electrode leading to super saturation and precipitation of ZnO. There are problems associated with forming ZnO films for use in OPVs, firstly and most commonly is the film thickness. Thick ZnO layers can be detrimental to all parameters in OPV performance due to issues with charge extraction and reduction in layer transparency so therefore it is a necessity to keep layer thickness < 200 nm. The second is the orientation of the ZnO film, as the orientation and termination can greatly affect the work function and charge transport of the film.

The details of the ED process are summarised schematically in **Figure 2.3** which shows the three electrode system set up consisting of the working electrode onto which the ZnO is deposited (either ITO or transparent gold electrodes (tAu)), an Ag/AgCl/KCl (3.5 M) reference electrode and a platinum mesh counter electrode. The ED of ZnO onto ITO substrates has been previously optimised and the conditions were maintained for both ITO and tAu electrodes.^{131, 186} A 0.13 M

solution of $\text{Zn}(\text{NO}_3)_2$ was stirred and maintained at $85\text{ }^\circ\text{C}$, with a solution pH of 2.5.^{131, 186, 197} A potential of -1.3 V was applied versus the Ag/AgCl electrode and the deposition was stopped once a charge of 0.15 C cm^{-2} passed. The chemical process is summarised below and involves the reduction of NO_3^- (which are used due to their high solubility and therefore fast deposition rates) at the cathode to form the hydroxide precursor which is key for the precipitation of ZnO.

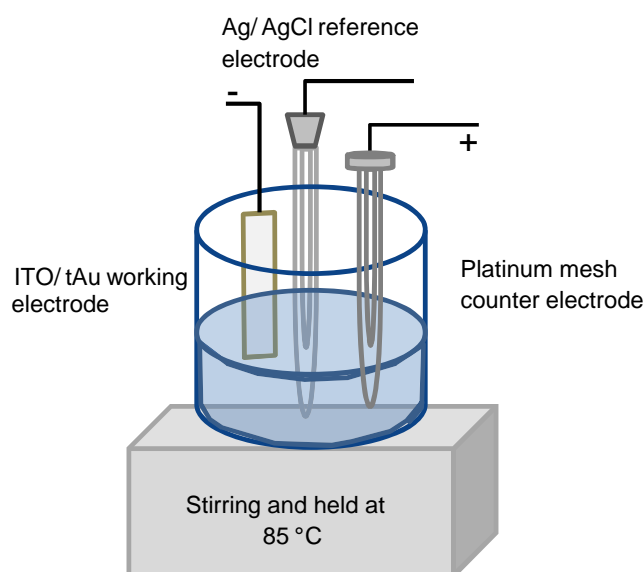


Figure 2.3 Schematic illustrating the electrodeposition process, with the Ag/Ag Cl reference electrode, ITO or transparent gold working electrode and the platinum mesh counter electrode.

2.1.3 Vacuum Deposition

2.1.3.1 *Material Purification*

Improved device efficiencies require materials of high purity and fine control over growth parameters during film formation. For this reason, most materials were purified by sublimation prior to deposition.^{198,199} The process consists of the impure material being placed in the end of a quartz tube under vacuum (10^{-5} mbar), which is heated with a tube furnace to ensure a controlled heating rate/time. Typically the temperature was raised by ~ 1 °C per minute until the sublimation temperature is reached. Exposing only part of the quartz tube to the furnace sets up a thermal gradient, allowing the sublimed material to travel down the tube until it reaches the colder regions where it condenses. By the end of the process, only the desired material will be present in the middle of the tube, as materials that sublime at a lower temperature will travel further down the tube and those that sublime at a higher temperature will be left at the end of the tube.

2.1.3.2 *Organic Molecular Beam Deposition*

Organic molecular beam deposition occurs under a vacuum allowing the deposition of thin solid films with thicknesses ranging from molecular monolayers to a few hundred nanometres. The deposition conditions allow controlled and reproducible growth of complex architectures with well-defined thicknesses and growth rates.²⁰⁰ Each material was deposited using a Kurt J. Lesker Spectros system and independently calibrated prior to use.

The purified materials are placed inside an evaporation source which is shown schematically in **Figure 2.4 [a]**. Deposition typically occurs at 10^{-7} mbar for increased control, and to prevent contamination and oxidation. The cell is heated to the materials sublimation temperature of the material, which is typically between 100 °C and 450 °C for organic materials. A schematic of the spectros system is shown in **Figure 2.4 [b]** and includes a rotating shelf to ensure homogenous film formation along with a mechanical shutter so the desired material deposition rate can be achieved prior to deposition onto the substrate surface. Film thickness is measured using a quartz crystal microbalance (QCM) which calculates the mass per unit area by measuring the change in frequency of the crystal. The QCM values are calibrated by comparing deposited thickness to those measured by step-edge atomic force microscopy (AFM).

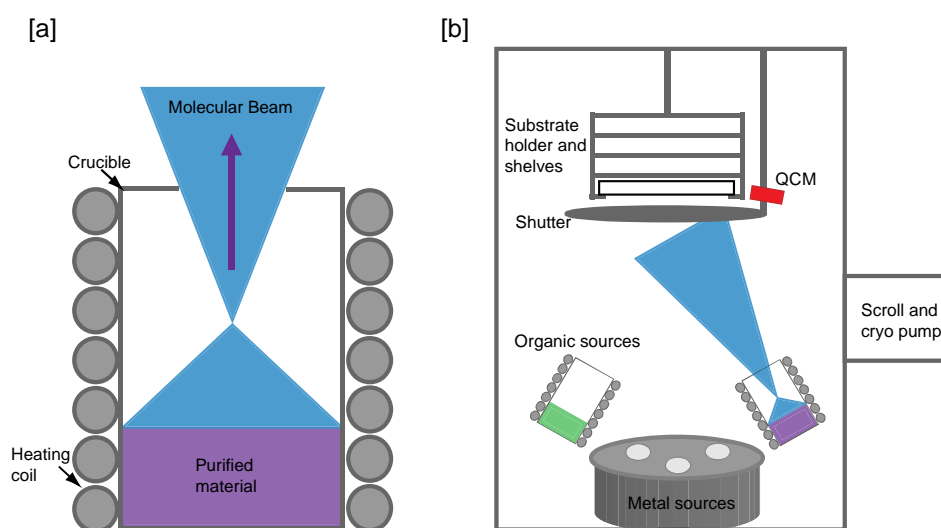


Figure 2.4 [a] Diagram of an evaporation source showing the formation of a molecular beam of the purified material and **[b]** a schematic of the Kurt J Lesker spectros system used.

Figure 2.5 shows a schematic of the ITO substrate (**[a]**) and the device after all layer have been subsequently deposited (**[b]**). For device fabrication, organic materials are deposited onto the rotating substrate to ensure complete coverage of the ITO substrate. Metal oxides can also be deposited in the same way but require high temperature thermal sources. The top contact was achieved by evaporating aluminium through a shadow mask to give the required active area. The active area of the electrodes was varied from 0.06 cm^2 to 1.00 cm^2 , with the typical active area for cell fabrication being 0.16 cm^2 . Details about film growth (film thicknesses, rates etc.) for each vacuum deposited material are included in the relevant results section.

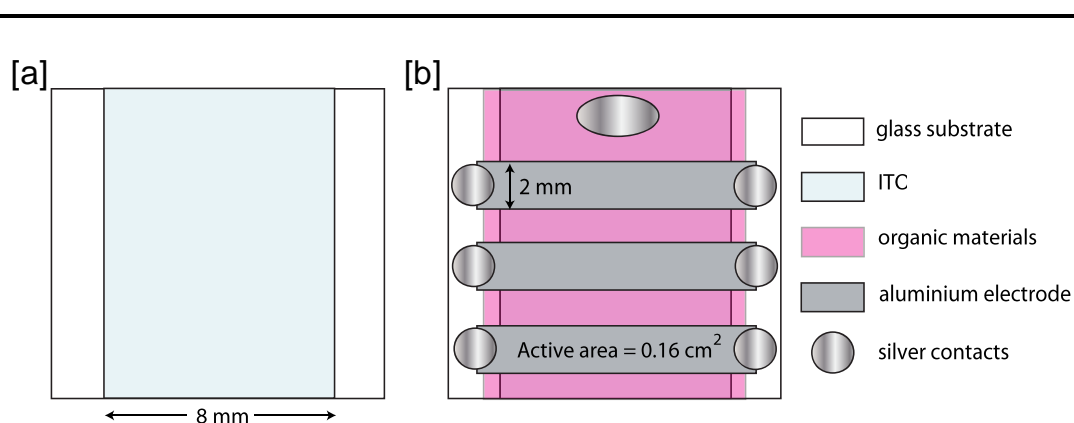


Figure 2.5 [a] ITO substrate and [b] device schematic with individual layers indicated in the key.

2.2 Thin Film Analysis

2.2.1 Absorption spectroscopy

Absorption spectroscopy is a simple analytical technique that is used in quantitative characterisation of solutions or thin films. Photons with specific wavelengths are absorbed by a material if they have an energy comparable to an allowed transition of the material. This absorption causes excitation of electrons to higher energy states with an optical spectrometer monitoring the reduction in light intensity this causes.

The amount of light, I , transmitted through an absorbing compound can be related to its concentration by Beer-Lambert's law:

$$A = -\log_{10} \left(\frac{I}{I_0} \right) = \varepsilon_{\lambda} bc \quad \text{Equation 2.4}$$

The law states a logarithmic dependence between absorbance, A , and the ratio of the incident light intensity, I_0 , and the attenuated light leaving the sample, I . ε_{λ} is the molar extinction coefficient for a given wavelength, b is the path length and c is the concentration, given by moles per unit volume. In solids, the concentration is related to the molecular mass and density. For thin films, the molar extinction coefficient and concentration are defined by the absorptivity of the material, α . The film thickness is defined by the term, L .

$$A = -\log_{10} \left(\frac{I}{I_0} \right) = \alpha L \quad \text{Equation 2.5}$$

In the field of photovoltaics, a simple technique such as UV-Vis absorption spectroscopy is essential. It enables the absorption characteristics of active layers to

be analysed, which is important for monitoring capability of the chosen materials to harvest as much of the solar spectrum as possible. It can also reveal a change in film structure with a more crystalline solid giving a red shift in the absorption spectra. The transmittance and band gaps of electrodes and interlayers (ILs) can also be measured which is important to ensure a limited amount of parasitic absorption.

Electronic absorption spectra were obtained using a Perkin-Elmer Lambda 25 spectrometer.

2.2.2 Photoluminescence Spectroscopy

Luminescence is the emission of light, with one of the forms being photoluminescence (PL) where the process is initiated by photoexcitation from any form of electromagnetic radiation. When a material is exposed to incident light of sufficient energy, photons are absorbed and electronic excitations are induced, this is shown in **Figure 2.6**, which shows schematically the different optical band-to-band excitations. After excitation, it decays to the lowest vibrational level of the excited state giving the excess energy to the surroundings/crystal lattice. From here, the system can relax from the excited state to the ground state. Since in this process energy is lost, the emitted photon will be of longer wavelength than the excited photon. This difference between the peak of the excitation band and emission band is known as a Stoke's shift.

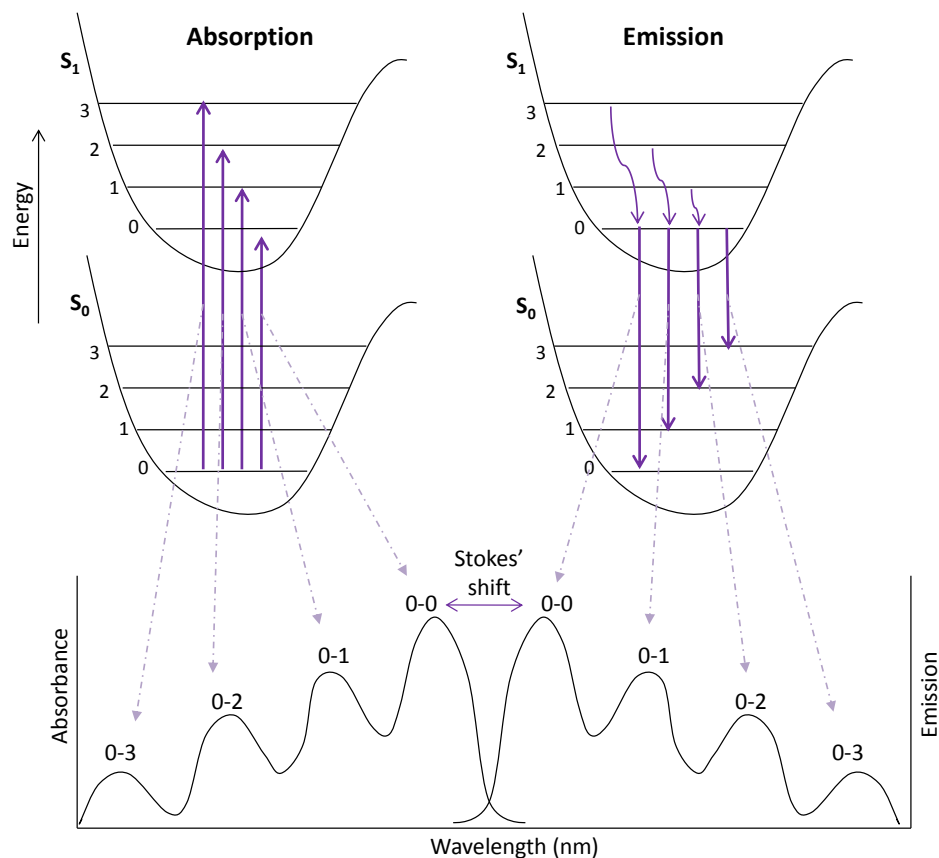


Figure 2.6 Jablonski diagram showing an example of absorption and emission spectra.²⁰¹ Stokes shift is indicated.

The excited states relax to their ground state either by radiative, k_r , or non-radiative decay k_{nr} . If the relaxation process is radiative, the emitted light is photoluminescence.²⁰² If the relaxation is non-radiative the energy has been dissipated into the surrounding crystal lattice. This decay has a lifetime, τ , which depends on the material of interest.

$$\tau = \frac{1}{k_r + k_{nr}} \quad \text{Equation 2.6}$$

PL is a non-destructive technique that requires minimal sample preparation. It can be used to probe many important materials properties as it measures the energy of the

emitted light which relates to the difference in energy levels between the transitions, and it also monitors the quantity of emitted light. This information can be used to infer the band gap of a material, impurities and defect levels as well as recombination and quenching efficiencies.

A Fluorolog®-3 Spectrofluorometer from HoribaJobin Yvon was used for PL measurements.

2.2.3 Ellipsometry

Ellipsometry is a non-destructive optical technique that is used to study the change in polarisation of light when it is reflected or transmitted from a sample. It evolved from the work in the late 19th century by Paul Drude who used polarised light to study optical properties and thickness of thin metallic films. The basic principle involves illuminating a sample with a collimated beam of polarised light and analysing the polarisation of the reflected beam. Ellipsometry is predominately used to measure film thicknesses, chemical composition, complex refractive index and uniformity.

One possible set-up, illustrated below in **Figure 2.7** involves a light source, polariser, sample, polarisation analyser and a detector. In this case the light beam is linearly polarised, and as it reflects from the surface of a sample it becomes elliptically polarised. As it interacts with a sample, any changes to the emerging beam can provide useful information that is specific to each material. The reflected light is passed through a second, rotating polariser and the intensity at each angle of the polariser is measured. When the light hits the detector, it is changed into an electronic signal and two parameters can be extracted, the phase difference (Δ) and

the amplitude ratio (Ω). These parameters are wavelength and angle of incidence specific. The parameters obtained (Δ , Ω) cannot be directly converted into the parameters of interest, so a model of the layer stack must be constructed. Regression analysis is then used to choose the best fitting model to provide the parameters of interest. The film thickness can be extracted from looking at the interference from light that is reflected from the surface and light that travels through the film. The optical properties, n (refractive index) and k (extinction coefficient) can also be obtained and it is these that are of interest for the field of OPVs. This is because the refractive index describes how light will propagate through a medium and the extinction coefficient is the imaginary part of the complex index of refraction and relates to absorption.

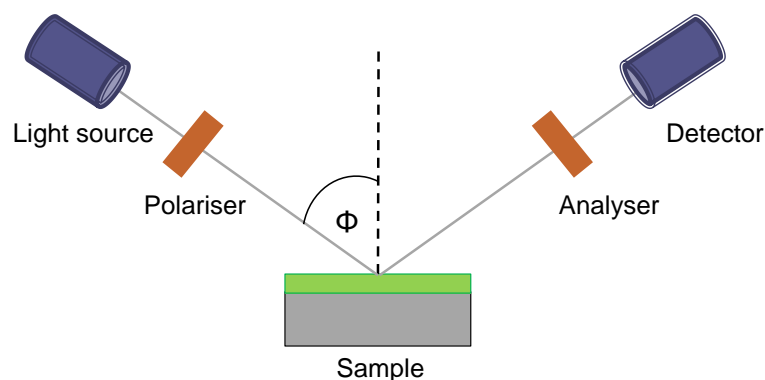


Figure 2.7 Schematic of a general spectroscopic ellipsometry set up.

The n and k values used in the optical model in this work were either obtained from literature or acquired at the University of Birmingham using a UVISSEL ellipsometer (Jobin-Yvon/Horiba, UK) with a Xe light source, over the wavelength range of 250 – 800 nm and at an incidence angle of 70 °. Film thicknesses and optical properties were modelled using a three phase ambient/film/quartz model, in which the layer

was assumed to be isotropic. An Adachi-new Forouhi dispersion formula was employed to obtain the optical constant for the film.^{203, 204}

2.2.4 Optical Modelling

For OPVs the Beer-Lambert law cannot be used to calculate the absorption of each layer within the device because the layers are much thinner than the penetration depth and interference effects play a significant part. This is enhanced due to the highly reflective electrode commonly used and the difference in dielectric constants at each interface, both of which impact the optical electric field in the device.

In order to determine the optical electric field intensity inside the device, optical modelling was carried out using the transfer matrix method, taking account of both material properties and potential reflection and interference effects which are important on this scale.^{205 206} This enables the absorption efficiency, or absorptance, η_A of a multilayer stack to be calculated:

$$\eta_A = 1 - T - R, \quad \text{Equation 2.7}$$

where T is transmittance and R is reflectance for each interface in the stack. The model does not account for diffuse scattering and assumes the each interface is optically flat.

The optical electric field intensity for each wavelength in each layer can be calculated by this method, when the layer thicknesses and complex refractive indices (n and k) are known. Complex refractive index data in this work was either obtained experimentally by ellipsometry or from literature.

Optical modelling enables an estimation of η_A (the quantum efficiency of absorption within a film) and, by integrating against the solar spectrum (AM1.5G), an estimate of the current generation for each layer. This value however does not account for the losses associated with the other three steps in the operation of an organic solar cell. This means that unless a value for the internal quantum efficiency (*IQE*) can be accurately obtained, the prediction of J_{SC} should be treated as the upper limit. The *IQE* can be estimated experimentally considering the *EQE* of the device, given that:

$$IQE = \eta_{ED}\eta_{CC}\eta_{CT} = \frac{EQE}{\eta_A} \quad \text{Equation 2.8}$$

The optical modeling script used in this thesis was originally created by Dr Felix Braun (Jenny Nelson's Group, Imperial College London), but adapted by Dr Thomas Howells and used in **Chapter 5**. To account for the diffusion length the output from the optical field calculations was input into a custom 1D finite difference diffusion equation solver with the optical calculations converted into an exciton generation rate at nanometre increments within the layer. Current generation is then defined as the flux of excitons through each dissociating interface.

2.2.5 Atomic force microscopy

Atomic force microscopy (AFM) is a versatile technique that can image, characterise and manipulate matter with high spatial resolution. It was invented by Binnig *et al.* in 1986 and was first commercially available in 1989.²⁰⁷ The main benefit of AFM is that it can probe the features of both conductive and non-conductive samples,

monitoring the close range tip-sample interatomic interactions. This generates a topographical map of surface features. The technique provides vital information in the field of OPVs as the surface properties of a layer can have a significant effect on cell performance.

An AFM set up is shown schematically in **Figure 2.8**. Located at the end of cantilever is the tip which is typically ~ 3 -6 microns long. The amount of force between the tip and sample at any given time follows Hooke's law and is dependent on the spring constant of the cantilever and distance between the tip and sample. The forces measured depend on the influence of attractive and repulsive forces as the tip approach the surface, shown in **Figure 2.8 [a]**. In the non-contact region (typically hundreds of angstroms from surface) the interactions between the cantilever and the surface are attractive, including electrostatic and van der Waals interactions. As the tip is brought closer (less than a few angstroms from the surface) the interatomic interactions between the cantilever and the surface are dominated by repulsive forces including hard sphere repulsion, repulsive van der Waals and electron-electron coulombic interactions. These repulsive forces cause the tip to bend up.

When imaging the motion across the surface is controlled using a feedback loop and piezoelectronic scanners. The output from the laser is positioned on the parabolic end of the cantilever which is reflected into a photodetector with four quadrants, which generate a voltage proportional to the light hitting each quadrant. Any differences measured between the four segments indicate the position of the laser spot, this is relayed to the controller, ensuring the set point for deflection or amplitude is kept constant. A topographic image is obtained by the distance the scanner moves in the z direction being stored in the computer relative to the spatial variation in the x-y direction.²⁰⁸ Different scanning modes operate in different

regions of the curve, contact mode operates in the repulsive region, non-contact mode (where the tip does not contact the surface but oscillates above the adsorbed fluid layer) uses the attractive region whereas tapping mode (also known as alternating contact mode) operates between the two. In contact mode, a tip is brought to the surface, ensuring that a tip-sample distance is maintained depending on the set point used. When the spring constant of the cantilever is less than the forces between the probe and sample, the tip starts to bend towards the surface. The sample is moved laterally and a feedback loop is used to keep the cantilever deflection constant by changing the probe height z while scanning in x and y and therefore a nearly constant force is maintained between tip and surface during imaging. The advantages of contact mode are the high lateral resolution and quick imaging of hard samples. Therefore, contact mode was utilised for imaging of some metal oxide thin films and when using conductive AFM. The drawback however is that contact mode can lead to large shear forces on the surface, damaging softer samples.

All images of organic materials that would be susceptible to such damage were taken using tapping mode AFM. In tapping mode, the cantilever is oscillated close to its resonant frequency using a piezoelectric element. When the oscillating tip interacts with the surface the amplitude of the oscillations is dampened. An oscillation amplitude set point is chosen by the user, which ensures a constant tip-sample interaction is maintained by monitoring the oscillation amplitude using the four-quadrant photodiode and controlled using the z -piezo and feedback loop. This allows an image of the surface to be obtained.

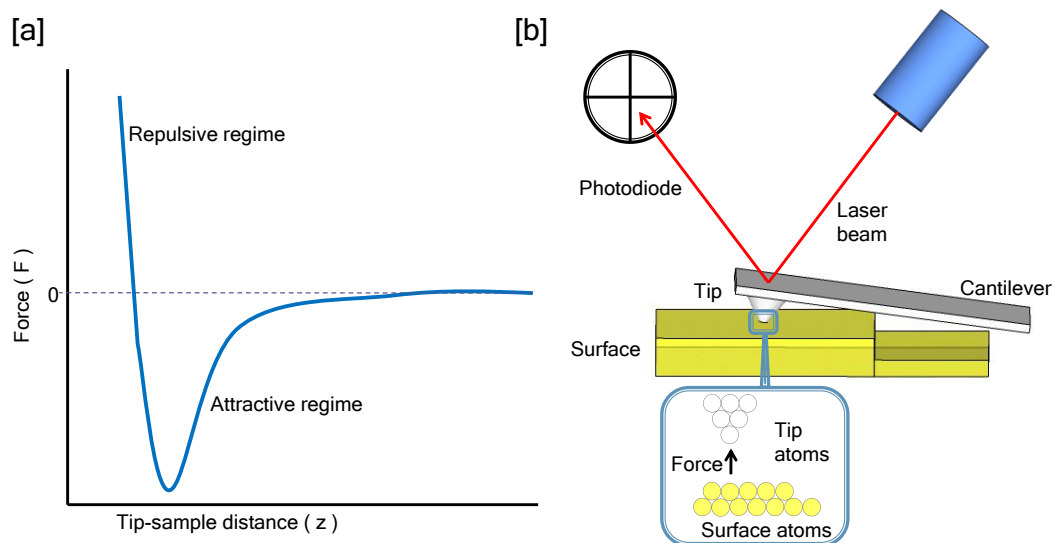


Figure 2.8 A schematic showing [a] the force curve obtained with increasing tip-sample distance (z) and [b] the AFM set-up.

All images were taken using an Asylum Research MFP-3D using Olympus AC240-TS Si cantilevers with a resonant frequency of 70 kHz and a tip radius of 9 nm.

2.2.5.1 Conductive AFM

Conductive atomic force microscopy (CAFM) can be used to characterise electrical properties of a sample at high resolution. A voltage is applied between the sample and the conductive AFM tip and the current flow is measured as a function of tip location whilst scanning the sample surface in contact mode. This results in simultaneously obtained topography images and current distribution maps. This is a useful property as it allows any changes in conductivity to be compared to any differences in features on the samples surface.

The MFP-3D was fitted with an ORCA integrated tip-holder and current preamplifier (20 nA) for CAFM measurements. Both the topography and current distribution images were obtained simultaneously using Au/Cr coated cantilevers which act as a nanoelectrode and form the top contact (Olympus TR400PB, tip radius < 40 nm, spring constant 0.06 N m^{-1}). A contact of silver paint was added to the film of interest and a sample bias was applied via a wire from the OCRA tip holder. A $500 \text{ M}\Omega$ resistor was used to limit the current.

2.2.6 Electron Microscopy

Electron microscopy (EM) utilises a beam of electrons to create an image of the specimen. This allows images with a higher magnification and greater resolution to be formed, compared to using a light microscope where the resolution is limited due to Abbe's formula. Ruska demonstrated that a magnetic coil could act as an electron lens which led to the development of the electron microscope during his PhD in 1933 and in 1986; Ruska won the Nobel Prize in Physics for his contribution to electron optics.

EM can be carried out on bulk samples in the form of scanning electron microscopy (SEM) or on thin specimens on the films in the form of transmission electron microscopy (TEM). These techniques give the ability to image the sample down to the nanometre range as well as providing compositional and structural information of the film of interest. Both techniques utilise an electron beam to result in high-resolution images of the specimen.

SEM produces high-resolution images, revealing details in the 1-5 nm range through the use of electrons. A monochromatic stream of electrons is fired from the top of the

microscope by an electron gun which is held in a vacuum. The beam of electrons follows a vertical path as it is constricted by a series of electromagnetic lenses and apertures. The energy of the incident electron beam, E_b (adjusted via the acceleration voltage) defines the penetration depth into the sample whereas the electron-beam current I_b (adjusted by filaments or apertures) alters the electron-injection rate into the sample.

When primary electrons hit the sample, energy can be lost by a variety of mechanisms, including secondary electrons (SEs), back scattered electrons (BSEs), auger electrons, light emission (cathodoluminescence) and x-ray emission. The electrons typically used for imaging are SEs, however BSEs which have more energy and a defined direction are also typically detected in high resolution SEMs and can provide information about the distribution of elements in the sample. The electrons are attracted and collected by a positively biased collector grid which then produces a signal.

The sample must be electrically conductive and grounded in order to be imaged effectively; this prevents charging of the specimen which would occur because of the accumulation of static electric fields. For non-conductive samples this is achieved by sputtering a thin conductive layer of either Au, Au:Pd or carbon using a sputter coater held under low vacuum which ionises argon gas under an electric field. Argon, which is positively charged, accelerates into the material sources, knocking atoms from the surface and onto the sample.

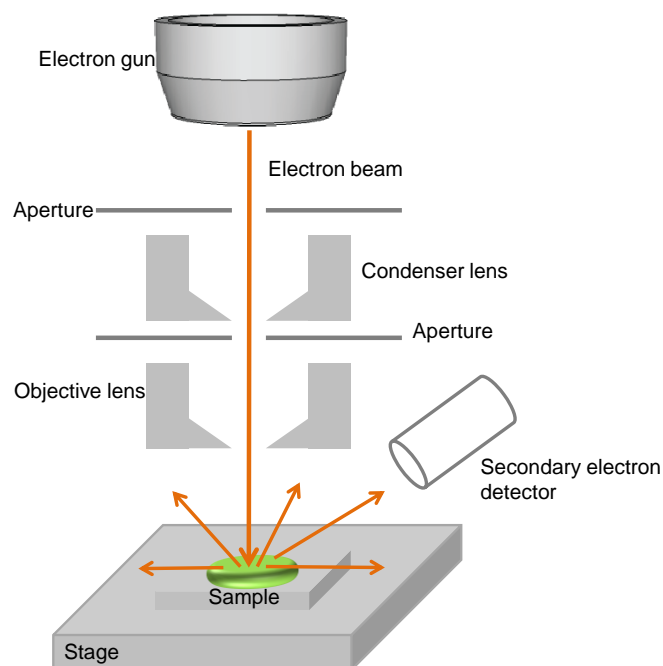


Figure 2.9 Schematic of the SEM set-up.

Images for this thesis were obtained using either a Zeiss 55VP SEM with SEs and BSEs detectors (**Chapter 3**) or a LEO Gemini 1525 field emission gun scanning electron microscope (FEG-SEM) with an accelerating voltage 5 kV (**Chapter 6**).

2.2.7 X-Ray Diffraction

X-ray diffraction (XRD) is a versatile, non-destructive technique that gives information about the chemical composition and crystallographic structure of a material. A crystal is the arrangement of solid atoms, ions or molecules in a 3D pattern, forming a symmetric motif. This regular, repeating array is called the crystal lattice, with each repeat unit forming a point within the lattice. The lattice points can be connected to form a 3D box and it is this that defines its unit cell. The unit cell is characterised by three unit vectors a , b , c and three angles α (between bc -axes), β

(between ac-axes) and γ (between ab-axes). The relationship between (a, b, c) and (α, β, γ) defines the unique shape and size of the unit cells and symmetry motif. The arrangement of unit cells must not have any space between them, so due to this restriction, the unit cells are constrained to 14 unique crystal lattices called Bravais lattices. The Miller indices define the orientation of the plane within the unit cell. The point at which the plane intercepts with the unit cell axes are defined by the Miller indices (hkl) which are indicated in **Figure 2.10**. The indices are given as a series of three integers $(1/h, 1/k, 1/l)$, with a (100) plane indicated on the diagram. The arrangement forms a series of parallel planes with spacing, d_{hkl} .²⁰⁹

Bragg in 1912 defined a simple relationship to understand how diffraction related to relative positions of point objects in space. When a monochromatic x-ray beam with wavelength λ hits a surface at angle θ , the atomic planes cause interference as the x-rays leave the crystal. Constructive interference is only observed when the reflected waves are in phase. This occurs when the difference in length of the path of incident and reflected waves are an integer number of wavelengths, n , of the wavelength of the incident x-rays. In these conditions Bragg's law (*Equation 2.9*) is satisfied meaning that the reflected waves are in phase and hence interfering constructively, resulting in intense peaks known as Bragg's peaks.

$$n\lambda = 2d\sin\theta \qquad \text{Equation 2.9}$$

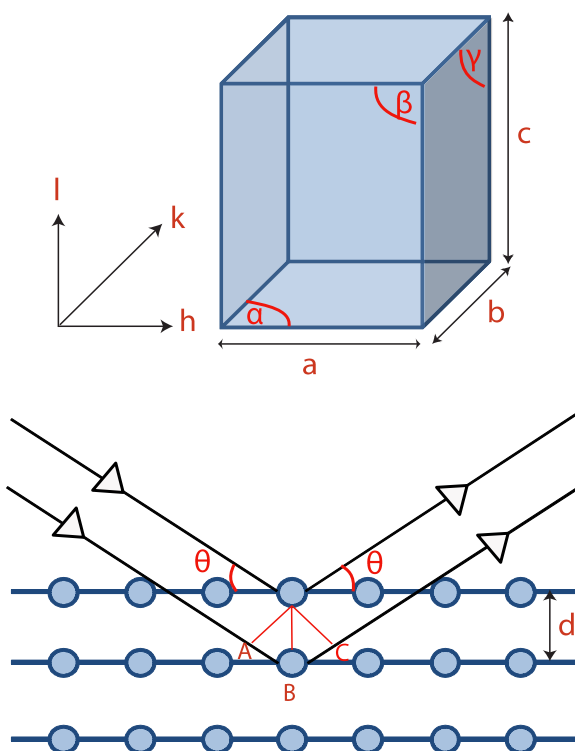


Figure 2.10 Lattice parameters with lengths a , b , c and angles α , β , γ . A schematic of x-ray diffraction is also shown.

In this study the XRD data was obtained by Dr Amy Cruickshank using Philips PANalytical X'Pert PRO MPD diffractometer, with Cu K_α radiation and a Ni filter, operated at 40 kV / 40 mA.

2.3 Energetic Characterisation

2.3.1 Kelvin Probe

Kelvin probe (KP) is a non-destructive, non-contact analytical technique that measures changes in contact potential difference (CPD) between a reference material and a sample that have been brought into close proximity. **Figure 2.11** shows the

energy level diagram with two materials of different work functions, the sample surface of interest (Φ_s) and gold oscillating tip (Φ_t). In **Figure 2.11 [a]** the tip and sample are not in electrical contact and are separated by a set distance, with the vacuum levels aligned. When two materials are in electrical contact, electrons flow from the material with a lower work function to the one with a higher work function, **Figure 2.11 [b]**. As the materials are set up as a parallel plate capacitor, surface charges form positive charges on the material of lower work function and negative charges on the material of higher work function. This creates an electric potential between the two materials and in response the electronic states shift relative to one another. This flow of charges induces an alignment of the Fermi levels and a potential gradient (V_{CPD}).

The tip is mounted just above the sample and is vibrating vertically at a given frequency. This creates an AC current which varies depending on distance from the sample. To measure the V_{CPD} , an applied DC voltage is gradually ramped to nullify this current, indicated on **Figure 2.11 [c]** by V_{DC} . Once this bias equals that of the V_{CPD} but with the opposite direction, the applied bias is equal to the difference in work function between the two materials:

$$\Delta\Phi = \Phi_s - \Phi_t. \quad \text{Equation 2.10}$$

The KP technique therefore can only detect the CPD and therefore the actual work function is deduced when referenced to the surface of material with a known work function. The material used as a reference was highly oriented pyrolytic graphite (HOPG, $\Phi = 4.475$ eV) which is chosen as it is chemically inert and does not form significant interface dipoles with typical ambient contaminants. This is vital as due to the nature of the technique, the measurements are very sensitive to any changes to

the surface including absorption, evaporation, surface charging and oxide layer imperfections, so care must be taken in sample preparation.

In this instance all measurements were carried out in a nitrogen filled glove box using a Besocke Delta Phi GmbH KP (Kelvin Probe S and Kelvin 07 electronic control) in a Faraday cage. The gold probe (2.5 mm diameter) was oscillated using a piezoelectric transducer which was positioned ~ 1 mm above the sample. For consistency samples were replicated and readings were taken at various locations across the surface.

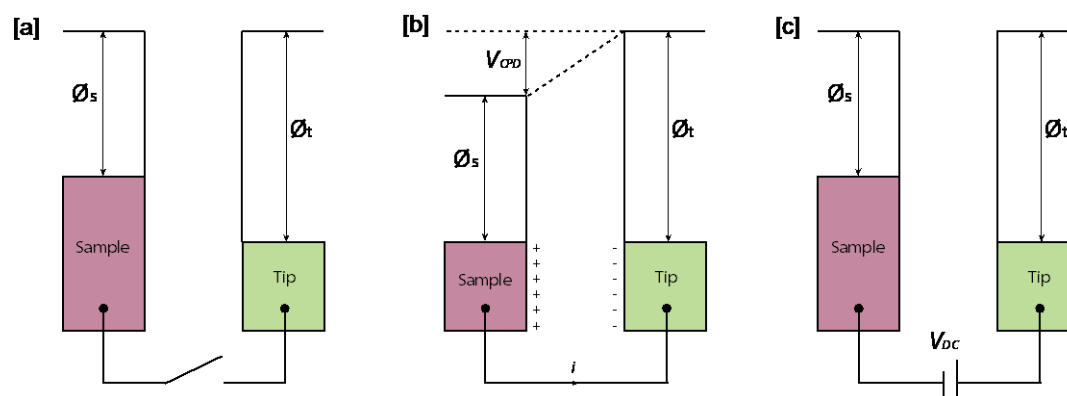


Figure 2.11 Electronic energy levels of the sample and conductive tip for three different cases [a] the tip and sample are separated by a set distance with no electrical contact, the work functions are also indicated ϕ_s and ϕ_t for the sample and tip respectively. [b] Tip and sample in electrical contact, the Fermi levels equalize and [c] external bias is applied (V_{DC}) between the sample and the tip to nullify the CPD.²¹⁰

2.3.2 Photoelectron Spectroscopy

Photoelectron spectroscopy (PES) involves the measurement of the KE distribution of electrons ejected from a material illuminated by photons of a known energy, in order to study the composition and electronic state of the sample. The energy of the photoemitted electron is dependent on the energy of the incoming photon of energy ($h\nu$) and the energy state in which it existed. In x-ray photoelectron spectroscopy (XPS), soft x-rays are used ($h\nu = 200 - 2000$ eV) to examine core energy levels which have binding energies (E_{BE}) that are specific to the atomic and chemical environment. Ultraviolet photoelectron spectroscopy (UPS) however, uses UV radiation ($10 - 45$ eV) to measure the outermost electrons held in the valence levels. Both XPS and UPS are summarised schematically in **Figure 2.12**. The basis of both of these techniques lies in the photoelectric effect for which Einstein won the Nobel Prize in Physics in 1921.²¹¹

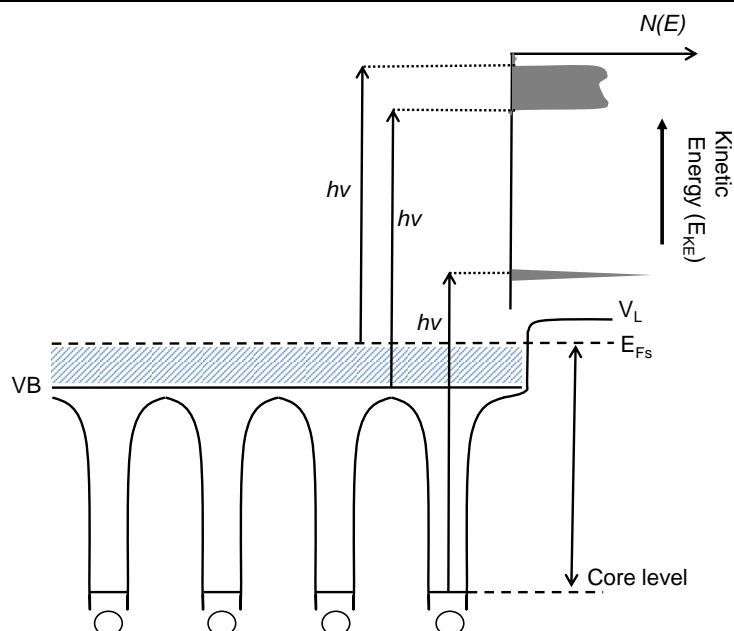


Figure 2.12 A schematic summarizing the energetics of the photoemission experiment. The positions of the VB, E_{Fs} and V_L have been indicated.

2.3.2.1 X-Ray Photoelectron Spectroscopy (XPS)

XPS utilises x-ray photons possessing a kinetic energy between 200 – 2000 eV, which causes the ionization of atoms via the photoemission of electrons with characteristic kinetic energies. The technique was pioneered by Siegbahn and co-workers and is utilised for material composition and stoichiometric analysis of the material of interest.²¹²

The technique involves a sample, being held under vacuum that is irradiated with a high energy monochromatic beam. This is typically either a Mg K_α (1253.6 eV) or Al K_α (1486.6 eV) soft x-ray source. This interaction causes electrons to be emitted by the photoelectric effect, where conservation of energy requires that photons can induce electron emission from the solid as long as the photon energy is greater than the work function. The E_{BE} of the emitted electron is given by

$$E_{BE} = h\nu - \phi - E_{KE}, \quad \text{Equation 2.11}$$

where h is Planck's constant and ν is the frequency of radiation in Hz, E_{KE} is the kinetic energy of the emitted electron, and ϕ is the work function of the spectrometer.

The electrons that are emitted have a kinetic energy and some of the electrons are emitted at the correct angle to enter the hemispherical analyser. Changing the voltage between the inner and outer hemispheres brings electrons of different energies on to the channeltrons. Therefore by sweeping the analyser through the full kinetic energy range offered by the source, a plot of counts/sec versus kinetic energy is obtained. Modern analysers and x-ray sources offer resolution < 1 eV, therefore different chemical states can be clearly resolved. The binding energy is the difference between

the initial and final states of the atom during the photoemission process. The binding energy increases with atomic number and decreasing orbital quantum number, with any subtle variations being due to differences in chemical potential and polarizability. This rather simplistic view is expanded via the consideration of initial and final state effects.²¹³ The *p*, *d* and *f* levels have two equivalent final states, spin up and spin down resulting in a doublet peak due to spin-orbit splitting ratio of 1:2 ($p_{1/2}, p_{3/2}$) for the *p* levels, 2:3 ($d_{3/2}, d_{5/2}$) for the *d* and 3:4 ($f_{5/2}, f_{7/2}$) for *f* levels.

XPS is a surface sensitive technique, the inelastic mean free path (IMFP) of electrons is small and therefore the electrons that are detected without undergoing inelastic energy losses originate from the top few atomic layers (up to 10 nm). The IMFP varies as a function of energy, so the “universal curve” which gives the average distance between inelastic collisions needs to be considered especially for compositional analysis. Photoionisation can typically lead to the emission of two electrons, a photoelectron and an Auger electron. The photoelectron is illustrated in **Figure 2.13 [a]**, these are the electrons leave the sample without energy loss and prove to be the most useful. As emission of an electron leaves behind a hole, an Auger electron emission or x-ray fluorescence can occur. Auger electron emission is the most common and typically occurs 10^{-14} seconds after photoemission. This is illustrated in **Figure 2.13 [b]** and involves an outer electron falling from a higher level to fill an initial core hole and the energy produced in this process leads to the emission of a second electron.

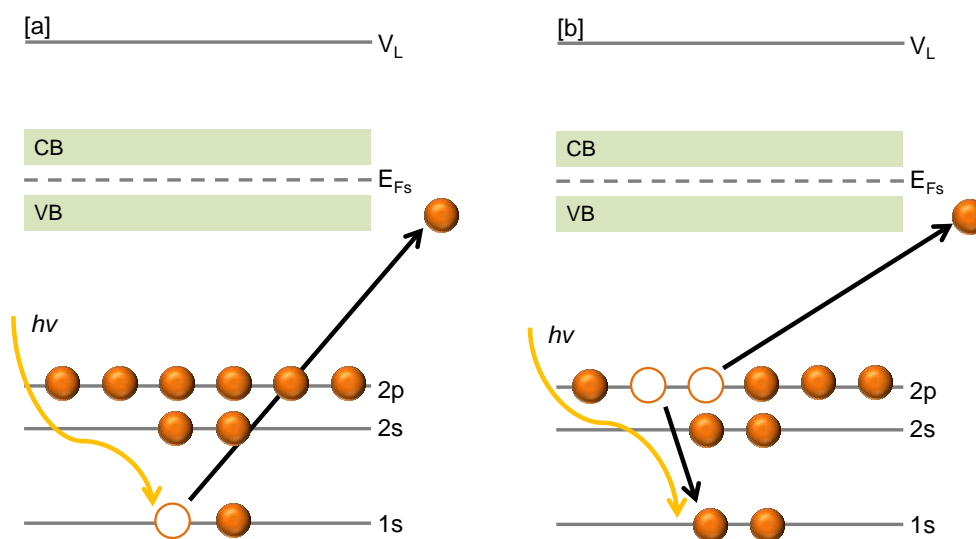


Figure 2.13 XPS emission for a model atom. **[a]** incoming photon causes emission of an electron from the core 1s level, **[b]** Auger emission – an outer electron falls into inner orbital vacancy, emitting a second electron.

In this thesis, the measurements were taken *ex-situ* after loading into an ultra-high vacuum system with a base pressure of $\sim 2 \times 10^{-11}$ mbar. XPS measurements were performed using a monochromated Al K_{α} x-ray source (Omicron XM 1000, $h\nu = 1486.6$ eV) and detected using an Omicron Sphera electron analyser at a take-off angle (TOA) of 90° or 30° . The TOA was varied to probe different depth due to different surface sensitivities. A pass energy of 10 eV was employed for both core levels and VB (resolution = 0.47 eV). Peak fitting and analysis is a key factor for data interpretation. In all instances, the binding energies of all spectral features were referenced to the C 1s peak for carbon contamination (284.6 eV), and a Shirley background was utilised in the analysis of the core levels. Peak fitting involves careful consideration of the bonding environment and therefore any effect this would have on the FWHM, for instance main metal peaks have a much narrower FWHM than a C 1s peak. For metal peaks asymmetric Lorentzian lineshapes were used, the

asymmetry occurring as a result of coupling with conduction band electrons. As well as elemental analysis, stoichiometric ratios can be accurately determined. These values were calculated by using the Schofield relative sensitivity factors (RSF) and variations of the IMFP with binding energy which are built in to CasaXPS, and an analyser transmission function calculated from polycrystalline Ag, Cu and Au foils.²¹⁴

2.3.2.2 Ultraviolet Photoelectron Spectroscopy (UPS)

UPS is a similar process to XPS, but in this instance the sample is irradiated with photons of a much lower energy as the UV photons are generated from a helium discharge lamp. The gas, depending on the conditions, provides energy of 21.2 eV (He I) or 40.82 eV (He II) and this radiation is used to excite valence electrons. This allows the detection of VB or HOMO energy levels as well as work function measurements. A typical UPS spectrum is shown in **Figure 2.14** given on a binding energy scale. This is calculated from *Equation 2.11* as the energy source ($h\nu$) is known and the kinetic energy of the emitted electrons is measured using a hemispherical analyser. This spectrum is displayed such that the E_{Fs} is at 0 eV (by taking into account the work function of the spectrometer).

At the secondary electron cut off (or high binding energy cut off), there is a tail of inelastically scattered electrons which have been emitted from the valence band states and scattered as they have approached the surface. Biasing the film is essential, as it moves the secondary electron cut-off from the drop-off in detection in the analyser, allowing the work function to be accurately determined.

$$\phi_{\text{sample}} = h\nu - BE_{\text{secondary electron}} \quad \text{Equation 2.12}$$

At the other end of the spectrum, the low binding energies, the valence band emissions occur, which tend to be formed from a combination of narrow high density of states e.g. O 2s. This enables the $\text{HOMO}_{\text{onset}}$ or VB_{onset} to be determined, calculated as an additional binding energy below the E_{F_s} of the material. This is useful in organic materials for calculating the ionisation potential (IP) when combined with the work function.

$$IP = \phi + \text{HOMO}_{\text{onset}} \quad \text{Equation 2.13}$$

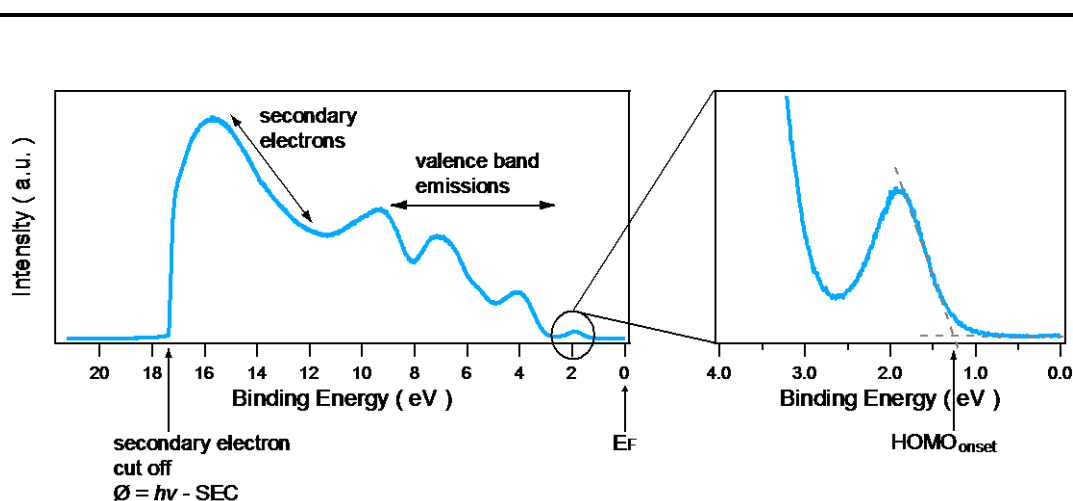


Figure 2.14 An example of an UPS spectrum, in this case for 12 nm of CIAIPc. The E_F and ϕ (calculated from the secondary electron cut off) have been indicated. The diagram on the right shows the low binding energy spectra, the $\text{HOMO}_{\text{onset}}$ is calculated by the intercept with the energy axis.

Ultraviolet photoelectron spectroscopy (UPS) measurements were taken in the same UHV chamber as the XPS measurements. The spectra were obtained using He I emission ($h\nu = 21.2$ eV) from a Focus HIS 13 vacuum ultraviolet photon source, with an applied bias voltage of ~ 10 V.

2.4 Device Characterisation

2.4.1 Sun and Solar Spectrum

The sun is a blackbody emitter, a light source which absorbs all radiation on its surface and emits radiation based on its temperature. The spectral irradiance from a blackbody source is given by Planck's radiation law:

$$F(\lambda) = \frac{2\pi hc^2}{\lambda^5 \left(\exp\left(\frac{hc}{k\lambda T}\right) - 1\right)} \quad \text{Equation 2.14}$$

where λ is the wavelength of light, T is the temperature of the blackbody (K), F is the spectral irradiance ($\text{W m}^{-2} \mu\text{m}^{-1}$), h is Planck's constant, c is the speed of light and k is Boltzmann's constant. The sun's surface is called the photosphere and is modelled at a blackbody temperature of $5730 \pm 90 \text{ K}$.²¹⁵

The solar radiation at the Earth's surface varies throughout the day due to a variety of effects including atmospheric effects (such as absorption and scattering), time of day, variations in the atmosphere (e.g. water vapour, clouds), latitude of the location and seasons. These effects can have a distinctive impact on the radiation at the Earth's surface, with specific gases such as ozone, water vapour and carbon dioxide absorbing photons, leading to troughs in spectral irradiance. The radiation loss through the atmosphere has an angle dependency which is defined by a value called the air mass (AM). AM 0, as shown in **Figure 2.15**, is the solar radiation that reaches a point just outside the Earth's atmosphere and is used to estimate cell performance in space. AM 1 is when the sun is directly overhead, and thus is the minimum path length for light reaching the surface.

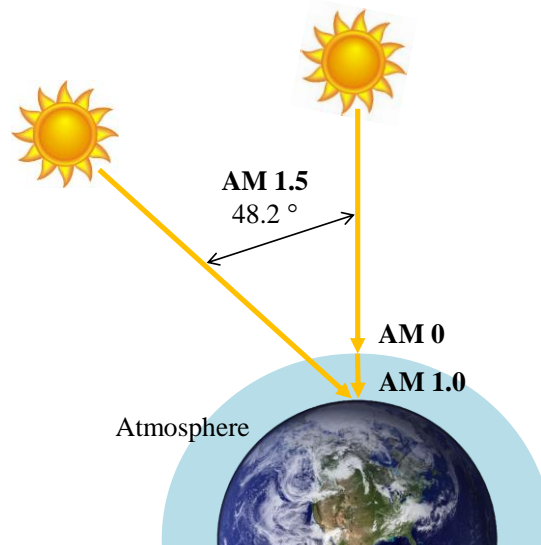


Figure 2.15 Schematic showing the air mass coefficient which is related to the path length through the Earth's atmosphere.

Due to the large number of variables, testing methods have had to be standardised in order to ensure fair comparisons between different organisations and for theoretical calculations and solar simulator design. This is achieved using a defined spectrum and power intensity. The typical standard in laboratory measurements is AM 1.5 G, equivalent to where the sun is at a 48.2° angle from the Earth's surface. G stands for global radiation; including both diffuse sky radiation and direct (D) solar radiation. The American Society of Testing and Materials (ASTM) justified the AM 1.5 G standard "because they are representative of average conditions in the 48 contiguous states of the United States". The spectral profile of AM 0 and AM 1.5 G is shown in **Figure 2.16** with the interactions with atmospheric compounds indicated on the graph.

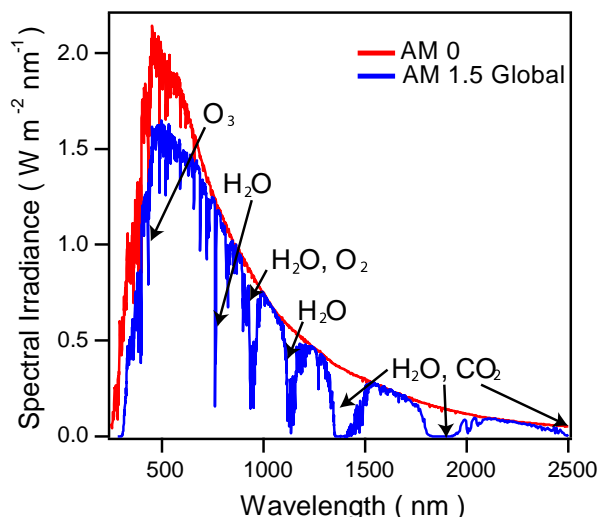


Figure 2.16 Spectral profile for AM 0 (red line) and AM 1.5 Global (blue line). Also indicated are the spectral troughs caused by interaction with atmospheric compounds.

Throughout this work, current density - voltage (J - V) measurements were recorded using a Keithley 2400 sourcemeter with a solar irradiation of AM1.5G simulated with a Newport Oriel solar simulator at an intensity of 100 mW cm^{-2} . This was calibrated against a Fraunhofer calibrated silicon photodiode (PV Measurements Inc.) with a KG-5 filter.

2.4.2 Current density-voltage Curves

Current density-voltage curves (J - V) are used to characterise device performance under solar illumination. This is achieved by sweeping an applied bias across a defined operational range, whilst recording the current-density either in dark or illuminated conditions. An example J - V curve for a solar cell is shown below in **Figure 2.17** both in the dark (dotted line) and under illumination (solid line). An

ideal dark curve follows that of a diode, with zero current density at negative bias and an exponential increase at forward bias for voltages larger than V_{bi} .

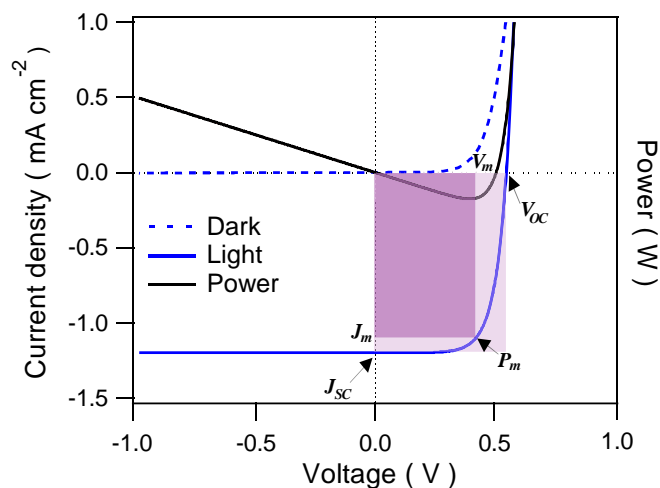


Figure 2.17 An example of a typical OPV cell. The J - V characteristics are shown under dark conditions (blue dotted line) and under illumination (blue solid line). Also shown is the power produced by the cell (black solid line). The key parameters that can be extracted from this graph are also indicated.

The illuminated J - V curve is a superposition of the J - V curve of the diode behaviour and that of the light-generated current, giving the diode law:

$$I = I_0 \left[\exp \frac{qV}{nk_B T} - 1 \right] - I_L \quad \text{Equation 2.15}$$

where I is the net current flowing through the diode, I_0 is the dark saturation current, V is the voltage applied across the terminals of the diode, q is the electron charge, n is the diode ideality factory, k_B is the Boltzmann's constant, T is temperature and I_L is the light generated current.

From the example solar cell, a number of parameters can be obtained. The J_{SC} is the photocurrent density under zero applied bias giving a measure of the photocurrent collected at the electrodes. Assuming homogenous charge generation the short

circuit current is proportional to area of the cell so is therefore defined as a density. V_{OC} defines the voltage across the cell under open-circuit conditions (i.e. at infinite load resistance) and occurs when the net current through the device is zero. The power produced by the cell can also be easily calculated due to the relationship of $P = IV$ and the maximum power output (P_m) of the device defines the maximum current and voltage at maximum power, J_m and V_m . The FF gives the ideality of the J - V curves from the ratio of the maximum power output (dark purple box) to the theoretical maximum power output (light purple box), given by:

$$FF = \frac{J_m V_m}{J_{sc} V_{OC}} \quad \text{Equation 2.16}$$

The PCE , the most important metric in an OPV cell is therefore given by:

$$\eta_P = \frac{J_m V_m}{P_{inc}} = \frac{J_{sc} V_{OC} FF}{P_{inc}} \quad \text{Equation 2.17}$$

where P_{inc} is the incident optical power density (typically 100 mW cm^{-2} for AM 1.5G solar spectrum)

During operation, solar cells show non-ideal behaviour owing to the nature of the cell fabrication and because of this the efficiency is reduced due to the dissipation of power due to internal resistances. The most common of which are series resistance (R_S) and parallel shunt resistance (R_{SH}) and are included in the simple equivalent cell model highlighted in **Figure 2.18**.²¹⁶

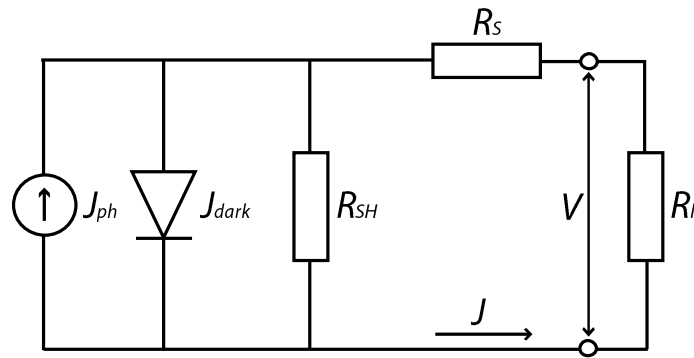


Figure 2.18 A simple equivalent cell model with a current source J_{ph} . The series and shunt resistances are indicated by R_S and R_{SH} respectively.²¹⁷

The impact of the R_S and R_{SH} is shown in **Figure 2.19**. The series resistance is estimated from the slope near V_{OC} , and in an ideal case should be zero. The series resistance typically stems from issues associated with bulk resistances between the active layers and electrodes and contact resistances at interfaces.^{218, 219} R_S can also increase if thicker layers are used, resulting in incomplete collection of photo generated charges. Controlling R_S is paramount as it can have a dramatic impact on the FF on the device, and with very large R_S values also cause the J_{SC} to decrease.

The R_{SH} is parallel to the load and is responsible for current losses in the cell. The R_{SH} can be estimated from the slope near the point of J_{SC} . The cause of this resistance is due to recombination of charge carriers, and current leakage from pinholes and traps in the film. In an ideal solar cell, R_{SH} would be infinite, so the current flowing through R_{SH} is zero.

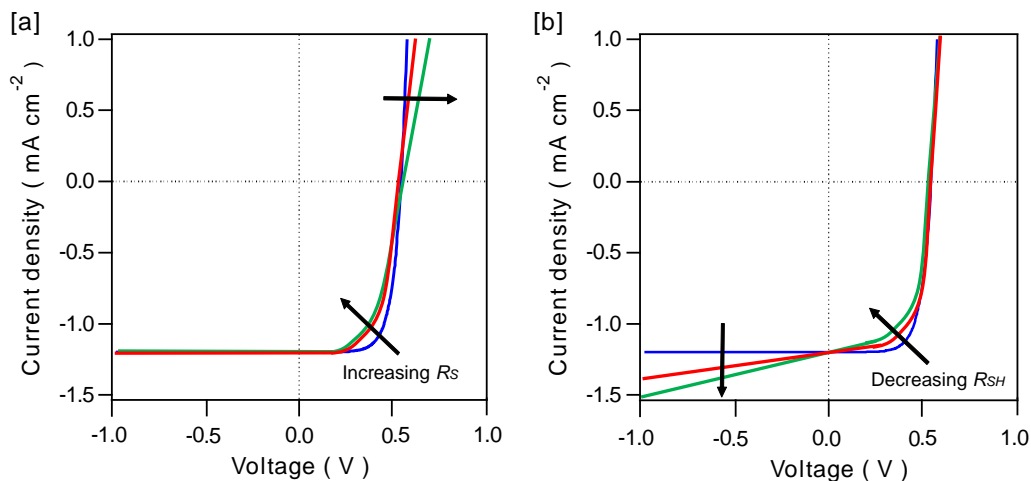


Figure 2.19 The effect of internal resistances on the shape of the J - V curves for [a] R_s and [b] R_{SH} .

2.4.3 External Quantum Efficiency

EQE defines the ratio of the number of charge carriers collected per photon at a particular wavelength (λ), and can be thought of as a monochromatic efficiency of a PV cell:

$$EQE(\lambda) = \frac{J_{sc}(\lambda)}{qN(\lambda)} \quad \text{Equation 2.18}$$

where $N(\lambda)$ is the incident photon density flux and q is the elementary charge. EQE provides important information about the contribution of each organic material to the performance of the cell, highlighting areas of the solar spectrum that could be improved from enhanced contribution.

EQE measurements were obtained using light from a Sciencetech solar simulator with a xenon arc lamp and a computer controlled PTI monochromator. The intensity

of the mechanically chopped (510 Hz) monochromatic light was calibrated with a Si photodiode of known responsivity (818UV, Newport) as a reference cell before the current from the unknown device was measured in the same geometry. The current measurements were performed with a current-voltage amplifier (Femto DHPA-100) and lock-in amplifier (Stanford Research Systems SR 830 DSP). The lock-in amplifier is necessary for measuring small signals with lots of noise as it allows AC/DC noise to be rejected before the signal is measured. It enables the signal to be averaged to shorter time constants, allowing faster, more accurate results. The Si photodiode is used as a reference to determine the *EQE* of the device; the ratio of current produced by the device to that of the diode with a known response allows calculation of the unknown *EQE* as follows:

$$\frac{J_{SC}(\lambda) \text{ device}}{J_{SC}(\lambda) \text{ ref}} = \frac{EQE \text{ device}}{EQE \text{ ref}} \quad \text{Equation 2.19}$$

For a single active layer device, the *EQE* will show contribution only over the wavelength range given by the absorption spectra of the organic material (accounting for any optical effects). For cells with multiple layers however, accurate determination of the contribution of each material to the device can only be achieved if the absorption spectra of the materials do not greatly overlap. Ideally a device would have a high *EQE* response at each wavelength of the solar spectrum.

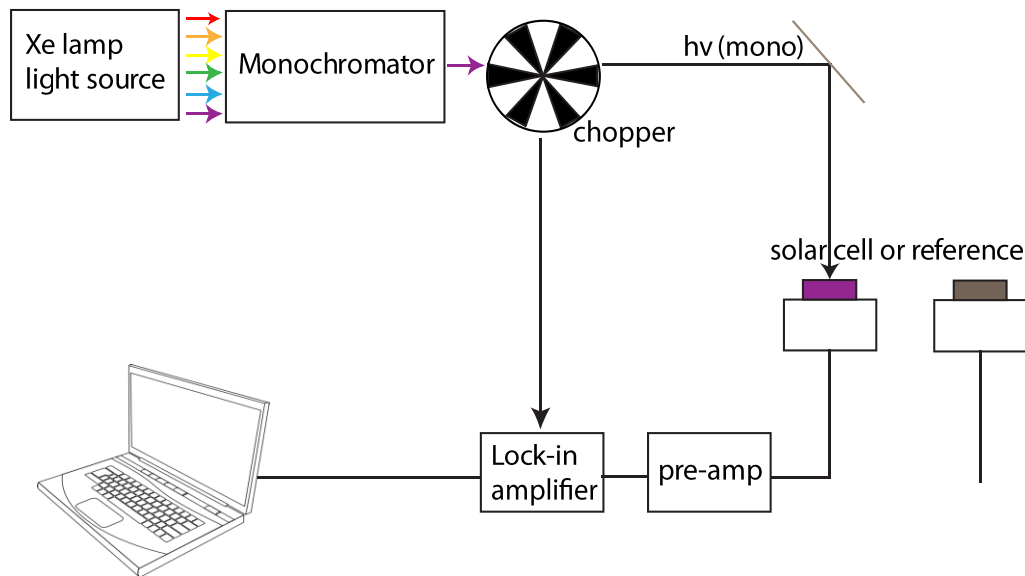


Figure 2.20 A diagram illustrating a typical set up of an *EQE* system.

3 Hybrid Device Fabrication

3.1 Introduction

3.1.1 Hybrid Devices

ZnO is a good candidate for an alternative acceptor material as it has desirable properties such as efficient electron transport and the potential to tune the position of the CB resulting in controllable interface gaps (I_g) when combined with different donor materials. The I_g is defined as the difference between the HOMO of the donor and the LUMO of the acceptor. The I_g is known to be significant in the field of (H)OPVs as the maximum achievable V_{OC} of the cell can be predicted by the I_g minus any losses due to thermodynamic and dissociation losses, band bending, energy losses at the contacts and recombination.²²⁰⁻²²³

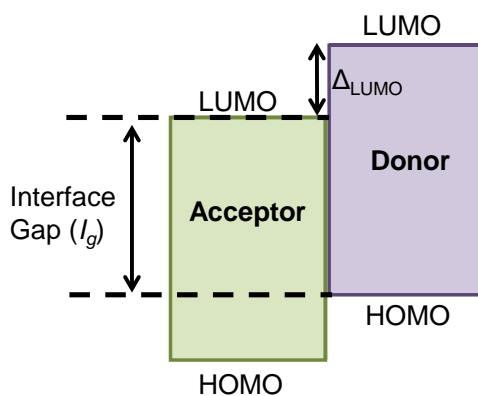


Figure 3.1 A schematic of a D/A heterojunction for two organic materials with the relative HOMO and LUMO level positions indicated. Also shown is the relative Δ_{LUMO} gap.

For the most commonly used organic acceptor material, C₆₀, one of the limitations is the poor V_{OC} that is achieved with a significant number of organic donor materials due to the deep lying LUMO level (~ 4.5 eV), and therefore the associated losses as a result of an excessively large energy offset (Δ_{LUMO}).^{224, 225} Therefore, despite C₆₀ functioning as an efficient acceptor material, there is the opportunity of improving the V_{OC} further by exploiting other material combinations that increase I_g .²²⁶

The properties of ZnO enable it to be used in a variety of HOPV architectures, the simplest of which being a bilayer structure with a single absorbing material, typically a polymer donor layer. The origin of the V_{OC} for true hybrid cells is an area still under wide debate. If it is assumed that the I_g is directly related to the V_{OC} of the device (similar to the organic-organic interface in OPVs), the use of different donor materials or tuning the energy levels of the metal oxide could result in large improvements in the V_{OC} . Ferreria *et al.* investigated two ZnO deposition methods, a SG derived ZnO layer and the formation of ZnO nanoparticles synthesised in methanol.²²⁷ In a simple bilayer device with P3HT, the V_{OC} was increased from 0.4 V to 0.6 V simply by replacing the ZnO SG layer with ZnO nanoparticles. This was attributed to the increase in ZnO band gap, resulting in a larger I_g .

Replacement of the polymer donor with a SM material to date has not achieved comparable performances.^{75, 228} Vacuum deposited SM are beneficial as they allow controlled growth of very thin layers of organic material, allowing the interface properties to be probed systematically in order to explore the impact of the inorganic/organic junction on device performance. There have been a limited number of studies investigating TMO/organic SM interfaces with reported HOPV performances considerably lower than that of TMO/polymer cells.⁶⁸

3.1.2 Aims

In this chapter the viability of ZnO as an acceptor material in HOPVs is investigated. ZnO layers are solution processed by the SG method as this offers a simple production method for high quality films at low cost. The morphological differences of SG derived thin films with processing condition are investigated. Using an optimised, reproducible ZnO layer, the effects of varying the processing temperature is investigated and equated to device performance. The films are subsequently characterised by a variety of methods including AFM to study any morphological differences and XPS to understand film properties and composition. Further energetic analysis is obtained using KP, monitoring any changes in surface work function. The results highlight that the performance of bilayer HOPV devices can be significantly enhanced simply by optimising the ZnO thin film processing conditions.

3.2 Film Optimisation

3.2.1 Sol-gel process

ZnO thin films were fabricated on either pre-patterned ITO coated glass substrates (Thin Film Devices, 145 nm ITO thickness) or quartz substrates following the four-stage cleaning process outlined in **Section 2.1** and exposure to UV/ozone for 30 minutes. In this section the solution recipe, summarised schematically in **Figure 3.2**, consisted of a 0.15 M or 0.25 M precursor solution containing acetone (VWR, 99.9 %), zinc acetate (Aldrich, 99.99 %) and 2-amino ethanol (Aldrich, 99.5 %, 5 % vol.) which were used as the solvent, solute and chelating agent respectively. In all instances the solution was stirred for 1 hour, then spin coated onto the desired substrates for 60 seconds at 3000 rpm. The films were then treated to different annealing temperatures for 1 hour in air to allow conversion to ZnO (~45 nm thick).

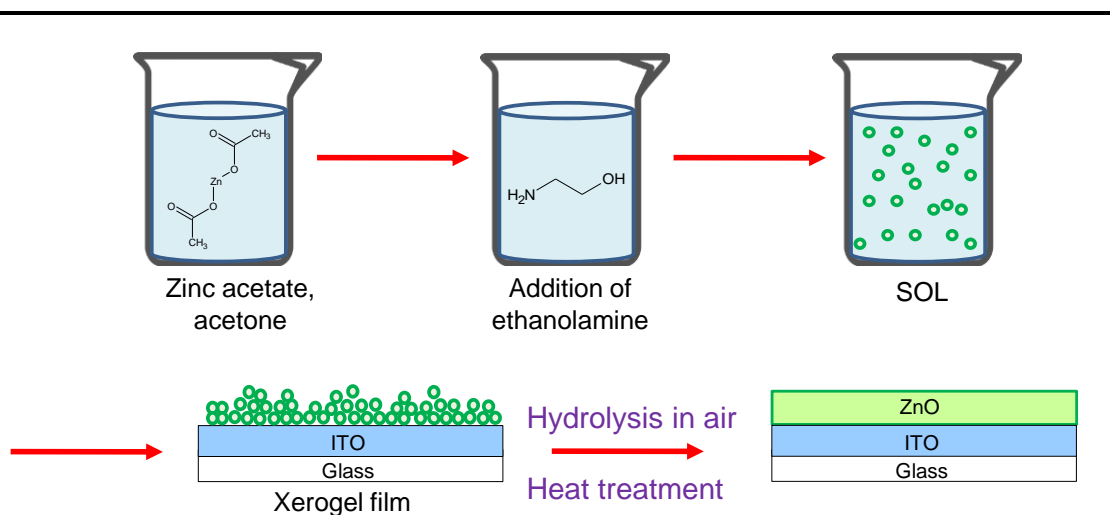


Figure 3.2 A schematic summarising the procedure for generating ZnO thin films.

3.2.2 Morphology Control

3.2.2.1 Nanoridged ZnO Thin Films

Figure 3.3 shows AFM images of **[a]** a bare ITO substrate, **[b]** a 0.25 M ZnO thin film spun directly onto an ITO substrate and left to dry at room temperature and **[c]** a 0.25 M ZnO thin film that has been annealed at 240 °C for 1 hour. The bare ITO substrate has a smooth surface morphology with a surface roughness parameter (R_q) of < 1 nm. When a ZnO film is spin coated and allowed to dry in ambient conditions, the result is a rough inconsistent film with an R_q of 10.2 nm (**Figure 3.3 [b]**). For the annealed film, **Figure 3.3 [c]**, it can be seen that there is clear distinction in film morphology across the film surface, with nanoridged regions (centre of the image) and areas with a much smoother surface morphology. The 20 x 20 μm scan has an R_q of 6.6 nm when averaged across the entire film surface. A cross-sectional height (**Figure 3.3 [d]**) shows the inconsistency in film formation. The first 0-5 μm has a large height variation of up to ~ 35 nm from peaks to troughs, whereas the smooth section of the film has a height variation of less than 10 nm. Due to the strong desire for ZnO to spontaneously form nanoridges it is necessary to control the film fabrication procedure to ensure reproducible thin layers for the application in HOPVs.

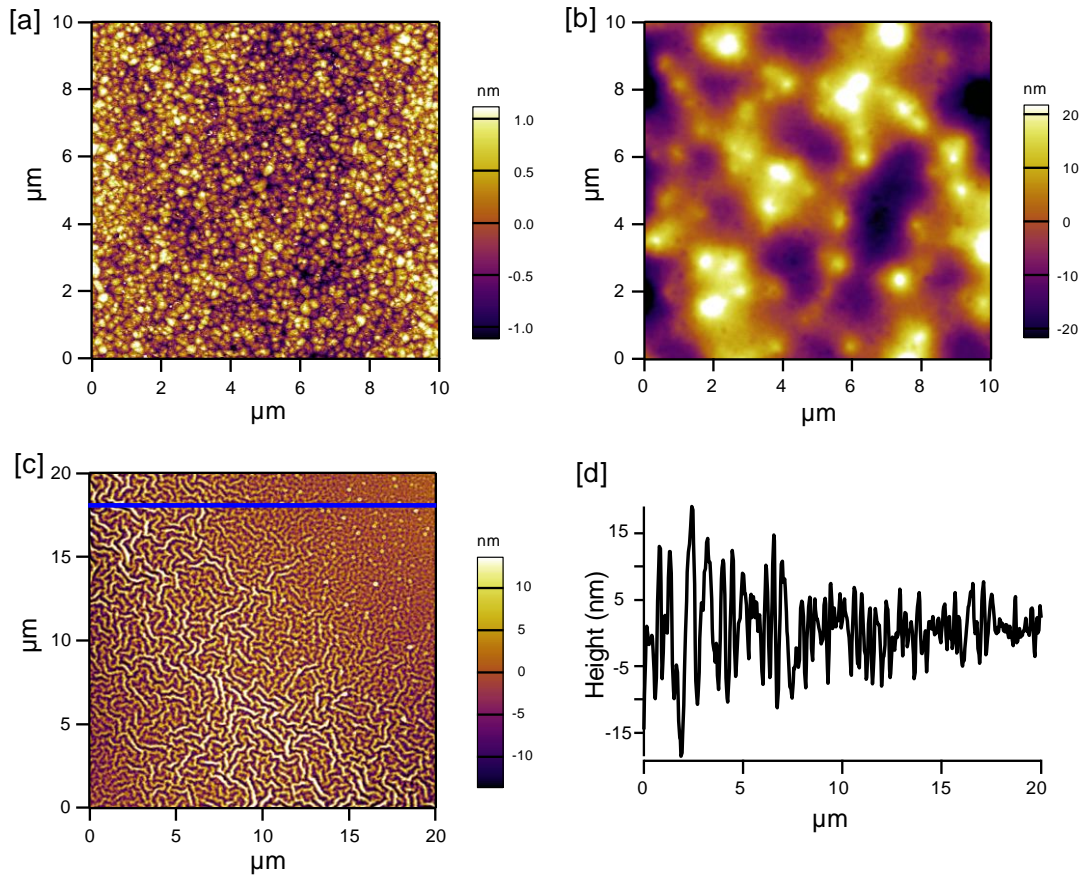


Figure 3.3 AFM images of [a] a bare ITO substrate ($R_q = 0.6$ nm), [b] a spun ZnO thin film that has been left to dry in ambient conditions ($R_q = 10.2$ nm), [c] a ZnO thin film annealed to 240 °C highlighting the inconsistent morphology ($R_q = 6.6$ nm) and [d] the height profile is shown for blue line indicated on image [c]. This shows the differences in peak to trough distances when comparing the nanoridged and smooth area of the film.

The thermal annealing step is crucial to convert the SG derived thin film to a ZnO layer. It also governs the orientation of the thin film during the evaporation of the solvent and is necessary for the removal of any organic contaminants. The nanoridged pattern on the surface of the ZnO thin films is a result of stress predominantly due to the differences in the thermal expansion coefficients of the ZnO film and the ITO substrate. This is a common and causes pattern features in films,^{229, 230} and happens when the film is being annealed, causing bending within the gelled film. Some remaining solvent gets trapped within the film, and as the

film is annealed this gets drawn from the structure and causes the network to contract and bend but not to fracture. Kwon *et al.* studied sol-gel derived ZnO films and found that the nanoridged structure was a prominent feature when the annealing temperature was greater than the boiling point of the specific solvent.²³¹ In this instance, Kwon *et al.* found that annealing the film for prolonged periods of times did not alter the skeletal wavelengths of the individual wrinkles, with each giving a periodic wave pattern, but saw an increase in the number density of branches.

3.2.2.2 Impact of Processing Temperature

To study in the impact of processing temperature on the formation of nanoridged architectures, ZnO thin films were annealed at a range of temperatures for 1 hour. This is summarised in a series of 10 x 10 μm AFM scans shown in **Figure 3.4** for 0.25 M ZnO films annealed at **[a]** 120 °C, **[b]** 240 °C, **[c]** 360 °C and **[d]** 480 °C. At 120 °C, a smooth homogenous morphology was formed with a R_q of 1.4 nm. If the annealing temperature is increased, a nanoridged ZnO structure was produced as shown in **[b-d]** with R_q values of 7.4 nm, 6.8 nm and 6.9 nm for a 240 °C, 360 °C and 480 °C respectively. From the AFM images there are no significant differences in nanoridge formation for **[c]** and **[d]** despite a significant change in processing temperature.

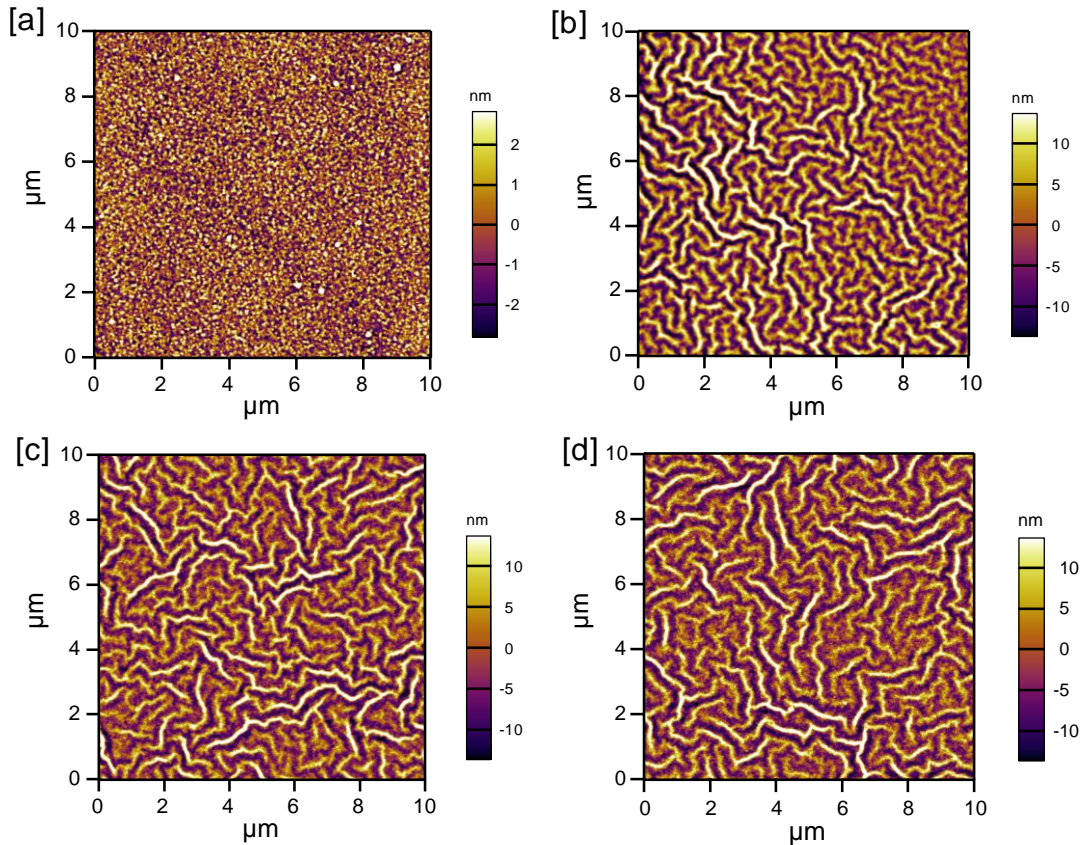


Figure 3.4 AFM images of sol-gel derived films annealed for 1 hour at different temperatures: [a] a film annealed to 120 °C ($R_q = 1.4$ nm), [b] 240 °C ($R_q = 7.4$ nm), [c] 360 °C ($R_q = 6.8$ nm) and [d] 480 °C ($R_q = 6.9$ nm).

3.2.2.3 Controlling Nanoridge Formation

There have been a number of publications which focus on ZnO nanoridged thin films and their application as extracting layers for OPV devices. Chen *et al.* showed that nanoridged ZnO interlayers penetrate through the active layer of the polymer active materials causing large leakage currents and lowering the V_{OC} .²³² This of course is undesirable and their approach was to improve the active layer coverage by using

chloroform with a lower boiling point solvent to discourage penetration of the nanoridges due to increased evaporation rate.

In order to create desirable smooth films the impact of post spin coating treatment was studied, carefully monitoring any differences in film morphology. After spin coating, films were either left to dry in ambient conditions for 15 minutes prior to the annealing step (shown in **Figure 3.5 [a, c]**) or placed immediately on the hot plate (**Figure 3.5 [b, d, e, f]**). As can be seen in **Figure 3.5 [a, b]** for a 0.25 M ZnO film annealed at 120 °C, regardless of the step prior to annealing both treatments result in a smooth film formation with an $R_q < 1$ nm. However, when the temperature is increased to 160 °C a change in morphology is seen between treatments. By leaving the film to dry in ambient conditions for a minimum of 15 minutes, a smooth homogenous film is formed with an R_q of 3 nm (**Figure 3.5 [c]**). If however, the films are directly placed on to the hot plate (following the spin coating step), the impact of annealing drives the spontaneous formation of the nanoridged network and gives an R_q of > 10 nm (**Figure 3.5 [d]**). Solution concentration is also an important factor with a smooth film formed regardless of the processing temperature if the concentration is lowered to 0.15 M. This is shown for a 120 °C film (**Figure 3.5 [e]**) and a 160 °C film (**Figure 3.5 [f]**) with both films annealed immediately after spin coating.

Despite the 0.15 M solution consistently giving smooth homogeneous films, there was a series of problems when trying to implement this layer into devices. This is likely to be due to the low concentration of the solution, resulting in inconsistency between batches of solutions. It was therefore concluded that the 0.25 M solution would be used for spin coating, and the films would be left to dry in air prior to

annealing. These optimum conditions would be used to investigate the use of ZnO layers in hybrid devices.

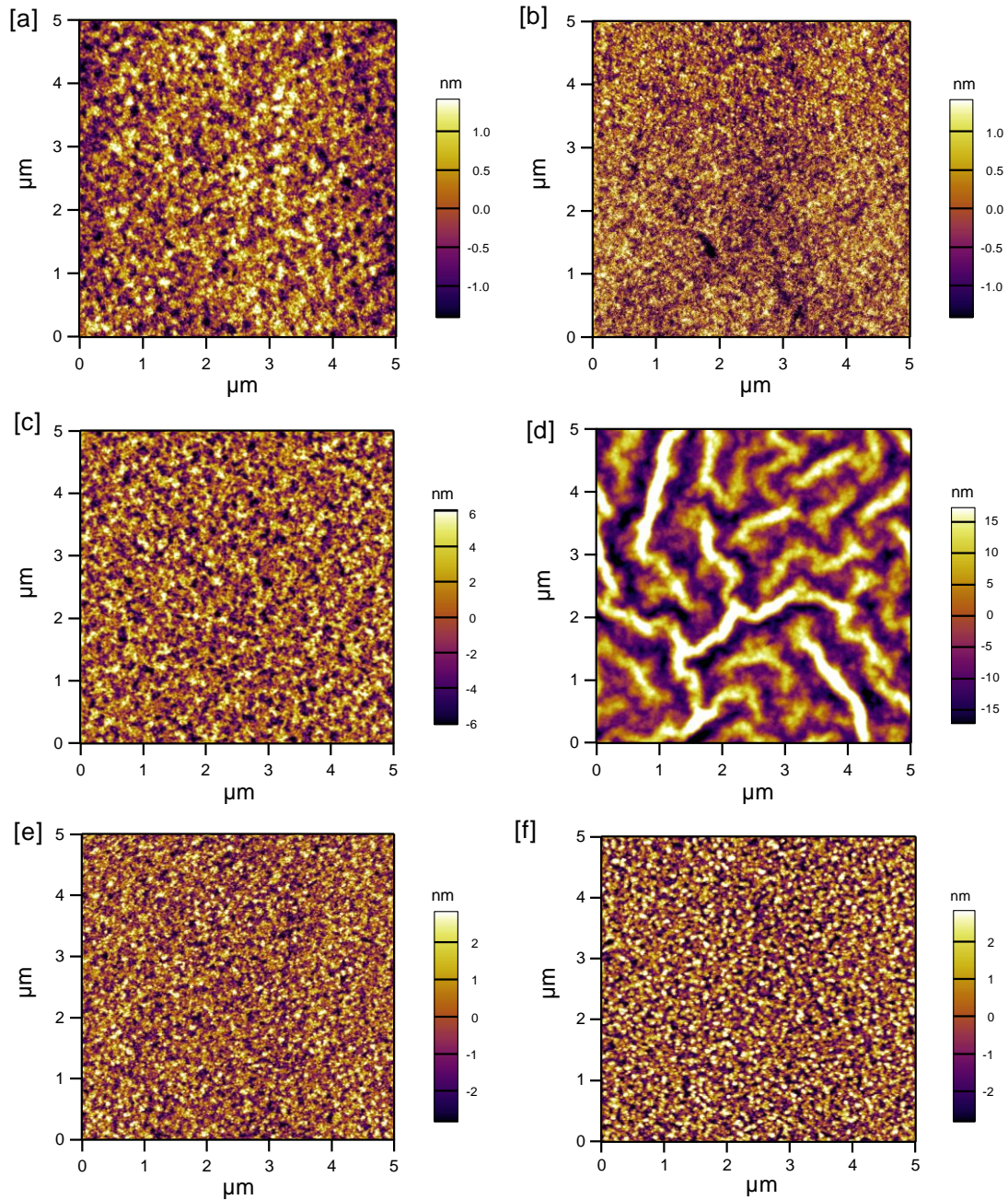


Figure 3.5 AFM images of films annealed to 120 °C with [a] a drying step and [b] annealed immediately; films annealed to 160 °C with [c] a drying step and [d] annealed immediately. Also shown are films processed at a lower solution concentration of 0.15 M and annealed immediately to [e] 120 °C and [f] 160 °C.

3.3 Characterisation of the Optimised Layer

In order to create a smooth reproducible morphology, ZnO thin films were spun from an optimised 0.25 M solution and left to stand in air for fifteen minutes before annealing. For the following section, the films were treated at two different annealing temperatures, 120 °C (ZnO_{120°C}) and 160 °C (ZnO_{160°C}) for 1 hour in air.

3.3.1 Conductivity of ZnO layer

CAFM was used to study the effect of the processing temperature on the surface conductivity of the ZnO thin films. **Figure 3.6** shows simultaneously obtained topography images [**a-b**] and current distribution maps [**c-d**] of ZnO_{120°C} [**a, c, e**] and ZnO_{160°C} [**b, d, f**]. The topography of both films is similar, with a surface roughness of 0.9 nm for [**a**] ZnO_{120°C}, whereas [**b**] ZnO_{160°C} has a slightly higher surface roughness of 1.95 nm. The current distribution maps were acquired whilst applying a 6 V bias, highlighting the distinct difference in the surface currents obtained by varying film preparation conditions. The average current for ZnO_{120°C} was 63 pA [**c**], significantly lower than the average current of 1.2 nA obtained for ZnO_{160°C} [**d**] under the same conditions. The differences in surface conductivity are likely to be due to different phases of the ZnO layer which influences the currents expected and hence the interaction between the tip and the surface.²³³

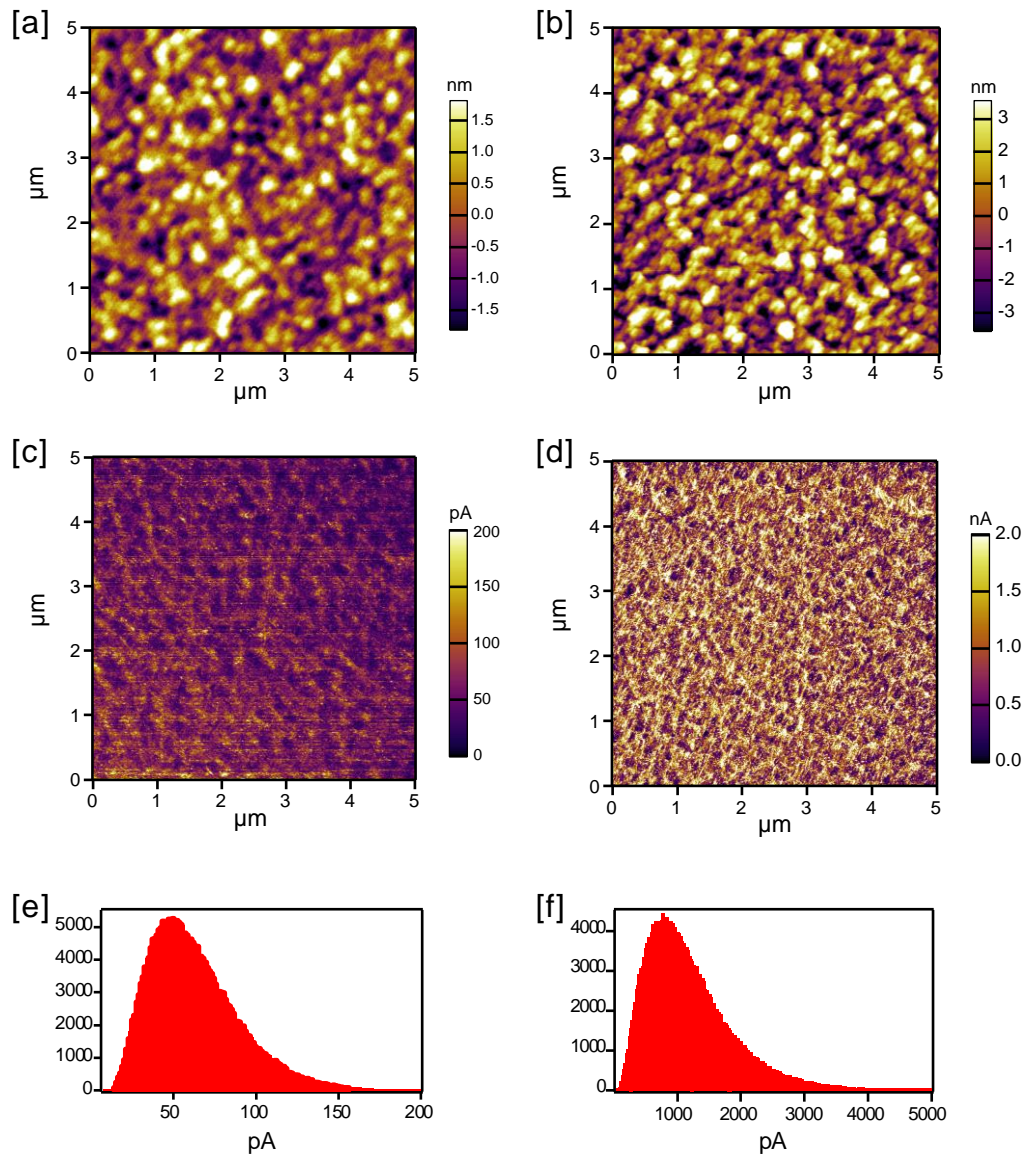


Figure 3.6 [a] Topographic AFM images of [a] 120 °C and [b] 160 °C and the corresponding current distribution maps at 6 V for [c] 120 °C and [d] 160 °C. Histograms showing the current distributions are also shown for [e] ZnO_{120°C} and [f] ZnO_{160°C}.

3.3.2 Absorption spectroscopy

The electronic absorption characteristics of the two films are summarised in **Figure 3.7**; with the films exhibiting a high transparency of > 95 % across the visible and near-infrared range (400 – 700 nm). E_g were calculated from the absorption profiles by the method for non-crystalline semiconductors,^{234, 235} giving a relationship between the absorbance, α , and energy, E shown in *Equation 3.1*:^{234, 235}

$$\alpha \propto \frac{1}{E} \cdot (E - E_g)^2 \quad \text{Equation 3.1}$$

By plotting the energy (eV) versus $(E \times \alpha)^{1/2}$, E_g can be estimated as the intercept with the energy axis, (shown in **Figure 3.7 [b]**) giving band gaps of 3.26 eV and 3.15 eV, for ZnO_{120°C} and ZnO_{160°C} respectively. These values are consistent with the optical band gaps previously reported for ZnO thin films and show only slight variation between the two different processing temperatures.¹⁵⁰

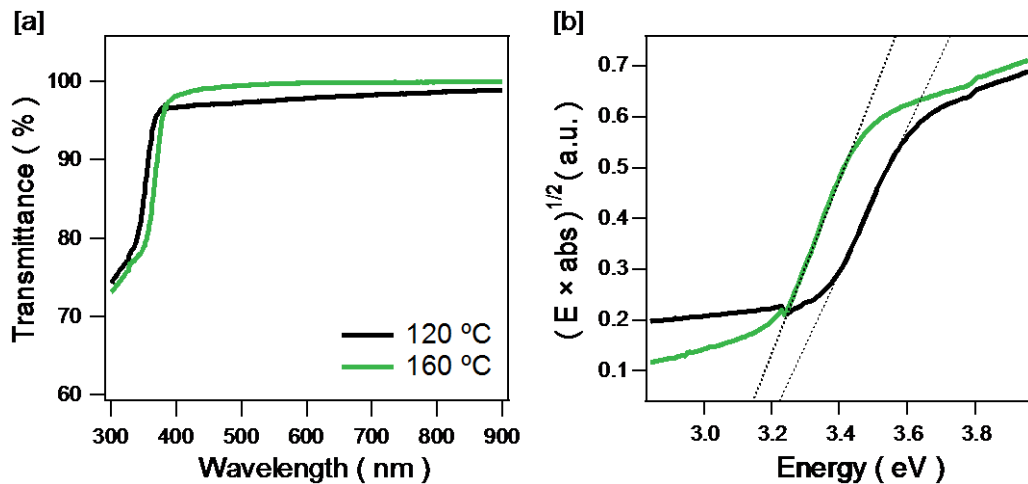


Figure 3.7 [a] Transmittance data for a ZnO thin film spin-coated onto a quartz substrate with a quartz background for ZnO_{120°C} (black solid line) and ZnO_{160°C} (green solid line). **[b]** Determination of E_g by plotting $(E \times \text{abs})^{1/2}$ as a function of energy (eV) and determining the intercept with the energy axis (shown with dotted lines).

3.3.3 Quenching Ability

The effect of processing temperature on the ability of the layer to quench excitons from an absorbing donor material was studied by PL spectroscopy. Single layers of SubPc both with and without ZnO were grown on a quartz substrate at a deposition rate of 2 Å/s, and the PL spectra are shown in **Figure 3.8**. An excitation wavelength of 570 nm as it is the onset of the main absorption peak (see inset), with the PL response measured from 580 to 760 nm. (It should be noted here that the feature at > 725 nm is a spectral response of the lamp/substrate). For a single layer of SubPc there are two characteristic peaks; one at 615 nm and one ~ 715 nm. The feature at 615 nm is the response from the main absorption band of SubPc and a Stokes shift of 15 nm can be seen.²³⁶ The peak at ~ 715 nm however is not featured in the absorption of SubPc (see inset) and is only present in the PL of a solid state film. The intensity of this feature can vary from growth to growth and the origin has not yet been explained in the literature, with one possible hypothesis being due to SubPc dimers present within the film.

For ZnO to be able to effectively function as an electron acceptor the layer has to be able to quench any excitons generated within the SubPc film. A quenching efficiency can be estimated by normalising the PL intensity without the presence of a quenching layer and monitoring the overall reduction in intensity if a quenching layer is used. On addition of a ZnO layer the excitons generated in the SubPc film are quenched, showing a reduction of 20 % for ZnO_{120 °C} (black solid line) and 40 % for the ZnO_{160 °C} layer (green solid line) at 615 nm. The second feature at ~ 715 nm is also quenched by a similar amount. This study suggests that the ZnO film is capable of quenching excitons generated by the SubPc film, although the quenching

efficiency is low. These values suggest that both layers have acceptor properties and are able to dissociate excitons. Due to the large reduction in PL intensity for ZnO_{160 °C}, and therefore the greater ability to dissociate excitons, it would be assumed that the film processed at the higher temperature would be more effective as an acceptor material.

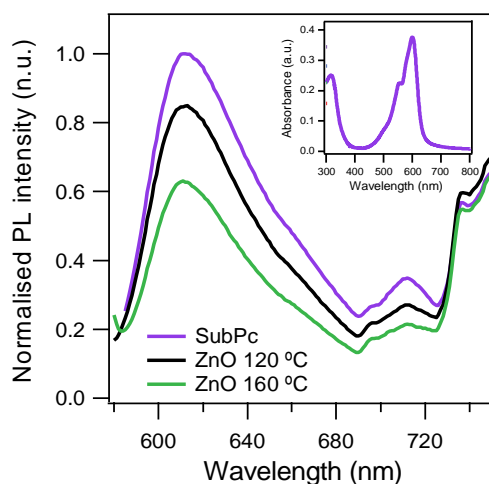


Figure 3.8 Normalised PL spectra of a 15 nm SubPc film with and without a quencher layer. A single SubPc layer is shown (purple) and a SubPc layer deposited on top of a ZnO_{120°C} film (black solid line) and ZnO_{160°C} film (green solid line). The inset shows the absorption of a 15 nm SubPc layer.

3.3.4 Energetic Analysis

To gain insight into the influence of processing temperature on ZnO composition, the films were further characterised using XPS at a take-off angle of 90 °. The full survey spectra is shown in **Figure 3.9 [a]** with all main features labelled, there are no extra features present when comparing the film annealed to 120 °C (black solid line) and 160 °C (green solid line). In **Figure 3.9 [b]**, the Zn 2p peaks are shown for

ZnO_{120 °C} and ZnO_{160 °C}, with two peaks observed, 2p_{3/2} (1020.8 eV) and 2p_{1/2} (1043.9 eV) in a 2:1 ratio due to spin-orbit splitting.

There are more significant differences however when looking at the O 1s for the two films, which coincide with differences in ratios. **Figure 3.9 [c]**, shows the comparative study of the core O 1s region, which comprises two unique components, a wurtzite lattice component with zinc coordinated to oxygen (O1s_A, 529.4 eV), and a broad O 1s (O1s_B, 530.8 eV) which can be attributed to contaminants. The full width half-maximum (FWHM) of the two components differs, 1.09 and 1.85 eV for O1s_A and O1s_B respectively. This is due to the difference in bonding environment, with a narrower peak a result of coordination to the Zn atom. Also, O1s_B is significantly wider due to surface adsorbates such as surface carbonaceous species such as CO, CO₂, CO₃²⁻.¹⁵¹ Surface adsorbates are a significant feature due to the surface sensitivity of XPS (with an estimated penetration depth in the region of 5-10 nm). The two main contaminants present in O1s_B can also be attributed to materials present in the SG process, COH from the ethanolamine stabiliser and COO⁻ (BP > 300 °C) which can be identified as the oxygen present in the zinc acetate raw material. Stoichiometric analysis of each sample was obtained by comparing the elemental composition of zinc to oxygen, which is summarised in **Table 3.1**. The ratios are calculated using the Schofield relative sensitivity factors (RSFs) which are built in to the software of CasaXPS and the analyser transmission function.

The ratio of Zn 2p : O 1s_B decreases from 1 : 1.42 for ZnO_{120 °C} to 1 : 0.96 for ZnO_{160 °C}, due to the removal of the raw material contaminants. The presence of contaminants is also apparent when looking at the C1s spectra for each film, shown in **Figure 3.9 [d]**. This C1s spectra is fitted with three main components, the first

due to C-C and C-H at 284.6 eV and at higher binding energies the ethanolamine (285.7 eV, C-NH₂ and C-OH) and zinc acetate precursor (289.3 eV, COO⁻).

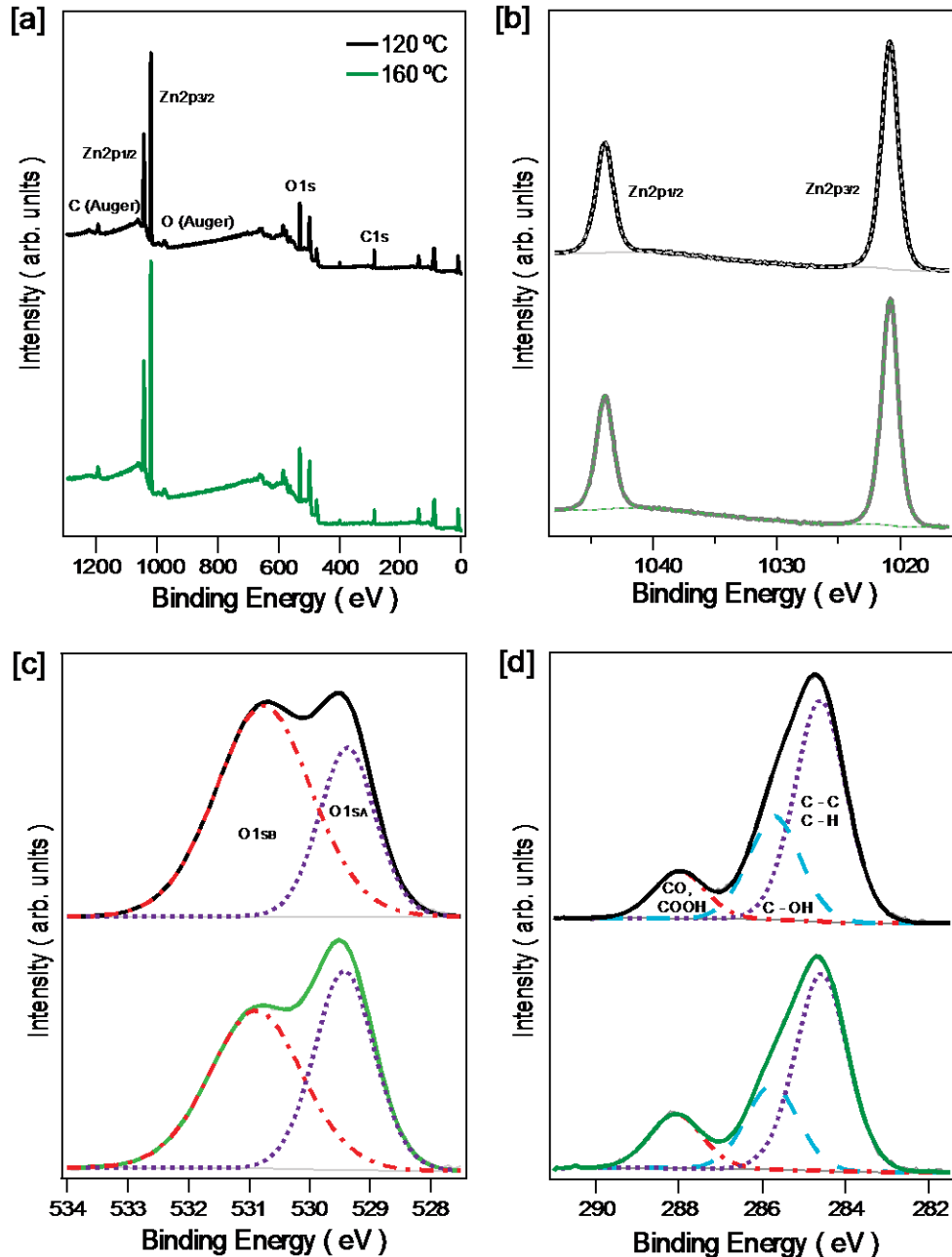


Figure 3.9 XPS spectra of [a] survey scan, [b] Zn 2p which contains two peaks Zn 2p_{3/2} and Zn 2p_{1/2} in a 2:1 ratio owing to spin-orbit splitting, [c] O 1s, where two components are present O 1s_A (bound ZnO) and O 1s_B (contaminants present) and [d] C 1s. Both films, 120 °C (black solid line) and 160 °C (green solid line) are shown.

Table 3.1 A summary of the binding energies, FWHM and compositions (%) for Zn 2p and O 1s contributions.

	120 °C			160 °C		
	eV	FWHM	%	eV	FWHM	%
Zn 2p_{3/2}	1020.8	1.54	28.6	1020.8	1.53	28.8
Zn 2p_{1/2}	1044.0	1.60	27.9	1043.9	1.58	29.2
O 1s_A	529.4	1.09	13.9	529.4	1.16	18.8
O 1s_B	530.8	1.85	29.6	530.9	1.79	23.2
Zn 2p_{3/2} : O 1s			1 : 0.49			1 : 0.64
Zn 2p_{3/2} : O 1s_A			1 : 1.42			1 : 0.96
Zn 2p_{3/2} : O 1s_B						

3.4 Impact of processing temperature

The role of defect states and the impact they have on carrier concentration and the work function is still widely debated. A recent paper by Greiner *et al.* reported that a change in cationic oxidation state can result in a significant change in the work function of the TMO layer.²³⁷ This in turn could have an effect on the capability of the metal oxide to work as an electron acceptor due to variations of the ZnO CB and VB with respect to the V_L , and in turn exciton dissociation at the interface with the organic donor material. As shown in **Section 3.3.4**, by increasing the processing temperature by 40 °C, there is a change in the stoichiometry of the ZnO films with a Zn $2p_{3/2}$: O1s_A ratio of 1 : 0.49 for ZnO_{120°C} to 1 : 0.64 for ZnO_{160°C}. This suggests that an increase in temperature leads to an increase in the conversion to ZnO, which may in turn alter the work function of the layer.

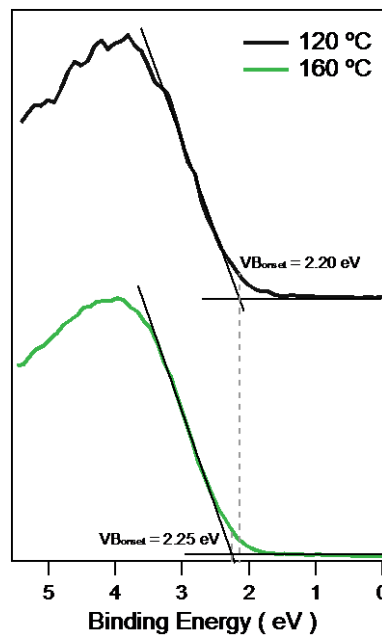


Figure 3.10 VB onset for ZnO_{120°C} (black solid line) and ZnO_{160°C} (green solid line). The VB onset is calculated by the intercept with the binding energy axis.

KP measurements were carried out to determine the work function of the two ZnO films. There is a significant difference in the work function of the layers, from 3.20 eV to 3.80 eV for ZnO_{120°C} and ZnO_{160°C} respectively. The VB edge XPS spectra for the two ZnO films are shown in **Figure 3.10** to provide further understanding of the electronic properties. The position of the E_{Fs} was determined by extrapolating the leading edge of the VB photoemission to the intercept with the background level. The E_{Fs} for ZnO_{120°C} is 2.20 eV above the VB, giving a VB position of 5.40 eV below the V_L . In the case ZnO_{160°C}, the E_{Fs} is similar at 2.25 eV, but the film has a much deeper VB position of 6.05 eV below the V_L owing to the larger measured work function. The CB of the ZnO films has been estimated from the optical band gap (**Figure 3.7**) of these thin films to give a CB position relative to the measured VB by XPS of 2.14 eV (ZnO_{120°C}) and 2.90 eV (ZnO_{160°C}). This is summarised schematically in **Figure 3.11**.

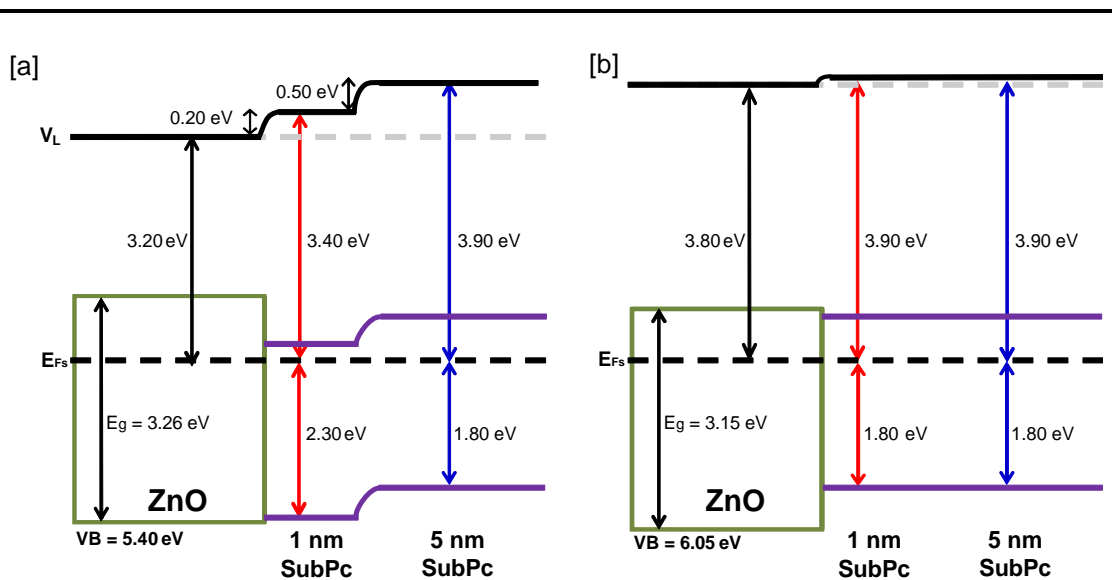


Figure 3.11 Energy level diagrams for [a] ZnO_{120 °C} / SubPc and [b] ZnO_{160 °C} / SubPc with deposition of 1 and 5 nm of SubPc. The positions of the E_{Fs} , VB and CB of the ZnO layers were determined by KP, XPS and UV-Vis respectively.

By sequentially depositing thin layers of the SubPc onto the ZnO surface further information can be gained about the electronic properties of the D/A interface. It is key to note here that unlike the small interfacial dipoles formed at an organic-organic interface, large V_L shifts would be expected for an inorganic-organic interface. Therefore, measurements indicating the energy level offsets in this region are essential for understanding device parameters.^{226, 238} **Figure 3.11** shows the change in work function with subsequent growth of SubPc, measured using KP. For ZnO_{120°C} the work function is increased from 3.20 eV to 3.40 eV with addition of 1 nm SubPc, resulting in a V_L shift of 0.20 eV. The work function increases further to 3.90 eV for a 5 nm SubPc layer. With deposition on ZnO_{160 °C} there is only a subtle change in work function from 3.80 eV to 3.90 eV, and a small resultant vacuum level shift, for both the 1 and 5 nm thicknesses of the SubPc. The work function saturates past 5 nm of SubPc, and remains constant at 3.90 eV for both ZnO thin films.

The position of the HOMO level of SubPc is included in **Figure 3.11**, which is calculated by assuming an ionisation IP for SubPc of 5.70 eV.^{134, 164} For organic/organic junctions the I_g of the D/A interface, is known to directly influence V_{OC} . If the same principle is used here, the maximum obtainable V_{OC} can be estimated from the difference between the HOMO_{SubPc} and E_{F_s} . This estimation is made due to the *n*-type nature of ZnO thin films and the presence of gap states that have been shown to lie close to the materials E_{F_s} and can extract electrons.⁵⁹ Band bending in the near interfacial region of the organic (< 5 nm) would be expected to provide an additional driving force for photocurrent extraction, and hence a larger expected V_{OC} . Thus, the interfacial region is of more significance than the bulk (> 5 nm) collection levels of the organic. Thereby, if you consider the difference in

HOMO onsets with a 1 nm SubPc layer, the I_g decreases from 2.30 eV (ZnO_{120°C}) to 1.80 eV (ZnO_{160°C}) and hence a resultant decrease in cell V_{OC} would be expected.

3.5 Device Fabrication

To validate this hypothesis, bilayer HOPV cells were fabricated with the architecture: ITO / ZnO (45 nm) / SubPc (15 nm) / MoO_x (15 nm) / Al. A control device without the use of ZnO was also grown for comparison: ITO / SubPc (15 nm) / MoO_x (15 nm) / Al. This is represented schematically below in **Figure 3.12** which shows a summary of the energy levels of the materials used. The predicted work function of the transparent electrode ITO and back contact Al is also shown.

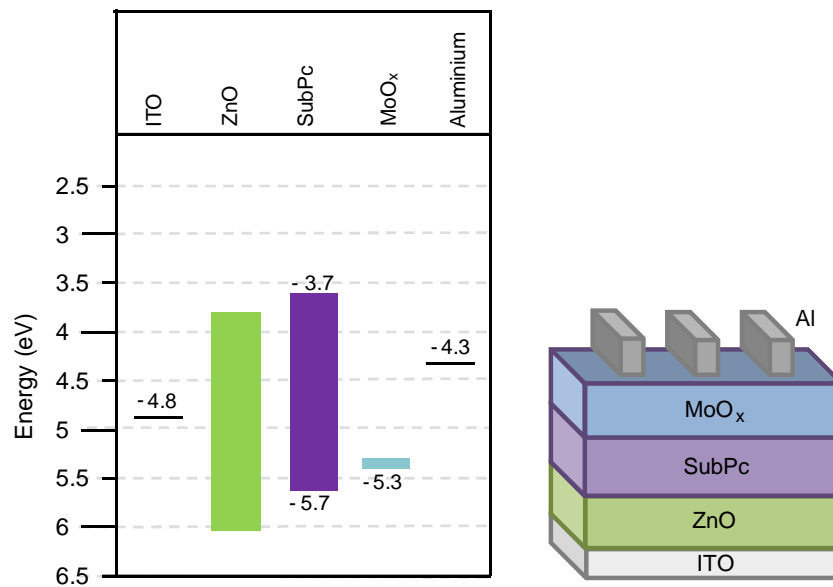


Figure 3.12 Schematic showing the energy levels for the inverted hybrid device ITO / ZnO (45 nm)/ SubPc (15 nm) / MoO_x (15 nm) / Al. The bilayer architecture is also shown.

The key device parameters are shown in **Table 3.2**, with the corresponding *J-V* plots in **Figure 3.13 [a]**. The thickness of the SubPc layer was kept constant at 15 nm as it is in line with previously published exciton diffusion lengths.^{239, 240} The control device did not employ any ZnO to emphasise the role of ZnO as an efficient electron acceptor. The devices with a ZnO layer significantly outperform the control device,

which has a low J_{SC} of 0.67 mA cm^{-2} and a PCE of only 0.05% , demonstrating clearly the suitability of ZnO as an inorganic electron acceptor in these HOPV devices.

As predicted, there is a significant improvement in V_{OC} from 0.82 V for ZnO_{160°C} to 1.18 V for ZnO_{120°C}, demonstrating clearly the direct correlation between I_g and the achievable V_{OC} for these hybrid devices. Another factor contributing to the difference in V_{OC} could be the suppression in dark current due to lower mobility of the films. However this affect is likely to be more of a secondary causation.

The voltage achieved for this cell is very high for a single junction cell and shows the potential of SM organic donors to be utilised with TMO acceptors for high performance. The enhanced I_g , along with the high IP SubPc donor results in higher V_{OC} values than obtained with polymeric alternatives such as P3HT, which typically yield values less than 0.7 V .²²⁷ There is approximately a 1 eV difference between the predicted I_g and the measured V_{OC} of the device, which is not uncommon for excitonic solar cells due to the losses associated such as the exciton binding energy, recombination of charge transfer states and the diffusion of charge carriers to the electrodes.¹⁰² Also owing to the nature of the ZnO film and the fact that there are likely to be gap states near to/around the E_{FS} it is difficult to pinpoint the exact energy at which charges will be extracted.

The wide band gap ZnO electron accepting layer has high transparency across the entire visible range, so does not contribute to the photocurrent generation during device operation. This is shown in **Figure 3.13 [b]**, with the SubPc layer only contributing to the EQE for both device architectures, despite this, the optimised ZnO/SubPc hybrid devices gave a relatively high J_{SC} of $> 1.5 \text{ mA cm}^{-2}$. This is far

greater than other TMO/small molecule hybrid devices, where the best published value for J_{SC} currently stands at 0.015 mA cm^{-2} .⁷⁷ This indicates that both films are both efficient at splitting excitons at the interface with SubPc, also shown by PL in **Figure 3.8** which had a reduction in PL intensity of the SubPc film of 20 % and 40 % for $\text{ZnO}_{120^\circ\text{C}}$ and $\text{ZnO}_{160^\circ\text{C}}$ respectively.

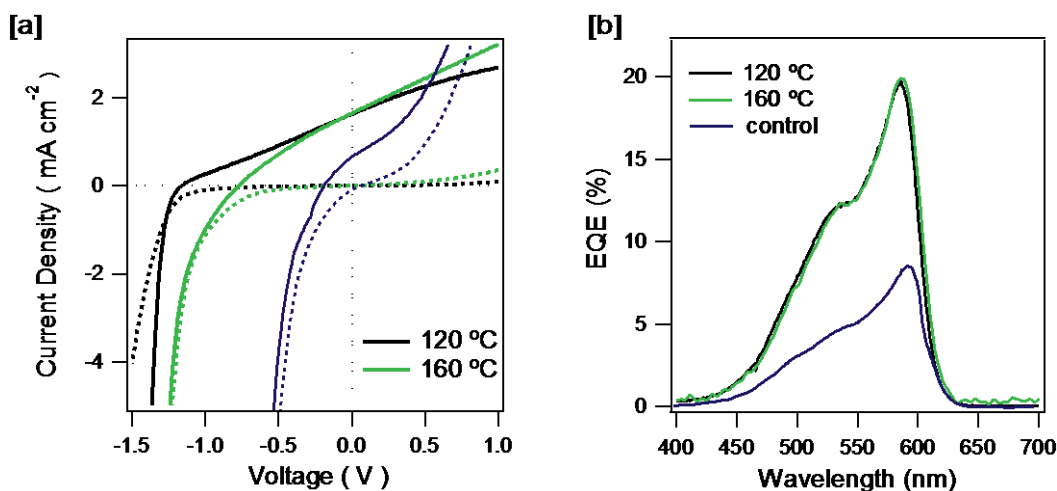


Figure 3.13 [a] Averaged J - V plots under illumination of 100 mW cm^{-2} for the control device (blue line), $\text{ZnO}_{120^\circ\text{C}}$ (black solid line) and $\text{ZnO}_{160^\circ\text{C}}$ (green solid line), also shown is the corresponding dark J - V plots (dotted lines). [b] Representative EQE for each device.

The main limitation of the devices is the low FF of 0.25 and 0.29 for $\text{ZnO}_{120^\circ\text{C}}$ and $\text{ZnO}_{160^\circ\text{C}}$ respectively, and this is likely to be due to a photoconductivity effect in the layer, with shunts being exposed when scanning. Despite a 6 V bias being applied during the CAFM measurements there is a poor averaged surface current of 63 pA for $\text{ZnO}_{120^\circ\text{C}}$ which can be seen in **Figure 3.5 [c]**. The average current is greatly improved to 1.2 nA for $\text{ZnO}_{160^\circ\text{C}}$ (**Figure 3.5 [d]**) which in turn explains the improvement in FF to 0.29. This is likely to be due to removal of impurities and adsorbates on the surface at the higher annealing temperature (seen by XPS), improving the surface conductivity and resistance. Despite the low FF , the PCE of

the devices increases from 0.39 % ($\text{ZnO}_{160^\circ\text{C}}$) to 0.47 % ($\text{ZnO}_{120^\circ\text{C}}$) merely by a 40 °C decrease in the ZnO processing temperature, with the improvement primarily attributed to the increase in V_{OC} . The voltage exceeds that of SubPc/ C_{60} devices, which are reported at approximately 1.05 V,¹³⁵ showing the potential of ZnO as a low temperature, cheap scalable alternative to C_{60} for use in bilayer HOPV cells.²⁴¹

Table 3.2 Averaged HOPV device characteristics for hybrid devices: ITO/ $\text{ZnO}_{(120^\circ\text{C}, 160^\circ\text{C})}$ / SubPc (15 nm) / MoO_x (15 nm) / Al and the control device without an acceptor layer.

Temp (°C)	J_{SC} (mA cm⁻²)	V_{OC} (V)	<i>FF</i>	<i>PCE</i> (%)
$\text{ZnO}_{120^\circ\text{C}}$	1.61	1.23	0.23	0.45
$\text{ZnO}_{160^\circ\text{C}}$	1.65	0.82	0.29	0.38
Control	0.67	0.24	0.32	0.05

3.6 Donor Layer Comparison

The relationship between I_g and V_{OC} in HOPVs can also be explored using donors with varying IP values. To study this, HOPVs using three different donor materials (SubPc, ClAlPc, P3HT) were fabricated on the ZnO_{120 °C} layer. SubPc and ClAlPc were vacuum deposited directly onto the ZnO substrate with a layer thickness of 20 nm. A solution processed donor P3HT was also used for comparison. 200 mg of P3HT was dissolved in 1 mL of 1,2-dichlorobenzene in a nitrogen filled glove box and left to stir overnight. The solution was then filtered prior to spin coating at 800 rpm onto the ZnO substrate, giving an overall active layer thickness of ~ 15 nm. This film was annealed to 140 °C for 20 minutes. For all devices a 15 nm MoO_x layer was used as the hole transporting layer with an aluminium back reflective electrode.

The J - V curves and EQE for each of the three donor materials are shown in **Figure 3.14** and the performance parameters are summarised in **Table 3.3**. From the J - V curves it can be seen that there is also a significant change in the J_{SC} of each device. It should be noted here that due to the different absorption coefficients, absorption maxima of each material and the L_D for each, all devices would need to be individually optimised. The importance of optical considerations will be discussed further in **Chapter 5**. The EQE for each device matches the absorption spectra of the donor material showing that in all three systems, ZnO does not contribute to the photocurrent. The FF of each system also differs significantly which could be due to a difference in recombination dynamics for each D/A interface,²⁴² or another likely cause is a mobility mismatch between the two different types of material.²⁴³

By utilising three different donor materials with different HOMO levels, 5.7 eV (SubPc), 5.4 eV (ClAlPc) and 5.0 eV (P3HT), the magnitude of the I_g will reduce

with respect to the position of the ZnO E_{FS} . This is shown schematically in **Figure 3.14 [c]**. The V_{OC} decreases from 1.12 V to 0.82 V to 0.47 V for SubPc, CIAIPc and P3HT with ZnO respectively, directly in line with the predicted changes from the I_g . This result helps to verify the assumption that the I_g is comparable to that of an organic-organic interface and shows the potential of this type of HOPV with a variety of organic SMs.

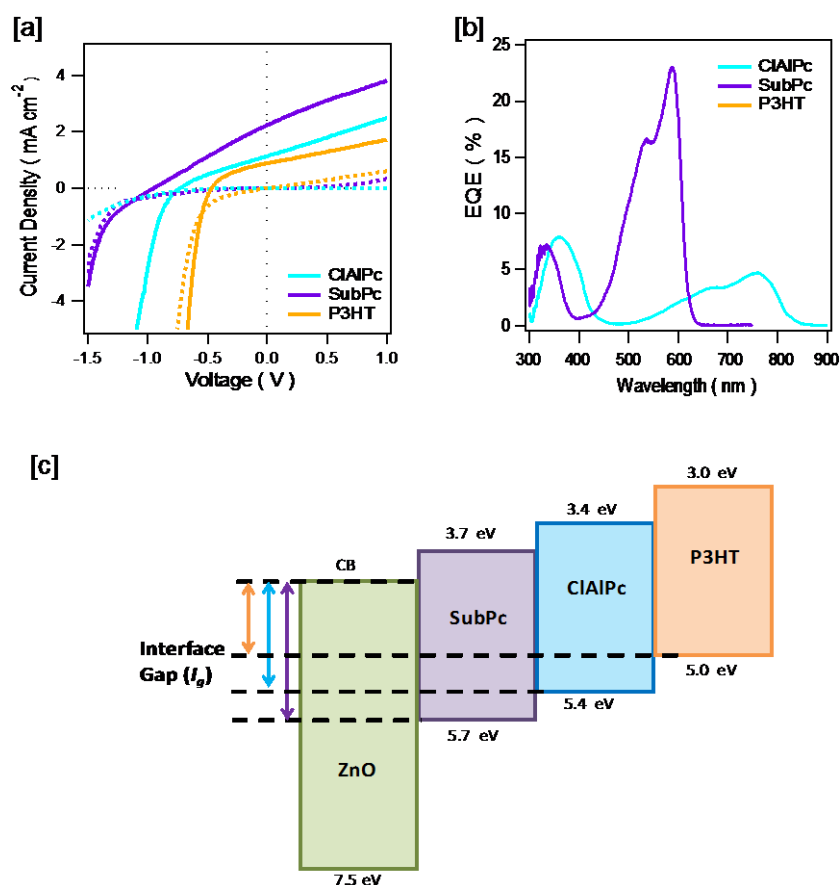


Figure 3.14 [a] Averaged J - V plots under illumination of 100 mW cm^{-2} for SubPc (purple solid line), CIAIPc (light blue solid line) and P3HT (orange solid line). Also shown are the corresponding dark J - V plots (dotted lines). **[b]** The EQE for SubPc (purple), CIAIPc (blue) and P3HT (orange). **[c]** A schematic of the three organic donors used with different HOMO levels ranging from 5.7 eV to 5.4 eV to 5.0 eV for SubPc, CIAIPc and P3HT with respect to the ZnO acceptor layer.

Table 3.3 Averaged HOPV device characteristics for the three different hybrid devices: ITO/ ZnO (120 °C) / donor / MoO_x (15 nm) / Al.

Temp (°C)	J_{SC} (mA cm⁻²)	V_{OC} (V)	FF	PCE (%)
SubPc	2.10	1.12	0.24	0.58
ClAlPc	1.08	0.82	0.32	0.29
P3HT	0.76	0.59	0.47	0.23

3.7 Conclusions

Chapter 3 demonstrates that ZnO films fabricated using the SG process can be incorporated in HOPV devices with a SM organic donor layer. The effect of processing temperature and processing conditions on the morphology of ZnO has been shown. It is clear that the processing steps need to be controlled in order to create reproducible films. This can be achieved either by leaving the film to dry at room temperature prior to annealing.

An optimised smooth ($R_q < 1$ nm) ZnO thin film was then further characterised by a range of techniques including XPS, UV-Vis and KP. The impact of processing temperature (at 120 °C or 160 °C) was closely studied in order to monitor any changes in the ratio of the ZnO 2p_{3/2} : O1s_A. A more oxygen deficient ZnO film resulted in a decrease in the work function of the layer, from 3.80 eV for ZnO_{160 °C} to 3.20 eV for ZnO_{120 °C} but an increase in the overall I_g with a SubPc donor. HOPV devices showed an increase in V_{OC} of 0.36 V, from 0.82 V for ZnO_{160 °C} to 1.18 V for ZnO_{120 °C}, a consequence of the increased I_g between the SubPc / ZnO. The results demonstrate that ZnO can be used as an electron acceptor SM hybrid planar bilayer cells achieving a PCE of 0.45 %, two orders of magnitude larger than previously reported small molecule hybrid cells.^{75, 77, 241}

Three different donor materials were utilised with the optimised ZnO thin film to study if the I_g could be directly related to the V_{OC} of the device. Two vacuum deposited layers, SubPc and ClAlPc were compared to the solution processed P3HT donor. This decrease in I_g in the series of cells resulted in a decrease in V_{OC} from 1.12 V (SubPc) to 0.82 V (ClAlPc) to 0.47 V (P3HT).

4 Evaluation of energetic measurement techniques

4.1 Introduction

UPS is a technique that is commonly used to investigate the energetic difference between the HOMO level and the $E_{F,S}$, as well providing the work function of a given material. It is this measurement of IP (that can be inferred from the addition of the $\text{HOMO}_{\text{onset}}$ and the work function) that makes UPS a more informative technique than other methods such as KP. It is also appealing as the measurements are taken in UHV conditions. For UPS, a negative bias is necessary to enable electrons with low kinetic energies to be detected efficiently. This is important as it means that values obtained by UPS will represent the lowest energy at which electrons are able to escape under the UV radiation, whereas KP gives a measure of the average work function under the tip and therefore can lead to an overestimation.^{244, 245}

UPS however is not without its issues. It must be stressed that care should be taken when comparing literature values as large variations can occur. This can simply be due to differences in sample preparation methods, conditions and handling of the materials. This is due to two factors, firstly the surface sensitivity of UPS (typical penetration depth ~ 5 nm) makes the measurements very susceptible to surface contamination, and also due to the irradiation damage that can be caused from exposing the sample to intense UV radiation, typically He I (21.2 eV). This high intensity photon irradiation can cause changes to the surface composition of materials, particularly to metal oxide materials if prepared *ex-situ*.²⁴⁶

Of course, energetic determination is not just limited to UPS and KP, there have been a variety of reports looking at energetic changes using a number of techniques. Cyclic voltametry (CV) has been used to study the electrochemical properties of an analyte in solution allowing the HOMO of an organic material to be measured.²⁴⁷ LUMO levels can be estimated by the absorption onset of the organic material, or more accurately through the use of inverse photoemission spectroscopy (IPES) by measuring the emission of photons after exposure to an electron beam.²⁴⁸ All of these methods provide a useful insight into the energetics of materials that are pivotal to device performance. Variations in results obtained between each method however can occur and this must be carefully considered when sourcing values from literature.

Detailed discussions surrounding the issues associated with UPS however remain limited, with a small number of studies looking into variability in particular for metal oxides. In a study by Davis *et al.*,²⁴⁵ the authors discuss the need to calculate IP without UHV conditions. In this paper, photoelectron spectroscopy in air (PESA) is presented as an alternative to UPS. The method relies on a monochromatic UV source which ionises oxygen molecules in air allowing determination of IP in an ambient environment, and the authors showed the validity of this technique. Alternatively, Gutmann *et al.* investigated the impact of UV and X-ray radiation on TiO₂ surfaces and found that a reduction in work function of 0.5 eV occurred due to the photochemical hydroxylation of oxygen vacancies present on the TiO₂ surface.²⁴⁹ This study concluded that the high energy photon source is responsible, measuring only a 0.02 eV shift in work function using low intensity x-ray photoemission spectroscopy (LIXPS).

4.1.1 Aims

The aim of this section is to highlight the issues surrounding the different methods for calculating energetic values and to outline the care that must be taken in order to accurately determine both work function and IP. In order to do this, the same devices as discussed in **Chapter 3** are investigated using UPS and this is compared to the data presented previously. This chapter outlines the issues encountered using these techniques on metal oxide layers that are not grown *in-situ*, discussing surface contamination and also the impact of UV radiation on sensitive materials such as ZnO. The change in IP and work function as a function of time compared to any changes in composition that are observed by XPS is also shown.

4.2 UPS Studies on ZnO

4.2.1 Probing energy levels of sol-gel ZnO_{120 °C}

UPS studies were carried out to determine the electronic characteristics of the ZnO and SubPc films. **Figure 4.1** shows the UPS spectra obtained with sequential deposition of thin layers of the organic material of interest, SubPc. UPS measurements were taken as the thickness of SubPc was varied from 1 nm to 15 nm (device layer thickness). This approach is used due to the small probing depth of UPS, allowing a thickness profile of the interface to be obtained, which is represented in the schematic.

Analysis of the spectra presented in **Figure 4.1** revealed a work function of 3.10 eV for ZnO_{120 °C} sample. As discussed previously, this low work function is likely to be due to oxygen vacancies which act as n-type dopants, decreasing the work function of the oxide when compared to the stoichiometric material.²³⁷ Greiner *et al.* discussed the effect of adsorption of gas-phase molecules altering the work function of the metal oxide thin film, a problem which is associated with using solution based processes (compared to *in-situ* growth) to form ZnO films.²³⁷ They also highlight that leaving a sample in vacuum for several hours can alter the work function by up to 0.5 eV. With this in the mind, the work function was measured immediately after loading into UHV. The addition of 1 nm thick SubPc film results in a significant V_L shift of 0.50 eV, due to an increase in the work function to 3.60 eV. The work function increases further, to 3.85 eV, in the case of a 5 nm thick SubPc layer where the work function saturates.

4.2.2 Probing energy levels of sol-gel ZnO_{160 °C}

Values obtained from UPS measurements for ZnO_{160 °C} are shown in **Figure 4.2**. The work function is measured at 3.70 eV with a marginal shift for ZnO_{160 °C} / SubPc_{1 nm} to 3.75 eV. With 5 nm of SubPc the work function increases to 3.85 eV, resulting in a small V_L shift. The VB for ZnO_{160 °C} is 3.90 eV below the E_{FS} giving an IP of 7.60 eV, 0.3 eV greater than ZnO_{120 °C}. The HOMO_{onset} for ZnO_{160 °C} / SubPc_{1 nm} is 1.80 eV below the E_{FS} which is substantially smaller when compared to ZnO_{120 °C} / SubPc_{1 nm}. As before however, the HOMO saturates at 1.90 eV for ZnO_{160 °C} / SubPc_{5 nm} giving SubPc an IP of 5.75 eV.

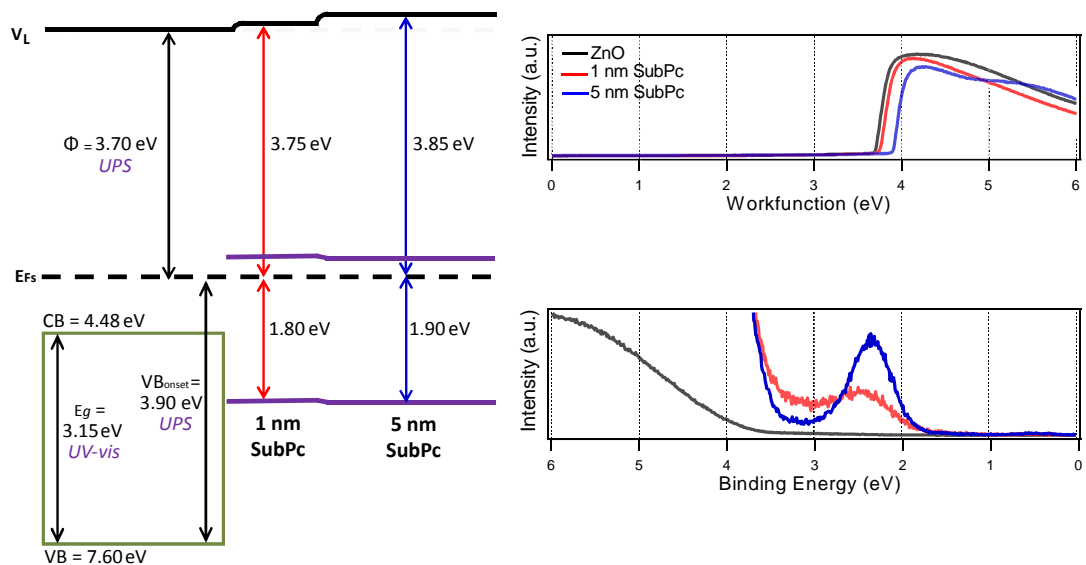


Figure 4.2 A schematic of the values obtained from UPS, along with the spectra from which these numbers were obtained. To simplify the diagram this has only been shown for ZnO_{160 °C} (black line), ZnO_{160 °C} / 1 nm SubPc (red line) and ZnO_{160 °C} / 5 nm SubPc (blue line).

4.3 Comparison of Techniques

The UPS data in **Section 4.2** is compared to the values obtained in **Section 3.4** to monitor if altering the experimental method changed the findings. Ideally both studies should give the same results as identical films were used ($\text{ZnO}_{120\text{ }^\circ\text{C}}$ / $160\text{ }^\circ\text{C}$ / SubPc). Both sets of results support the findings that the energetic profile of ZnO can be altered simply by varying the processing temperature. By altering the energy levels, the interface energetics is changed which impacts the V_{OC} of a device.

The issue however between these two studies is that the absolute values of the CB and VB positions are significantly different depending on the technique used. This is shown schematically in **Figure 4.3**, which shows the obtained values at both temperatures. The diagram also indicates which technique was used to obtain the results (UPS, UV-vis, KP or XPS). It should be noted that the method to calculate E_g (using UV-Vis) was consistent throughout.

The work function values are similar for both methods, with KP giving values on average 0.1 eV higher. This is not entirely surprising as KP gives the average work function beneath the oscillating tip. The measurement of the VB_{onset} however is significantly different and introduces concerns when evaluating which technique to use. When using XPS, the VB_{onset} is measured at 2.20 eV and 2.25 eV below the E_{F_s} for $\text{ZnO}_{120\text{ }^\circ\text{C}}$ and $\text{ZnO}_{160\text{ }^\circ\text{C}}$ respectively. UPS however calculates the VB_{onset} at 4.20 eV and 3.90 eV below the E_{F_s} for $\text{ZnO}_{120\text{ }^\circ\text{C}}$ and $\text{ZnO}_{160\text{ }^\circ\text{C}}$ respectively. As a consequence of the VB position when the CB is estimated (from the E_g), the level is significantly lower than the E_{F_s} , 0.96 eV and 0.78 eV below the E_{F_s} for $\text{ZnO}_{120\text{ }^\circ\text{C}}$ and $\text{ZnO}_{160\text{ }^\circ\text{C}}$ respectively. This phenomenon is not seen when using XPS to calculate VB_{onset} .

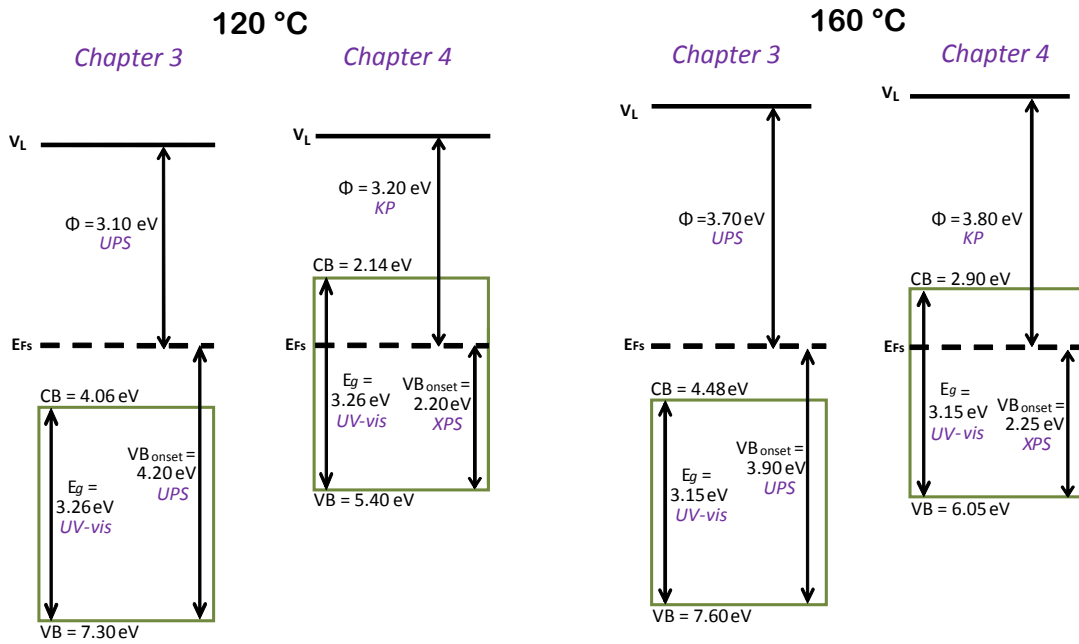


Figure 4.3 A schematic showing the energetic values obtained for a $ZnO_{120\text{ }^\circ\text{C}}$ and $ZnO_{160\text{ }^\circ\text{C}}$ SG derived film. The diagrams indicate the CB and VB positions for each system and also the method used to obtain this value. When UPS is used, the CB position is calculated as being over 0.7 eV below the E_{Fs} for both ZnO films.

4.3.1 Charge neutrality level

The CB lying below the E_{Fs} has been previously reported in the literature for TCOs.²⁵⁰ This property has been explored when studying the cause of conductivity in these layers. Common for all the TCOs studied is the size mismatch between the large cation and the oxygen anion as well as the highly electronegative nature of the O 2s orbital. Various studies have found that if the oxygen vacancies are significant enough, one CB level is present that is significantly below the rest. This is referred to as the CB minimum (CBM).

The CBM was explored by King *et al.* who suggested that it was due to a difference in the position of the charge neutrality level (CNL), shown schematically in **Figure 4.4**.²⁵⁰ All defects, impurities and surface states either have donor-like or acceptor-like character resulting in states lying close to either the CB (donor states) or the VB (acceptor states). The CNL is defined as the point at which they have equal acceptor and donor like properties. If there is a tendency for these states to be donor-like, (common for TCOs), the E_{F_s} lies below the CNL and the CBM is low lying (**Figure 4.4 [b]**).

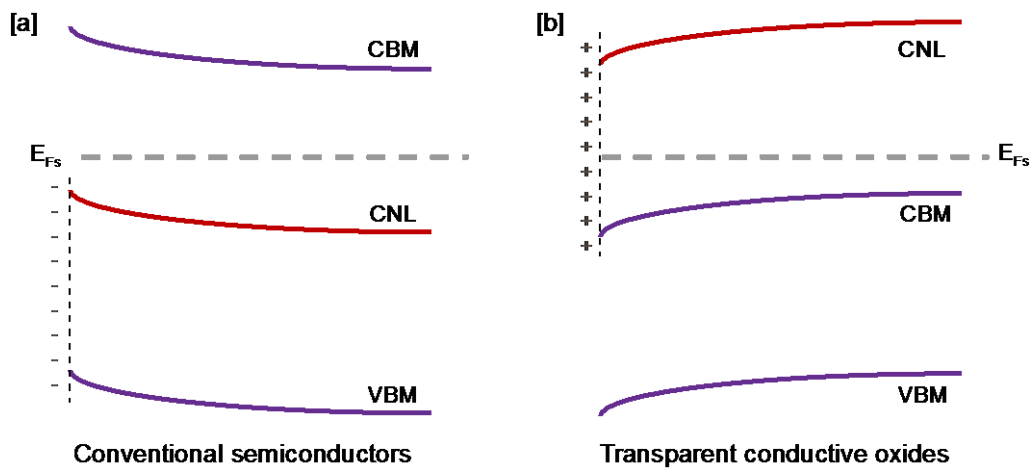


Figure 4.4 Schematic adapted from King *et al.* showing the energetic and common band bending for **[a]** conventional semiconductors and **[b]** transparent conducting oxides.²⁵⁰

This work suggests that the low lying CBM is entirely plausible. The position of the CBM is dependent on both the material and the film carrier concentration (which denotes the number of electrons and holes that participate in conduction). The low lying CBM is found when using UPS, a widely recommended technique. There are discrepancies however for this material set as the ZnO thin films produced from the SG method have a low conductivity, so it is unlikely that this explanation can be applied here, placing doubt on whether this low lying CB is a realistic conclusion.

4.4 Film Stability with Various Techniques

4.4.1 UPS

As UPS is surface sensitive the measurements are susceptible to surface contamination, and also irradiation damage can be caused from exposing the sample to intense UV radiation, typically He I (21.2 eV). To monitor any variability in UPS measurements with film degradation, a sample prepared *ex-situ* was loaded in a UHV system and immediately tested to minimise the time the sample spent under vacuum. The process was optimised to ensure the sample was positioned and immediately measured to minimise film degradation before any data was obtained. The samples were then scanned repeatedly for one hour to monitor any changes in the spectral features with UV radiation.

4.4.1.1 *UPS degradation of ZnO_{120 °C}*

The degradation of the ZnO_{120 °C} film during UPS measurements is shown in **Figure 4.5**. The results show that UV radiation impacts both the work function values and the $V_{B_{onset}}$. The work function is lowered by 0.55 eV after exposure to UV radiation for one hour, with the biggest change occurring in the first few minutes (a 0.25 eV reduction after four minutes exposure). This is significant as experimentally any delay in obtaining measurements, changes in data acquisition time and even direction of measurement (i.e. low to high kinetic energy) can result in major variations in the values obtained. This is problematic as there is likely to be a change in work function

of the film in the time it takes to set-up the technique even when care is taken to ensure this process is as reproducible as possible.

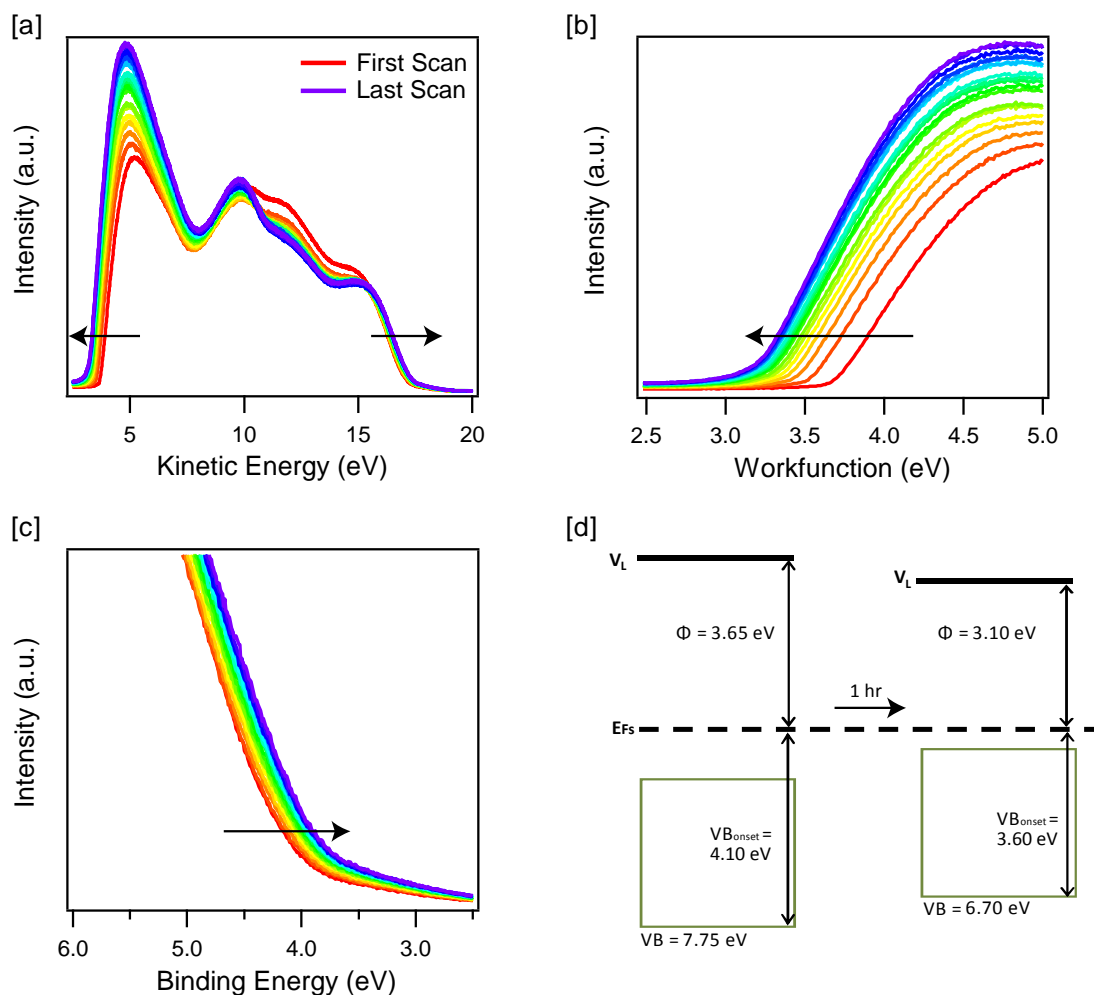


Figure 4.5 Variation in the UPS spectra with time for ZnO_{120 °C} with subsequent scans indicated by the arrows for **[a]** the entire kinetic range, **[b]** the work function and **[c]** the $V_{B_{onset}}$. A schematic is also shown (**[d]**) highlighting the change that occurs after exposure to UV radiation for 1 hour.

A change in work function for ZnO under UV conditions has been reported elsewhere in the literature,²⁵¹⁻²⁵³ with an increase seen in the photoconductivity of ZnO upon exposure to UV light. It has been hypothesised that this enhancement

occurs as UV radiation introduces holes which are attracted to charged oxygen molecules on the surface and therefore induce desorption of oxygen absorbed from the surface. This has been investigated in numerous OPV reports investigating improvement in ZnO based devices upon “photo-annealing”.²⁵² There have been limited publications however about whether UPS can therefore be deemed as a suitable technique for the measurement of any metal oxides that are UV sensitive. **Figure 4.5 [c]** also shows a significant change of 1.05 eV in IP from 7.75 eV to 6.70 eV. The change is significant as the VB_{onset} is fundamental to the material. This suggests that UV radiation causes a reduction in O 2p intensity, therefore changing the VB states and it is not merely the removal of contamination layers.

4.4.1.2 *UPS degradation of ZnO_{160 °C}*

The change in both work function and VB_{onset} also occurs for ZnO_{160 °C}, but the reduction is less significant. Under the same UV conditions the work function changes from 3.80 eV to 3.65 eV and the change mainly occurs during the initial scan and stabilises quickly. There is still however a large shift in VB_{onset} of the film from 7.70 eV to 7.15 eV, pushing the estimated CB position closer to the E_{F_s} . The data is shown in **Figure 4.6** and represented schematically in **Figure 4.6 [d]**. This highlights that even with an increased annealing temperature; the ZnO film is still susceptible to UV radiation.

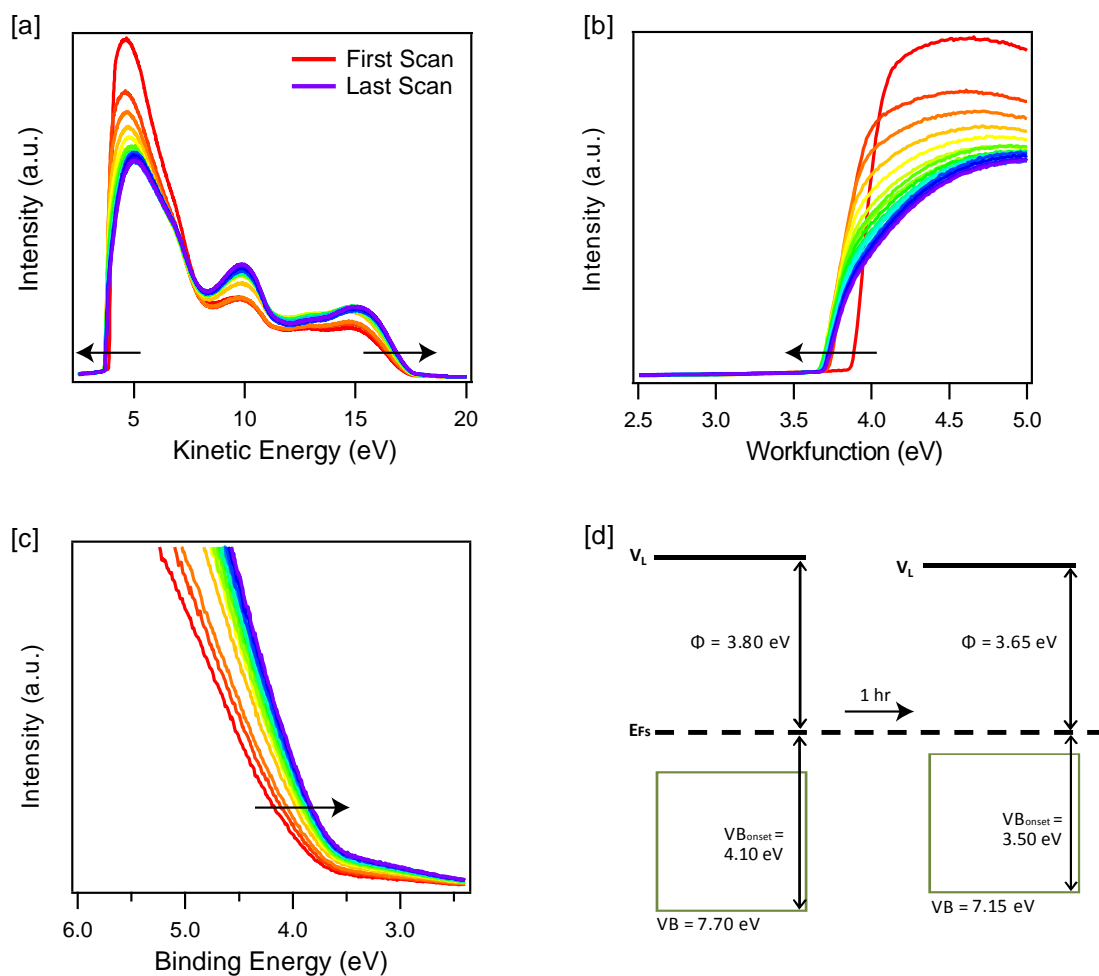


Figure 4.6 Variation in the UPS spectra with time for ZnO_{160 °C} for [a] the whole spectra, [b] the work function and [c] the VB_{onset} . A schematic is also shown ([d]) highlighting the significant change that occurs after exposure to UV radiation for 1 hour.

4.4.1.3 Changes to film composition

To monitor the changes to the film composition under UV radiation, XPS spectra were recorded before and after the 1 hour exposure to UV detailed above. **Figure 4.7** shows the O 1s spectra recorded at a take-off angle of 90°. The component at ~ 529 eV is the bulk ZnO component (O 1s_A), whereas the component at a higher binding energy arises from atmospheric contamination (O 1s_B), typically due to molecules

such as water and hydroxides which have been absorbed. It is clear from the spectra that there is a significant change under the exposure to a UV source, with the variation shown quantitatively in **Table 4.1**.

After UV exposure, there is no change in the peak position of each feature but the percentage composition however changes significantly. The ratio for ZnO $2p_{3/2} : O 1s_A$ changes from 1 : 0.43 to 1 : 0.50 at 120 °C, suggesting the UV radiation triggers further conversion of the starting materials to ZnO. There is no such change for ZnO_{160 °C} with any subtle differences being within the error of the technique. For both films however there is a significant removal of the contamination layer of 19 % and 15 % for ZnO_{120 °C} and ZnO_{160 °C} respectively. This verifies that the changes in work function for both films are likely to be due to the removal of the contamination layer at the surface.

Table 4.1 A comparison of the percentage composition for both films indicating the changes in composition after the UPS measurements. The measurements were obtained at a TOA of 90°.

90° TOA	120 °C				160 °C			
	Fresh		After UPS		Fresh		After UPS	
	eV	%	eV	%	eV	%	eV	%
Zn $2p_{3/2}$	1021.0	39.4	1021.0	41.6	1021.3	43.6	1021.3	45.5
O $1s_A$	529.5	16.9	529.5	20.7	529.9	29.6	529.9	30.2
O $1s_B$	530.8	43.4	530.8	37.7	531.3	26.8	531.3	24.3
Zn $2p : O 1s_A$	1 : 0.43		1 : 0.50		1 : 0.68		1 : 0.66	
Zn $2p : O 1s_B$	1 : 1.11		1 : 0.90		1 : 0.62		1 : 0.53	

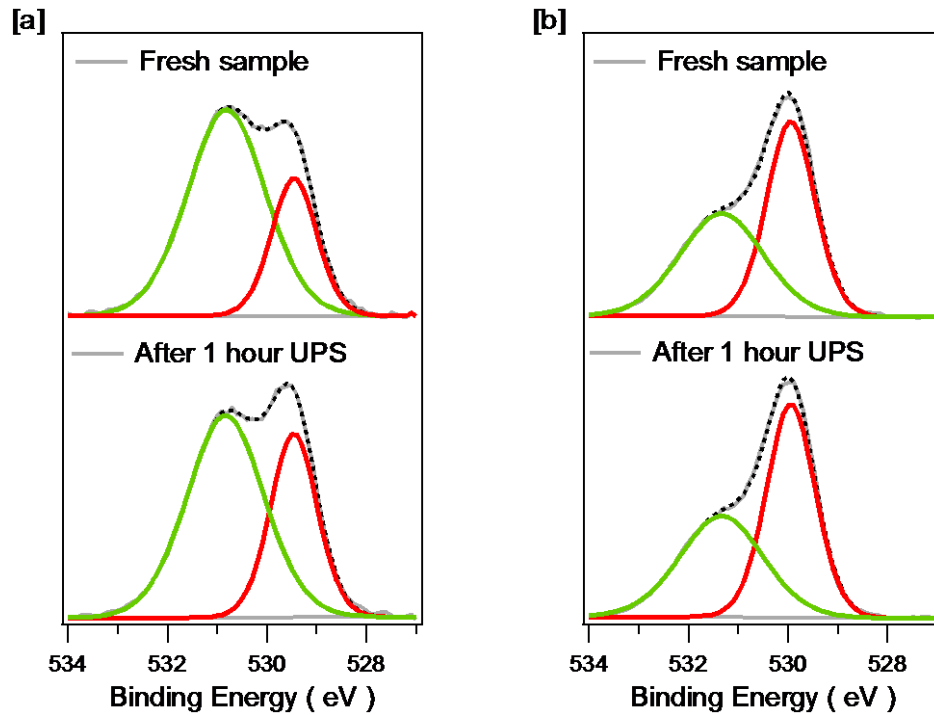


Figure 4.7 O 1s spectra of the ZnO film at a take-off angle of 90° is shown before and after exposure to a UV source for [a] ZnO_{120 °C} and [b] ZnO_{160 °C} with the bulk component (red line, O 1s_A) and contamination layer (green line, O 1s_B) indicated.

4.4.1.4 Angle dependence

To look more closely at the role of surface contaminants the experiment was repeated with a fresh sample at a take-off angle of 30° . The percentage of surface contaminants increases significantly, which is to be expected due to the reduction in penetration depth. There is also more contribution from oxygen in the ZnO lattice, suggesting that more of the surface is oxygen terminated as the penetration depth is likely to be in the range of 5 \AA .

Table 4.2 A comparison of the percentage composition for both films indicating the changes in composition after the UPS measurements. The measurements were obtained at a TOA of 30°.

30° TOA	120 °C				160 °C			
	Fresh		After UPS		Fresh		After UPS	
	eV	%	eV	%	eV	%	eV	%
Zn 2p _{3/2}	1021.0	34.3	1021.0	35.4	1021.4	38.6	1021.4	40.6
O 1s _A	529.5	18.5	529.5	22.5	530.0	30.8	530.0	34.6
O 1s _B	530.8	47.2	530.8	42.2	531.4	30.6	531.	24.9
Zn 2p: O 1s _A	1 : 0.54		1 : 0.64		1 : 0.80		1 : 0.85	
Zn 2p: O 1s _B	1 : 1.38		1 : 1.19		1 : 0.79		1 : 0.61	

The angle dependence at both processing temperatures is more clearly represented by the bar charts in **Figure 4.8**, considering only the elemental composition of Zn 2p_{3/2} and O 1s. It can be seen that for ZnO_{120 °C} this is clearly dominated by the influences of surface contaminants, exceeding 35 % even after exposure to UV radiation for 1 hour. The level of contaminants is significantly lower at 160 °C showing that increasing the annealing temperature does results in either the removal of more contaminants from the fabrication step or a reduction in the sticking coefficient of the adsorbates.

Zhang *et al.* studied the impact of core level XPS on single crystals of ZnO, distinguishing between Zn and O termination faces.²⁵⁴ The surface coverage of each is not affected by the presence of a contamination layer providing the thicknesses are equivalent. The contamination layer however does alter the O 1s spectra considerably (similarly to those in **Figure 4.7**), but owing to the binding energy being in excess of 1 eV removed from the bulk ZnO component, it was concluded

there was no impact on accurate determination of the ZnO bound in the lattice. The impact of contaminants on Zn and O terminated ZnO(001) surfaces was explored further by Coppa *et al.* looking at methods of effectively removing surface layers.²⁵⁵ It was found that extreme conditions (0.05 Torr of 20 % O₂ / 80 % He plasma at 525 °C for 30 minutes) were necessary to do so. As well as complete removal of the contamination peak in the XPS spectra, a 0.5 eV shift in the UPS was observed.

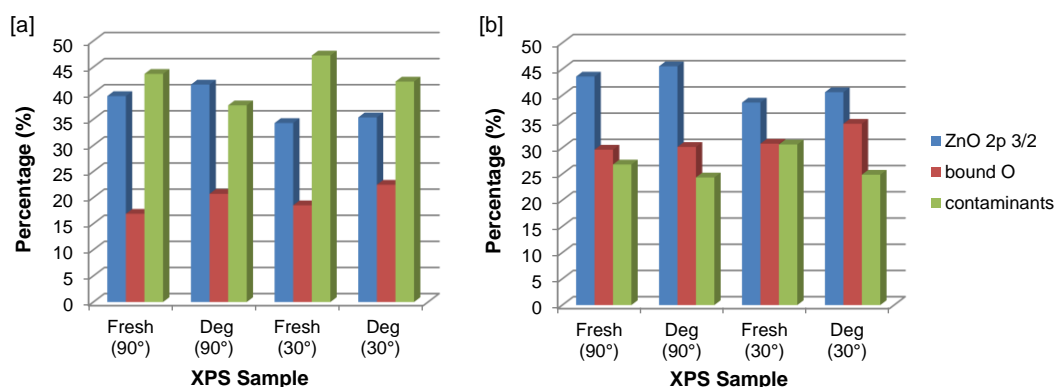


Figure 4.8 Bar charts showing the distribution of elements at TOA of 90° and 30° for [a] ZnO₁₂₀ °C and [b] ZnO₁₆₀ °C.

4.4.2 XPS

The results presented in **Section 4.4.1** show significant changes with exposure time using UPS. If the desire is to limit radiation damage to the surface, the lower count rates in XPS (and thereby longer exposure times) have often resulted in XPS being deemed a non-viable technique to measure the VB of TCOs such as ZnO. In a publication by Greiner *et al.* it is suggested that XPS is an inadequate method for the determination of VB_{onset} values due to the increased power of radiation and extended acquisition times (> 2 hr).²³⁷ To investigate this claim, numerous scans on the two ZnO films were obtained over a 2 hr period, and are shown in **Figure 4.9**. The data highlights the need for long acquisition times in order to reduce the signal to noise ratio and hence obtain a more accurate VB_{onset} value. It is clear however that there are no significant differences between the first, last and averaged scans shown by the red, blue and green lines respectively, with no significant change in VB_{onset} despite exposure to an x-ray source for 2 hours.

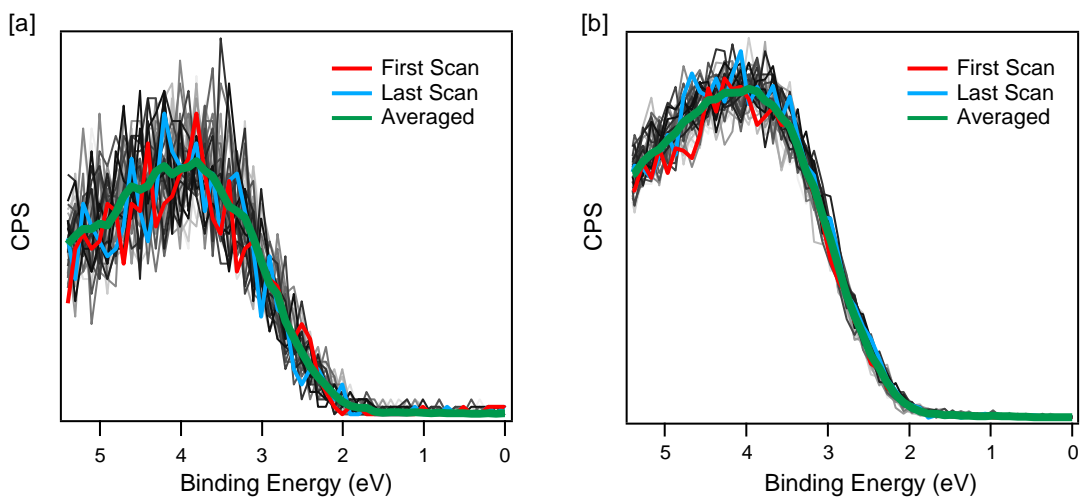


Figure 4.9 VB XPS spectra obtained by repeated measurements over a 2 hour period for **[a]** $ZnO_{120\text{ }^{\circ}C}$ and **[b]** $ZnO_{160\text{ }^{\circ}C}$. The first, last and averaged scans are indicated by the red, blue and green lines respectively.

This investigation clearly contradicts other reports stating that XPS is an inadequate technique for obtaining VB_{onset} values due to prolonged use of a soft x-ray source. The work presented here shows that it is more than just exposure time that needs to be considered when stipulating which technique would be most appropriate for data acquisition. The low count rate of XPS is due to a less intense source and also the variation in the photoionization cross section for O 2s and Zn 4s, shown in **Figure 4.10** needs to be considered. The photoionization cross section shows the probability that a photon of a given energy (from 10 eV – 1500 eV) can be absorbed by an atom to emit an electron from its electronic state. The cross section is ~ two orders of magnitude higher for incident He I (21.2 eV) than an Al K_{α} (1486.6 eV) source, highlighting how susceptible the ZnO film is to UV radiation even during limited exposure times.

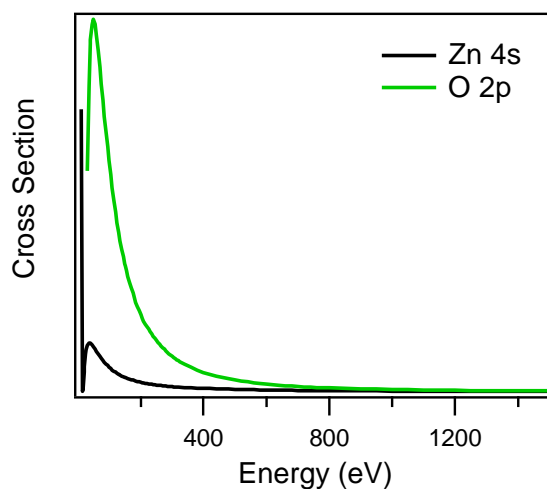


Figure 4.10 The photo-ionization cross section of Zn 4s and O 2p from 10 eV – 1500 eV. The values were obtained from Sincrotrone Trieste SCpA (www.elettra.trieste.it).

4.4.3 KP with light

The sensitivity of metal oxides to UV light is not just limited to solution processed fabrication methods. ITO substrates formed from sputtering were investigated to monitor the impact of light on the substrate work function. To achieve this freshly ITO substrates were exposed to ozone and loaded into a nitrogen filled glove box and the substrates were placed under a light source of 100 mW cm^{-2} AM 1.5 G either in the presence of a 400 nm UV longpass filter or left as loaded. The work function was measured by KP, monitoring the change in 5 minute intervals over a two hour period (**Figure 4.11 [a]**). Without a UV filter, the work function is reduced by 0.55 eV simply by exposure to the light source for 5 minutes. Subsequent changes from this point on are then more gradual. In the presence of a UV filter however, there is no significant change in recorded work function, with the value fluctuating around $4.9 \text{ eV} \pm 0.1 \text{ eV}$.

The impact of a change in work function under illumination is shown by the inverted device ITO / C₆₀ / SubPc / MoO_x / Al. The *J-V* scans under constant illumination are shown in **Figure 4.11 [b]**. Upon initial scan, there is an S-shaped kink, which has been related to reduced interface recombination velocity at one of the electrodes and is detrimental to the *FF* of the cell.²⁵⁶ By exposing the film to light there is a reduction in the s-shaped kink under constant illumination, resulting in an improvement in the *FF*. This can be attributed to the work function of the substrate aligning more closely with that of the acceptor material C₆₀, improving the overall device performance.¹¹⁷ The mechanism postulated is analogous to other metal oxides where the UV irradiation induces photogenerated holes which recombine with

absorbed O_2^- releasing O_2 . This removes the surface dipole thereby reducing the work function of the film.

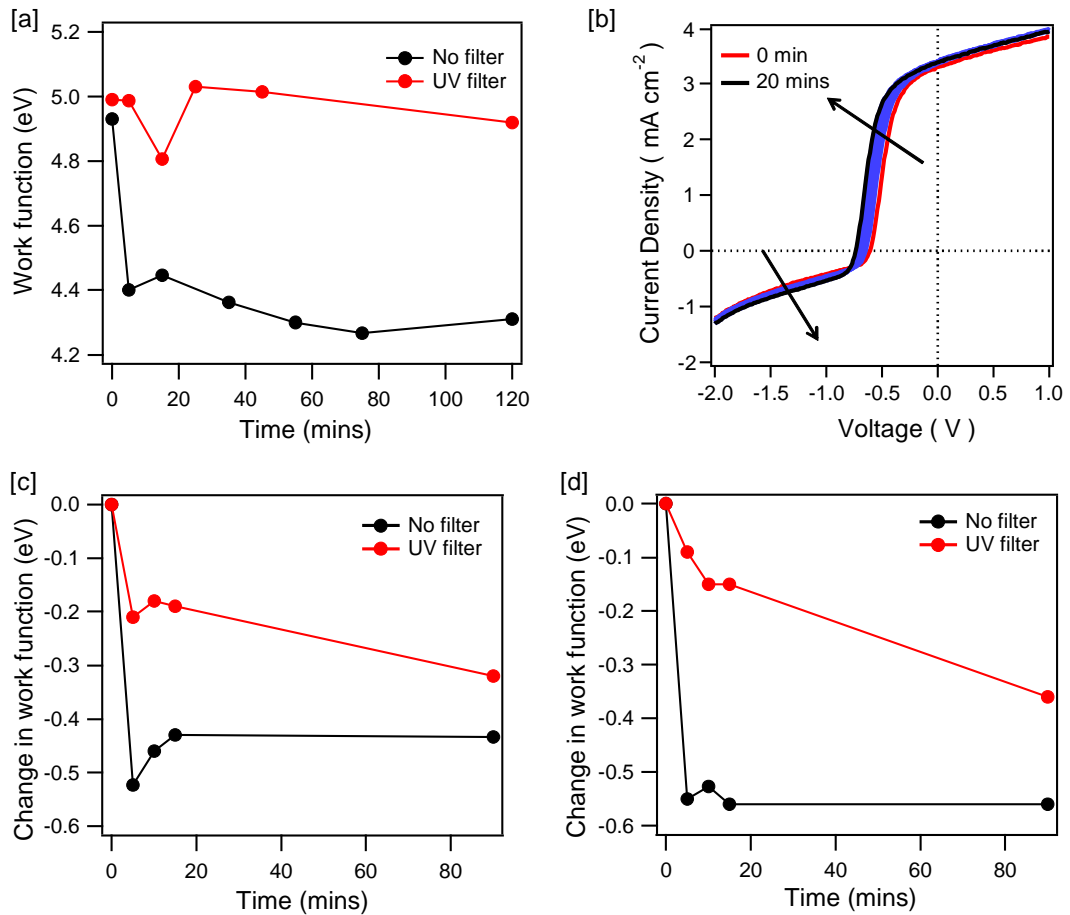


Figure 4.11 [a] Change in work function of an ITO substrate with and without the use of a UV filter, [b] the change in cell performance of an ITO / C₆₀ / SubPc / MoO_x / Al device under exposure to 100 mW cm⁻² AM 1.5G. The change in work function with and without a UV filter is also explored for [c] ZnO_{120 °C} and [d] ZnO_{160 °C}.

This approach was applied to the two ZnO films discussed previously. Identical ITO/ZnO films were prepared and annealed to either 120 °C or 160 °C for 1 hour. Once cooled, the films were transferred to the nitrogen filled glove box and the initial work function was measured for each film. The films were then placed under

AM 1.5G with or without a UV filter with the work function measured in 5 minute increments. **Figure 4.11** shows the change in work function for [c] ZnO_{120 °C} and [d] ZnO_{160 °C}. Without a filter, the work function lowers by 0.5 eV ± 0.1 eV with only 5 minutes of light exposure and this value remains stable over the 90 minutes. When a UV filter is used however, the change in work function is less significant, with a 0.2 eV and 0.1 eV reduction for ZnO_{120 °C} and ZnO_{160 °C} respectively. This value reduces more gradually over the 90 minute period to 0.32 eV and 0.35 eV from the initial value showing that with a UV filter the change in work function is substantially reduced even with prolonged periods of light exposure. This highlights that the modification to the ZnO film surface is caused by the presence of UV light regardless of the intensity of the source.

4.5 Conclusion

The aim of this section was to provide an overview as to why despite initial energetic profiling using UPS, further exploratory work resulted in questions about the reliability of the results. The benefits of UPS as a technique are widely discussed in literature as it provides the absolute minimum in work function value due to biasing of the film. This is unlike KP which can only provide an average relative work function under an oscillating tip when compared to a reference material such as HOPG. Therefore it is widely accepted in literature that UPS measurements should be taken where possible as this technique is deemed to have more merit.

It has been concluded that ZnO thin films deposited using the SG process, cannot be investigated using UPS as the values obtained are not accurate and reproducible. Experimentally it is difficult to ensure that the exposure time to the He source is both constant and minimal with repeated measurements resulting in a large variation in absolute values. For KP on the other hand, there was less variability in measured work function over a large sample set, and the film represents the surface that will be used for the formation of hybrid devices.

The use of XPS analysis before and after UPS exposure has revealed that the main spectral change is due to removal of the contaminant layer, exposing more of the bound ZnO sample. This results in a significant change in both the work function of the film and the VB_{onset} (such a change has not been discussed in literature). The use of VB XPS has shown that there is no significant change in values recorded over the required acquisition time using a soft x-ray source so therefore it presents an alternative method for calculating the VB_{onset} for metal oxide thin films.

These simple experiments highlight the care that must be taken when obtaining energetic values from UPS. It should be noted that the film which is being investigated should be explored in detail to discover whether UPS can be deemed an accurate way of obtaining work function and $V_B/HOMO_{onset}$ values. There is also the consideration of which technique accurately represents that of a working device with KP/XPS carried out in the dark whereas UPS may give a more accurate indication of a working system due to exposure to UV light. However, the delicate nature of some of these films to a UV source (either using simulated AM 1.5G irradiation or UPS) shows that it is not merely related to power of radiation. This is a key problem when using UPS to construct an energetic diagram and helps explain why there is such a significant spread in reported values.

5 Optical Spacing

5.1 Introduction

5.1.1 Background

There has been a drive to improve the J_{SC} in the field of OPV, which is limited due to the narrow absorption bands of the organic materials utilised and the unfavourable overlap with the solar spectrum.²⁵⁷ The poor absorption is due to the significant difference between the optical penetration depth and the charge transport within the layers. If the active layer thickness is increased to enhance the absorption, (and hence the J_{SC}), there are considerable losses which mean that the improvement in absorption does not result in an improved device performance. This is a result of unbalanced charge transport, increased probability of charge recombination and often a reduction in the internal electric field.²⁵⁸

Many light trapping schemes have been explored to improve the overall J_{SC} including surface texturing, which increases the cell absorption by scattering, periodic nanostructures,²⁵⁹ photonic crystals²⁶⁰ and micro cavities.²⁶¹ There are questions surrounding the experimental complexities with many of these approaches and whether they could be considered as viable options for large scale fabrication of OPV devices. This is mainly because of the problems in controlling film formation on a nanometre scale, without having any detrimental impact on cell performance.²⁶²

A simple method to improve absorption is through the use of an optical spacer layer. To function effectively this layer must not have a strong absorption of solar

illumination, have appropriate energy levels to inject or collect either hole/electron (depending on cell architecture), be robust to subsequent layers (whether this be organic materials or a hot metal electrode deposition) and be sufficiently conductive.²⁶³ This layer is typically placed in between the active materials and the reflective back metal contact. This is because the light intensity is zero at the metallic electrode, so a spacer can be implemented to place the active material in a more favourable optical field, improving the overall absorption in the layer.

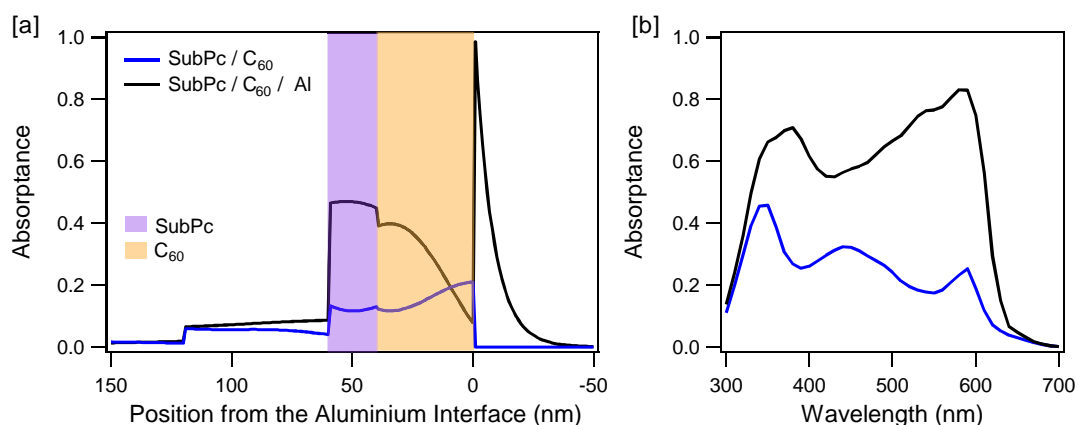


Figure 5.1 [a] The total absorbance of a SubPc/C₆₀ device without (blue solid line) and with (black solid line) a reflective metal contact and [b] the wavelength dependence of the absorbance for SubPc/C₆₀ device without (blue solid line) and with (black solid line) a metallic electrode.

A reflective electrode is paramount to achieving good currents within a cell; this is simply because owing to the small active layer thicknesses, reflections are incredibly important at this scale. This is accounted for within the model which uses a transfer matrix method to account for absorption, transmission and reflections within the device in order to accurately determine the most appropriate position and layer thickness of all layers within the structure. This is highlighted in **Figure 5.1** which shows the absorbance relative to both position within the architecture [a] and

wavelength dependence [b] for a SubPc (15 nm)/C₆₀ (40 nm) active layer with and without a reflective electrode. The figure highlights the importance of utilising a reflective back contact to maximise light absorption, with an aluminium electrode increasing the *EQE* contribution across all wavelengths.

This principle has been successfully implemented in many different device architectures, exploring a range of spacer layers investigated. For a polymeric device, Kim *et al.* have demonstrated this concept in a BHJ OPV cell by utilizing a solution processed TiO_x layer as a spacer layer between the polymeric blend active layer and the metal electrode. The result is a substantial improvement of up to ~ 40 % in *EQE* across the spectral range, which results in an enhancement of 50 % in the *J_{SC}* of the device.²⁶⁴ A similar improvement was seen elsewhere using a 39 nm ZnO layer, showing a strong correlation between theoretical and experimental active layer dependence across a wide range of active layer thicknesses.²⁵⁷

Another important field for the use of spacer layers is in multistack devices where the performance is typically dictated by the current limiting cell providing there are no changes in the electric field in the device. There have been numerous reports on the most effective layers that can be used in this instance and the importance of placing different band gap materials in the most effective architecture possible to match the optical properties.²⁶⁵ For polymeric tandems for instance, as the layer thickness of each subcell is considerably higher than a SM device it is most effective to place the low band gap polymer in the back cell so low energy photons pass through the front cell and are not absorbed.²⁶⁶ There are also instances whereby the use of a spacer layer may not lead to improved device performance, placing a cell in an interference minimum lowering the overall cell performance.³⁹ Therefore careful

theoretical and experimental studies are required for each different cell architecture to ensure the overall absorption has reached its potential.

5.1.2 Aims

The aim of the chapter is to bridge the gap between polymer and SM hybrid solar cells to show that SM materials can be a viable planar HOPV cell by improving the overall J_{SC} of the device through the careful implementation of an optical spacer layer. In this work a MoO_x interlayer is used as a hole extracting layer due to its good energy level alignment with the HOMO of SubPc,²⁶⁷ and it also protects the sensitive organic SubPc layer from damage during deposition of the Al electrode. Furthermore, MoO_x is exploited as an optical spacer layer in the inverted HOPV devices, by varying the distance of the SubPc layer from the Al electrode. From an experimental perspective, vacuum deposition of SubPc and MoO_x allows a highly controlled film growth process,²⁴ with accuracy on the subnanometre scale. This makes it possible to tailor the device layer thicknesses to the optimal structure predicted by optical modelling.²⁶³ The ZnO/SubPc devices demonstrate that the use of high absorption coefficient SM organic semiconductors combined with high quality TMO films creates a viable opportunity to produce new types of HOPV cells.

5.2 Film Optimisation and Characterisation

5.2.1 Sol-gel process

In this chapter, the SG recipe from **Chapter 3** was modified in order to improve long term solution stability, allowing the same solution to be used for multiple batches of devices. A 0.25 M precursor solution containing ethanol (Aldrich, denatured) and zinc acetate (Aldrich, 99.99 %) was left to stir vigorously at 80 °C for 2 hours before the stabiliser, 2-amino ethanol (Aldrich, 99.5 %, 5 % vol.) was added. The solution was left at 60 °C, and allowed to stir overnight prior to spin coating on to ITO coated substrates.³⁶ The freshly spin coated films were left in air for fifteen minutes before being annealed to 160 °C for 1 hour in air to convert to ZnO. This process is summarised schematically in **Figure 3.2** and the process was adapted from a method published by Kyaw *et al.*, where a ZnO electron selective layer was used to invert the polarity of the device for the use in solution processed SM BHJ solar cells.³⁶ The Kyaw *et al.* method utilised a 0.1 M solution in the SG process, but following ZnO film optimisation a 0.25 M was deemed to be more desirable due to an improved reproducibility and consistency across the batches.

5.2.2 Morphology and Structure

Due to the strong tendency of ZnO to form a variety of nanostructures, as shown in **Chapter 3**, the film treatment was controlled to ensure reproducible thin film layers. **Figure 5.2** shows AFM images of [a] the ZnO thin film as spincoated and [b] following the annealing step. For consistent smooth homogenous morphology ($R_q <$

1.0 nm), all samples were left for 15 minutes at room temperature prior to heating and as a result the surface roughness was lowered from [a] 5.6 nm to [b] < 1.0 nm. The film thickness was determined using step-edge AFM measurements, giving films approximately 30 nm thick.

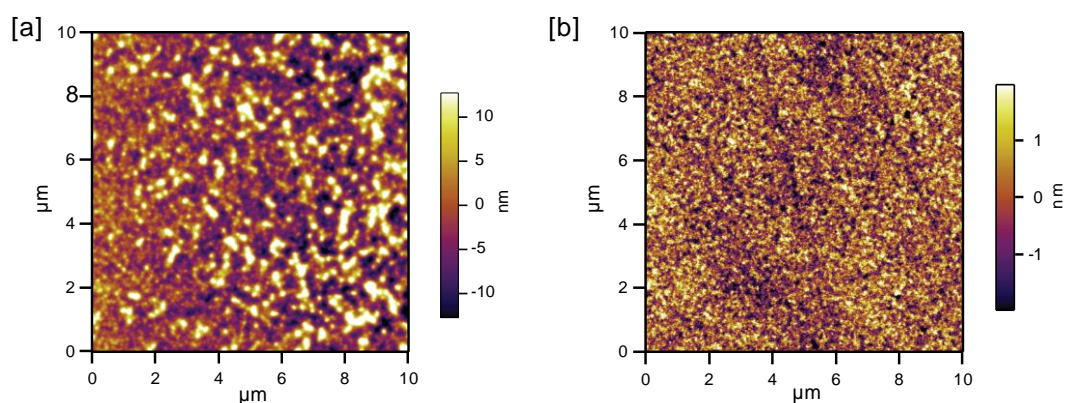


Figure 5.2 AFM images of: [a] ZnO films prior to heat treatment ($R_q = 5.6$ nm) and [b] ZnO with a drying step resulting in smooth homogeneous film formation ($R_q = < 1.0$ nm).

In this study, the organic donor, SubPc was directly deposited by vacuum deposition on top of the ZnO films. Therefore, it is desirable to study the impact of morphology on subsequent growth of organic layers. **Figure 5.3** shows AFM images of a 15 nm SubPc layer directly deposited at 2 Å/s on top of either a bare ITO substrate or directly onto a ZnO film that had been annealed to 160 °C. The surface shows a similar morphology on both substrates and no increase in surface roughness as a result of the morphology of the underlying layer. This shows that ZnO as an acceptor layer is not causing any changes in film growth which could result in a current leakage.

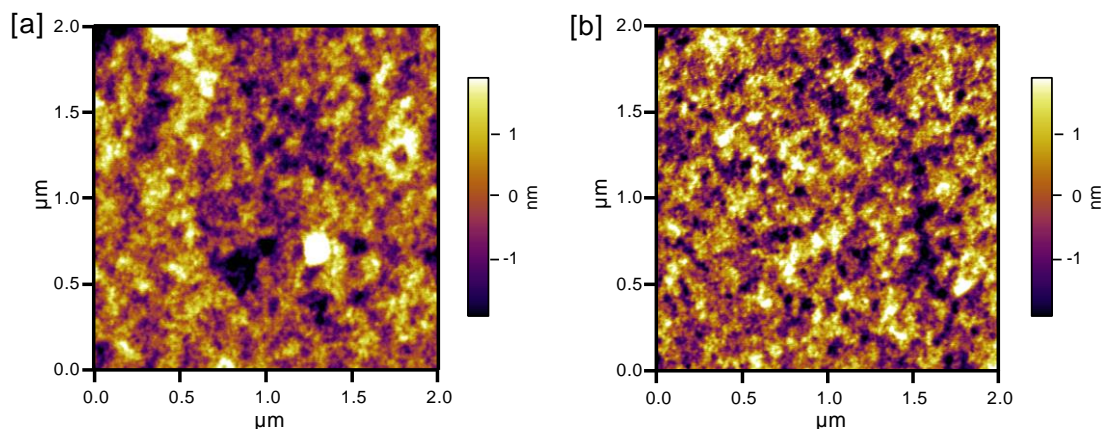


Figure 5.3 AFM topographical images of [a] ITO / 15 nm SubPc ($R_q = 0.9$ nm) and [b] ITO / ZnO / 15 nm SubPc. ($R_q = 0.9$ nm).

5.2.3 Absorption spectroscopy

The electronic absorption characteristics are summarised in **Figure 5.4**, with the transmittance of the [a] ZnO and [b] MoO_x shown along with [d] the absorption spectra of SubPc. The transmission of ZnO on a quartz substrate is > 95 % across all wavelengths. The optical band gap has also been calculated from the energy (eV) versus $(E \times \alpha)^{1/2}$ plot shown in the inset, from the method for non-crystalline semi-conductors (*Equation 3.1*) giving a band gap of 3.05 eV.

The transmittance of the hole extracting layer and optical spacer, MoO_x, was measured on a quartz substrate for a 5, 20, 40, 60 and 80 nm thick films, (**Figure 5.4 [b]**). At low MoO_x thicknesses (5 nm) the layer does not significantly compete for absorption with SubPc as the transparency is > 95 % at 590 nm. As the thickness of MoO_x is increased, the transparency decreases across all wavelengths, but remains above 70 % even with the use of an 80 nm layer. The location of the high transmittance peak is sensitive to layer thickness, with a peak at 390 nm for a 60 nm

layer and 420 nm for an 80 nm layer. This shows that any subtle difference in film thickness would affect not only the intensity but the position of the peak. The shift in transmittance of the MoO_x thin film is due to optical effects within the layer. **Figure 5.4 [c]** shows the optical modelling of MoO_x on a quartz substrate confirming the presence of this high transmission peak at 80 nm.

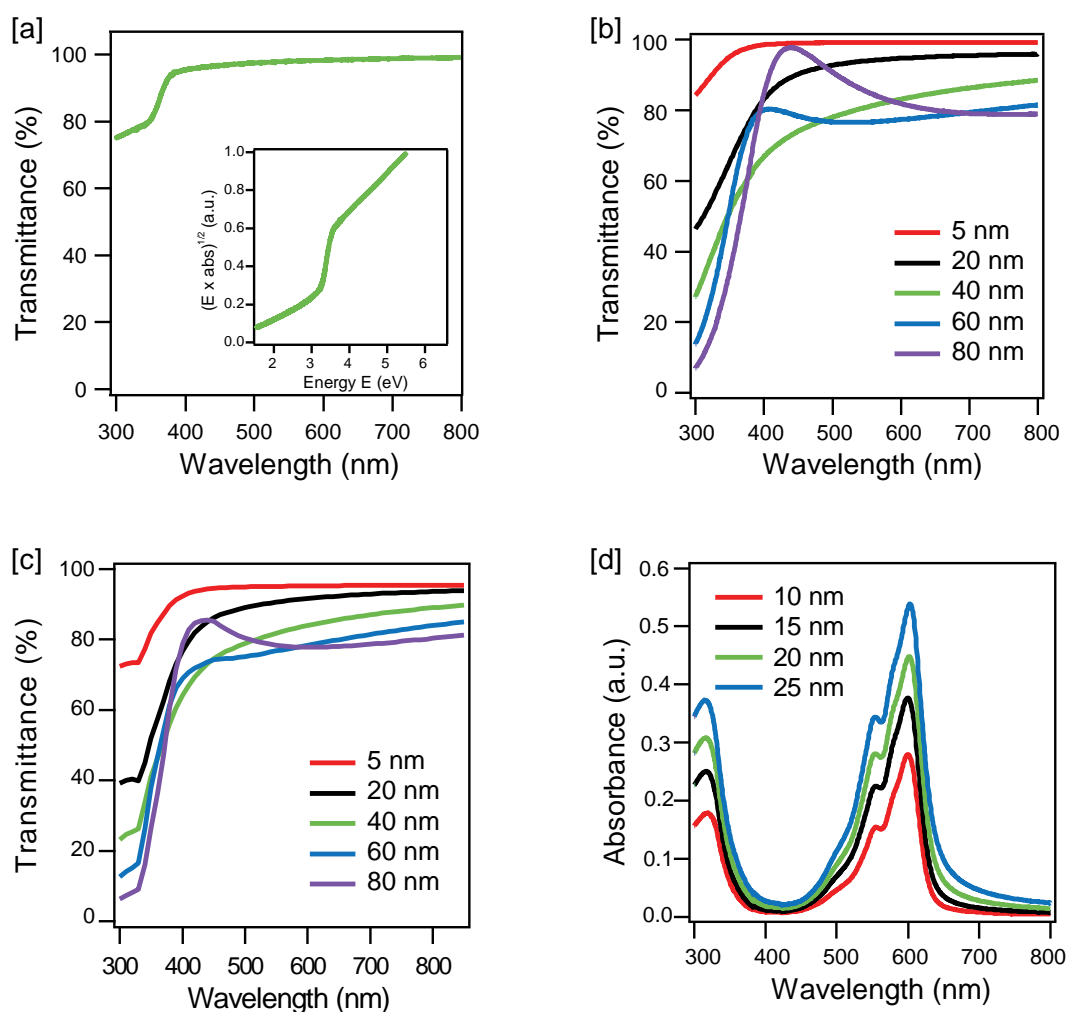


Figure 5.4 [a] The transmission of ZnO 160 °C (green line) on a quartz substrate is shown, the inset shows the energy (eV) versus $(E \times \alpha)^{1/2}$ plot [b] the transmittance for 5, 20, 40, 60 and 80 nm thick MoO_x layer [c] transmittance of a 5, 20, 40, 60 and 80 nm thick MoO_x layer calculated by optical modelling [d] the electronic absorption spectra on a quartz substrate for 10, 15, 20 and 25 nm of SubPc.

The absorption of SubPc is also shown, and resembles that of other phthalocyanine materials with a shift to shorter wavelengths as a result of a reduction in ring size from 18- π system to 14- π system.¹⁶² **Figure 5.4 [d]** shows the absorption of 10, 15, 20 and 25 nm thick layers of SubPc on a quartz substrate. The absorption can be explained by the Gouterman Four Orbital Model, which gives a theory for the two bands due to mixing of two HOMO and two LUMO levels giving rise to two excited states.^{268, 269} One state is lower in energy, the Q band, which is the origin of the SubPc absorption maximum located at 590 nm and an associated vibronic band at 540 nm, and one higher in energy, the Soret B band, located at 310 nm.

5.2.4 Refractive index

The refractive index data was either acquired from literature or obtained using a UVISEL ellipsometer (Jobin-Yvon/Horiba, UK) with a Xe light source, over the wavelength range of 250 – 800 nm and at an incidence angle of 70 °. For ZnO thin films there is a wealth of previously published data available, however any slight tweak to the synthetic method results in significant changes to film thickness and properties. Due to the sensitivity in production method, identical ZnO layers (outlined in **Section 5.2.1**) were deposited on silicon and quartz substrates. The optical properties of MoO_x thin films were also investigated, in this instance various thickness were vacuum deposited on quartz and silicon substrates. The refractive index data for these materials is shown in **Figure 5.5 [a]**. Film thicknesses and optical properties were modelled using a three phase ambient/film/quartz model, in which the layer was assumed to be isotropic. An Adachi-new Forouhi dispersion formula was employed to obtain the optical constant for the film.^{203, 204} Refractive

index data for SubPc is widely available in literature, and is shown in **Figure 5.5**

[b].¹⁶³

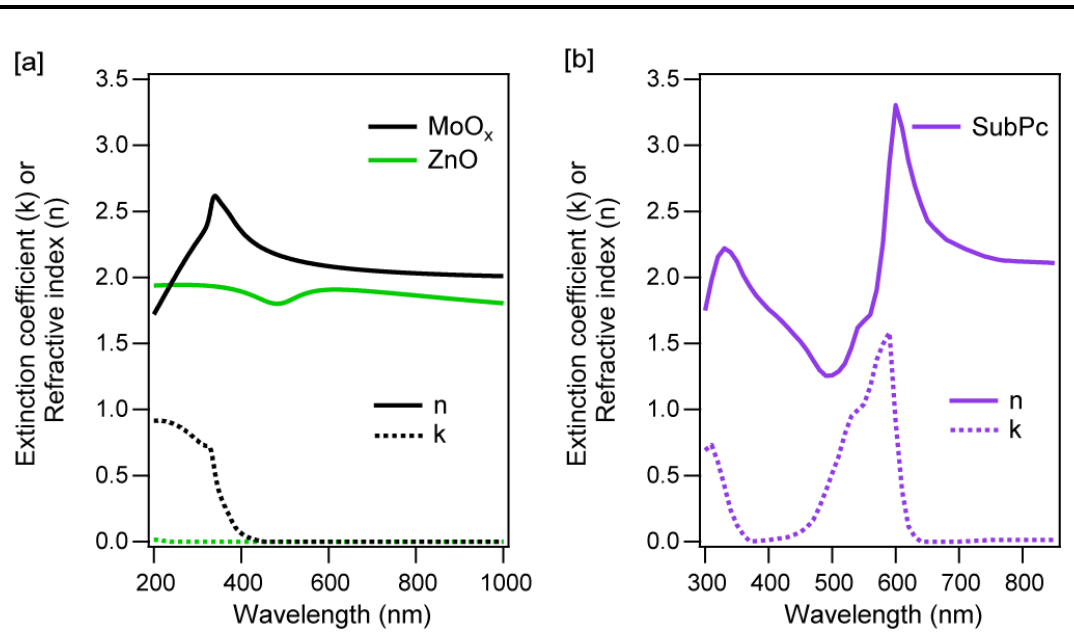


Figure 5.5 Extinction coefficient (k, dashed lines) and refractive index (n, solid lines) [a] ZnO (green) and MoO_x (black) obtained using a UVISEL ellipsometer and [b] SubPc (purple) where the data was obtained from literature.¹⁶³

5.3 Optical Modelling

5.3.1 Electric Field

In a planar heterojunction, the photocurrent generated in OPVs is restricted due to the limit placed on the layer thickness by the L_D , so that the excitons generated can diffuse to the heterojunction and be dissociated prior to non-radiative relaxation.²⁷⁰ The L_D of SubPc has been reported to vary between 8 and 28 nm,^{239, 240} significantly lower than the optical penetration depth and as a consequence, when light travels through a film in this thickness range it is only partially absorbed. Owing to the thickness of the donor layer material being below the optical penetration depth, interference occurs within the layer due to the reflective electrode. It is therefore critical that this thin layer is placed at a maximum in the optical field to maximise exciton generation.

Figure 5.6 [a] shows the optical electrical field for the layer architecture ITO / ZnO (30 nm) / SubPc (10 nm) / MoO_x (5 nm) / Al with respect to the aluminium electrode. The positions of subsequent layers are indicated schematically by different coloured boxes, MoO_x (blue), SubPc (purple) and ZnO (green). Since SubPc is the only current contributor and is significantly out of its absorption maximum, the number of photons that can be absorbed within the layer are limited. The optical electric field differs with material properties and thicknesses owing to the complex refractive indices of the interlayers. The impact of increasing the MoO_x layer thickness to 40 nm is shown in **Figure 5.6 [b]**. The donor material is placed further into its absorption maximum at 590 nm improving absorption in the cell, showing in this instance MoO_x functions as an optical spacer layer. There is potential to improve

this further, however if this layer thickness is increased further to 80 nm, shown in **Figure 5.6 [c]**, the electric field at 590 nm significantly decreases reducing the potential number of photons that can be harvested with this architecture. This demonstrates very clearly the need for consideration of the optical properties and tuning of the spacer layer thickness.

This feature needs to be considered across all wavelengths and total absorption plots are shown in **Figure 5.6 [d-f]** for a **[d]** 5 nm, **[e]** 40 nm and **[f]** 80 nm MoO_x layer. This diagram considers the photons absorbed from 300 to 800 nm within each layer of the cell architecture, rather than considering the electric field at one wavelength. As can be seen with the blue box, MoO_x does absorb some of the overall light (typically below 400 nm, as shown in **Figure 5.4 [b]**), which in turn will limit the overall absorption possible with the SubPc layer. It can however clearly be seen that the overall absorptance within the cell for a 10 nm active layer thickness is greatly improved with a spacer layer 40 nm thick.

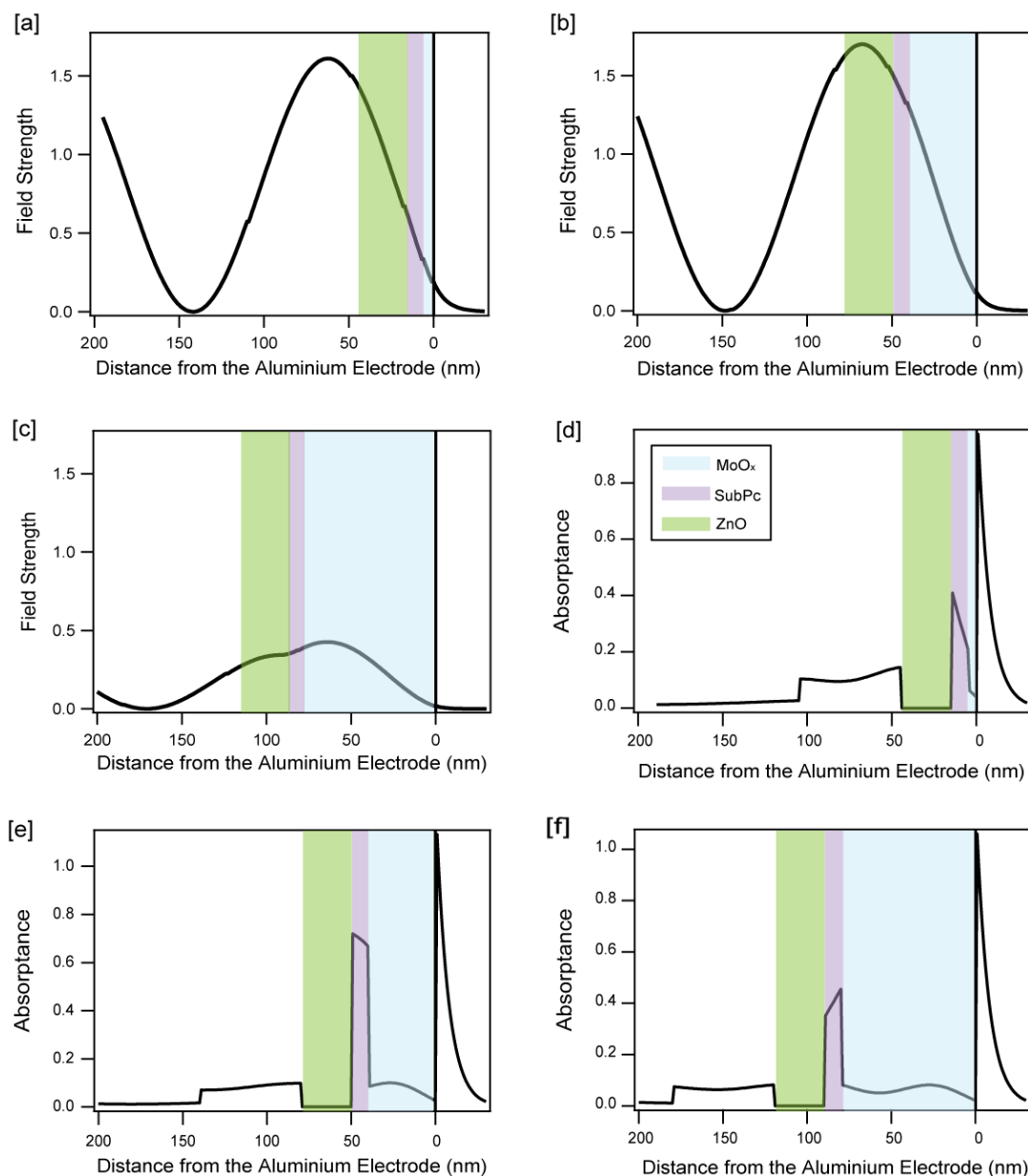


Figure 5.6 Electric field plots at the SubPc absorption maximum ($\lambda = 590$ nm), showing a low field strength with 5 nm MoO_x [a] and an improved field strength with 40 nm MoO_x [b], this is reduced for 80 nm MoO_x [c]. The total absorbance (across all wavelengths) is also shown with respect to the aluminium electrode for 5 nm MoO_x [d], 40 nm MoO_x [e] and 80 nm MoO_x [f]. The positions of the materials with thickness are indicated by blue, purple and green boxes for MoO_x, SubPc and ZnO respectively.

5.3.2 Predicted Current Generation

The HOPV cell architecture: ITO/ZnO (30 nm)/SubPc (x nm)/MoO_x (y nm)/Al with varying active layer thickness, SubPc, x , from 10 to 25 nm and MoO_x optical spacer film thickness, y , from 10 to 80 nm was modelled in order to monitor the impact a spacer layer would have on current generation. **Figure 5.7 [a]** shows a contour plot of the modelled current in the cell, by considering the total absorption in the cell with only SubPc contributing to the current. With a 10 nm SubPc layer, the estimated current generation increases by 162 % simply by increasing the MoO_x thickness from 10 to 50 nm, with a predicted J_{SC} of 2.0 and 4.9 mA cm⁻² respectively. Any further increase in spacer layer thickness results in a decrease in the predicted current since the active layer is no longer placed in its absorption maximum. In this instance an *IQE* of 100 % is assumed. As the thickness of SubPc is increased, the model predicts an increase in current generation as the layers are more absorbing. As the SubPc layer thickness increases, it is predicted to be less susceptible to changes in MoO_x thickness, shown by a smaller improvement of 39 % in current for 25 nm SubPc from a 10 nm (5.2 mA cm⁻²) to a 40 nm (7.2 mA cm⁻²) MoO_x layer.

The limitation of this model is that it assumes that the *IQE* (η_{ED} , η_{CT} , η_{CC}) is not dependent on the layer thickness of each component. To account for the L_D of the organic material, the output from the optical field calculations was input into a custom 1D finite difference diffusion equation solver with the optical calculations converted into an exciton generation rate at nanometre increments within the layer, assuming a L_D of 10 nm for SubPc.^{239, 240} Further assumptions are necessary, firstly that the ZnO/SubPc boundary is fully exciton dissociating, the SubPc/MoO_x

boundary is exciton blocking, whilst recombination is considered based on the exciton lifetime and exciton density at each position in the layer. This is iterated until a steady state solution is achieved, with excitons quenched at the ZnO/SubPc boundary considered to be generating useable current, with $\eta_{CC} = 100\%$. **Figure 5.7 [b]** shows a contour plot of the modelled current generation in the cell.

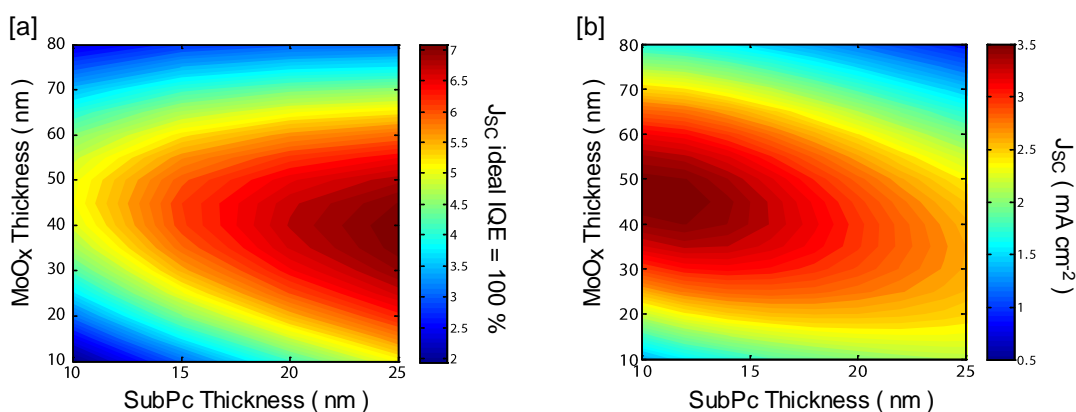


Figure 5.7 Contour plot of **[a]** exciton generation with SubPc versus MoO_x thickness, **[b]** the modelled current generation with a diffusion correction (assuming SubPc has an $L_D = 10$ nm).

Unsurprisingly due to a given L_D of 10 nm the estimated current generation for an optimised cell is at its highest for thinner SubPc layers, with no favourable increase in current generation with an increase in the active layer thickness. This is because as the layer thickness increases, despite there being an increase in exciton generation, there is a lower proportion that are able to reach the interface to be separated into free charges for useable current. The current however is greatly affected when MoO_x is utilised as an optical spacer layer. Considering a 10 nm SubPc layer, with a typical MoO_x hole transporting layer thickness of 10 nm, the model predicts a J_{SC} of 1.4 mA cm⁻². By increasing the thickness to 50 nm, a 155 % improvement in the J_{SC} is

estimated, reaching 3.5 mA cm^{-2} . With any further increase in spacer layer thickness, the predicted current decreases due to the SubPc layer no longer being placed in the absorption maximum. If a thicker SubPc layer is modelled the impact of the spacer layer is greatly reduced as a proportion of the active layer is already positioned further away from the reflective back contact. Considering a 25 nm SubPc layer, the predicted current varies from 2.16 to 2.62 to 0.92 mA cm^{-2} for a 10, 40 and 80 nm MoO_x layer respectively.

5.4 Device Fabrication

Devices using the HOPV inverted architecture ITO / ZnO (30 nm) / SubPc (x nm) / MoO_x (y nm) / Al were fabricated. Following the solution processed ZnO acceptor layer, all subsequent layers were vacuum deposited onto the prepared films before the Al electrode was deposited through a shadow mask to give an active area of 0.16 cm². The SubPc layer was deposited at a rate of 2 Å s⁻¹ and the MoO_x layer at a reduced rate of 0.3 Å s⁻¹ to prevent damage to the underlying organic material. A total of 40 devices were fabricated with varying layer thickness of SubPc, x , and MoO_x, y , in order to compare the predicted currents (**Figure 5.7 [b]**) to the experimental values.

Figure 5.8 [a] shows the J - V curves of the planar inverted HOPV devices under both illumination and dark conditions for a 15 nm SubPc layer with a 10, 40 and 80 nm MoO_x layer, with key parameter changes compared to MoO_x thickness (**Figure 5.8 [b]**). A high V_{OC} of 1.10 V is achieved due to the large offset between the low lying SubPc HOMO and the E_{FS} (discussed in detail in **Chapter 3**). From **Figure 5.8 [b]**, it can also be seen that the FF , although limiting the cell performance at ~ 0.25 , does not change with spacer layer thickness, suggesting that the MoO_x layer is sufficiently conductive to allow good transport of holes to the Al electrode even at thicknesses approaching 100 nm.

The V_{OC} also remains constant across all devices, and as a result the individual device performance is largely dependent on the J_{SC} . There is a clear improvement in J_{SC} with an increase in spacer layer thickness from 1.51 mA cm⁻² (10 nm) to 2.48 mA cm⁻² (40 nm) where it reaches its maximum, but a further increase to an 80 nm

layer results in a lower J_{SC} of 1.85 mA cm^{-2} , due to positioning the SubPc layer out of its absorption local maximum. As a result, the PCE improves from 0.45 % (10 nm) to 0.73 % (40 nm), before a reduction to 0.55 % with an 80 nm spacer layer.

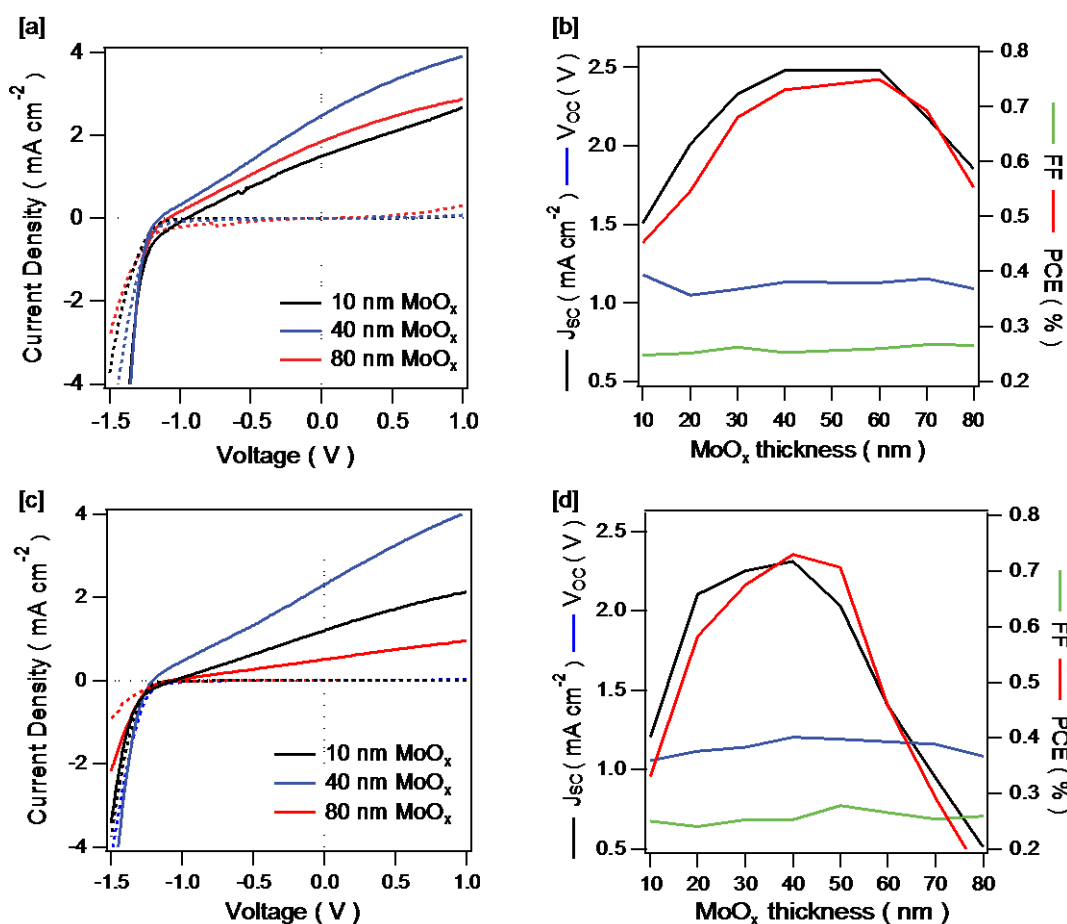


Figure 5.8 Summary of device performance for a 15 nm layer [a, b] and a 25 nm layer [c, d]. $J-V$ plots of the HOPV device with varying MoO_x thicknesses are shown in [a] and [c], with the corresponding dark $J-V$ plots are shown as dotted lines. [b] and [d] show a summary of all device parameters with varying MoO_x thicknesses.

If the thickness of SubPc is increased further to beyond the predicted L_D , despite the predicted increase in absorption within the layer, there is a trade off with the number of excitons that are dissociated at the SubPc / ZnO interface. The model however does predict an improvement in J_{SC} with an increase in spacer layer thickness, this is

replicated in the device performance. Devices with 25 nm of SubPc show a clear improvement in J_{SC} with thicker MoO_x layers from 1.31 mA cm⁻² (10 nm) to 2.32 mA cm⁻² (40 nm) where it reaches its maximum, further increase to an 80 nm layer results in a poor J_{SC} of 0.51 mA cm⁻², shown in **Figure 5.8 [c-d]**. The overall trend in *PCE* follows the same increasing trend with 0.30 % (10 nm), 0.70 % (40 nm) and 0.15 % (80 nm), over a two-fold increase in performance with a 40 nm spacer layer. One thing to note is the *FF* of these devices, if the SubPc layer deposited is significantly thicker than its L_D , it would be expected that the *FF* would be lowered with respect to the 15 nm SubPc devices. This is not the case in this instance, suggesting that the issue with conductivity of the ZnO layer significantly impacts the device performance and is the major obstacle for improving these hybrid architectures further.

The contour plots shown in **Figure 5.9** show the comparison of **[a]** the modelled current generation with a diffusion correction to **[b]** that of the experimental J_{SC} for the 40 different cell architectures discussed earlier. When comparing these values there is a good agreement between the predicted and experimental values, with larger currents observed at SubPc thicknesses between 10 and 15 nm, and a steady improvement in current as the MoO_x thickness is increased up to ~ 40 nm. It is clear however that there is a discrepancy between the absolute values, with the model overestimating the predicted current generation for each device. This is simply because other loss mechanisms such as charge transport and charge recombination are not accounted for within the model, therefore losses can be expected experimentally.

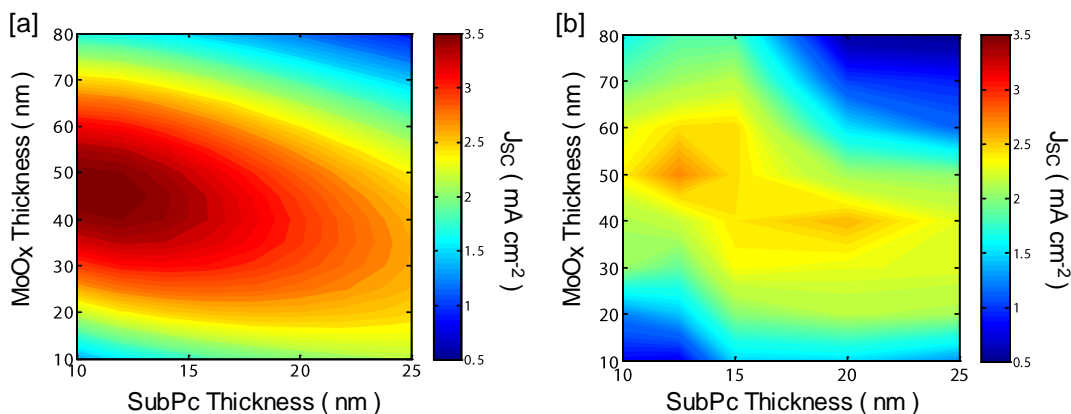


Figure 5.9 Contour plot of [a] the modelled current generation with a diffusion correction (assuming SubPc has an $L_D = 10$ nm) and [b] the experimental J_{SC} for a 40 different cell architecture with varying SubPc and MoO_x thicknesses.

Figure 5.10 [a] compares the *EQE* spectra of devices with a 15 nm SubPc layer and MoO_x layer thicknesses of 10, 40 and 80 nm. Also shown is the *EQE* response for a typical C₆₀/SubPc device and one device without the presence of an acceptor layer or dissociating interface. This device has been used as a control to show that the ZnO does in fact function as an efficient acceptor, improving the response of the SubPc donor layer. The *EQE* maximum of the fullerene-based device is in the same spectral range as the SubPc, but an additional high *EQE* response at lower wavelengths (~ 350 nm) is seen which matches the absorption of C₆₀. These devices therefore would have a higher overall current as there are two materials contributing, which span the spectral range. The peak *EQE* at approximately 590 nm varies from 19 % (10 nm) to 32 % (40 nm) to 29 % (80 nm) for ZnO/SubPc. This is a significant contribution given that the peak *EQE* is 4.8 % when no acceptor layer is present and only reaches 28 % when the efficient acceptor C₆₀ is used. When compared to the control device, there is a more than four-fold increase in *EQE* which provides good evidence for the claim that the ZnO is behaving as an efficient electron acceptor, rather than the

device exhibiting only Schottky-like behavior. The *EQE* of SubPc with a 25 nm layer is also shown, **Figure 5.9 [b]**, with MoO_x layer thickness of 10, 40 and 80 nm, the peak *EQE* varies from 20 to 27 to 9 %. The optimum *EQE* response is achieved for a 15 nm SubPc layer with a MoO_x thickness of 40 nm, with a peak at 32 % which is comparable to other D/A heterojunctions published, such as SubPc/F₁₆CuPc.²⁷¹

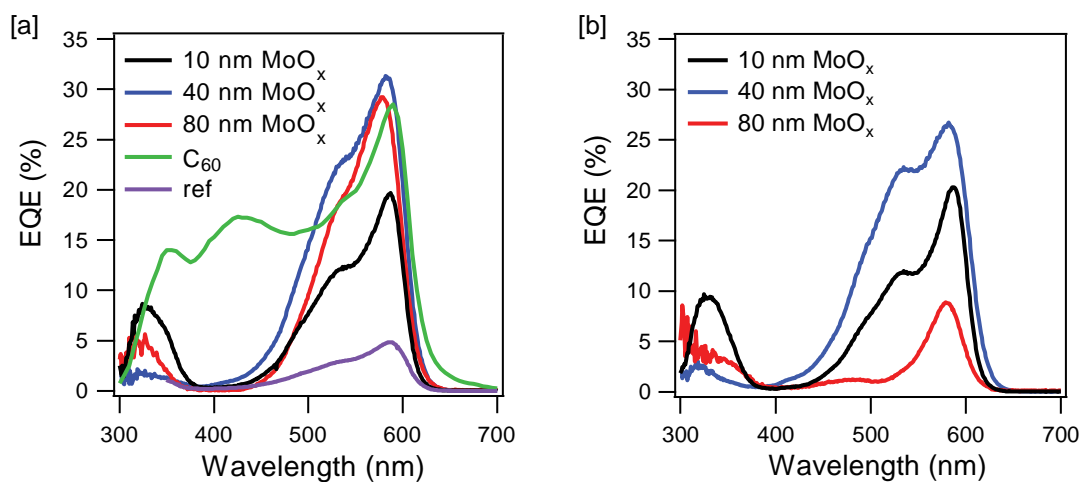


Figure 5.10 External quantum efficiency of the devices with **[a]** a 15 nm SubPc layer and **[b]** a 25 nm SubPc layer. Also shown in **[a]** is the *EQE* comparison to a C₆₀/SubPc device and a reference device without the presence of an acceptor layer. In all cases the contribution at around ~590 nm is from the SubPc layer.

5.5 Conclusion

Chapter 5 aims to address the issue of low performing hybrid organic solar cells. This is achieved through the use of the inorganic optical spacer layer MoO_x . The success of this strategy was predicted first by optical modelling and then confirmed experimentally. Optical modelling was used to predict the layer thicknesses required for optimum cell performance and the models accuracy was further improved by adding a diffusion length parameter, as without it the model simply predicts an improvement in J_{SC} with a thicker active layer.

A series of 40 devices were subsequently fabricated to compare the models predictions to the cell performance of the hybrid organic-inorganic bilayer device. The SubPc and MoO_x layers were vacuum deposited allowing for fine control of layer thickness on a sub nanometre scale. The MoO_x layers were deposited at a reduced rate (0.3 \AA s^{-1}) to ensure the thick MoO_x layers did not damage the underlying organic material. The results showed that with the use of an optical spacer layer, SubPc is shifted into its maximum optical electric field intensity, thereby achieving improved absorptance. The optimised device gave a high J_{SC} of 2.48 mA cm^{-2} and a *PCE* of 0.73 %, placing the ZnO/SubPc system in direct competition with polymer/TMO planar system, as well as nanostructured hybrid devices showing the potential of this type of hybrid cell.

6 Electron Extracting Layers

6.1 Aims

The aim of this chapter is to study the use of ZnO in the role as an electron extracting layer for both SM and polymeric active layers. Initially the commonly used vacuum deposited SubPc/C₆₀ heterojunction is investigated in a regular and inverted architecture highlighting the issues associated with using BCP in an inverted architecture. An optimised ZnO thin film is studied for its viability as an alternative material for use with SM OPV devices.

This is expanded further by investigating a polymer blend, P3HT:PCBM. This system is used as it is a well-known polymeric device which has been widely reported in the literature. The benefit of using an optimised photoactive system published elsewhere is that in controlled conditions any changes in device performance could solely be attributed to the interlayer used. In collaboration with Imperial College London, the formation of ED layers is explored as an alternative method to derive ZnO layers. The ED layer was deposited on either ITO or a transparent gold electrode that had been previously reported as a competitive electrode for the use in OPVs.²⁷² ZnO interlayers deposited either by ED or the SG process are processed on the two electrodes and the films are characterised and their performances compared.

6.2 SubPc/C₆₀ system

6.2.1 Absorption Spectroscopy

The SubPc/C₆₀ system is widely used in SM OPV cells due to the complementary absorption of the organics and the large interface gap at the D/A interface.¹⁶⁴ **Figure 6.1** shows the absorption of SubPc and C₆₀ and the corresponding transmittance of the hole transporting layer (HTL) MoO_x. The 40 nm C₆₀ layer exhibits strong absorption in both the UV (300-400 nm) and visible spectrum (up to 700 nm). Due to the high transparency of the MoO_x layer, it is not likely to negatively impact the possible J_{SC} that can be generated within the active layer.

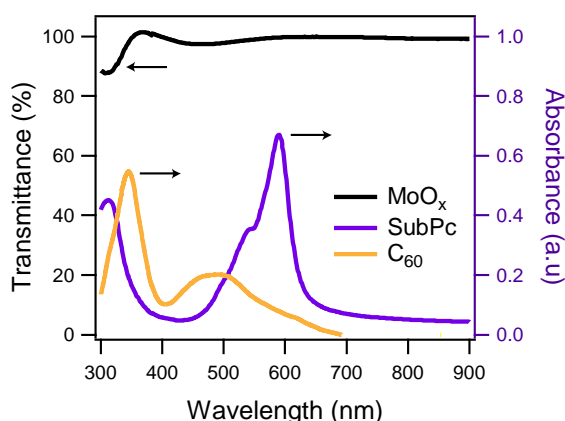


Figure 6.1 The transmission of 5 nm MoO_x layer (black line) on a quartz substrate and the absorbance of a 15 nm SubPc layer (purple line) and 40 nm C₆₀ layer (orange line).

6.2.2 Regular vs Inverted Devices

Conventionally SubPc/C₆₀ is grown in a regular device architecture utilising ITO as the hole extracting electrode. With this regular architecture, BCP is commonly used

as the exciton blocking layer and a sacrificial layer to prevent damage from the hot Al on the active layers.²⁷³ Owing to the insulating properties of BCP, a thin layer (8 nm) is necessary for optimum device performance as with thicker layers there is an increased R_S leading to a reduction in FF .^{274, 275} The deposition of Al on top of BCP is paramount to good device performance, as the deposition of Al causes defect states within the BCP which improves charge extraction and therefore performance.²⁰⁶ Alternative layers including tris(acetylacetonato)ruthenium (III) ($\text{Ru}(\text{acac})_3$), self-assembled monolayers (SAMs) or metal oxides such as TiO_x , ZnO or aluminium doped zinc oxide (AZO),²⁷³ have been suggested as alternatives as they do not require cathode induced damage for good charge transport.

The need for hot metal deposition to ensure good charge transport means there is an issue with adopting an inverted architecture when using BCP. In order to study this two cells were grown, an optimised regular: ITO / MoO_x (5 nm) / SubPc (15 nm) / C_{60} (40 nm) / BCP (8 nm) / Al and optimised inverted: ITO / BCP (8 nm) / C_{60} (40 nm) / SubPc (15 nm) / MoO_x (15 nm) / Al device. The energy diagrams and a schematic of each cell is summarised in **Figure 6.2**. The averaged J - V curves and cell performance parameters are subsequently summarised in **Figure 6.3 [a]** and **Table 6.1** respectively. It can be seen that the regular device structure shows good photovoltaic behaviour (as published elsewhere)¹³⁵ and there is no issue with charge extraction as can be seen by the relatively high FF of 0.52. The V_{OC} of 1.07 is also in line with predictions for this system, showing that there are no issues with energetic alignment at either electrode/interlayer interface. As a result a reasonable high PCE of 2.64 % is achieved.

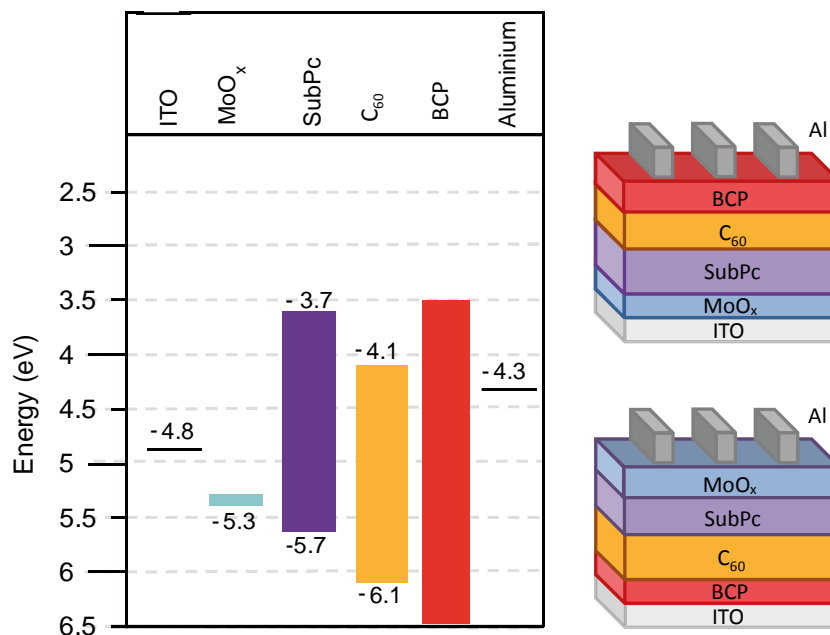


Figure 6.2 Schematic showing the energy levels for the regular device ITO / MoO_x (5 nm) / SubPc (15 nm) / C₆₀ (40 nm) / BCP (8 nm) / Al. A schematic comparing the regular and inverted architecture is also shown.

For an inverted architecture the BCP layer is deposited directly onto the ITO substrate resulting in an immediate issue with charge extraction shown by the very pronounced s-shaped kink. This kink suggests that there is charge accumulation somewhere in the device. One plausible suggestion is that electrons are being collected at a lower rate, leading to electrons being accumulated at the BCP/C₆₀ interface. This introduces a barrier for charge extraction, reducing the FF to 0.40 and the V_{OC} is subsequently reduced to 0.97, resulting in a PCE of 1.82 %. The performance of the inverted device rapidly improves as a function of exposure to AM 1.5G illumination from a solar simulator (as shown in **Figure 6.3 [b]**), showing that there is a reduction in charge build up resulting in an improvement in the FF and PCE to 0.49 and 2.08 % respectively. The organic materials however still degrade

despite being encapsulated and a reduction in J_{SC} is seen so the PCE is unable to match that of the regular device architecture.

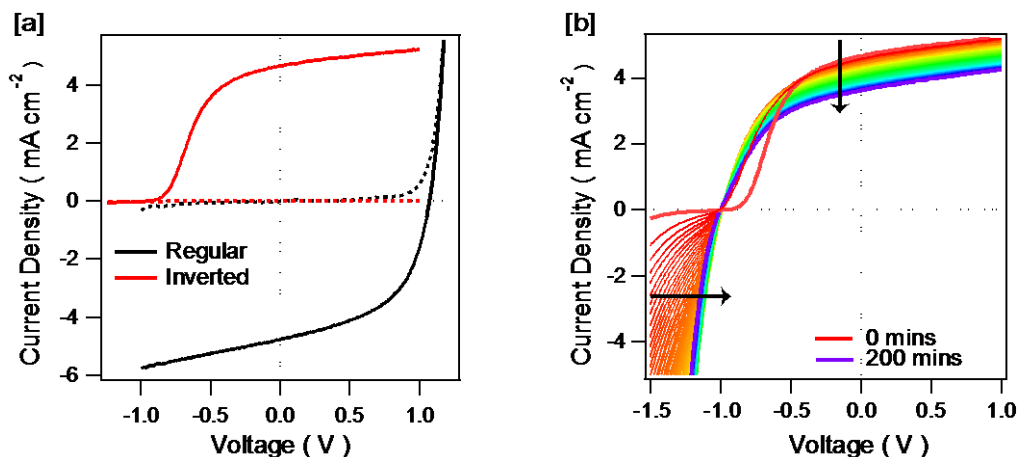


Figure 6.3 [a] J - V curves for the regular (black line) and inverted (red line) SubPc / C₆₀ device structures with the corresponding dark J - V curves (dotted lines). [b] J - V curves for the inverted devices scanning once a minute for 200 minutes. The arrows indicate the direction of parameter change with subsequent scans.

Table 6.1 Averaged device characteristics for the regular ITO / MoO_x (5 nm) / SubPc (15 nm) / C₆₀ (40 nm) / BCP (8 nm) / Al and inverted ITO / BCP (8 nm) / C₆₀ (40 nm) / SubPc (15 nm) / MoO_x (15 nm) / Al device architecture. The performance characteristics of the inverted architecture after 30 minutes and 200 minutes degradation are also shown.

Architecture	Time (mins)	J_{SC} (mA cm ⁻²)	V_{OC} (V)	FF	PCE (%)
Regular	0	4.76	1.07	0.52	2.64
Inverted	0	4.68	0.97	0.40	1.82
Inverted	30	4.35	0.99	0.49	2.08
Inverted	200	3.62	1.00	0.45	1.65

6.2.3 ZnO as an ETL

In order to function as an effective transport layer, there are many desirable properties the interlayer must have such as high transparency, low cost, scalability and the correct energetics. As discussed earlier and shown through the implementation of MoO_x as an optical spacer in **Chapter 5**, metal oxides are a promising alternative to organic interlayers such as BCP. ZnO is a good candidate as it provides good energy alignment with C₆₀, can be processed by a range of methods and exhibits a relatively high transparency regardless of film thickness. In this chapter the ZnO layer was formed from a 0.25 M ZnO solution in 2-propanol, with an optimised layer produced at a spin speed of 5000 rpm. The film was subsequently annealed at 160 °C for 1 hour and allowed to cool slowly to room temperature prior to deposition of the active layers.

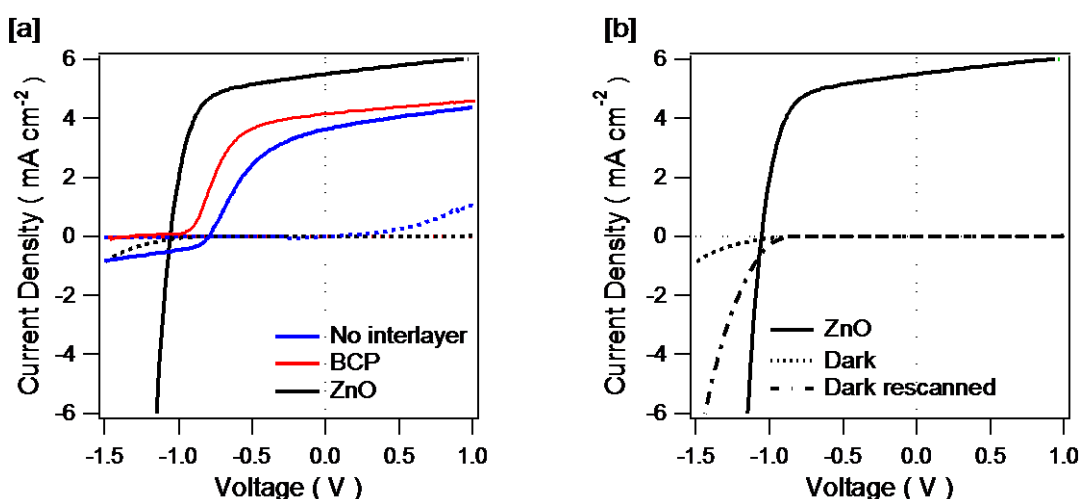


Figure 6.4 [a] Averaged J - V curves showing a comparison of the various electron extracting layers: no interlayer (blue solid line), BCP (red solid line), and ZnO (black solid line), the corresponding dark curves are also shown (dotted lines) and [b] ZnO (black solid line) and the dark J - V plots, initial (dotted line) and the dark J - V after exposure to light (dashed line).

Figure 6.4 [a] and **Table 6.2** show a performance comparison between inverted devices using the optimised ZnO layer to that of a bare ITO substrate and the BCP interlayer from the same batch of devices to reduce any variation due to external factors. If the electron acceptor, C₆₀, is deposited directly onto the ITO substrate, the cell performance is significantly lowered across all device parameters. The V_{OC} is lowered to 0.82 V due to a large energetic mismatch between the work function of ITO and the electron affinity of the C₆₀ acceptor. This results in a significant barrier for charge extraction with a reduced FF and thus a J_{SC} of only 3.05 mA cm⁻². If BCP is used the performance is similar to that discussed previously, with a lower FF , V_{OC} and in this instance the J_{SC} is lower at 3.90 mA cm⁻². The use of an optimised ZnO layer results in a significantly higher cell performance due to a J_{SC} of 5.37 mA cm⁻² and a FF of 0.65. It must be noted that there is an issue however with the behaviour of the cells dark curves, with the J - V dark curve showing little diodic behaviour at negative bias. This occurs across all the SG processed ZnO interlayers used in this section, and exists only until the device is illuminated, shown in **Figure 6.4 [b]**. When the dark curve is rescanned after exposure to light a more typical diodic behaviour is seen, likely due to an improved mobility of the ZnO film after light exposure.

Table 6.2 Averaged device characteristics for the inverted device: ITO / interlayer (varied) / C₆₀ (40 nm) / SubPc (15 nm) / MoO_x (15 nm) / Al.

Interlayer	J_{SC} (mA cm⁻²)	V_{OC} (V)	FF	PCE (%)
None	3.05	0.82	0.43	1.07
BCP	3.90	1.01	0.46	1.77
ZnO_{160 °C}	5.37	1.05	0.65	3.42

6.3 ZnO with polymer blend

6.3.1 Transparent Conductive Electrodes

To function as a TCE, the material should have a low sheet resistance, high transparency and ideally be applicable to large scale manufacture. To date, ITO is the electrode of choice for most optoelectronic devices due to high carrier concentration and high transparency across the visible and near infrared spectral range. ITO has been produced from a wide range of methods including magnetron sputtering and ion beam sputtering to produce smooth, high quality films. Indium, the principal material of ITO, is scarce and costly (due to high demand), with a recent study by Azzopardi *et al.* attributing most of the material cost (> 31 %) due to the ITO electrode alone.¹¹⁴ The impact of this is that the long term demand for ITO for all optoelectronic applications may be difficult to meet.^{276, 277}

Aside from cost, ITO is not without its problems. There are issues when considering flexible OPVs attributed to the brittle nature of conductive oxide electrodes,²⁷⁸ poor energetic alignment with many organics, and the incompatibility with some methods of film production. High temperature annealing is a key step for the majority of methods for achieving low sheet resistances. This however is not viable for flexible polyethylene terephthalate (PET), so the resulting sheet resistance typically is > 60 Ω sq⁻¹. With all this in mind there has been a strong research drive to present viable alternatives. These include AZO (which is lower in cost but still has issues with mechanical flexibility),^{279, 280} conductive polymers,^{22, 127} graphene,^{281, 282} carbon nanotubes²⁸³ and metal grids.²⁸⁴

Stec *et al.* have investigated the use of 8 nm thick Cu, Ag, Au and Cu/Ag bilayer electrodes on either glass or flexible PET and PEN substrates.^{272, 285} In these studies, evaporation of atmospherically stable metals is suggested as a simple alternative to ITO. One of the issues associated with the use of metals is their highly absorbing nature, which can be somewhat addressed through the use of randomly distributed micrometer-sized apertures improving the overall transparency.

6.3.2 Deposition Techniques

Two ZnO deposition methods were compared; ED and SG. These films were processed on two TCEs, ITO (Psiotec or Thin Film Devices) and ultrathin gold electrodes on glass (tAu). Transparent Au (tAu, $\sim 11 \Omega \text{ sq}^{-1}$) electrodes were supplied that were formed using a mixed mono-layer of the molecular adhesives 3-aminopropyltrimethoxysilane (APTMS) and 3-mercaptopropyltrimethoxysilane (MPTMS), with 8.4 nm of Au deposited on top at a rate of 0.1 nm s^{-1} .²⁷² For the SG process a ZnO film was prepared following the method discussed in **Section 6.2.3** to give two different substrates, one on the ITO electrode (ITO / ZnO_{SG}) and the other using tAu (tAu / ZnO_{SG}).

ED was carried out using a method previously published elsewhere¹⁸⁶ which has been discussed in detail in **Section 2.1.2.3**. This process again generated two different ZnO films, one using ITO as the working electrode (ITO / ZnO_{ED}) and the other using tAu (tAu / ZnO_{ED}). It should be noted here that a different ITO supplier was used for the ED process; this is because longer substrates were required in order for an electrical contact to be attached to the top of the substrate. Following

deposition, the substrate was then cleaved to match the area of the ITO and tAu substrates used in the SG process.

6.3.3 Transmittance

The transparencies of each of the four layers are compared in **Figure 6.5**, with reference to each electrode. The ITO / ZnO_{SG} layer has a high transparency (> 90 %) across the visible range, greater than that of the electrode due a change in refractive index causing the film to be antireflective. Film production via ED results in a much thicker layer (necessary to ensure complete coverage) and thus negatively impacts the transparency of the layer, which peaks at 520 nm with a transparency of 87 %. The estimated E_g from is shown in the inset of **Figure 6.5 [a]/[b]**, with the two different methods giving an E_g of 3.20 eV and 2.97 eV for ITO / ZnO_{SG} and ITO / ZnO_{ED} respectively.

Transparency is one of the main limitations for the use of tAu in OPVs, which remains < 60 % across the majority of the visible spectrum. The highly absorbing nature of gold means that despite only an 8.4 nm layer, the number of photons that can be absorbed is still limited, lowering the J_{SC} . Similarly to the ITO electrode, tAu / ZnO_{SG} has an increased transparency owing to optical reflections when compared to the reference. The E_g is estimated in the inset, giving 3.20 eV and 2.94 eV for tAu / ZnO_{SG} and tAu / ZnO_{ED} respectively, similar to the values obtained for each on ITO.

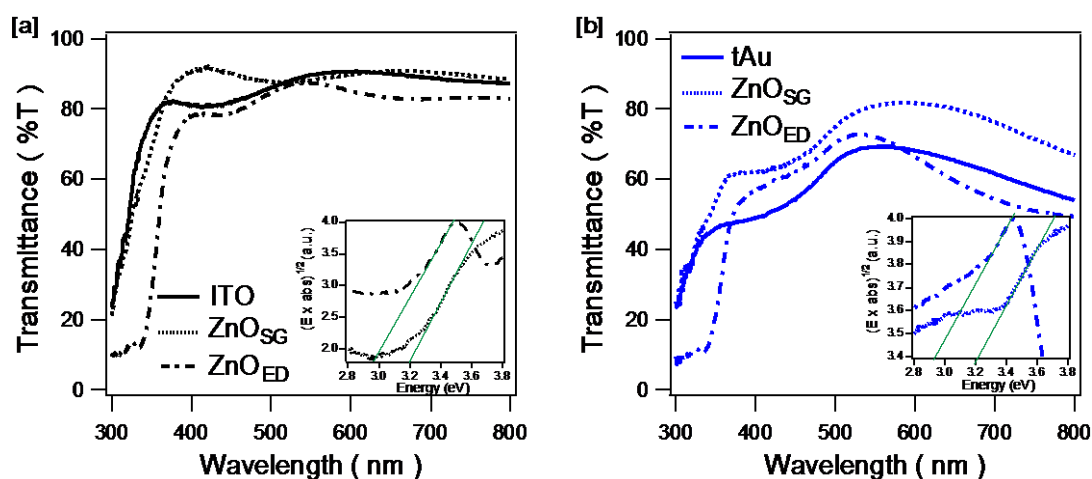


Figure 6.5 Transmittance data shown for [a] an ITO substrate, SG derived ZnO layer and ED film and [b] a tAu electrode, and the electrode with a SG or ED ZnO layer. For all ZnO films, the E_g has also been calculated by plotting $(E \times \text{abs})^{1/2}$ as a function of energy (eV) and is shown in the insets.

6.3.4 Surface Morphology and Conductivity

6.3.4.1 Electrodes

The surface morphology of each layer was investigated using contact mode AFM with CAFM used to study the difference in surface conductivity across each of the electrodes. **Figure 6.6** shows simultaneously obtained topography images and current distribution maps along current and height cross-sections for ITO (supplied by Thin Film Devices, ITO_A), ITO (supplied by Psiotec, ITO_B) and tAu. These three electrodes were cleaned using the typical four-stage cleaning process and exposed to ozone for 30 minutes. The films were then left to stand in air for one hour. The surface roughness of 2.3 nm, 4.8 nm and 2.3 nm was measured for ITO_A, ITO_B and

tAu respectively. In this instance the Psiotec substrates (ITO_B) had a larger surface roughness with platelets of the ITO visible in **Figure 6.6 [b]**. The ITO_A and tAu electrodes however had a smooth continuous morphology which can be seen in **Figure 6.6 [a]** and **[c]**.

High, continuous electrode conductivity is paramount for OPV devices to ensure effective charge collection and to lower any resistive issues. It is also a necessary parameter for the ED as the process relies on the substrate conductivity for film formation. **Figure 6.6** shows the current distribution maps for **[d]** ITO_A, **[e]** ITO_B and **[f]** tAu electrode. The maps for all films were acquired whilst applying the same +100 mV bias, indicating that any changes in surface conductivity is due to the electrode. It can be clearly seen that there is a large variation in surface conductivity, with some areas of little or no conductivity and other areas showing the conductive nature in all electrodes. The distribution of current is significantly different between samples. For ITO_A the variation of current is lower, with the majority lying close to 200 pA, with only 8.9 % of the film having a current of less than 50 pA. For ITO_B however, the range is much greater with a significant proportion of the surface exhibiting low surface conductivity (57.4 % of the surface is below 50 pA). From the cross-section it is clear that there is no relation between surface conductivity and topography. For the tAu substrate there are several raised features on the films surface that exhibit poor conductivity.

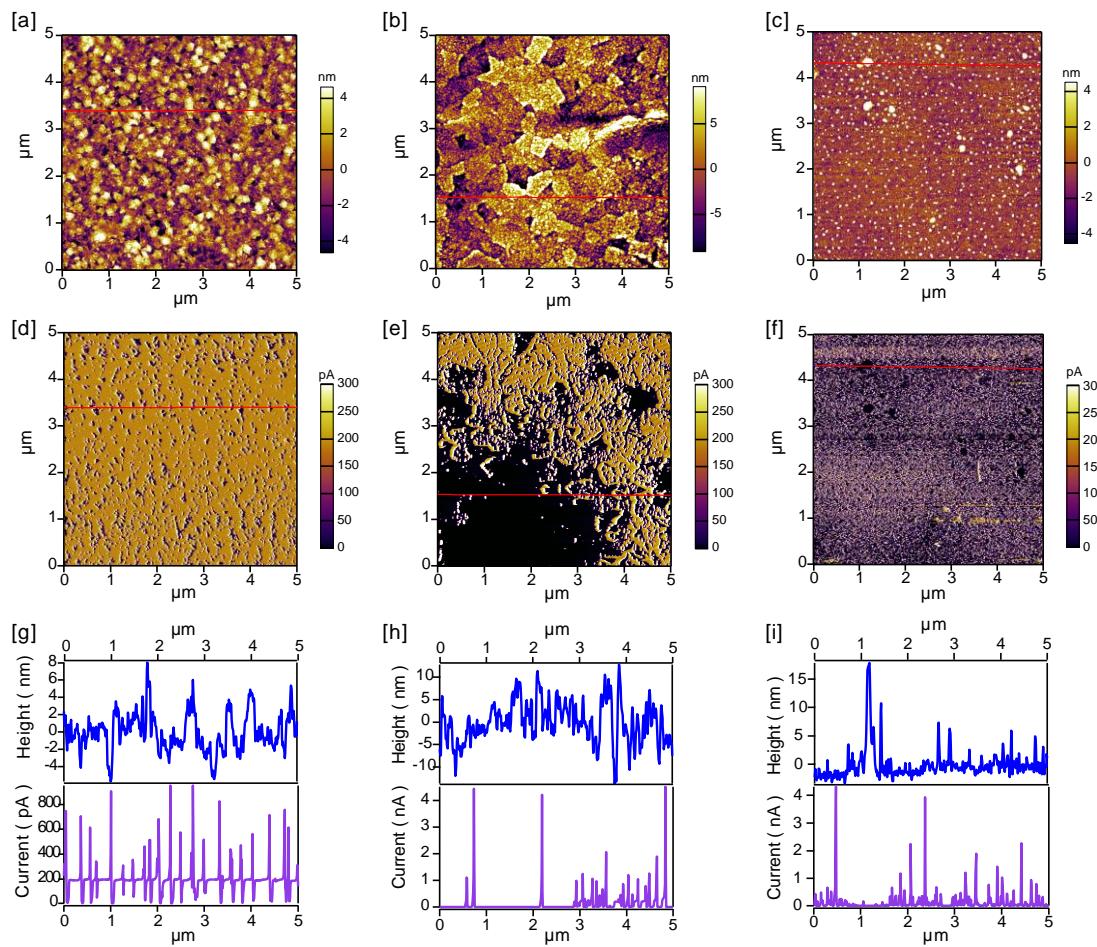


Figure 6.6 Topographic AFM images of **[a]** ITO (Psiotec, ITO_A), **[b]** ITO (Psiotec, ITO_B) and **[c]** tAu and corresponding current distribution maps at +100 mV bias for **[d]** ITO_A, **[e]** ITO_B and **[f]** tAu. A cross section of both topography and current distribution is shown in **[g]** ITO_A, **[h]** ITO_B and **[i]** tAu.

6.3.4.2 *Impact of Ozone Exposure*

Conductivity is introduced to indium oxide (InO) (a wide bandgap insulator) via interstitial tin dopants and removal of oxygen from the InO lattice. This can result in non-uniform reactivity and doping of the ITO substrate, leading to variations in electrical properties. Armstrong *et al.* have used CAFM to look at the issues associated with this and the impact of the cleaning process.^{116, 286} The authors studied the existence of contamination layers, as clean ITO has been found to have high reactivity to H₂O and common surface contaminants, which leads to variations across the ITO surface.^{287, 288} The study found that samples that were detergent/solvent cleaned had only 10 – 20 % of the surface with a current greater than 0.5 nA (with -1 V bias applied), but noted that the conductivity varied significantly between samples. The conductivity was shown to greatly improve either with oxygen plasma or acid treatment; however despite enhanced electrical activity this was only short lived.

Figure 6.7 shows a similar study with ITO_B subject to the same four-stage cleaning process, but one substrate was exposed to air for one hour and the other substrate had been freshly exposed to ozone. The topography shows minimal difference in surface roughness measured (4.8 nm and 4.4 nm). Histograms for both films are also shown and as discussed previously ITO_B has a large proportion of the film with a surface current below 100 pA (61 %). Also seen in the histogram is another peak at ~ 200 pA, showing there is a proportion of the film that is significantly more conductive. For the film freshly exposed to ozone, the majority of the film has a higher surface conductivity, with only 10.2 % of the surface having a current less than 400 pA. The current distribution maps show despite the ozone treatment, there are still sections of

the film that are effectively dead spots, with little or no conductivity (3.9 % below 100 pA). This improvement in conductivity with exposure to ozone is unsurprising and is consistent for all the substrates used in this study.

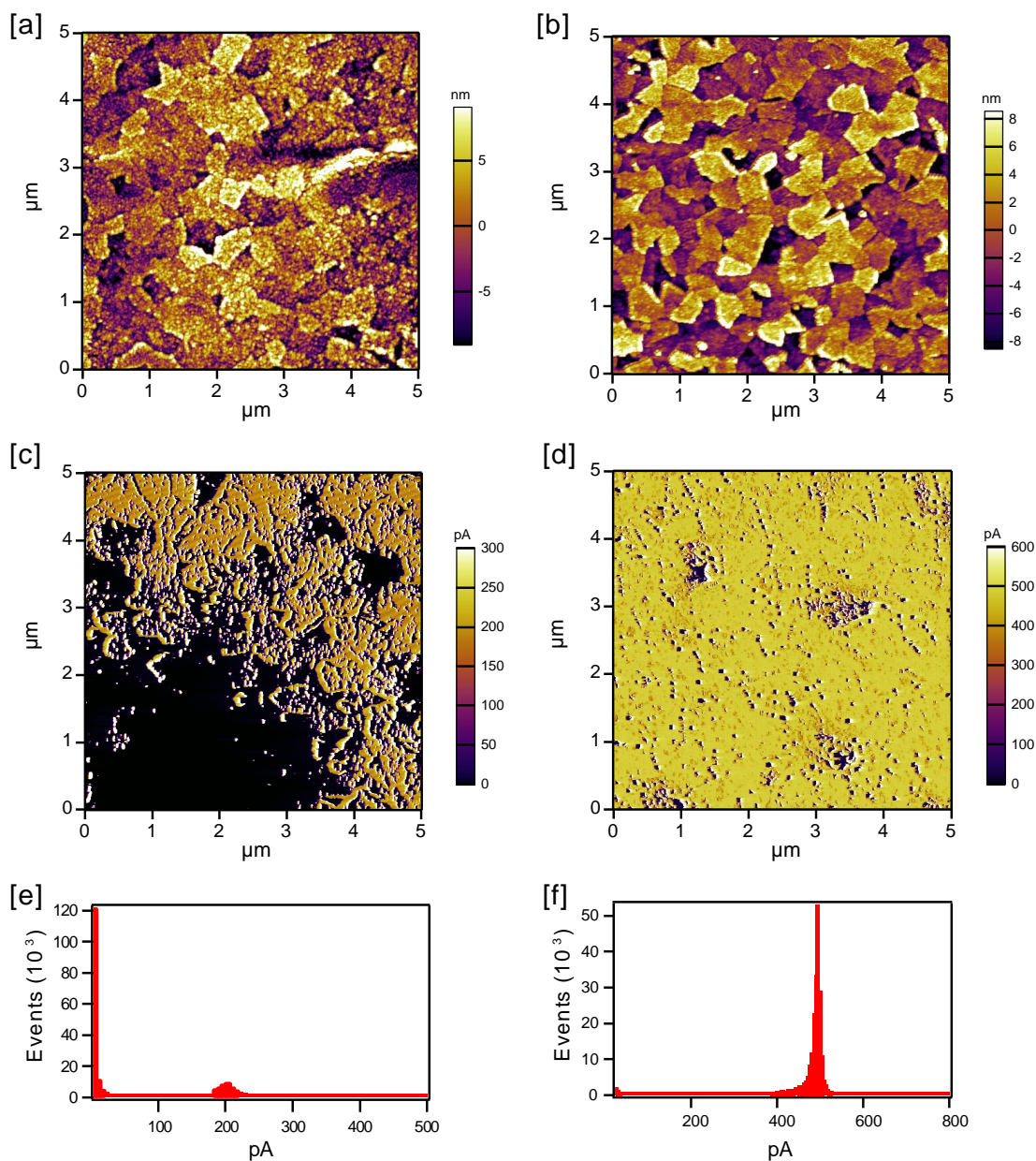


Figure 6.7 Topographic AFM images of [a] ITO_B and [b] ITO_B immediately after exposure to ozone. Current distribution maps are also shown, with a bias of 100 mV for [c] ITO_B, and 200 mV for [d] ITO_B film freshly exposed to ozone. Histograms are also shown [e] and [f].

6.3.4.3 CAFM of ED ZnO films

The electrode shown in **Figure 6.7** is placed into a 0.13 M $\text{Zn}(\text{NO}_3)_2$ solution maintained at 85 °C for the ED process. As it is clear that the surface conductivity can be lowered substantially just leaving the film in air, it is therefore apparent that method for ZnO deposition is going to be faced with some issues, with the surface conductivity altering dramatically prior to ZnO deposition. Small changes in timescales between cleaning and ED are likely to directly impact the ZnO films formed.

Figure 6.8 shows the topography AFM and current distribution for both the ED films (with a +500 mV bias applied). For the ITO / ZnO_{ED} the surface roughness of the film is 23 nm. One plausible reason for this high roughness is the changes in conductivity of the various sections/faces of the ITO substrate causing the deposition to be inhomogeneous. Due to the polycrystalline nature of ITO, the growth of the ZnO layer is likely to differ depending on surface conductivity and the orientation and crystallinity of the ITO. This results in areas of the sample where there is no growth of the ZnO layer, likely to be due to the dead spots on the ITO substrate. This can be seen more clearly in the SEM image in the inset of **Figure 6.8 [a]** which shows an area with dead spots where there is no growth of the ZnO layer and the underlying ITO substrate can be seen. The rough surface is also highlighted in the cross section, showing height variation of up to 70 nm, which may hinder the performance of the OPVs. The current distribution for ITO / ZnO_{ED} is shown in **Figure 6.8 [c]**, with an average current of 105 pA. There is a variation in surface conductivity but this occurs consistently across the film with no large areas of poor conductivity.

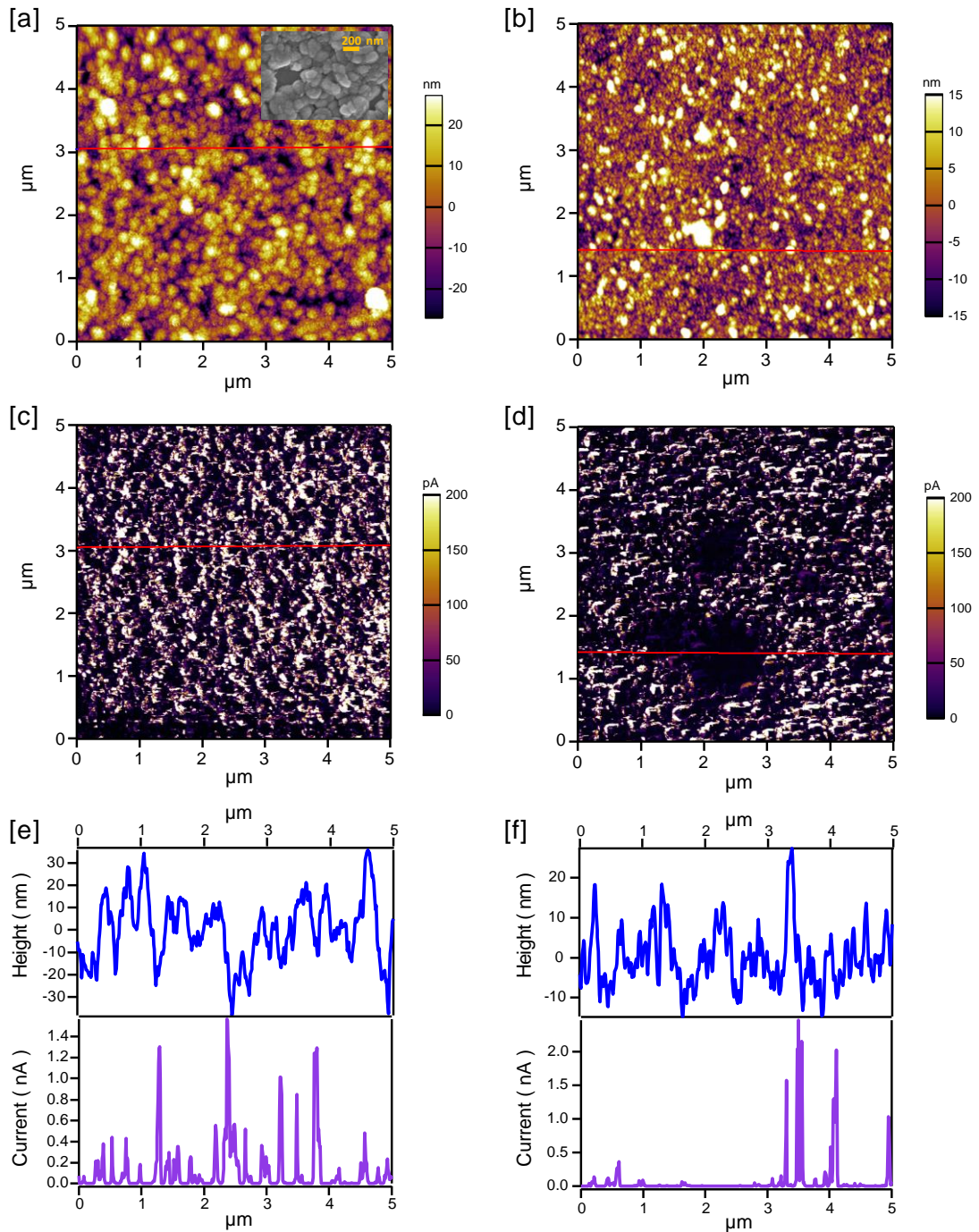


Figure 6.8 Topographic AFM images of [a] ITO_B/ZnO_{ED} and [b] tAu/ZnO_{ED} and current distribution maps are also shown, with a bias of +500 mV applied for [c] ITO_B/ZnO_{ED}, and [d] tAu/ZnO_{ED}. A cross section of both topography and current distribution is also shown in [e] ITO_B/ZnO_{ED} and [f] tAu/ZnO_{ED}. The inset in [a] shows an SEM image of ITO_B/ZnO_{ED} with holes through to the substrate.

For the tAu, owing to its smooth surface and consistently high conductivity across the film, this is likely to aid the deposition of ZnO and the result can be seen in topography image of tAu / ZnO_{ED} in **Figure 6.8 [b]**. The deposition of ZnO is consistent across the film, and the film has a much lower surface roughness of 7.6 nm, with smaller crystallinities when compared to **Figure 6.8 [a]**. However despite a lower overall surface roughness the tAu / ZnO_{ED} film has issues with conductivity. This can be seen in **Figure 6.8 [d]** and this is a key feature at various locations across the substrate. These large area ($\sim 1 \mu\text{m}^2$) dead spots do not relate to any change in morphology, more clearly seen in **Figure 6.8 [f]**. The inconsistency in surface conductivity of the tAu / ZnO film results in 80 % of a film with a current below 50 pA for this section of the film.

6.3.4.4 *CAFM of sol-gel derived ZnO films*

The variation of surface conductivity for the SG derived films on ITO_A and tAu has also been studied and the results are shown in **Figure 6.9**. Owing to the low conductivity of the films generated by the SG process a +2 V bias was required for both films. The topographic image of ITO / ZnO_{SG} has a nanoridged structure, resulting in a surface roughness of 3.8 nm. The interesting feature is that the current distribution map also exhibits a nanoridged structure with variation in conductivity; the areas of high/low current however differ to the topography image. On average the features of the film with a large height appear to have a lower conductivity; this however is not consistent for the entire film. The average current for this film was measured at 58 pA. It can also be seen from the histogram in **Figure 6.9 [g]** that there is a high proportion of the film with low current ~ 20 pA. There is also a

variation in surface conductivity with only 20 % of the film having a current greater than 200 pA.

The surface roughness for the tAu / ZnO_{SG} is lower at 1.2 nm showing a smoother film formation when using the tAu with no pronounced nanoridged structure seen. The histogram for the tAu substrate however differs with a much lower average current of 44 pA. In this instance, only 0.5 % has a current greater than 200 pA. This shows that even though the films appear to have no distinctive differences in topography, the conductivity is influenced by the underlying substrate. This is not entirely surprising, as the way in which a SG derived film is formed depends heavily on the surface properties of the underlying layer.

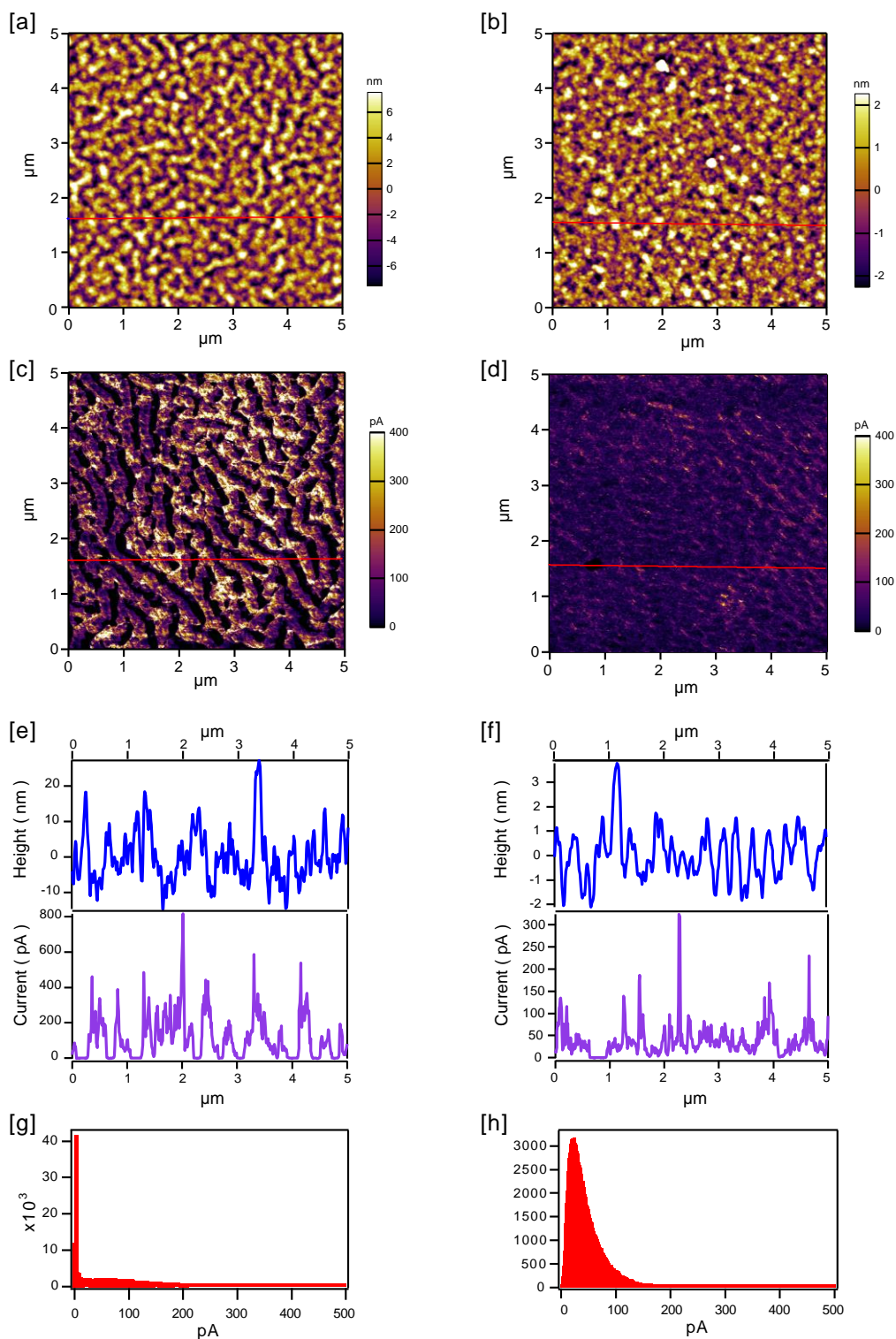


Figure 6.9 Topographic AFM images of [a] ITO_A/ZnO_{SG} and [b] tAu/ZnO_{SG} along with current distribution (+2 V bias) for [c] ITO_A/ZnO_{SG}, and [d] tAu/ZnO_{SG}. Cross section of both topography and current distribution are shown in [e] ITO_A/ZnO_{SG} and [f] tAu/ZnO_{SG} with histograms of current distributions for [g] ITO_A/ZnO_{SG} and [h] tAu/ZnO_{SG}.

6.3.5 Structural Characterisation

The XRD data obtained for both substrates with and without the ED layer is shown in **Figure 6.10**. The SG derived layers have not been shown as due to poor crystallinity only the peaks corresponding to the underlying substrate were seen. For the ED layers, the substrate peaks have been indicated by an asterisk. The XRD data for the ITO electrode shows polycrystalline behaviour, with a (222) preferred orientation (JCPDS 01-076-0152). For the gold substrate however, the XRD indicates one orientation (111) (JCPDS 00-004-0784).

When the ZnO layers are deposited on top of the ITO_B and tAu electrodes, the growth is multidirectional showing that the film is polycrystalline regardless of the underlying electrode. The preferred orientation for both is the same (002), however the textured coefficients differ with each orientation; this is shown in **Table 6.3**. The table shows the peaks which have been identified as Wurtzite ZnO (JCPDS 01-080-0074) and the textured coefficients (TC) for each ZnO reflection. The texture coefficient has been calculated from the following:

$$TC(hkl) = \frac{I(hkl)}{I_0(hkl)} / \frac{1}{n} \sum \frac{I(hkl)}{I_0(hkl)} \quad \text{Equation 6.1}$$

$TC(hkl)$ is the texture coefficient of each specific plane (hkl), $I(hkl)$ is the measured intensity, $I_0(hkl)$ is the relative intensity factor of the JCPDS and n is the number of peaks that have been considered.²⁸⁹ As shown in **Table 6.3** the ZnO polycrystalline film consists of significant non polar (100), (101) and polar (002) faces.

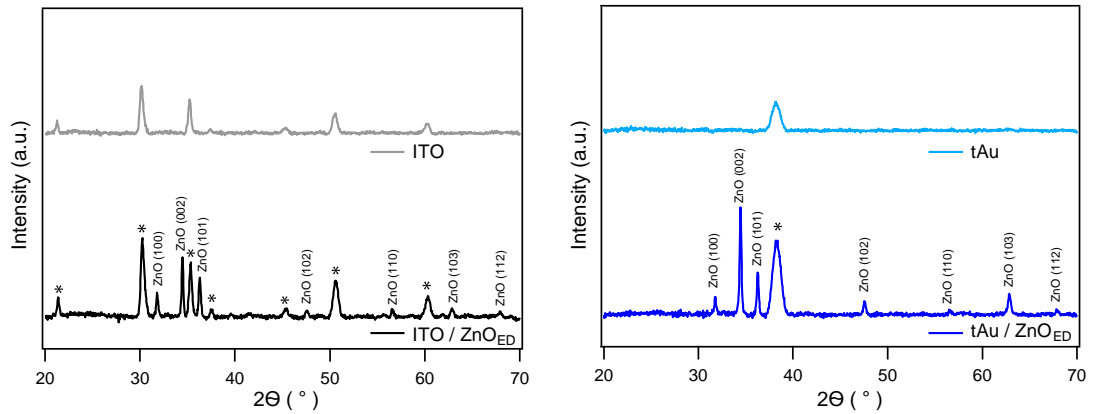


Figure 6.10 XRD of the ITO / ZnO_{ED} film (black solid line) and the tAu / ZnO_{ED}. For reference the XRD of the substrates is also shown and subsequently for the ED layers the peaks corresponding to the substrate have been indicated with an asterisk.

Table 6.3 TC values for the ED ZnO films showing the differences in crystal plane orientation showing the Miller indices (*hkl*) and the peak positions (2θ (°)). The ZnO TC values were calculated using Wurtzite ZnO (JCPDS 01-080-0074).

ZnO reflection (<i>hkl</i>)	2θ (°)	Texture Coefficient (<i>TC(hkl)</i>)	
		ITO B-ED ZnO	tAu B-ED ZnO
100	31.8	0.90	0.29
002	34.5	2.93	2.39
101	36.3	0.82	0.39
102	47.5	0.67	0.57
110	56.6	0.50	0.11
103	62.8	0.70	0.73
112	68.0	0.49	0.24

6.3.6 Compositional Differences

To understand any differences in composition of the ZnO thin films, XPS data was obtained for each thin film. The Zn and O spectra have been summarised in **Table 6.4** which shows the difference between the Zn : O ratio for both the oxygen bound to zinc in the lattice (O 1_{SA}) and the oxygen corresponding to impurities trapped within the film (O 1_{SB}). **Figure 6.11** shows the O 1s spectra for each film, with the ZnO O 1_{SA} (red peak) at 530.0 eV and the O 1_{SB} (green peak) at around 531.0 eV. The O 1_{SB} peak has a broader FWHM (~1.95) due to the overlap for each of the species present which cannot be individually identified. The measured counts are shown by the grey line with the corresponding envelope shown by the dotted black (ITO) and blue (tAu) lines.

The Zn 2p_{3/2} : O1_{SA} ratio remains constant with electrode despite deposition method. For the ITO substrates the ratio is ~1 : 0.70 for both SG and ED layers whereas when the tAu electrode is used, the films are more oxygen deficient, and ZnO is produced has a Zn 2p_{3/2} : O1_{SA} ratio of ~1 : 0.60. This is a subtle but noticeable difference between the two electrodes. The contaminants levels however show a significant difference in the Zn 2p_{3/2} : O1_{SB} ratio which is related to the deposition method, with SG giving a ratio of ~1 : 0.65 on both electrodes whereas ED has a ratio > 1 : 1.00. The high O1_{SB} components are not entirely surprising, owing to the methods of deposition for each ZnO thin film. For the SG process impurities are mainly due to surface contaminants with some contribution caused by reagents being trapped within the film. For the ED however the process involves dipping the substrate into a 0.13 M Zn(NO₃)₂ held at 85 °C. Despite this being a successful low temperature method leading to high film crystallinity without the need of thermal annealing, it

does however mean contaminants can be readily trapped at the films surface. Fryar *et al.* investigated the effect of fluid layers on different terminated ZnO faces and found the ZnO can stabilise thick fluid layers on its surface which are then difficult to remove merely by drying.²³³ In particular, the O-terminated surface is hydrophilic so electrons in the dangling bonds on the face can react strongly with H⁺ ions. XPS is surface sensitive and therefore further analysis would be necessary to investigate any change in stoichiometry with film depth.

Table 6.4 A summary of the binding energies (eV), FWHM and compositions (%) for the Zn 2p_{3/2} and O1s contributions as shown above in **Figure 6.11**. This first table shows the two SG derived layers; ITO / ZnO_{SG}, tAu / ZnO_{SG} and the second table shows the ED layers; ITO / ZnO_{ED} and tAu / ZnO_{ED}.

	ITO SG			tAu SG		
	eV	FWHM	%	eV	FWHM	%
Zn 2p _{3/2}	1021.3	1.60	43.6	1021.4	1.57	43.7
O 1s _A	529.9	1.15	29.6	529.9	1.19	25.8
O 1s _B	531.3	1.97	26.8	531.5	1.73	30.5
Zn 2p _{3/2} : O 1s _A			1 : 0.68			1 : 0.59
Zn 2p _{3/2} : O 1s _B			1 : 0.62			1 : 0.70

	ITO ED			tAu ED		
	eV	FWHM	%	eV	FWHM	%
Zn 2p _{3/2}	1021.4	1.63	25.9	1021.4	1.55	28.5
O 1s _A	530.0	1.13	17.8	530.0	1.04	26.6
O 1s _B	531.5	1.88	31.9	531.4	2.15	28.6
Zn 2p _{3/2} : O 1s _A			1 : 0.69			1 : 0.58
Zn 2p _{3/2} : O 1s _B			1 : 1.23			1 : 1.01

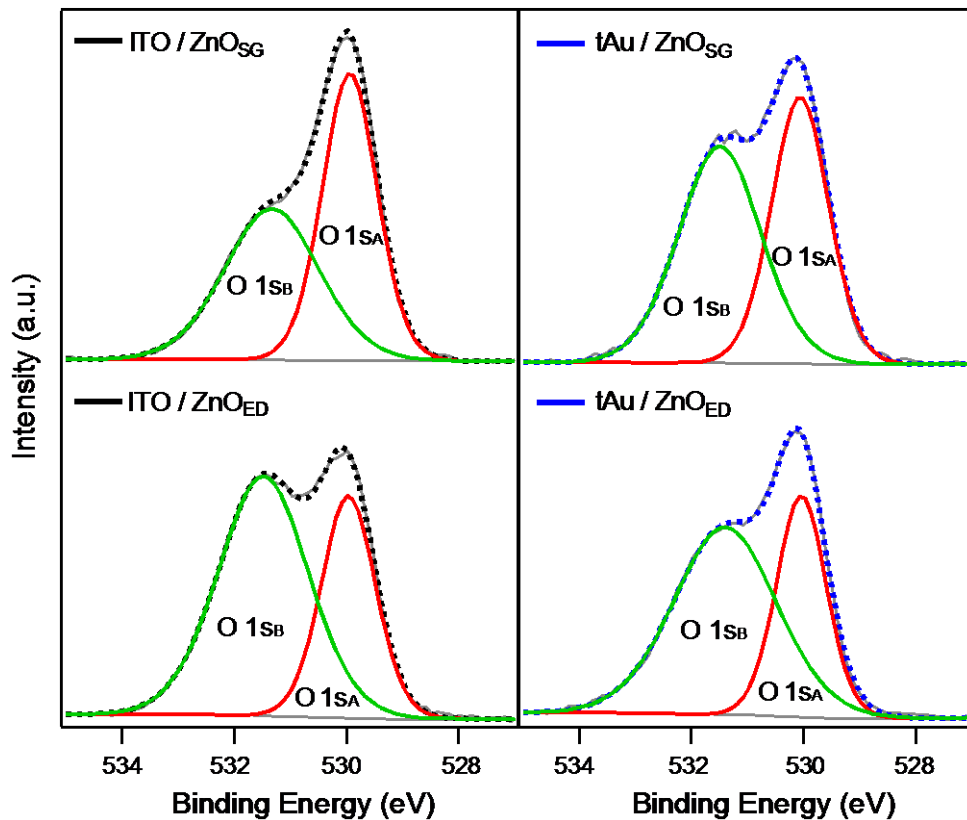


Figure 6.11 XPS spectra of O 1s showing it is composed of two species, the red peak is O 1s_A (bound ZnO) and green peak is of the O 1s_B (contaminants).

6.3.7 Work function measurements

In order to understand the differences between the processing methods in terms of the electronic properties of the thin films, UPS measurements were carried out. The films were prepared *ex-situ* and loaded into a UHV system. The UPS spectra for each of the four films are shown in **Figure 6.12**. As chemisorbed species on the surface can alter the electronic properties, ideally the surface would either be prepared in a UHV environment, or undergo polishing and annealing steps to ensure

any contaminants were removed from the films surface. This however is not applicable for solution processed thin films due to the severity of this cleaning preparation step. Uhlrich *et al.* investigated impact of ozone exposure, and annealing polar and non-polar ZnO single crystals and found that annealing could result in a change in ionization potential > 0.4 eV.²⁹⁰

It is apparent from the UPS measurements that for the SG process the values are consistent for each substrate and are similar to those measured in **Chapter 4**. For both ITO / ZnO_{SG} and tAu / ZnO_{SG} the work function of the measured layers is 3.80 eV and the VB onset a further 3.90 eV from the E_{Fs} giving a VB position of 7.70 eV. However, for the ED layers the work function of each film differs with a work function of 3.95 eV and 3.50 eV for ITO / ZnO_{ED} and tAu / ZnO_{ED} respectively. The VB onset also differs with a value of 5.10 eV (ITO / ZnO_{ED}) and 5.40 eV (tAu / ZnO_{ED}) below the E_{Fs} . As a result the VB positions measured are very similar at 9.05 eV on an ITO substrate and 8.90 eV on a gold electrode. This deeper VB is in line with measured values recorded for a range of ZnO thin film production methods published elsewhere,^{36, 62} and is summarised schematically in **Figure 6.12**. Due to the instability of the ZnO under UV light highlighted in **Chapter 5**, it should be noted that there is some uncertainty surrounding these values due to the subtle changes in surface contaminants (likely to be removed under UV light) which can have a dramatic impact on the values recorded during UPS. To minimise these issues, all samples were subjected to the same conditions before loading with a bias of 10.0 V in order to give a direct comparison between each film.

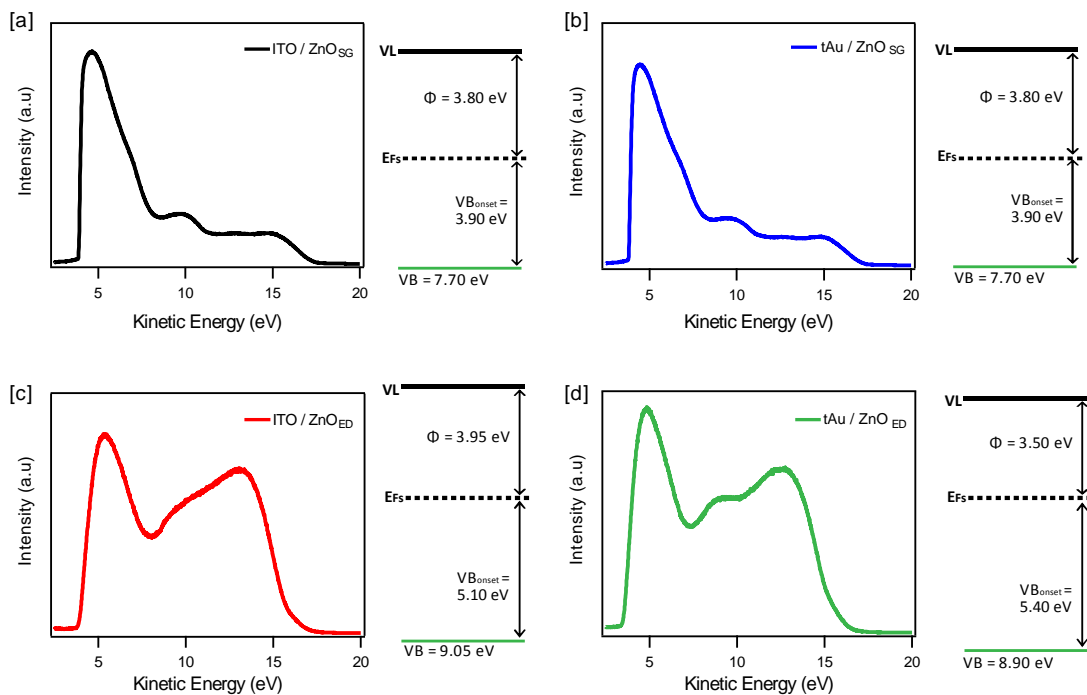


Figure 6.12 UPS spectra for [a] ITO / ZnO_{SG}, [b] tAu / ZnO_{SG}, [c] ITO / ZnO_{ED} and [d] tAu / ZnO_{ED}. A schematic is also shown for each to highlight the differences in measured energy levels.

6.3.8 Device Performance

The inverted polymer devices, electrode ITO/tAu / ZnO_{SG/ED} / P3HT:PCBM / WO_x (10 nm) / Al were fabricated. WO_x was used in this instance due to improved energy level alignment with the polymeric donor P3HT. For the polymer blend, 20 mg of both P3HT and PCBM were dissolved in 1 ml of 1,2-dichlorobenzene in a nitrogen filled glove box and left to stir overnight. A filtered solution (0.20 μm, PTFE filter) was spin coated onto the previously prepared substrates (ITO / ZnO_{SG}, ITO / ZnO_{ED}, t-Au / ZnO_{SG}, t-Au / ZnO_{ED}) at 1000 rpm, slow dried at room temperature under a petri dish and then annealed at 140 °C for 20 minutes. WO_x was vapour deposited using a Kurt J. Lesker Spectros system onto the prepared films followed by an Al top

contact through an electrode shadow mask, giving an active area of 0.06 cm^2 . An active area of 0.06 cm^2 was used due to the inconsistency of the ITO / ZnO_{ED} film formation and to reduce the likelihood of pixels shorting. All devices were tested under a nitrogen atmosphere in a sealed sample holder. The device architecture is shown schematically for each of the two electrodes in **Figure 6.13**.

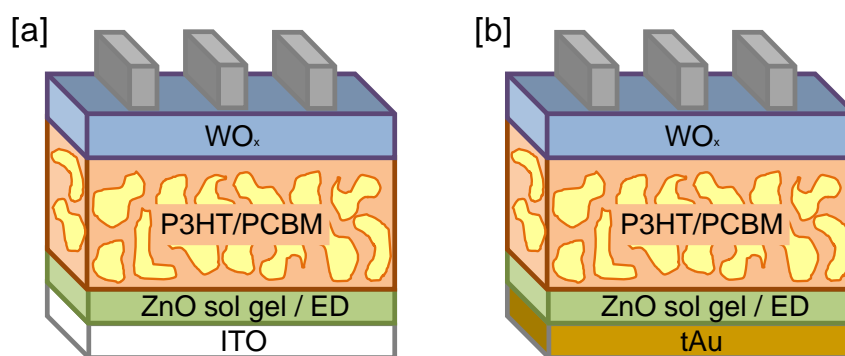


Figure 6.13 A schematic of the different device architecture used in this section.

Figure 6.14 [a] shows the J - V curves of the bilayer devices under both dark and illumination conditions with only the TCE and/or the electron transport layer (ETL) varied. The device parameters for each are summarised in **Table 6.5**. The J_{SC} for each of the devices follows the expected trend from the transparency of the electrode / ETL shown in **Figure 6.13** with the ITO / ZnO_{SG} device having the highest J_{SC} of 9.66 mA cm^{-2} . This is reduced by 6 % if an ED derived ZnO layer is used as the interlayer, merely due to the reduction in transparency across the visible spectrum. There is also a larger variation in J_{SC} for ITO / ZnO_{ED} across pixels and devices shown by a standard deviation of 1.02 compared to 0.59 for the SG layer. This is due to the differences in transparency across the film for the ED layer. The J_{SC} of the tAu

electrodes are significantly lower due to the issues with transparency of the gold films maximising only at $\sim 60\%$. When a ZnO layer is deposited on top, the transparency of the film significantly increases due to optical properties of the thin film. As a result the devices have an averaged J_{SC} of 8.15 and 7.49, a 16% and 22% reduction in J_{SC} for tAu / ZnO_{SG} and tAu / ZnO_{ED} respectively when compared to ITO / ZnO_{SG}.

Table 6.5 Averaged device characteristics for four different devices: electrode ITO/tAu / ZnO_{SG/ED} / P3HT:PCBM / WO_x / Al. The standard deviation for each parameter is shown in brackets.

Electrode	Method	J_{SC} (mA cm ⁻²)	V_{OC} (V)	FF	PCE (%)
ITO	SG	9.66 (0.59)	0.57 (0.02)	0.57 (0.05)	3.22 (0.43)
ITO	ED	9.11 (1.02)	0.53 (0.02)	0.48 (0.03)	2.38 (0.42)
tAu	SG	8.15 (1.07)	0.57 (0.01)	0.59 (0.04)	2.82 (0.53)
tAu	ED	7.49 (1.11)	0.39 (0.13)	0.40 (0.10)	1.28 (0.79)

The FF is another feature which is affected by the choice of deposition method. For the SG method a FF of ~ 0.58 is achieved for both electrodes. This is typical for a P3HT:PCBM system and similar values have been published elsewhere.¹⁷⁴ The reduction in FF to 0.48 and increase in R_S for ITO / ZnO_{ED} can be attributed to the increase in surface roughness compared to that of the SG derived films, as shown earlier in **Figure 6.8**. However for tAu / ZnO_{ED} the averaged FF is considerably lower at 0.40 with a large variation across pixel resulting in a standard deviation 0.10. Unlike ITO / ZnO_{ED} this cannot be attributed to the large surface roughness, which is in the region of 10 nm so other losses must be considered in this instance.

As can be seen by the averaged J - V curve, the device is very leaky and has issues with a lower R_{SH} .

The V_{OC} of the devices also varies considerably. Unsurprisingly with the same energetics shown in **Figure 6.12** the V_{OC} of the SG derived layers is constant regardless of electrode, with a V_{OC} of 0.57 which is the expected value for this device architecture. The V_{OC} for the ED layers however is reduced to 0.53 V for ITO / ZnO_{ED} and the averaged V_{OC} is much lower for the tAu (0.39 V). The main issue with the tAu / ZnO_{ED} device is the inconsistency across pixels due to leaks with a variation between 0.18 V and 0.56 V and therefore the averaged V_{OC} is considerably lower than voltages achieved on some pixels.

Due to the issues associated with the ED thin films the device performance is therefore noticeably lower. The PCE for the SG derived layers are 3.22 % and 2.82 % for ITO / ZnO_{SG} and tAu / ZnO_{SG} respectively, with the difference due to the transparency issues associated with the Au electrode. The PCE was 2.38 % (ITO / ZnO_{ED}) and 1.28 % (tAu / ZnO_{ED}). The fundamental issue with the ITO / ZnO_{ED} films is the roughness of the formed layer, and the overall film thickness (> 230 nm measured by SEM), reducing the overall transparency. This is an issue with ED as a technique as maintaining controlled growth with thin metal oxide layers to ensure it does not have an adverse effect on transparency is difficult. One of the suggestion for increased film roughness is due to the polycrystalline nature of the ITO resulting in different growth rates of the ZnO on the different crystal faces, supported by the low roughness when using gold as the substrate which only has one preferred orientation (111). The issue with the tAu / ZnO_{ED} devices however is not initially apparent when just considering the surface roughness of the film. CAFM explored in *Section 6.3.3.3* showed that despite the film exhibiting a low surface roughness there

are large dead spots across the film ($> 1 \mu\text{m}^2$) and this is a common feature at various locations across the film which in turn is likely to cause variations in both V_{OC} and FF .

Figure 6.14 [b] shows the EQE for each of the device architectures used. In this instance due to a large variation from pixel to pixel, an EQE has been used that best represents the average performance of the cell. The first thing to note is that for ED layers, the onset in EQE response does not occur until 330 nm, this matches the transmittance spectra shown in **Figure 6.5**, with a thick ZnO layer varying the optical properties of the film. The EQE also scales with the measured currents for each, with the main limitation in EQE response for the tAu substrates, limiting the response of the PCBM in the EQE . The ITO / ZnO_{SG} has the highest EQE response across nearly all wavelengths, with a maximum value of 55 % at 510 nm.

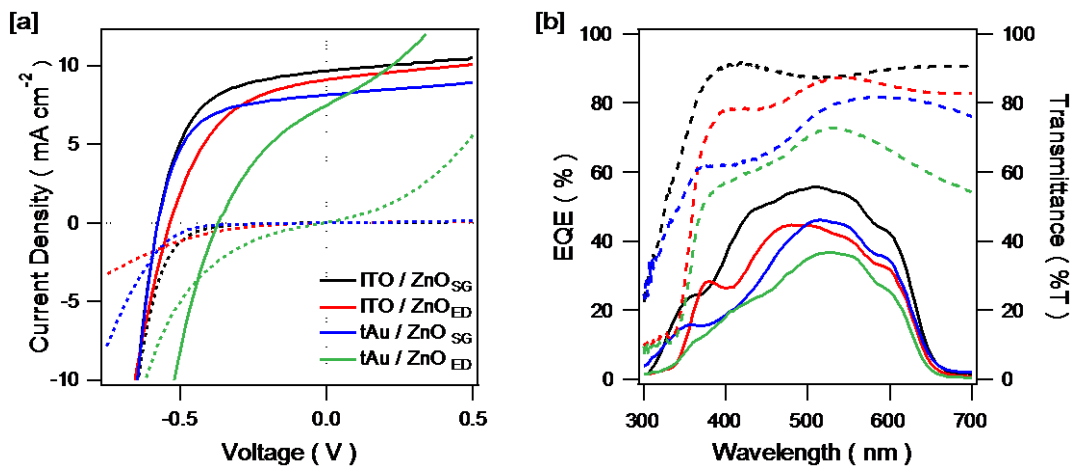


Figure 6.14 [a] Averaged current density vs voltage characteristics for ITO / ZnO_{SG} (black solid line), ITO / ZnO_{ED} (red solid line), tAu / ZnO_{SG} (blue solid line) and tAu / ZnO_{ED} (green solid line). The corresponding dark current density-voltage plots are shown with the dotted lines. Also shown in **[b]** is a representative EQE of the all the devices used (solid line), with the corresponding transmittance for each film.

6.4 Conclusions

In this chapter the use of ZnO as an ETL has been explored focusing on two commonly used active layers. In the first section of this chapter the combination of a solution processed ZnO layer is explored with the commonly used vacuum deposited small molecules SubPc / C₆₀. A SG derived ZnO layer was optimised showing it to be a viable alternative to BCP when adopting an inverted architecture. BCP, a highly insulating material, requires the introduction of defects states to effectively extract charges. This is normally achieved when a hot metal contact is deposited on top. This process does not occur when an inverted architecture is adopted, and although the *FF* can be improved by illumination on the film by the time a respectable *FF* is reached, the illumination causes a reduction in the cells performance due to a lower *J_{SC}*.

ED and SG derived ZnO films were also compared, but owing to the large surface roughness of the ED films the performance was explored using a P3HT:PCBM active layer. In this section, the film characteristics were compared with particular interest in how the substrate used can impact the deposition of the ZnO film. This was achieved by using a tAu substrate as a direct comparison to the commonly used ITO. The main limitation of the tAu film is the transmission which is > 30 % lower than that of ITO.

These studies found that the surface morphology varied depending on deposition technique with a nanoridged structure (discussed previously in **Chapter 3**) for SG films, but this was not a feature for the ED materials regardless of substrate. The transmission of the ED films was also lower across all wavelengths due to the issues with controlling film growth and thickness using this technique. Over several

batches of ZnO ED deposited films, the film thickness was on average recorded at 200 nm, compared to 40 nm for SG films.

As well as film thickness, another key issue with ED process is the impact of dipping the film into a solution as this is likely to impact the surface conductivity and therefore the deposition of the subsequent ZnO layers. This phenomenon was explored using CAFM, and it was found that the conductivity of the electrodes could be improved through ozone exposure but this was only temporary with the current typically reducing to around 100 pA when being left in air. CAFM also highlighted issues with the films that cannot be seen in the topography. This was insightful for explaining why there was such a variation in cell performance for tAu / ZnO_{ED} despite the films surface appearing smooth and homogenous, the surface had large areas with little or no conductivity. This results in a low *PCE* of 1.28 % for a P3HT:PCBM device, compared to 3.22 % for the ITO / ZnO_{SG} film.

7 Conclusions and Future Work

7.1 Overview

Continuous advancements in materials, concept development and scientific understanding are necessary in order to make (H)OPV a viable, clean renewable energy source. Despite OPVs surpassing the 10 % milestone, more research is imperative to ensure this source reaches its potential as a cost effective energy power source. One field of OPVs that has attracted considerable scientific output is the use of inverted cell architectures, with a low work function modified ITO as a transparent electron extracting electrode. Inverted architectures are desirable as they offer the potential of using solution processed low work function IL for electron transport with a heat treatment step if required, preventing damage to the active layer. The architecture can also improve light harvesting as with active materials in an alternate position. Therefore there is the potential to place the D and A in a more favourable optical field depending on the band gap of the material. This thesis has focused on optimising a ZnO layer and improving cell performance in inverted OPV and HOPV devices.

7.1.1 ZnO as an acceptor material

ZnO is a widely published, extensively researched oxide semiconductor. This material is considered for a broad range of applications due to its large piezoelectric coefficient, low cost, non-toxicity and abundance. **Chapter 3** focused on the use of

ZnO as an alternative acceptor material in a true hybrid device. This field has been dominated by ZnO combined with polymeric materials and the results have been noteworthy, at 2 % efficiency, considering only one material contributes to the J_{SC} . The performance with SM organic semiconductor materials however, have shown significantly less potential, with the highest performing cell currently standing at 0.017 %.⁷⁸ The focus of this chapter was to close the gap on the performances of the two types of hybrid cells.

Initial studies concentrated on the morphology of ZnO thin films which are prone to readily and spontaneously form nanostructures. Controlling the morphology of these layers is vital in order to ensure reproducible smooth layers for reliable and consistent device performance. This was achieved by controlling the concentration, annealing temperature and processing conditions. The optimum annealing temperature and conditions were essential as they governed the removal of the organic components from the precursor blend necessary. The orientation of the film due to differences in thermal expansion of the ZnO film and ITO substrates which often result in a nanoridged film were also controlled. Smooth ZnO thin films were produced using an optimised 0.25 M solution which was spin coated then left to stand in air for fifteen minutes before annealing.

The optimised film was utilised with a SubPc organic donor layer for the formation of hybrid devices. The principle of hybrid solar cells and interfacial states formed between the inorganic and organic layer are still not fully understood, so an assumption has to be made that the energetics at the interface determine the maximum achievable V_{OC} , similar to an organic/organic heterojunction. XPS and KP measurements of the ZnO/SubPc interface showed that the ZnO preparation conditions, particularly the annealing temperature, have a significant impact on the

composition of the ZnO layers and the electronic properties of the interface, most notably the work function and hence the I_g . The performances achieved significantly outperform other results in the same field in the literature, with a *PCE* of 0.38 % (ZnO_{120 °C}) and 0.45 % (ZnO_{160 °C}). The difference in cell performance was attributed to a change in V_{OC} between the two device architectures, with the lower temperature processing at 120 °C resulting in a ZnO work function of 3.20 eV and the highest V_{OC} of 1.18 V, a consequence of the increased I_g . These results suggest that the use of SM organic semiconductors with high quality TMO films represent a good opportunity to produce new types of HOPV devices, with precise control of donor material offered by vacuum deposition.

7.1.2 Probing material energetics

Chapter 4 investigated two techniques commonly used to form an energetic profile at the interface between two materials of interest. UPS is widely regarded as the technique of choice because it provides the absolute minimum work function as a result of film biasing as opposed to KP which provides the average work function. UPS also provides additional information, the HOMO/VB onset, whereas only the VB onset can alternatively be probed using XPS due to the photoionization cross section.

Despite the two techniques providing similar conclusions to explain performance differences with processing temperature, the respective positions of CB/VB of ZnO were significantly different. In order to investigate this further, UPS measurements were obtained every minute for one hour. This revealed a significant decrease in work function directly related to exposure time. Due to sensitivity of the ZnO films,

scanning direction (i.e. from low to high/high to low kinetic energy), scan rate and subtle differences in start time/film alignment made a considerable difference to the values obtained. These changes corresponded to a removal of contaminants at the surface (investigated by XPS before and after the UPS measurements). From this study, it should be noted that the material under investigation should be explored in detail to discover whether UPS is an accurate way of obtaining the work function and $V_B/HOMO_{\text{onset}}$ values alike prior to publication.

7.1.3 Improvement in J_{SC}

One of the main limitations of the hybrid solar cells discussed in **Chapter 3** was the low J_{SC} . The implementation of an optical spacer layer has proven to be a beneficial approach to reduce these losses and has been successfully implemented in a range of devices. In **Chapter 5** this potential for cell improvement was considered further. The hybrid cell architecture was modelled using n and k data obtained for the optimised ZnO thin film. Unsurprisingly, when just considering light absorption by the active layers, the model predicted a significant increase in current due to the increased number of photons absorbed with thicker donor layers. In reality, this of course was not the case, with an increase in film thickness resulting in a reduction in FF due to increased recombination and an imbalance of charges. To account for this, the diffusion length (taken from literature) was implemented into the model, giving an exciton generation rate at nanometre increments within the layer and a revised prediction of the current with different thicknesses of the donor and spacer layer.

To confirm the success of this strategy, the predicted model was evaluated experimentally. By increasing the MoO_x thickness from 10 to 40 nm the J_{SC}

remarkably increased by 64 % from 1.51 mA cm^{-2} to 2.48 mA cm^{-2} , and resulted in a similar 62 % improvement in *PCE* from 0.45 % to 0.73 %. If the spacer layer thickness is increased further, the photocurrent decreased due to shifting the SubPc layer out of its maximum optical electric field intensity. The optimised device also gave a high peak *EQE* response of 32 %, placing the ZnO/SubPc system in direct competition with the state-of-the-art polymer/TMO planar system.

7.1.4 ZnO as an Efficient Electron Extracting Layer

Efficient charge selective contacts in OPV devices are a critical layer in order to minimise any recombination losses and extract the maximum achievable performance for a given system. ZnO as a potential electron extracting layer was investigated in **Chapter 6**. Initially ZnO was presented as a direct replacement for BCP which is inefficient when grown in an inverted architecture as it requires the introduction of defect states for efficient cell performance. An optimised ZnO layer was shown to be a viable alternative for inverted architectures giving a *PCE* of 3.42 % with a C₆₀/ SubPc active layer.

Alternate ZnO layers were formed by the ED process (Imperial College London). Owing to the high surface roughness of these films, a polymeric active layer, P3HT:PCBM was deemed the most suitable active material combination. The performances of these cells were compared to the optimised ZnO SG derived layers. The use of different transparent conductive electrodes (ITO and tAu) were also explored to investigate how the underlying electrode can impact ZnO film formation.

The main difference between electrodes was the transmission with tAu > 30 % lower than that of ITO. The transmission was also reduced for the ED films due to issues with controlling film growth and complications with minimising overall film thickness (commonly resulting in a film thickness > 200 nm) and resulted in rougher films when compared to the SG process.

The practicality of the ED process was investigated using CAFM. The process of ED relies on a conductive electrode which is held in the required solution until the processing conditions have been applied. CAFM revealed that merely leaving the electrodes in air resulted in a reduction in current with 61 % of the surface below 100 pA (at a +100 mV bias), which is likely to cause issues when depositing the ZnO film. The technique was also insightful for explaining why the tAu / ZnO_{ED} had low cell performance despite the films surface appearing smooth and homogenous, with CAFM revealing large areas with little or no conductivity.

It was concluded that in all instances the ITO outperformed the tAu electrodes. The main parameter for this was the J_{SC} due to a higher transmittance of the electrode. Also, in all instances the SG films outperformed the ED films. This was due to a reduction in FF likely to be due to an increased surface roughness when adopting an ED route for ZnO film production and a reduced optical transparency. The performance was further reduced for tAu / ZnO_{ED}, with a low PCE of 1.28 % for a P3HT:PCBM device due to issues in conductivity, compared to 3.22 % for the ITO / ZnO_{SG} film. This shows the viability of the ZnO_{SG} film as an extracting layer in combination with polymeric donor materials.

7.2 Future work

The work presented here provides an important step in understanding the fundamental principles governing the operation of hybrid solar cells and probing the interface between two different material classes. In order to truly reach their potential the research community ideally needs to continue investigate the impact of combining two materials with such dissimilar dielectric constants and mobilities.

It has been widely published that ideally the donor material should have a band gap of ~ 1.5 eV to be able to harvest a large proportion of the solar spectrum while still maintaining a LUMO level offset sufficient enough for charge extraction. Inorganic materials offer a potential partnership to the organic donor material due to the ability to tune the energy levels through the alterations to the processing steps or as a result of modifications to the dimensions of a nanoparticle. This, if successfully implemented offers tunability and the potential of maximising the V_{OC} . The reproducibility, scalability and stability are of course all fundamental features that need to be met for hybrid solar cells to be a potential long term solution.

The work demonstrated in **Chapter 3** revealed that ZnO thin films are a potential acceptor material, with a simple SG method processing effective layers. The ZnO/SubPc device architecture was the first of its kind in the field with any significant performance. This shows that the TMO/SM architecture is worth developing further, with future work focusing on improving the FF of the devices (attributed to a poor surface conductivity). This potentially can be achieved by either altering the production method or by introducing dopants such as gallium to the SG recipe to increase the conductivity and therefore improve the FF .

The study revealed significant differences in performance simply by varying the processing temperature by 40 °C. XPS was effectively used to gain insight into the impact this had on properties of the film at the surface which is vital when considering the formation at the interface. Secondary Ion Mass Spectrometry (SIMS) could potentially be another interesting technique offering the potential of composition changes within the film with depth.

Chapter 4 highlights a very important issue when obtaining energetic measurements using a UV source. This development is significant in the field, as the susceptibility of the material to a UV source is not commonly mentioned in literature. This is applicable in a broad sense as the possibility of film damage during data acquisition needs to be ruled out. This research is significant as literature values that previously have been accepted may not provide the most accurate results.

The material combination of an inorganic acceptor and small molecule donor offers the potential of inverted tandem cells, with each sub cell only having one material contributing to the overall J_{SC} . This offers the potential of harvesting across the entire solar spectrum, while maintaining the properties of the inorganic material throughout each sub-cell. A future consideration should be to use a ZnO/organic molecule solution processed blend or implementing ZnO vertically-aligned nanostructures to provide a higher interfacial area between the donor and acceptor material and for efficient charge transfer. This work is necessary to truly close the gap on the hybrid inorganic/polymeric research as prior to this study; ZnO with an organic small molecule has not shown any potential as a working material combination.

References

1. *International Energy Outlook 2013*, U.S. Energy Information Administration, 2013
2. *62nd edition of the BP Statistical Review of World Energy*, BP, 2013
3. N. R. Council, *Hidden Costs of Energy - Unpriced Consequences of Energy and Production and Use*, The National Academies Press, Washington, D.C, 2010.
4. S. Saoshiro, in *Reuters*, Reuters, 2011.
5. S. B. Darling and F. You, *RSC Advances*, 2013, **3**, 17633-17648.
6. J. R. Moreira and A. D. Poole, *Hydropower and its constraints*, Island Press, Washington, DC, USA, 1993.
7. D. H. Wirth, in *Division Director Photovoltaic Modules, Systems and Reliability*, Fraunhofer ISE, May 28. 2014.
8. U. K. Government, Renewable statistics, 8 May, 2014.
9. A. E. Becquerel, *Comptes Rendus*, 1839, **11**, 561-567.
10. W. Smith, *Nature*, 1873, **7**, 303.
11. C. E. Fritts, *American Journal of Science*, 1883, **26**, 465.
12. R. Ohl, *US Patent*, 1941.
13. M. A. Green, *Progress in Photovoltaics: Research and Applications*, 2009, **17**, 183-189.
14. D. M. Chapin, C. S. Fuller and G. L. Pearson, *Journal of Applied Physics*, 1954, **25**, 676-677.
15. *Bell Laboratories Record*, May 1955
16. S. De Wolf, A. Descoedres, C. Holman Zachary and C. Ballif, *Green*, 2012, **2**, 7.
17. J. Zhao, A. Wang, M. A. Green and F. Ferrazza, *Applied Physics Letters*, 1998, **73**, 1991-1993.
18. W. Shockley and H. J. Queisser, *Journal of Applied Physics*, 1961, **32**, 510.
19. http://www.nrel.gov/ncpv/images/efficiency_chart.jpg, Accessed May 22nd, 2014
20. S. Holger and F. C. Krebs, *Solar Energy Materials and Solar Cells*, 2004, **83**, 125.
21. A. Hübler, B. Trnovec, T. Zillger, M. Ali, N. Wetzold, M. Mingeback, A. Wagenpfahl, C. Deibel and V. Dyakonov, *Advanced Energy Materials*, 2011, **1**, 1018-1022.
22. N. K. Unsworth, I. Hancox, C. Argent Dearden, T. Howells, P. Sullivan, R. S. Lilley, J. Sharp and T. S. Jones, *Applied Physics Letters*, 2013, **103**, 173304.
23. A. A. Letailleur, F. Ribot, C. Boissière, J. Teisseire, E. Barthel, B. Desmazières, N. Chemin and C. Sanchez, *Chemistry of Materials*, 2011, **23**, 5082-5089.
24. M. Riede, T. Mueller, W. Tress, R. Schueppel and K. Leo, *Nanotechnology*, 2008, **19**, 424001.
25. F. C. Krebs, *Solar Energy Materials and Solar Cells*, 2009, **93**, 394-412.
26. Heliatek, Heliatek consolidates its technology leadership by establishing a new world record for organic solar technology with a cell efficiency of 12%, Accessed June 5th, 2013.

27. A. Pochettino, *Acad. Lincei Rend*, 1906, **15**, 355.
28. M. Volmer, *Annales Physik*, 1913, **40**, 775.
29. H. Hoppe and N. S. Sariciftci, *Journal of Materials Research*, 2004, **19**, 1924-1945.
30. P. J. Reucroft, K. Takahashi and H. Ullal, *Applied Physics Letters*, 1974, **25**, 664-666.
31. C. W. Tang, *Applied Physics Letters*, 1986, **48**, 183.
32. M. Hiramoto, H. Fujiwara and M. Yokoyama, *Journal of Applied Physics*, 1992, **72**, 3781-3787.
33. W. Cao and J. Xue, *Energy & Environmental Science*, 2014, **7**, 2123-2144.
34. L. Dou, J. You, Z. Hong, Z. Xu, G. Li, R. A. Street and Y. Yang, *Advanced Materials*, 2013, **25**, 6642-6671.
35. X. Xiao, J. D. Zimmerman, B. E. Lassiter, K. J. Bergemann and S. R. Forrest, *Applied Physics Letters*, 2013, **102**, 073302.
36. A. K. K. Kyaw, D. H. Wang, V. Gupta, J. Zhang, S. Chand, G. C. Bazan and A. J. Heeger, *Advanced Materials*, 2013, **25**, 2397-2402.
37. X. R. Tong, B. E. Lassiter and S. R. Forrest, *Organic Electronics*, 2010, **11**, 705-709.
38. M. Riede, C. Urich, J. Widmer, R. Timmreck, D. Wynands, G. Schwartz, W.-M. Gnehr, D. Hildebrandt, A. Weiss, J. Hwang, S. Sundarraj, P. Erk, M. Pfeiffer and K. Leo, *Advanced Functional Materials*, 2011, **21**, 3019-3028.
39. R. Schueppel, R. Timmreck, N. Allinger, T. Mueller, M. Furno, C. Urich, K. Leo and M. Riede, *Journal of Applied Physics*, 2010, **107**, 044503.
40. Y. Yuan, J. Huang and G. Li, *Green*, 2011, **1**, 65.
41. P. Gomez-Romero, *Advanced Materials*, 2001, **13**, 163-174.
42. M. Wright and A. Uddin, *Solar Energy Materials and Solar Cells*, 2012, **107**, 87-111.
43. H.-C. Chen, C.-W. Lai, I. C. Wu, H.-R. Pan, I. W. P. Chen, Y.-K. Peng, C.-L. Liu, C.-h. Chen and P.-T. Chou, *Advanced Materials*, 2011, **23**, 5451-5455.
44. W. W. He, K. J. Wu, K. Wang, T. F. Shi, L. Wu, S. X. Li, D. Y. Teng and C. H. Ye, *Scientific Reports*, 2014, **4**, 3715.
45. I. Gur, N. A. Fromer, M. L. Geier and A. P. Alivisatos, *Science*, 2005, **310**, 462-465.
46. S. Dayal, N. Kopidakis, D. C. Olson, D. S. Ginley and G. Rumbles, *Nano Letters*, 2009, **10**, 239-242.
47. J. Huang, Z. Huang, Y. Yang, H. Zhu and T. Lian, *Journal of the American Chemical Society*, 2010, **132**, 4858-4864.
48. I. Gonzalez-Valls and M. Lira-Cantu, *Energy & Environmental Science*, 2009, **2**, 19-34.
49. J. E. Brandenburg, X. Jin, M. Kruszynska, J. Ohland, J. Kolny-Olesiak, I. Riedel, H. Borchert and J. Parisi, *Journal of Applied Physics*, 2011, **110**, 064509.
50. M. Skompska, *Synthetic Metals*, 2010, **160**, 1-15.
51. J. Boucle, P. Ravirajan and J. Nelson, *Journal of Materials Chemistry*, 2007, **17**, 3141-3153.
52. N. C. Greenham, X. Peng and A. P. Alivisatos, *Physical Review B*, 1996, **54**, 17628-17637.
53. H. Weller, *Angewandte Chemie International Edition in English*, 1993, **32**, 41-53.

54. W. W. Yu, L. Qu, W. Guo and X. Peng, *Chemistry of Materials*, 2003, **15**, 2854-2860.
55. J. Jasieniak, L. Smith, J. v. Embden, P. Mulvaney and M. Califano, *The Journal of Physical Chemistry C*, 2009, **113**, 19468-19474.
56. M. Lira-Cantu, A. Chafiq, J. Faissat, I. Gonzalez-Valls and Y. Yu, *Solar Energy Materials and Solar Cells*, 2011, **95**, 1362-1374.
57. J. Huang, Z. Yin and Q. Zheng, *Energy & Environmental Science*, 2011, **4**, 3861-3877.
58. Y.-B. Hahn, *Korean Journal of Chemical Engineering*, 2011, **28**, 1797-1813.
59. L. Schmidt-Mende and J. L. MacManus-Driscoll, *Materials Today*, 2007, **10**, 40-48.
60. L. Motiei, Y. Yao, J. Choudhury, H. Yan, T. J. Marks, M. E. van der Boom and A. Facchetti, *Journal of the American Chemical Society*, 2010, **132**, 12528-12530.
61. D. C. Olson, Y.-J. Lee, M. S. White, N. Kopidakis, S. E. Shaheen, D. S. Ginley, J. A. Voigt and J. W. P. Hsu, *The Journal of Physical Chemistry C*, 2007, **111**, 16640-16645.
62. W. J. E. Beek, M. M. Wienk and R. A. J. Janssen, *Advanced Materials*, 2004, **16**, 1009-1013.
63. D. J. D. Moet, L. J. A. Koster, B. de Boer and P. W. M. Blom, *Chemistry of Materials*, 2007, **19**, 5856-5861.
64. D. C. Olson, S. E. Shaheen, M. S. White, W. J. Mitchell, M. F. A. M. van Hest, R. T. Collins and D. S. Ginley, *Advanced Functional Materials*, 2007, **17**, 264-269.
65. C. Goh, S. R. Scully and M. D. McGehee, *Journal of Applied Physics*, 2007, **101**, 114503.
66. T. Xu and Q. Qiao, *Energy & Environmental Science*, 2011, **4**, 2700-2720.
67. J. Davenas, V. Barlier, V.-B. Legaré, B. Canut, A. Rybak, A. Slazak and J. Jung, *physica status solidi (a)*, 2010, **207**, 1627-1630.
68. S. D. Oosterhout, M. M. Wienk, S. S. van Bavel, R. Thiedmann, L. Jan Anton Koster, J. Gilot, J. Loos, V. Schmidt and R. A. J. Janssen, *Nature Materials*, 2009, **8**, 818-824.
69. D. C. Olson, J. Piris, R. T. Collins, S. E. Shaheen and D. S. Ginley, *Thin Solid Films*, 2006, **496**, 26-29.
70. P. E. Shaw, A. Ruseckas and I. D. W. Samuel, *Advanced Materials*, 2008, **20**, 3516-3520.
71. L. Baeten, B. Conings, H.-G. Boyen, J. D'Haen, A. Hardy, M. D'Olieslaeger, J. V. Manca and M. K. Van Bael, *Advanced Materials*, 2011, **23**, 2802-2805.
72. P. Ruankham, L. Macaraig, T. Sagawa, H. Nakazumi and S. Yoshikawa, *The Journal of Physical Chemistry C*, 2011, **115**, 23809-23816.
73. W.-P. Liao and J.-J. Wu, *The Journal of Physical Chemistry Letters*, 2013, **4**, 1983-1988.
74. G. E. Morse and T. P. Bender, *ACS Applied Materials & Interfaces*, 2012, **4**, 5055-5068.
75. G. D. Sharma, R. Kumar, S. K. Sharma and M. S. Roy, *Solar Energy Materials and Solar Cells*, 2006, **90**, 933-943.
76. L. Shen, G. Zhu, W. Guo, C. Tao, X. Zhang, C. Liu, W. Chen, S. Ruan and Z. Zhong, *Applied Physics Letters*, 2008, **92**, 073307.
77. M. Izaki, R. Chizaki, T. Saito, K. Murata, J. Sasano and T. Shinagawa, *ACS Applied Materials & Interfaces*, 2013, **5**, 9386-9395.

78. M. Izaki, R. Hisamatsu, T. Saito, K. Murata, J. Sasano and T. Shinagawa, *RSC Advances*, 2014, **4**, 14956-14961.
79. B. O'Regan and M. Grätzel, *Nature*, 1991, **353**, 737-740.
80. M. Grätzel, *Journal of Photochemistry and Photobiology C: Photochemistry Reviews*, 2003, **4**, 145-153.
81. A. Hagfeldt, G. Boschloo, L. Sun, L. Kloo and H. Pettersson, *Chemical Reviews*, 2010, **110**, 6595-6663.
82. M. K. Nazeeruddin, E. Baranoff and M. Grätzel, *Solar Energy*, 2011, **85**, 1172-1178.
83. M. M. Lee, J. Teuscher, T. Miyasaka, T. N. Murakami and H. J. Snaith, *Science*, 2012, **338**, 643-647.
84. J. H. Noh, S. H. Im, J. H. Heo, T. N. Mandal and S. I. Seok, *Nano Letters*, 2013, **13**, 1764-1769.
85. J. H. Heo, S. H. Im, J. H. Noh, T. N. Mandal, C.-S. Lim, J. A. Chang, Y. H. Lee, H.-j. Kim, A. Sarkar, K. Nazeeruddin, M. Grätzel and S. I. Seok, *Nature Photonics*, 2013, **7**, 486-491.
86. P. P. Boix, K. Nonomura, N. Mathews and S. G. Mhaisalkar, *Materials Today*, 2014, **17**, 16-23.
87. M. Liu, M. B. Johnston and H. J. Snaith, *Nature*, 2013, **501**, 395-398.
88. H. J. Snaith, *The Journal of Physical Chemistry Letters*, 2013, **4**, 3623-3630.
89. B. Conings, L. Baeten, C. De Dobbelaere, J. D'Haen, J. Manca and H.-G. Boyen, *Advanced Materials*, 2014, **26**, 2041-2046.
90. A. Abrusci, S. D. Stranks, P. Docampo, H.-L. Yip, A. K. Y. Jen and H. J. Snaith, *Nano Letters*, 2013, **13**, 3124-3128.
91. J. M. Ball, M. M. Lee, A. Hey and H. J. Snaith, *Energy & Environmental Science*, 2013, **6**, 1739-1743.
92. D.-Y. Son, J.-H. Im, H.-S. Kim and N.-G. Park, *The Journal of Physical Chemistry C*, 2014, **118**, 16567-16573.
93. G. H. Wannier, *Physical Review*, 1937, **52**, 191-197.
94. J. Frenkel, *Physical Review*, 1931, **37**, 17-44.
95. S. Blumstengel, S. Sadofev, C. Xu, J. Puls and F. Henneberger, *Physical Review Letters*, 2006, **97**, 237401.
96. S. E. Gledhill, B. Scott and B. A. Gregg, *Journal of Materials Research*, 2005, **20**, 3167-3179.
97. Y. Lin, Y. Li and X. Zhan, *Chemical Society Reviews*, 2012, **41**, 4245-4272.
98. W. A. Luhman and R. J. Holmes, *Advanced Functional Materials*, 2011, **21**, 764-771.
99. S. Gélinas, A. Rao, A. Kumar, S. L. Smith, A. W. Chin, J. Clark, T. S. van der Poll, G. C. Bazan and R. H. Friend, *Science*, 2014, **343**, 512-516.
100. J. D. Servaites, M. A. Ratner and T. J. Marks, *Energy & Environmental Science*, 2011, **4**, 4410-4422.
101. A. Troisi, *Faraday Discussions*, 2013, **163**, 377-392.
102. D. Veldman, S. C. J. Meskers and R. A. J. Janssen, *Advanced Functional Materials*, 2009, **19**, 1939-1948.
103. J. Xue, S. Uchida, B. P. Rand and S. R. Forrest, *Applied Physics Letters*, 2004, **84**, 3013-3015.
104. T. M. Clarke and J. R. Durrant, *Chemical Reviews*, 2010, **110**, 6736-6767.
105. S. R. Forrest, *Nature*, 2004, **428**, 911-918.

106. H. Kim, C. M. Gilmore, A. Piqué, J. S. Horwitz, H. Mattoussi, H. Murata, Z. H. Kafafi and D. B. Chrisey, *Journal of Applied Physics*, 1999, **86**, 6451-6461.
107. A. M. Gheidari, E. A. Soleimani, M. Mansorhoseini, S. Mohajerzadeh, N. Madani and W. Shams-Kolahi, *Materials Research Bulletin*, 2005, **40**, 1303-1307.
108. C. W. Tang and S. A. VanSlyke, *Applied Physics Letters*, 1987, **51**, 913-915.
109. S. Schäfer, A. Petersen, T. A. Wagner, R. Kniprath, D. Lingenfeller, A. Zen, T. Kirchartz, B. Zimmermann, U. Würfel, X. Feng and T. Mayer, *Physical Review B*, 2011, **83**, 165311.
110. I. Hamberg, A. Hjortsberg and C. G. Granqvist, *Applied Physics Letters*, 1982, **40**, 362-364.
111. N. G. Patel, P. D. Patel and V. S. Vaishnav, *Sensors and Actuators B: Chemical*, 2003, **96**, 180-189.
112. D. S. Ginley, *Handbook of transparent conductors*, Springer New York, 2010.
113. R. Bel Hadj Tahar, T. Ban, Y. Ohya and Y. Takahashi, *Journal of Applied Physics*, 1998, **83**, 2631-2645.
114. B. Azzopardi, C. J. M. Emmott, A. Urbina, F. C. Krebs, J. Mutale and J. Nelson, *Energy & Environmental Science*, 2011, **4**, 3741-3753.
115. Y. Kato, M.-C. Jung, M. V. Lee and Y. Qi, *Organic Electronics*, 2014, **15**, 721-728.
116. N. R. Armstrong, P. A. Veneman, E. Ratcliff, D. Placencia and M. Brumbach, *Accounts of Chemical Research*, 2009, **42**, 1748-1757.
117. Y. Zhou, J. W. Shim, C. Fuentes-Hernandez, A. Sharma, K. A. Knauer, A. J. Giordano, S. R. Marder and B. Kippelen, *Physical Chemistry Chemical Physics*, 2012, **14**, 12014-12021.
118. M. O. Reese, M. S. White, G. Rumbles, D. S. Ginley and S. E. Shaheen, *Applied Physics Letters*, 2008, **92**, 053307.
119. R. Steim, F. R. Kogler and C. J. Brabec, *Journal of Materials Chemistry*, 2010, **20**, 2499-2512.
120. J. Yu, T.-L. Shen, W.-H. Weng, Y.-C. Huang, C.-I. Huang, W.-F. Su, S.-P. Rwei, K.-C. Ho and L. Wang, *Advanced Energy Materials*, 2012, **2**, 245-252.
121. N. Beaumont, I. Hancox, P. Sullivan, R. A. Hatton and T. S. Jones, *Energy & Environmental Science*, 2011, **4**, 1708-1711.
122. S. K. Hau, H.-L. Yip, O. Acton, N. S. Baek, H. Ma and A. K. Y. Jen, *Journal of Materials Chemistry*, 2008, **18**, 5113-5119.
123. C. J. Brabec, S. E. Shaheen, C. Winder, N. S. Sariciftci and P. Denk, *Applied Physics Letters*, 2002, **80**, 1288-1290.
124. G. Li, C.-W. Chu, V. Shrotriya, J. Huang and Y. Yang, *Applied Physics Letters*, 2006, **88**, 253503.
125. H. Gommans, B. Verreert, B. P. Rand, R. Muller, J. Poortmans, P. Heremans and J. Genoe, *Advanced Functional Materials*, 2008, **18**, 3686-3691.
126. P. Peumans, V. Bulović and S. R. Forrest, *Applied Physics Letters*, 2000, **76**, 2650-2652.
127. S. Kirchmeyer and K. Reuter, *Journal of Materials Chemistry*, 2005, **15**, 2077-2088.
128. M. Jørgensen, K. Norrman and F. C. Krebs, *Solar Energy Materials and Solar Cells*, 2008, **92**, 686-714.

129. M. P. de Jong, L. J. van IJzendoorn and M. J. A. de Voigt, *Applied Physics Letters*, 2000, **77**, 2255-2257.
130. K. Kawano, R. Pacios, D. Poplavskyy, J. Nelson, D. D. C. Bradley and J. R. Durrant, *Solar Energy Materials and Solar Cells*, 2006, **90**, 3520-3530.
131. S. Schumann, R. Da Campo, B. Illy, A. C. Cruickshank, M. A. McLachlan, M. P. Ryan, D. J. Riley, D. W. McComb and T. S. Jones, *Journal of Materials Chemistry*, 2011, **21**, 2381-2386.
132. T. Stubhan, N. Li, N. A. Luechinger, S. C. Halim, G. J. Matt and C. J. Brabec, *Advanced Energy Materials*, 2012, **2**, 1433-1438.
133. K. X. Steirer, P. F. Ndione, N. E. Widjonarko, M. T. Lloyd, J. Meyer, E. L. Ratcliff, A. Kahn, N. R. Armstrong, C. J. Curtis, D. S. Ginley, J. J. Berry and D. C. Olson, *Advanced Energy Materials*, 2011, **1**, 813-820.
134. I. Hancox, L. A. Rochford, D. Clare, P. Sullivan and T. S. Jones, *Applied Physics Letters*, 2011, **99**, 013304.
135. I. Hancox, P. Sullivan, K. V. Chauhan, N. Beaumont, L. A. Rochford, R. A. Hatton and T. S. Jones, *Organic Electronics*, 2010, **11**, 2019-2025.
136. K. Zilberberg, H. Gharbi, A. Behrendt, S. Trost and T. Riedl, *ACS Applied Materials & Interfaces*, 2012, **4**, 1164-1168.
137. T. Kuwabara, T. Nakayama, K. Uozumi, T. Yamaguchi and K. Takahashi, *Solar Energy Materials and Solar Cells*, 2008, **92**, 1476-1482.
138. G. L. Frey, K. J. Reynolds and R. H. Friend, *Advanced Materials*, 2002, **14**, 265-268.
139. T. K. Gupta, *Journal of the American Ceramic Society*, 1990, **73**, 1817-1840.
140. E. M. Kaidashev, M. Lorenz, H. v. Wenckstern, A. Rahm, H.-C. Semmelhack, K.-H. Han, G. Benndorf, C. Bundesmann, H. Hochmuth and M. Grundmann, *Applied Physics Letters*, 2003, **82**, 3901-3903.
141. A. M. Peiro, P. Ravirajan, K. Govender, D. S. Boyle, P. O'Brien, D. D. C. Bradley, J. Nelson and J. R. Durrant, *Journal of Materials Chemistry*, 2006, **16**, 2088-2096.
142. G. Adamopoulos, A. Bashir, W. P. Gillin, S. Georgakopoulos, M. Shkunov, M. A. Baklar, N. Stingelin, D. D. C. Bradley and T. D. Anthopoulos, *Advanced Functional Materials*, 2011, **21**, 525-531.
143. Y. Sun, J. H. Seo, C. J. Takacs, J. Seifert and A. J. Heeger, *Advanced Materials*, 2011, **23**, 1679-1683.
144. J. Bao, M. A. Zimmler, F. Capasso, X. Wang and Z. F. Ren, *Nano Letters*, 2006, **6**, 1719-1722.
145. S. Basu and A. Dutta, *Materials Chemistry and Physics*, 1997, **47**, 93-96.
146. D. C. Olson, Y.-J. Lee, M. S. White, N. Kopidakis, S. E. Shaheen, D. S. Ginley, J. A. Voigt and J. W. P. Hsu, *The Journal of Physical Chemistry C*, 2008, **112**, 9544-9547.
147. S. T. Meyers, J. T. Anderson, C. M. Hung, J. Thompson, J. F. Wager and D. A. Keszler, *Journal of the American Chemical Society*, 2008, **130**, 17603-17609.
148. A. Janotti and C. G. V. d. Walle, *Reports on Progress in Physics*, 2009, **72**, 126501.
149. V. Bhosle, A. Tiwari and J. Narayan, *Journal of Applied Physics*, 2006, **100**, 033713.
150. U. Ozgur, Y. I. Alivov, C. Liu, A. Teke, M. A. Reshchikov, S. Dogan, V. Avrutin, S.-J. Cho and H. Morkoc, *Journal of Applied Physics*, 2005, **98**, 041301.

151. E. L. Ratcliff, A. K. Sigdel, M. R. Macech, K. Nebesny, P. A. Lee, D. S. Ginley, N. R. Armstrong and J. J. Berry, *Thin Solid Films*, 2012, **520**, 5652-5663.
152. C. Klingshirn, *A European Journal of Chemical Physics and Physical Chemistry*, 2007, **8**, 782-803.
153. D. P. Norton, Y. W. Heo, M. P. Ivill, K. Ip, S. J. Pearton, M. F. Chisholm and T. Steiner, *Materials Today*, 2004, **7**, 34-40.
154. Z. Y. Xiao, Y. C. Liu, R. Mu, D. X. Zhao and J. Y. Zhang, *Applied Physics Letters*, 2008, **92**, 052106.
155. M. Joseph, H. Tabata and T. Kawai, *Japanese Journal of Applied Physics*, 1999, **38**, 1205.
156. N. McKeown, *Phthalocyanine materials - Synthesis, structure and function*, Cambridge University Press, Cambridge, 1998.
157. R. P. B. Linstead, *Report of the British Association for the Advancement of Science*, 1933, **465**.
158. H. Lee, J. W. Jung, T. Deno and M. Ohwa, Google Patents, 2011.
159. E. Ortí, J. L. Brédas and C. Clarisse, *The Journal of Chemical Physics*, 1990, **92**, 1228-1235.
160. K. M. S. Karl M. Kadish, Roger Guilard, *The Porphyrin Handbook*, San Diego, California, 2003.
161. A. Meller and A. Ossko, *Monatshefte für Chemie / Chemical Monthly*, 1972, **103**, 150-155.
162. C. G. Claessens, D. Gonzalez-Rodriguez and T. Torres, *Chemical Reviews*, 2002, **102**, 835-853.
163. H. H. P. Gommans, D. Cheyns, T. Aernouts, C. Giroto, J. Poortmans and P. Heremans, *Advanced Functional Materials*, 2007, **17**, 2653-2658.
164. K. L. Mutolo, E. I. Mayo, B. P. Rand, S. R. Forrest and M. E. Thompson, *Journal of the American Chemical Society*, 2006, **128**, 8108-8109.
165. P. Sullivan, A. Duraud, I. Hancox, N. Beaumont, G. Mirri, J. H. R. Tucker, R. A. Hatton, M. Shipman and T. S. Jones, *Advanced Energy Materials*, 2011, **1**, 305-305.
166. H. W. Kroto, J. R. Heath, S. C. O'Brien, R. F. Curl and R. E. Smalley, *Nature*, 1985, **318**, 162-163.
167. W. Kratschmer, L. D. Lamb, K. Fostiropoulos and D. R. Huffman, *Nature*, 1990, **347**, 354-358.
168. D. C. a. B. R. P. Heremans, *Accounts of Chemical Research*, 2009, **42**, 1740-1747.
169. B. P. Rand, J. Xue, S. Uchida and S. R. Forrest, *Journal of Applied Physics*, 2005, **98**, 124902.
170. G. Yu, J. Gao, J. C. Hummelen, F. Wudl and A. J. Heeger, *Science*, 1995, **270**, 1789-1791.
171. L. Ye, S. Zhang, D. Qian, Q. Wang and J. Hou, *The Journal of Physical Chemistry C*, 2013, **117**, 25360-25366.
172. G. D. Sharma, P. Suresh, J. A. Mikroyannidis and M. M. Stylianakis, *Journal of Materials Chemistry*, 2010, **20**, 561-567.
173. B. Walker, C. Kim and T.-Q. Nguyen, *Chemistry of Materials*, 2010, **23**, 470-482.
174. M. T. Dang, L. Hirsch and G. Wantz, *Advanced Materials*, 2011, **23**, 3597-3602.

175. Y. Kim, S. Cook, S. M. Tuladhar, S. A. Choulis, J. Nelson, J. R. Durrant, D. D. C. Bradley, M. Giles, I. McCulloch, C.-S. Ha and M. Ree, *Nature Materials*, 2006, **5**, 197-203.
176. V. Saini, Z. Li, S. Bourdo, E. Dervishi, Y. Xu, X. Ma, V. P. Kunets, G. J. Salamo, T. Viswanathan, A. R. Biris, D. Saini and A. S. Biris, *The Journal of Physical Chemistry C*, 2009, **113**, 8023-8029.
177. H. Sirringhaus, P. J. Brown, R. H. Friend, M. M. Nielsen, K. Bechgaard, B. M. W. Langeveld-Voss, A. J. H. Spiering, R. A. J. Janssen, E. W. Meijer, P. Herwig and D. M. de Leeuw, *Nature*, 1999, **401**, 685-688.
178. T.-A. Chen, X. Wu and R. D. Rieke, *Journal of the American Chemical Society*, 1995, **117**, 233-244.
179. M. D. McGehee, *MRS Bulletin*, 2009, **34**, 95-100.
180. A. J. Moulé and K. Meerholz, *Advanced Materials*, 2008, **20**, 240-245.
181. A. Ng, X. Liu, W. Y. Jim, A. B. Djurišić, K. C. Lo, S. Y. Li and W. K. Chan, *Journal of Applied Polymer Science*, 2014, **131**, 39776.
182. B. A. Collins, J. R. Tumbleston and H. Ade, *The Journal of Physical Chemistry Letters*, 2011, **2**, 3135-3145.
183. M. Al-Ibrahim, O. Ambacher, S. Sensfuss and G. Gobsch, *Applied Physics Letters*, 2005, **86**, 201120.
184. Y. Zhao, Z. Xie, Y. Qu, Y. Geng and L. Wang, *Applied Physics Letters*, 2007, **90**, 043504.
185. W. Wang, H. Wu, C. Yang, C. Luo, Y. Zhang, J. Chen and Y. Cao, *Applied Physics Letters*, 2007, **90**, 183512.
186. B. N. Illy, A. C. Cruickshank, S. Schumann, R. Da Campo, T. S. Jones, S. Heutz, M. A. McLachlan, D. W. McComb, D. J. Riley and M. P. Ryan, *Journal of Materials Chemistry*, 2011, **21**, 12949-12957.
187. Y. Bessekhoud, D. Robert and J. V. Weber, *Journal of Photochemistry and Photobiology A Chemistry*, 2003, **157**, 47-53.
188. D. P. Macwan, P. N. Dave and S. Chaturvedi, *Journal of Materials Science*, 2011, **46**, 3669-3686.
189. H. Dislich and E. Hussmann, *Thin Solid Films*, 1981, **77**, 129-140.
190. C. Brinker and G. Scherer, *The Physics and Chemistry of Sol-Gel Processing*, Academic Press Limited, London, 1990.
191. J. Livage, *Journal of Solid State Chemistry*, 1986, **64**, 322-330.
192. N. Niederberger and N. Pinna, *Metal Oxide Nanoparticles in Organic Solvents*, Springer, 2009.
193. S. Hellstrom, *Stanford University*, 2007.
194. K. Norrman, A. Ghanbari-Siahkali and N. B. Larsen, *Annual Reports Section C Physical Chemistry*, 2005, **101**, 174-201.
195. S. Peulon and D. Lincot, *Advanced Materials*, 1996, **8**, 166-170.
196. M. Izaki and T. Omi, *Applied Physics Letters*, 1996, **68**, 2439-2440.
197. A. C. Cruickshank, S. E. R. Tay, B. N. Illy, R. Da Campo, S. Schumann, T. S. Jones, S. Heutz, M. A. McLachlan, D. W. McComb, D. J. Riley and M. P. Ryan, *Chemistry of Materials*, 2011, **23**, 3863-3870.
198. R. F. Salzman, J. Xue, B. P. Rand, A. Alexander, M. E. Thompson and S. R. Forrest, *Organic Electronics*, 2005, **6**, 242-246.
199. F. Yang, M. Shtein and S. R. Forrest, *Nature Materials*, 2005, **4**, 37-41.
200. W. Kowalsky, T. Benstem, A. Bohler, S. Dirr, H. H. Johannes, D. Metzendorf, H. Neuner, J. Schobel and P. Urbach, *Physical Chemistry Chemical Physics*, 1999, **1**, 1719-1725.

201. A. J. Lewis, *Characterisation of organic materials for photovoltaic devices*, PhD thesis, University of St. Andrews, 2006.
202. T. H. Gfroerer, in *Encyclopedia of Analytical Chemistry*, John Wiley & Sons, Ltd, 2006.
203. S. Adachi, *Physical Review B*, 1991, **43**, 12316-12321.
204. A. R. Forouhi and I. Bloomer, *Physical Review B*, 1986, **34**, 7018-7026.
205. L. A. A. Pettersson, L. S. Roman and O. Inganäs, *Journal of Applied Physics*, 1999, **86**, 487-496.
206. P. Peumans, A. Yakimov and S. R. Forrest, *Journal of Applied Physics*, 2003, **94**, 3693.
207. G. Binnig, C. F. Quate and C. Gerber, *Physical Review Letters*, 1986, **56**, 930-933.
208. F. J. Giessibl, *Reviews of Modern Physics*, 2003, **75**, 949.
209. K. Van Holde, P. S. Ho and C. Jonhson, *Principles of Physical Biochemistry*, Prentice Hall, Lebanon, Indiana, U.S.A, 2nd Edition edn., 2005.
210. W. Melitz, J. Shen, A. C. Kummel and S. Lee, *Surface Science Reports*, 2011, **66**, 1-27.
211. http://www.nobelprize.org/nobel_prizes/physics/laureates/1921/index.html, Accessed May 23rd, 2014
212. N. Bloembergen, A.L. Schawlow and K. Siegbahn, *Electron Spectroscopy for Atoms, Molecules and Condensed Matter. Nobel Lectures, Physics 1981-1990*, World Scientific Publishing Co., Singapore, 1993.
213. I. G. John C. Vickerman, *Surface Analysis: The Principal Techniques*, John Wiley & Sons, West Sussex, United Kingdom, 2009.
214. N. Farley, *Casa XPS Manual, 2.3.15, Introduction to XPS and AES*, www.casaxps.com, 2009.
215. J. E. Parrott, *Solar Energy*, 1993, **51**, 195.
216. B. Qi and J. Wang, *Physical Chemistry Chemical Physics*, 2013, **15**, 8972-8982.
217. S. Choi, W. J. Potscavage and B. Kippelen, *Journal of Applied Physics*, 2009, **106**, 054507.
218. A. Guerrero, T. Ripolles-Sanchis, P. P. Boix and G. Garcia-Belmonte, *Organic Electronics*, 2012, **13**, 2326-2332.
219. J. D. Servaites, S. Yeganeh, T. J. Marks and M. A. Ratner, *Advanced Functional Materials*, 2010, **20**, 97-104.
220. W. J. Potscavage, S. Yoo and B. Kippelen, *Applied Physics Letters*, 2008, **93**, 193308.
221. R. A. Marsh, C. Groves and N. C. Greenham, *Journal of Applied Physics*, 2007, **101**, 083509.
222. A. Gadisa, M. Svensson, M. R. Andersson and O. Inganäs, *Applied Physics Letters*, 2004, **84**, 1609-1611.
223. T. Ishwara, D. D. C. Bradley, J. Nelson, P. Ravirajan, I. Vanseveren, T. Cleij, D. Vanderzande, L. Lutsen, S. Tierney, M. Heeney and I. McCulloch, *Applied Physics Letters*, 2008, **92**, 053308.
224. P. Peumans and S. R. Forrest, *Applied Physics Letters*, 2001, **79**, 126-128.
225. A. Wilke, J. Endres, U. Hörmann, J. Niederhausen, R. Schlesinger, J. Frisch, P. Amsalem, J. Wagner, M. Gruber, A. Opitz, A. Vollmer, W. Brütting, A. Kahn and N. Koch, *Applied Physics Letters*, 2012, **101**, 233301.

226. N. Beaumont, S. W. Cho, P. Sullivan, D. Newby, K. E. Smith and T. S. Jones, *Advanced Functional Materials*, 2012, **22**, 561-566.
227. S. R. Ferreira, R. J. Davis, Y.-j. Lee, P. Lu and J. W. P. Hsu, *Organic Electronics*, 2011, **12**, 1258-1263.
228. L. Shen, G. H. Zhu, W. B. Guo, C. Tao, X. D. Zhang, C. X. Liu, W. Y. Chen, S. P. Ruan and Z. C. Zhong, *Applied Physics Letters*, 2008, **92**, 073307.
229. J. B. Kim, P. Kim, N. C. Pegard, S. J. Oh, C. R. Kagan, J. W. Fleischer, H. A. Stone and Y.-L. Loo, *Nature Photonics*, 2012, **6**, 327-332.
230. N. Sekine, C.-H. Chou, W. L. Kwan and Y. Yang, *Organic Electronics*, 2009, **10**, 1473-1477.
231. S. J. Kwon, J.-H. Park and J.-G. Park, *Physical Review E*, 2005, **71**, 011604.
232. C.-S. Chen, P.-C. Yang, Y.-M. Shen, S.-Y. Ma, S.-C. Shiu, S.-C. Hung, S.-H. Lin and C.-F. Lin, *Solar Energy Materials and Solar Cells*, 2012, **101**, 180-185.
233. J. Fryar, E. McGlynn, M. O. Henry, A. A. Cafolla and C. J. Hanson, *Nanotechnology*, 2004, **15**, 1797.
234. H. Fritzsche, *Journal of Non-Crystalline Solids*, 1971, **6**, 49-71.
235. M. C. Gwinner, R. D. Pietro, Y. Vaynzof, K. J. Greenberg, P. K. H. Ho, R. H. Friend and H. Sirringhaus, *Advanced Functional Materials*, 2011, **21**, 1432-1441.
236. J. S. Park, Y.-T. Moon, D.-J. Kim, N.-M. Park, T. Yao and S.-J. Park, *Journal of Physics D: Applied Physics*, 2008, **41**, 165103.
237. M. T. Greiner, L. Chai, M. G. Helander, W.-M. Tang and Z.-H. Lu, *Advanced Functional Materials*, 2012, **22**, 4557-4568.
238. H. Ishii, K. Sugiyama, E. Ito and K. Seki, *Advanced Materials*, 1999, **11**, 605-625.
239. H. Gommans, S. Schols, A. Kadashchuk, P. Heremans and S. C. J. Meskers, *Journal of Physical Chemistry C*, 2009, **113**, 2974-2979.
240. R. R. Lunt, N. C. Giebink, A. A. Belak, J. B. Benziger and S. R. Forrest, *Journal of Applied Physics*, 2009, **105**, 053711.
241. C. A. Dearden, M. Walker, N. Beaumont, I. Hancox, N. K. Unsworth, P. Sullivan, C. F. McConville and T. S. Jones, *Physical Chemistry Chemical Physics*, 2014, **16**, 18926-18932.
242. B. Verreet, K. Cnops, D. Cheyns, P. Heremans, A. Stesmans, G. Zango, C. G. Claessens, T. Torres and B. P. Rand, *Advanced Energy Materials*, 2014, **4**, 1301413.
243. W. Tress, A. Merten, M. Furno, M. Hein, K. Leo and M. Riede, *Advanced Energy Materials*, 2013, **3**, 631-638.
244. J. S. Kim, B. Lägél, E. Moons, N. Johansson, I. D. Baikie, W. R. Salaneck, R. H. Friend and F. Cacialli, *Synthetic Metals*, 2000, **111-112**, 311-314.
245. R. J. Davis, M. T. Lloyd, S. R. Ferreira, M. J. Bruzek, S. E. Watkins, L. Lindell, P. Sehati, M. Fahlman, J. E. Anthony and J. W. P. Hsu, *Journal of Materials Chemistry*, 2011, **21**, 1721-1729.
246. M. Lira-Cantu, M. Khoda Siddiki, D. Muñoz-Rojas, R. Amade and N. I. González-Pech, *Solar Energy Materials and Solar Cells*, 2010, **94**, 1227-1234.
247. B. W. D'Andrade, S. Datta, S. R. Forrest, P. Djurovich, E. Polikarpov and M. E. Thompson, *Organic Electronics*, 2005, **6**, 11-20.
248. S. Hufner, J. Osterwalder, T. Riesterer and F. Hulliger, *Solid State Communications*, 1984, **52**, 793-796.

249. S. Gutmann, M. A. Wolak, M. Conrad, M. M. Beerbom and R. Schlaf, *Journal of Applied Physics*, 2010, **107**, 103705.
250. P. D. C. King, T. D. Veal, D. J. Payne, A. Bourlange, R. G. Egdell and C. F. McConville, *Physical Review Letters*, 2008, **101**, 116808.
251. D. A. Melnick, *The Journal of Chemical Physics*, 1957, **26**, 1136-1146.
252. M. R. Lilliedal, A. J. Medford, M. V. Madsen, K. Norrman and F. C. Krebs, *Solar Energy Materials and Solar Cells*, 2010, **94**, 2018-2031.
253. F. Verbakel, S. C. J. Meskers and R. A. J. Janssen, *Applied Physics Letters*, 2006, **89**, 102103.
254. L. Zhang, D. Wett, R. Szargan and T. Chassé, *Surface and Interface Analysis*, 2004, **36**, 1479-1483.
255. B. J. Coppa, C. C. Fulton, P. J. Hartlieb, R. F. Davis, B. J. Rodriguez, B. J. Shields and R. J. Nemanich, *Journal of Applied Physics*, 2004, **95**, 5856-5864.
256. J. Wagner, M. Gruber, A. Hinderhofer, A. Wilke, B. Bröker, J. Frisch, P. Amsalem, A. Vollmer, A. Opitz, N. Koch, F. Schreiber and W. Brütting, *Advanced Functional Materials*, 2010, **20**, 4295-4303.
257. J. Gilot, I. Barbu, M. M. Wienk and R. A. J. Janssen, *Applied Physics Letters*, 2007, **91**, 113520.
258. A. K. K. Kyaw, D. H. Wang, D. Wynands, J. Zhang, T.-Q. Nguyen, G. C. Bazan and A. J. Heeger, *Nano Letters*, 2013, **13**, 3796-3801.
259. Y.-S. Hsiao, F.-C. Chien, J.-H. Huang, C.-P. Chen, C.-W. Kuo, C.-W. Chu and P. Chen, *The Journal of Physical Chemistry C*, 2011, **115**, 11864-11870.
260. J. R. Tumbleston, D.-H. Ko, E. T. Samulski and R. Lopez, *Applied Physics Letters*, 2009, **94**, 043305.
261. Y. Long, *Applied Physics Letters*, 2009, **95**, 193301.
262. K. S. Nalwa, J.-M. Park, K.-M. Ho and S. Chaudhary, *Advanced Materials*, 2011, **23**, 112-116.
263. A. Hadipour, D. Cheyins, P. Heremans and B. P. Rand, *Advanced Energy Materials*, 2011, **1**, 930-935.
264. J. Y. Kim, S. H. Kim, H. H. Lee, K. Lee, W. Ma, X. Gong and A. J. Heeger, *Advanced Materials*, 2006, **18**, 572-576.
265. E. New, T. Howells, P. Sullivan and T. S. Jones, *Organic Electronics*, 2013, **14**, 2353-2359.
266. J. Gilot, M. M. Wienk and R. A. J. Janssen, *Advanced Materials*, 2010, **22**, 67-71.
267. I. Hancox, K. V. Chauhan, P. Sullivan, R. A. Hatton, A. Moshar, C. P. A. Mulcahy and T. S. Jones, *Energy & Environmental Science*, 2010, **3**, 107-110.
268. M. J. Gouterman, *Journal of Chemical Physics*, 1959, **30**, 1139.
269. K. Toyota, J.-y. Hasegawa and H. Nakatsuji, *The Journal of Physical Chemistry A*, 1997, **101**, 446-451.
270. B. Kippelen and J.-L. Bredas, *Energy & Environmental Science*, 2009, **2**, 251-261.
271. J. L. Yang, S. Schumann, R. A. Hatton and T. S. Jones, *Organic Electronics*, 2010, **11**, 1399-1402.
272. H. M. Stec, R. J. Williams, T. S. Jones and R. A. Hatton, *Advanced Functional Materials*, 2011, **21**, 1709-1716.
273. B. P. Rand, J. Li, J. Xue, R. J. Holmes, M. E. Thompson and S. R. Forrest, *Advanced Materials*, 2005, **17**, 2714-2718.

274. Y. Hirose, A. Kahn, V. Aristov, P. Soukiassian, V. Bulovic and S. R. Forrest, *Physical Review B*, 1996, **54**, 13748-13758.
275. J. Huang, J. S. Yu, H. Lin and Y. D. Jiang, *Journal of Applied Physics*, 2009, **105**, 073105.
276. T. Minami, *Semiconductor Science and Technology*, 2005, **20**, S35.
277. F. C. Krebs, T. Tromholt, M. Jørgensen, F. C. Krebs, T. Tromholt and M. Jørgensen, *Nanoscale*, 2010, **2**, 873-886.
278. D. R. Cairns, R. P. Witte, D. K. Sparacin, S. M. Sachsman, D. C. Paine, G. P. Crawford and R. R. Newton, *Applied Physics Letters*, 2000, **76**, 1425-1427.
279. A. Suzuki, T. Matsushita, Y. Sakamoto, N. Wada, T. Fukuda, H. Fujiwara and M. Okuda, *Japanese Journal of Applied Physics*, 1996, **35**, 5457.
280. T. Minami, S. Ida and T. Miyata, *Thin Solid Films*, 2002, **416**, 92-96.
281. J. Wu, H. A. Becerril, Z. Bao, Z. Liu, Y. Chen and P. Peumans, *Applied Physics Letters*, 2008, **92**, 263302.
282. Y. Zhou, C. Fuentes-Hernandez, J. Shim, J. Meyer, A. J. Giordano, H. Li, P. Winget, T. Papadopoulos, H. Cheun, J. Kim, M. Fenoll, A. Dindar, W. Haske, E. Najafabadi, T. M. Khan, H. Sojoudi, S. Barlow, S. Graham, J.-L. Brédas, S. R. Marder, A. Kahn and B. Kippelen, *Science*, 2012, **336**, 327-332.
283. M. W. Rowell, M. A. Topinka, M. D. McGehee, H.-J. Prall, G. Dennler, N. S. Sariciftci, L. Hu and G. Gruner, *Applied Physics Letters*, 2006, **88**, 233506.
284. Y. Galagan, *Photovoltaic Specialists Conference (PVSC), 2012 38th IEEE*, 2012, 003248-003248.
285. H. M. Stec and R. A. Hatton, *ACS Applied Materials & Interfaces*, 2012, **4**, 6013-6020.
286. M. Brumbach, P. A. Veneman, F. S. Marrikar, T. Schulmeyer, A. Simmonds, W. Xia, P. Lee and N. R. Armstrong, *Langmuir*, 2007, **23**, 11089-11099.
287. C. Carter, M. Brumbach, C. Donley, R. D. Hreha, S. R. Marder, B. Domercq, S. Yoo, B. Kippelen and N. R. Armstrong, *The Journal of Physical Chemistry B*, 2006, **110**, 25191-25202.
288. Y. Gassenbauer and A. Klein, *The Journal of Physical Chemistry B*, 2006, **110**, 4793-4801.
289. C. S. M. T. B. Barrett, *Structure of metals : crystallographic methods, principles and data*, Pergamon Press, Oxford, 1980.
290. J. J. Uhlich, D. C. Olson, J. W. P. Hsu and T. F. Kuech, *Journal of Vacuum Science & Technology A*, 2009, **27**, 328-335.